Anomalous spin dynamics in low-dimension: superdiffusion, subdiffusion, and solitons

Dissertation

zur Erlangung des akademischen Grades

Doctor of Philosophy
(Ph. D.)

vorgelegt von

Adam J. McRoberts

Max Planck Institut für Physik komplexer Systeme, Dresden

Wissenschaftlicher Betreuer

Prof. Dr. Roderich Moessner

vorgelegt der

Fakultät Physik
Bereich Mathematik und Naturwissenschaften
Technische Universität Dresden

MMXXIII

To Mum, Dad, Lucy, Molly, and Norrie

Contents

Introduction

As intimated by its title, this thesis is concerned with the anomalous and unexpected dynamical phenomena that can arise in magnetic systems. We will show that some of the simplest spin models can harbour a rich and vibrant phenomenology: with solitary excitations – unprotected by integrability – generating anomalous, superdiffusive hydrodynamics; a model of subdiffusion with a continuously tune-able dynamical exponent; a disorder-resistant regime of ballistic transport; and a new class of meta-stable, prethermal state.

Part of the contribution of this thesis – and a theme to which we shall oft return – is that many examples of phenomena that may, at first, appear to be intrinsically quantum-mechanical, can actually be reproduced in classical systems: the superdiffusion in the quantum Heisenberg chain is present also in the classical Heisenberg chain; its Bethe-ansatz quasiparticles become solitons in the classical limit; and the non-equilibrium transport of boundary-driven classical spin chains exhibits the same dynamical regimes as observed on a quantum simulator.

Indeed, the very idea of *classical* spin dynamics at all perhaps fits within this paradigm. I certainly recall being told that spin is an inherently quantum property – that "intrinsic angular momentum" has no classical analogue. Whilst this is technically true, it is only in the sense that *everything* is, fundamentally, quantum-mechanical; and, to the same extent that we may study the classical physics of bullets or billiards, we are perfectly at liberty to take the classical limit of spin dynamics.

At a quite unnecessary level of mathematical sophistication, a sphere S^2 is a symplectic manifold, endowed with the differential 2-form

$$d\omega = d\phi \wedge dz, \tag{1}$$

which simply measures the (oriented) surface area of the sphere. It is thus a valid phase space, on which Hamiltonian mechanics may be defined.

But perhaps a more physically appealing way of conceiving classical spin dynamics is to invert the procedure of canonical quantisation, familiar from elementary quantum mechanics. That is, instead of promoting variables to operators, and Poisson brackets to commutators, we relegate the spin operators to a unit-length vector, and define the fundamental spin Poisson brackets,

$$[\hat{S}_i^\mu, \hat{S}_j^\nu] = i\hbar\epsilon^{\mu\nu\lambda}\delta_{ij}\hat{S}_j^\lambda \quad \mapsto \quad \{S_i^\mu, S_j^\nu\} = \epsilon^{\mu\nu\lambda}\delta_{ij}S_j^\lambda. \tag{2}$$

Apart from the quantum-classical analogues, the second main thrust of this thesis is to provide a further illustration of the well-known point that when large numbers of degrees of freedom are coupled together, interesting things happen.

Even when we write down, arguably, the simplest possible interacting many-body model of magnetism – the classical Heisenberg chain – unexpected phenomena abound: from solitary excitations that perfectly maintain their form though a combination of interaction and dispersion, to the anomalously fast spin transport these solitons seed in thermal equilibrium, and the decay of domain walls made of linear spin waves into topological solitons when we include anisotropy.

Despite the apparent simplicity of many of the models we study here – and the fact that, for example, the classical Heisenberg chain has been studied for the better part of a century – it is only with modern computational resources and theoretical techniques that we have been able to start to sleuth out the subtle consequences of many-body interactions.

Overview of the thesis

I. Solitons

In the first part of this thesis we examine solitons – localised, non-dissipative excitations – in the dynamics of spin systems.

We open, in chapter 1, with a short account of the history of solitons, from their first observation, to the theories of shallow water and the Korteweg-De Vries model; their appearance in field theories like the sine-Gordon model; to the general description of integrable systems, such as the Toda lattice. We pay particular attention, of course, to solitons in spin models – especially those obtained by Ishimori in an integrable classical spin chain which bears his name.

In chapter 2 we present our work which establishes the existence of solitons in *non-integrable* spin chains. We begin by constructing exact static solitons in the Heisenberg chain, which we connect to the static Ishimori solitons via an adiabatic interpolation. We then use this adiabatic transform to construct moving Heisenberg solitons, which show no sign of having a finite lifetime. We further show that the interactions of these solitons are remarkably similar to the integrable case, and we establish their presence in low temperature thermal states – which will have important consequences in Part II.

In chapter 3 we consider a different set-up, and study the dynamics of domain walls in anisotropic spin chains. Our work shows a striking co-existence of linear and non-linear phenomena – to wit, we show that the free propagation and subdiffusive spreading of domain walls can be captured by non-interacting, linear spin wave theory; but that these domain walls are unstable to decay via the emission of topological solitons.

II. Superdiffusion

In Part II we will show how the solitons we have discovered play a hydrodynamic role, and find that superdiffusion, far from being limited to the special cases where the model is integrable, may be observed in non-integrable spin chains for (arbitrarily) long times, at low – but non-zero – temperatures.

We will, however, preface this with a review of the literature on superdiffusion in *integrable* spin chains in chapter 4.

Chapter 5 presents our work on the existence of superdiffusion in *non-integrable* spin chains – with a particular focus, again, on the classical Heisenberg chain. We show that

the Heisenberg chain exhibits long-lived superdiffusion of spin – with a striking scaling collapse of the correlation function onto the KPZ function across three decades of time at low temperature – but only ordinary diffusion of energy. We present an argument that explains this phenomenology in terms of the solitons we established in Part I.

Further, we examine how the time-scales and temperature-scales of superdiffusion depend on the degree of integrability breaking, by considering the model which interpolates between the Ishimori and Heisenberg chains (and which built the solitons of chapter 2); and, furthermore, show examples of other non-integrable spin chains evincing the same spin superdiffusion at low temperatures.

III. Subdiffusion

We turn, in part III, to the opposite kind of anomalous dynamics – subdiffusion. Chapter 6 provides a brief survey of this type of slow dynamics, and various mechanisms by which it can arise, including kinetic constraints, disorder, and higher-moment (e.g., the dipole moment) conservation of some charge density.

Chapter 7 contains our work on bond-disordered classical Heisenberg chains; the main contribution here is that we provide an interacting model with a continuously tune-able subdiffusive exponent, which we obtain analytically from a related, solvable phenomenological model. This also allows us to obtain the leading corrections to the asymptotic behaviour, clarifying the role of large sub-leading terms in hydrodynamic transport.

IV. Spin dynamics out-of-equilibrium

Parts I – III of this thesis are concerned either with the structure of single excitations above the ground state – an effectively zero temperature regime – or the dynamics of the spins in thermal equilibrium, finding anomalous hydrodynamics both faster and slower than ordinary diffusion. In Part IV, however, we will forswear the canonical ensemble entirely.

In chapter 8, we study the classical version of a boundary-driven quantum spin chain which was the subject of recent experiments by Google Quantum AI. We show that the observed dynamical regimes are not inherently quantum-mechanical, since the classical variant evinces the entire phenomenology observed in the quantum experiments. Moreover, we show that the classical chain is analytically tractable, and that, depending on the degree of anisotropy, either ballistic transport, subdiffusion, or localisation may be found.

We then go beyond the direct comparison with the quantum version and introduce quenched random couplings to the classical model. We find, most strikingly, that the *ballistic* transport regime survives, so long as the disorder is not strong enough to completely sever the chain. We further show how, if we do allow for very strong disorder, different subdiffusive exponents may be obtained.

In chapter 9, we address the consequences of non-reciprocal interactions – in essence, an evasion of Newton's third law – in periodically driven systems. This question emerges from the spin dynamics studied in the previous parts of this thesis because one of the main numerical methods we have used to calculate the time evolution is, intrinsically, a non-reciprocal periodic drive. Whilst Floquet theory – the study of periodically-driven *Hamiltonian* systems – is by now a well-developed field, non-reciprocal systems cannot be described by any Hamiltonian, time-dependent or static, and so the techniques of Floquet

theory do not, *a priori*, apply. The high-frequency regime of Floquet systems typically features long-lived meta-stable (prethermal) states, which has allowed the techniques of Floquet-engineering to produce novel prethermal phases of matter which have no equilibrium counterpart – but the theorem which establishes the prethermal plateau explicitly uses the Hamiltonian formalism.

Nevertheless, by combining the ingredients of non-reciprocity and periodic driving in the context of many-body spin dynamics, we uncover a new class of long-lived prethermal states – independently of dimensionality, support of interactions, or lattice geometry – indicating that non-reciprocal systems may offer a propitious arena to generate new material properties via Floquet-engineering.

Part I

Solitons

Chapter 1

Solitary excitations

Dissipation is a characteristic of all physical systems within common experience: a pond perturbed by a thrown stone soon returns to quiet stillness; radio signals become fainter as they fly out into space; the sound from a plucked string hangs in the air for a time, wavers, then is lost.

More precisely, we mean by dissipation that any finite energy becomes spread throughout the system, with no persistent, local excitations as $t \to \infty$. That is, quite generally, if we have some theory with dynamical variables $\phi(x,t)$ and energy density $\mathcal{E}_{[\phi]}(x,t)$ (bounded below by zero), a configuration is dissipative if, in the thermodynamic limit,

$$\lim_{t\to\infty} \max_x \mathcal{E}_{[\phi]}(x,t) = 0. \tag{1.1}$$

As long as the total energy of the configuration is finite, this is the generic situation. In certain theories, however, there are solutions to the equations of motion which defy this expectation: solitary excitations – solitons[1] – which preserve their spatial profile for all time and move with a constant velocity, enduring against the natural dispersiveness of wavepackets through their own self-interaction.

This peculiar combination of dispersion and interaction is intrinsic to a soliton's existence: non-interacting theories, such as the Klein-Gordon model or non-interacting spin-wave theory, can never admit solitons, as any configuration decomposes into Fourier modes of different velocities each carrying away some part of the total energy.

In this chapter, we will briefly tour the history of soliton excitations, from their first observation on the Union Canal in 1834 [2], to the shallow water model of Korteweg and De Vries [3], their appearance in more general field theories, and various manifestations in condensed matter contexts. We will then discuss their role in the general structure of integrable models, focusing particularly, with an eye to subsequent chapters, on spin chains.

[1] There is a view that the name of "soliton" should apply only to the local excitations of *integrable* models [1]. This is not unjustified, since integrability ensures that individual solitons are perfectly protected during collisions, and, thus, can be uniquely identified throughout any scattering process. Here, however, we prefer to take a view that is more lenient (though a mathematician may incline to call it insouciant): any excitation which is not dissipative in the sense of Eq. (1.1) will be dubbed a soliton. (Though the names "solitary waves" and "solitary excitations" will also be used interchangeably)

1.1 A trip down the Union Canal

1.1.1 Shallow water

The history of solitons begins with a chance encounter in 1834, when John Scott Russell first observed the phenomenon he dubbed the "wave of translation", chasing for two miles a wave "assuming the form of a large solitary elevation, a rounded, smooth and well-defined heap of water, which continued its course along the channel apparently without change of form or diminution of speed" [2].

Russell continued to investigate this phenomenon through experimental work in wave tanks. The solitary wave, however, was controversial; Airy and Stokes pointed out its existence conflicted with the hydrodynamic theories of Newton and Bernoulli. Nevertheless, in 1862 Bazin reported further observations after experiments were conducted in the Canal de Bourgogne [4].

Theoretical studies of solitary waves followed in 1871 from Boussinesq [5], and in 1876 from Lord Rayleigh [6]. Arguably, the most important milestone in the development of soliton theory was introduced in an overlooked footnote by Boussinesq in 1877 [7]; the content of which was rediscovered independently by Korteweg and De Vries in 1895 [3], whose names are borne by the KdV equation:

$$\frac{\partial \eta}{\partial t} = \frac{3}{2}\sqrt{\frac{g}{l}} \cdot \frac{\partial}{\partial x}\left(\frac{1}{2}\eta^2 + \frac{1}{3}\sigma\frac{\partial^2 \eta}{\partial x^2}\right), \tag{1.2}$$

in the original notation, where l is the average depth of the liquid, η is the liquid's height with respect to l, g is the acceleration due to gravity, and σ is related to the surface tension and density (assumed to be constant). The KdV equation is more commonly, however, quoted in its non-dimensionalised form

$$\partial_t \phi + \partial_x^3 \phi - 6\phi\partial_x \phi = 0, \tag{1.3}$$

where, by convention, η has been renamed to ϕ. It is well-known that there is set of soliton solutions to this equation, parameterised by their velocity[2] c, given by

$$\phi(x,t) = \frac{c}{2}\operatorname{sech}^2\left(\frac{\sqrt{c}}{2}(x - x_0 - ct)\right). \tag{1.4}$$

Whilst it is an interesting historical perspective, let us now leave the subject of shallow water and turn to the question of solitons in condensed matter, first in continuum field theories, and then in lattice models directly.

1.1.2 Field theories

As is often done in introductions to solitary waves (e.g., Ref. [1]) let us illustrate some of the main ideas by considering the ϕ^4-theory – which finds a plethora of applications as one of the

[2] In contrast to the ordinary (linear) wave equation, $\partial_t^2 \phi = c^2 \partial_x^2 \phi$, where the speed of the waves is fixed, the soliton velocity is a free parameter.

simplest non-trivial field theories, including in the description of Ising-like phase transitions. Here, our interest lies in this model as a classical field theory,

$$\mathcal{L} = \frac{1}{2}(\partial_t \phi)^2 - \frac{1}{2}(\partial_x \phi)^2 - \frac{\lambda}{2}\left(\phi^2 - \frac{\mu^2}{\lambda}\right)^2, \tag{1.5}$$

with non-dissipative solutions to the equations of motion,

$$\partial_t^2 \phi - \partial_x^2 \phi + 2\mu^2 \phi - 2\lambda \phi^3 = 0, \tag{1.6}$$

where $\mu^2, \lambda > 0$, such that we are in the parameter regime with two distinct ground states[3], $\phi = \pm\phi_0$, $\phi_0 = \sqrt{\mu^2/\lambda}$, and we have chosen the constant offset such that the ground states have zero energy. If we restrict our search, for simplicity, to time-independent configurations, it is easy to see that

$$\phi(x) = \pm\phi_0 \tanh(\mu x) \tag{1.7}$$

fulfils the requirements – it is a non-dissipative, finite energy, constant profile solution of the equations of motion – with the sign dependent on the boundary conditions. Since the ϕ^4-Lagrangian is Lorentz covariant, moving solitons are related to this static soliton by boosts.

The shallow water solitons of the KdV equation (1.3) have the same ground state (the same depth of liquid) at both spatial boundaries, and owe their existence to integrability (see §1.2); here, instead, the solitary waves are kinks which connect the different ground states, and are a particularly simple example of topological solitons – that is, their existence, and stability against small perturbations (though not against annihilation in kink–anti-kink collisions), is topologically guaranteed.

It is not necessary to deploy any heavy mathematical machinery to see this. Let us fix the boundary conditions at $t = 0$ to the different ground states, say,

$$\phi(x \to \pm\infty, t = 0) \to \pm\phi_0, \tag{1.8}$$

and assume only that the initial configuration has finite total energy. But since there are only two disconnected ground states, and the field ϕ evolves continuously, these boundary conditions cannot be changed by the time evolution, as that would violate energy conservation. Moreover, then, since ϕ is continuous,

$$\forall\, t \;\; \exists\, x \;\; \text{s.t.} \;\; \phi(x,t) = 0 \neq \pm\phi_0. \tag{1.9}$$

That is, for all times, there is at least one point where the field is not in its ground state configuration, and so has finite energy density – the topology of the boundary conditions ensures that *any* initial configuration must be non-dissipative, guaranteeing the existence of the solitons.

As this is a topological argument, it is obviously more general than this application to the ϕ^4-theory. Indeed, for any scalar field Lagrangian of the form

$$\mathcal{L} = \frac{1}{2}(\partial_t \phi)^2 - \frac{1}{2}(\partial_x \phi)^2 - V(\phi), \tag{1.10}$$

[3]The parameter regime with a unique ground state $\phi = 0$ serves as an example of an interacting model with no soliton solutions.

where the potential $V(\phi)$ has a discrete set of degenerate global minima, this argument asserts the existence of non-dissipative solitary wave solutions, though it is possible they may not have a closed form. A particularly important model of this class, which both possesses topological solitons as discussed above and is also fully integrable, is the sine-Gordon model,

$$\mathcal{L} = \frac{1}{2}(\partial_t \phi)^2 - \frac{1}{2}(\partial_x \phi)^2 - \frac{\mu^2}{\beta^2}\left(1 - \cos(\beta\phi)\right), \tag{1.11}$$

which arises, for example, as the bosonised description of the 1D Hubbard model [8]. The solitons interpolate between adjacent minima (depending on which branch of the arctangent is chosen), and have the form

$$\phi(x,t) = \frac{4}{\beta}\arctan(\exp(\pm\mu x)). \tag{1.12}$$

We briefly remark that for solitons in higher dimensions it is necessary to go beyond theories of scalar fields, either by introducing gauge degrees of freedom [1], or by including interactions between the different components of some vector field (as in the case of the skyrmions of the non-linear sigma model); but we will confine ourselves to 1D systems throughout this chapter.

For our last example of solitons in a 1D field theory, let us turn away from scalar fields and towards spin dynamics – the main subject of this thesis, after all – and consider the continuum limit of the Heisenberg chain, the lattice form of which is the subject of the next chapter. The Hamiltonian is given by

$$H = \frac{1}{2}\int dx\ (\partial_x \boldsymbol{S})^2, \quad |\boldsymbol{S}| = 1, \tag{1.13}$$

and the equations of motion follow from the continuum limit of the fundamental spin Poisson brackets (2),

$$\{S^\mu(x), S^\nu(x')\} = \epsilon^{\mu\nu\lambda}\delta(x - x')S^\lambda(x'). \tag{1.14}$$

This yields

$$\partial_t \boldsymbol{S} = \boldsymbol{S} \times \partial_x^2 \boldsymbol{S}, \tag{1.15}$$

and we quote the solitons from [9],

$$\begin{aligned}
&S^z(x,t) = 1 - 2\beta^2 \operatorname{sech}^2\left(\beta\sqrt{\omega}(x - vt - x_0)\right), \\
&S^x(x,t) + iS^y(x,t) = \sqrt{1 - S^z(x,t)^2}\exp(i\varphi(x,t)), \\
&\varphi(x,t) = \varphi_0 + \omega t + \frac{v}{2}(x - vt) + \arctan\left(\frac{\beta}{\sqrt{1-\beta^2}}\tanh(\beta\sqrt{\omega}(x - vt - x_0))\right),
\end{aligned} \tag{1.16}$$

where the solitons are indexed by a single complex parameter ζ, in terms of which

$$v = 4\mathrm{Re}\zeta, \quad \omega = 4|\zeta|^2, \quad \beta = \frac{\mathrm{Im}\zeta}{|\zeta|} \tag{1.17}$$

(alternatively, one could consider the the velocity and internal frequency as the two real parameters).

The continuum Heisenberg chain is integrable [10], and, like the shallow water waves, these solitons are non-topological in the sense that they connect the same ground state ($\boldsymbol{S} = \hat{\boldsymbol{z}}$) to itself at the boundaries.

1.1.3 Lattice models

All of our examples of solitons so far have been of continuum field configurations. It is arguably more natural, however, in condensed matter, to consider lattice models; and, moreover, only lattice models will appear in all of the subsequent chapters.

A brief digression is necessary, however, to clarify precisely how we will define a soliton on a lattice. The discrete definition of dissipation (1.1) is obvious enough, so long as a discrete energy density is defined, but we need to consider what is meant by a constant profile. For a continuum scalar field, the condition is the travelling wave ansatz,

$$\phi(x,t) = \phi(x - vt), \tag{1.18}$$

the lattice version of which is

$$\phi_i(t) = \phi_{i+n}(t + n/v); \tag{1.19}$$

which ensures that the profile periodically returns to itself, shifted by an integer number of sites.

With this issue cleared up, let us take for our first example a model which turns out to be a discretisation of the KdV equation. The Toda lattice [11],

$$H = \sum_j \frac{1}{2}p_j^2 + V(q_{j+1} - q_j), \quad V(r) = e^{-r} + r - 1, \tag{1.20}$$

has solitons given by

$$q_j(t) = \overline{q} + \log\left(\frac{1 + \frac{\gamma}{1-e^{-2\kappa}}\exp(-2\kappa j + 2\sigma t\sinh\kappa)}{1 + \frac{\gamma}{1-e^{-2\kappa}}\exp(-2\kappa(j+1) + 2\sigma t\sinh\kappa)}\right), \quad \overline{q} \in \mathbb{R} \tag{1.21}$$

where κ and γ are the two parameters indexing the solutions, related to the width and speed, $\overline{q}$ is the average displacement, and $\sigma = \pm 1$. Like the KdV equation, this is an integrable model [12, 13], and bears a similar relation to the (non-integrable) Fermi-Pasta-Ulam-Tsingou chain [14] as the Ishimori chain (see below) does to the Heisenberg chain (see Ch. 2).

For the second example we have the aforementioned Ishimori chain – an integrable lattice spin chain with known soliton solutions. This model is of particular importance to the next chapter, so we will discuss it in some detail here; the Hamiltonian is [15],

$$\mathcal{H} = -2J\sum_i \log\left(\frac{1 + \boldsymbol{S}_i \cdot \boldsymbol{S}_{i+1}}{2}\right). \tag{1.22}$$

As an integrable model [10, 15–20], it possesses an extensive set of locally conserved charges, besides energy and magnetisation, such as the torsion

$$\tau_i = \frac{\boldsymbol{S}_i \cdot (\boldsymbol{S}_{i+1} \times \boldsymbol{S}_{i-1})}{(1 + \boldsymbol{S}_i \cdot \boldsymbol{S}_{i+1})(1 + \boldsymbol{S}_i \cdot \boldsymbol{S}_{i-1})}, \tag{1.23}$$

which we will use in §2.5 to track soliton trajectories.

The one-soliton solutions are indexed by their inverse-width R and wavenumber k. Two further parameters, x_0 and η_0, are the collective co-ordinates, specifying the position of the

centre at $t = 0$ and the initial phase of the in-plane spin-components, respectively. The explicit solutions are

$$\begin{aligned}
S_i^x(t) &= \frac{\sinh 2R}{\cosh 2R - \cos 2k} \operatorname{sech} \xi_{i+1} \left(\cos \eta_i \left(\cosh 2R + \sinh 2R \tanh \xi_i\right) - \cos(2k - \eta_i)\right), \\
S_i^y(t) &= \frac{\sinh 2R}{\cosh 2R - \cos 2k} \operatorname{sech} \xi_{i+1} \left(-\sin \eta_i \left(\cosh 2R + \sinh 2R \tanh \xi_i\right) - \sin(2k - \eta_i)\right), \\
S_i^z(t) &= 1 - \frac{\sinh^2 2R}{\cosh 2R - \cos 2k} \operatorname{sech} \xi_i \operatorname{sech} \xi_{i+1},
\end{aligned} \tag{1.24}$$

where

$$\begin{aligned}
\xi_n(t) &= 2R \left(n - x_0 - \frac{1}{2}\right) - 2t \sinh 2R \sin 2k, \\
\eta_n(t) &= -2k \left(n - x_0 - \frac{1}{2}\right) + \eta_0 + 2t \left(1 - \cosh 2R \cos 2k\right).
\end{aligned} \tag{1.25}$$

We note that we have to slightly modify the lattice version of the travelling wave ansatz (1.19) to account for the precession of the in-plane components,

$$\begin{aligned}
S_{i+n}^x(t + n/v) &= \cos(n\omega/v) S_i^x(t) - \sin(n\omega/v) S_i^y(t), \\
S_{i+n}^y(t + n/v) &= \sin(n\omega/v) S_i^x(t) + \cos(n\omega/v) S_i^y(t), \\
S_{i+n}^z(t + n/v) &= S_i^z(t),
\end{aligned} \tag{1.26}$$

where v is the velocity of the soliton, and ω is the internal frequency, which, in terms of the chosen physical parameters R and k, are given by

$$v = \frac{\sinh 2R \sin 2k}{R}, \quad \omega = 2kv + 2(\cosh 2R \cos 2k - 1). \tag{1.27}$$

The limit $v \to 0$ (i.e., $k \to 0$) implies that the z-components become stationary, and the in-plane components precess with the internal frequency ω.

The total energy (measured by the Heisenberg Hamiltonian (2.1)), magnetisation (defined as the difference from the vacuum state, i.e., $M = \sum_{n \in \mathbb{Z}} (1 - S_n^z)$), and torsion carried by a soliton are, respectively,

$$E = 4 \tanh 2R, \quad M = \frac{2 \sinh 2R}{\cosh 2R - \cos 2k}, \quad \tau = 2Rv. \tag{1.28}$$

1.2 Integrable models and inverse-scattering

This discussion of solitons behoves at least a cursory review of the general structure of integrable systems, since we have mentioned integrability several times in the above. We shall be summary, since subsequent chapters consist of non-integrable models; but, for the sake of comparison, and because many of the results we have obtained for non-integrable systems bear a striking resemblance to the phenomenology commonly associated with integrability,

some of the salient points are outlined here. More detailed introductions to the subject may be found in Refs. [21, 22].

Integrable models are characterised by the possession of an extensive number of locally conserved charges, and, classically, can be solved by a canonical transformation to the so-called "action-angle" variables [22]. Integrability is equivalent to the existence of a Lax pair of operators L, P (defined in terms of the original dynamical variables) such that

$$\frac{dL}{dt} = [P, L]. \tag{1.29}$$

This implies an extensive hierarchy of conserved charges, since it follows therefrom that

$$\frac{d}{dt}\mathrm{tr}(L^n) = 0, \quad \forall\, n \in \mathbb{N}. \tag{1.30}$$

One of the consequences of this is that integrable models possess a "complete set" of quasiparticles, in the "inverse-scattering" sense that any state of the system can be decomposed into its quasiparticle content. For the integrable models of the previous subsection, of course, these quasiparticles are the solitons.

Heuristically, the inverse-scattering transform proceeds as follows. Consider a system of size L, in some arbitrary state. This state is embedded in some "quasiparticle vacuum" (usually a ground state) devoid of any solitons, of size $N \to \infty$.

We now let the system evolve in time. Since any excitation is initially confined to some finite region of size L, the average energy density is zero, and, in generic, dissipative systems, the finite total energy is eventually smeared throughout the chain, with no persistent, localised excitations. If the system supports solitons, however – and, in particular, if the model is integrable, the asymptotic state as $t \to \infty$ becomes a set of well-separated quasiparticles, each propagating with a characteristic constant velocity.

The utility of this setup becomes apparent when we consider how solitons scatter in integrable systems. Protected by integrability, the asymptotic trajectories of two solitons γ, γ' (where γ denotes the set of all parameters that define a particular soliton) are unchanged except for some scattering-shift $\Delta(\gamma;\gamma')$ (also known as a phase-shift); that is, assuming the solitons are well-separated at $t = 0$, the trajectory of the (centre of the) soliton γ is

$$x_\gamma(t) = x_\gamma(0) + v_\gamma t + \Delta(\gamma;\gamma'). \tag{1.31}$$

Further, any *multi-soliton* collision fully factorises into a sequence of two-body collisions,

$$x_\gamma(t) = x_\gamma(0) + v_\gamma t + \sum_\lambda \Delta(\gamma;\lambda), \tag{1.32}$$

where λ indexes the collision sequence. The use of this is in the "inverse" part of inverse-scattering: from the asymptotic state of well-separated solitons, we can perform a backwards linear extrapolation (we reverse the time evolution with quasiparticle scattering turned off), and the positions of the solitons after this extrapolation give a set of so-called impact-parameters x_∞ – the total shift to the trajectories of the quasiparticles – which encode the soliton structure of the finite-size initial state.

This forms the basis for the thermodynamic Bethe ansatz, which generalises the Gibbs ensemble to account for the hierarchy of conserved quantities, and on which generalised hydrodynamics (GHD) is built [21]. This will return in Ch. 4, as GHD has proved instrumental in our understanding of the anomalous hydrodynamics that many integrable models possess.

1.3 Outlook

In this chapter, we have reviewed the history of solitary waves, and given a (somewhat less restrictive than normal) definition of a soliton. We have seen how solitons arise in the context of the shallow water field theory of Korteweg and De Vries, and discussed how they can arise in other settings, stabilised either by topology, in the case of skyrmions and the ϕ^4-theory and related models; or by integrability, as in the sine-Gordon model, the Toda lattice, or the Ishimori spin chain, as well as the continuum Heisenberg model.

In a sense, however, these solitons owe their existence to these special properties of the models in which they arise. In more generic systems, it is often possible to construct *stationary* solitary solutions of non-linear equations of motion – but perfectly stable, propagating localised objects are not expected, in the absence of protection by topology or integrability [23].

It is to the question of whether this expectation can be confounded that we now turn. In the following Ch. 2 we will present evidence that (moving) solitons *can* survive, with apparently infinite lifetimes (as single excitations – they can still be slightly destabilised by collisions) without any topological protection, in a non-integrable spin chain.

Chapter 2

Solitons in the classical Heisenberg chain

The work in this chapter has appeared as part of the following article [24]:
Adam J. McRoberts, Thomas Bilitewski, Masudul Haque, & Roderich Moessner
Long-lived solitons and their signatures in the classical Heisenberg chain
Phys. Rev. E **106**, L062202 (2022)

In this chapter, we demonstrate the existence of solitons in the classical Heisenberg chain, where they are afforded protection neither by topology nor integrability. We will provide a direct construction of stable (*infinitely* long-lived) stationary solitons, and, by a connection to the Ishimori solitons (1.24), an adiabatic construction of *moving* solitons. A central result is the existence of a family of solitons which are stable over a broad parameter regime (see Fig. 3.3(a)). This is, *a priori*, very surprising for a chain so far believed to be essentially generic. Whilst we cannot prove that the stable adiabatic solitons are infinitely long-lived, there is no numerical indication of a finite lifetime.

Beyond the isolated solitons, we study two-soliton scattering and observe behaviour quite analogous to that of the integrable model. Further, for low-temperature thermal states, we show that solitons are present and can be individually identified even when their density is high; and, finally, by comparing the inverse-scattering of the classical Heisenberg and Ishimori chains we will go further and show that the solitons, in fact, comprise the main content of the low-temperature states.

The solitons we study here will return in Ch. 5, where we will argue they provide a physical basis for the robust KPZ scaling observed at low temperatures in the Heisenberg chain. For now, however, we return our attention to the solitary excitations themselves.

2.1 The classical Heisenberg chain

The classical Heisenberg chain is, perhaps – at least, conceptually – the simplest interacting many-body model of magnetism. The Hamiltonian is given by

$$\mathcal{H} = -J \sum_i \left(\boldsymbol{S}_i \cdot \boldsymbol{S}_{i+1} - 1 \right), \tag{2.1}$$

where $\mathbf{S}_i$ are classical $O(3)$ vectors at sites i of a chain, with nearest-neighbour ferromagnetic interaction strength J, and we have chosen the constant such that the fully-aligned (ferromagnetic) state has zero energy.

The equations of motion follow from the fundamental spin Poisson brackets (2); we thus obtain

$$\dot{\boldsymbol{S}}_i = J \boldsymbol{S}_i \times \left(\boldsymbol{S}_{i-1} + \boldsymbol{S}_{i+1} \right). \tag{2.2}$$

Despite its apparent simplicity, the classical Heisenberg chain remains far from completely understood. As we will discuss in Part II, for example, the nature of its hydrodynamics has been debated for decades, with predictions of ordinary diffusion [25–31] set against claims of different forms of anomalous behaviour [32–36].

2.2 Static solitons: a direct construction

Let us first construct exact, non-dissipative (i.e., soliton) static solutions of the classical Heisenberg chain. For this purpose, it is most expedient to re-write the equations of motion (2.2) in the canonical (ϕ, z) co-ordinates, where they take the form

$$\dot{z}_i = J\sqrt{1-z_i^2}\left[\sqrt{1-z_{i+1}^2}\sin(\phi_{i+1}-\phi_i) - \sqrt{1-z_{i-1}^2}\sin(\phi_i-\phi_{i-1})\right], \tag{2.3}$$

$$\dot{\phi}_i = J\frac{z_i}{\sqrt{1-z_i^2}}\left[\sqrt{1-z_{i+1}^2}\cos(\phi_{i+1}-\phi_i) + \sqrt{1-z_{i-1}^2}\cos(\phi_i-\phi_{i-1})\right] - J(z_{i+1}+z_{i-1}). \tag{2.4}$$

We use an ansatz based on the structure of the stationary ($k = 0$) Ishimori solitons (1.24). We set $z_0 = -1$, $\phi_{i<0}(0) = \varphi$, and $\phi_{i>0}(0) = \varphi + \pi$, for some arbitrary constant φ. If ϕ_i precesses with a uniform frequency, $\phi_i(t) = \phi_i(0) + \omega t$, then $\dot{z}_i = 0\ \forall i$ (the sine factors vanish at all times, unless they contain $i = 0$, in which case one of the square root factors vanishes instead).

We thus aim to find a set of z_i s.t. $\phi_i(t) = \phi_i(0) + \omega t$, for some chosen uniform frequency ω which characterises the soliton. Inserting these conditions into Eq. (2.4), we obtain the consistency equations

$$\omega = J\frac{z_i}{\sqrt{1-z_i^2}}\left(\sqrt{1-z_{i+1}^2} + \sqrt{1-z_{i-1}^2}\right) - J\left(z_{i+1}+z_{i-1}\right), \tag{2.5}$$

which, rearranged for z_i, become

$$\frac{z_i}{\sqrt{1-z_i^2}} = \cot(\theta_i) = \frac{\omega/J + z_{i+1} + z_{i-1}}{\sqrt{1-z_{i+1}^2} + \sqrt{1-z_{i-1}^2}}. \tag{2.6}$$

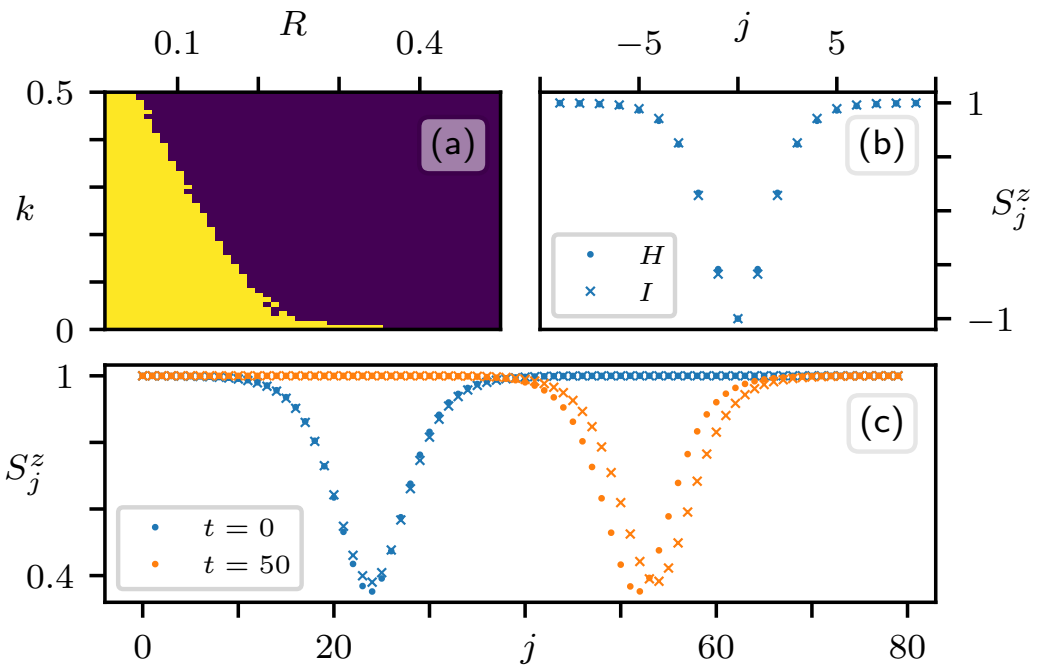

Figure 2.1: Solitons in the classical Heisenberg chain. (a) parameter space of Ishimori solitons for which we found an adiabatically connected soliton in the Heisenberg chain. (b) & (c) comparisons between adiabatically connected solitons (only $z-$component shown) in the Heisenberg (H, $\bullet$) and Ishimori (I, $\times$) chains. The solitons in (b) are stationary, $(R = 0.25, k = 0)$; and in (c) they move, $(R = 0.1, k = 0.15)$. The Heisenberg soliton moves at a slower velocity, but both preserve their initial profile.

We need $z_{-1} = z_1$ to ensure the exchange field at $i = 0$ is parallel to $\hat{\boldsymbol{z}}$, which implies $z_{-i} = z_i \ \forall i$. It thus suffices to solve the consistency equations for $i > 0$. We cannot do this in closed form, but the required z_i may be obtained numerically to arbitrary precision, for any choice of ω.

We note that $\cot : (0, \pi) \to \mathbb{R}, \theta \mapsto \cot(\theta)$ is a bijection, so, given z_{i-1} and z_{i+1}, Eq. (2.6) can be inverted for a unique z_i (so long as at least one of z_{i-1}, z_{i+1} is not at the poles). To solve the consistency equations iteratively, we choose the frequency ω, and begin with the sequence $z_2 = 0$, $z_{i>2} = 1$ (though all that is required is that $-1 < z_2 < 1$). We then obtain z_1 from Eq. (2.6). In the second step, we first solve for a new z_2, and then re-solve for z_1. Continuing the pattern, at the n^{th} step we solve for z_n, and then sweep back to z_1.

Of course, only finite-size solitons can be constructed numerically. We carry out the above procedure until we reach some final z_N (effectively, we approximate $z_{i>N} = +1$, and the chain that this describes has $2N + 1$ sites). To improve the solution, we then perform a number of sweeps in the forward direction, starting with z_1 and solving up to z_N.

To measure how well the numerical solution solves the consistency equations, we define

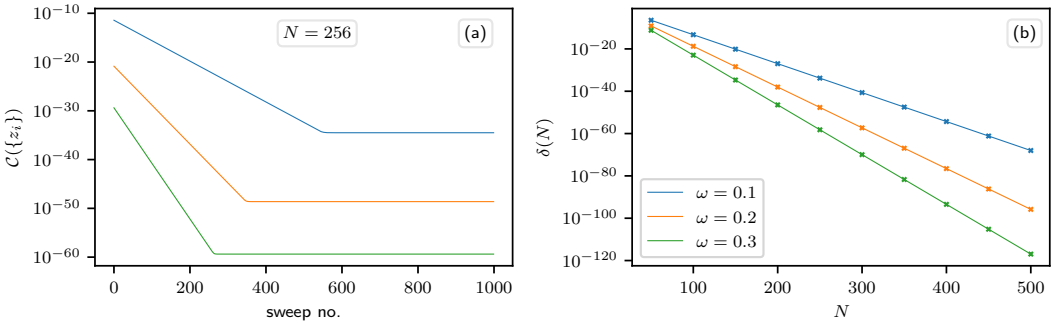

Figure 2.2: Convergence of the iterative procedure for solving the consistency equations (2.6) for selected frequencies and finite sizes. (a) shows the exponential convergence of the cost function to the plateau value, $\delta(N)$, with the number of forward sweeps (z_1 to z_N) – the starting values are those obtained after all the backward sweeps have been completed. (b) shows that $\delta(N) \to 0$ exponentially as $N \to \infty$.

the cost function

$$\mathcal{C}(\{z_i\}) = \left(\sum_{i=1}^{N+1} \left| z_i \left(\sqrt{1 - z_{i+1}^2} + \sqrt{1 - z_{i-1}^2} \right) - \sqrt{1 - z_i^2} \left(\omega/J + z_{i+1} + z_{i-1} \right) \right|^2 \right)^{1/2}, \tag{2.7}$$

shown in Fig. 2.2 versus the number of sweeps performed for select frequencies. We observe that the solution converges exponentially with the number of sweeps, to a plateau value $\delta(N)$ that exponentially decreases with system size.

Whilst we are unable to rigorously prove that the cost function converges to zero, we conjecture, based on the exponential convergence of the numerical solution, that the iterative procedure defines an exact solution of the consistency equations in the limit $N \to \infty$, and, thus, a static soliton of the Heisenberg chain.

2.3 Moving solitons: an adiabatic construction

Some of the models discussed in Ch. 1 possessed either Galilean or Lorentz covariance – from which it follows that moving solitons may be built from static solitons by a simple boost. The spin chains possess no such symmetry, and so the construction of moving solitons is more difficult.

A direct assault in the form of guessing exact solutions to the equations of motion is generally futile for non-integrable systems; instead, we take a more circumspect approach – we will attempt to continuously transform solitons of the Ishimori chain (1.22) into solitons of the non-integrable Heisenberg chain. We take a single soliton of the Ishimori chain (1.24) as the initial conditions, and slowly change the Hamiltonian from that of the Ishimori chain to that of the Heisenberg chain. Following this procedure, it may be directly verified that a static Ishimori soliton is adiabatically connected to the static Heisenberg soliton of §2.2 with the same total magnetisation.

At finite k (i.e., for moving solitons), we find that, for a wide range of Ishimori soliton parameters (R, k) (cf. Fig. 2.1(a)), this procedure successfully transforms the initial state into a soliton of the Heisenberg chain (2.1). We will examine the specific criteria used to determine whether the transformation is successful in §2.3.2, but we note here that there is no indication that these solitary excitations have a finite lifetime; whilst stationary solutions of non-linear classical equations of motion are well known, stable moving solitons are not expected to exist in a generic system [23]. From this perspective, the appearance of propagating, localised objects with apparently unlimited stability is remarkable.

2.3.1 The adiabatic transformation

To interpolate smoothly between the chains, we use the Hamiltonian

$$\mathcal{H} = -2J\gamma^{-1}\sum_i \log\left(1+\gamma\frac{\boldsymbol{S}_i\cdot\boldsymbol{S}_{i+1}-1}{2}\right), \tag{2.8}$$

where the Ishimori chain corresponds to $\gamma = 1$, and the Heisenberg chain to the limit $\gamma \to 0$; with $SO(3)$ symmetry preserved throughout. We set $J = 1$ in the following.

The equations of motion following from Eq. (2.8) are

$$\dot{\boldsymbol{S}}_i = 2\boldsymbol{S}_i \times \left(\frac{\boldsymbol{S}_{i-1}}{2-\gamma+\gamma\boldsymbol{S}_i\cdot\boldsymbol{S}_{i-1}} + \frac{\boldsymbol{S}_{i+1}}{2-\gamma+\gamma\boldsymbol{S}_i\cdot\boldsymbol{S}_{i+1}}\right). \tag{2.9}$$

To transform the initial state into a Heisenberg soliton we continuously tune the interpolating Hamiltonian (2.8) via a C^∞-smooth interpolation,

$$\gamma(t) = \begin{cases} 1 - \frac{e^{-t_A/t}}{e^{-t_A/t}+e^{-t_A/(t_A-t)}} & 0 < t < t_A \\ 0 & t \geq t_A \end{cases} \tag{2.10}$$

from $\gamma = 1$ at $t = 0$ to $\gamma = 0$ at some long adiabatic time t_A. We evolve an initial Ishimori soliton (R, k) under the dynamics of Eq. (2.9), with this time-dependent $\gamma(t)$ given by Eq. (2.10), for some adiabatic time t_A; we then evolve up to some later time t_f under the Heisenberg dynamics (2.1).

The resulting existence diagram (Fig. 2.1(a)) shows that the solitons are stable in the Heisenberg model over a remarkably large range of parameters (R, k), with the narrow solitons apparently becoming unstable first with increasing velocity ($\sim k$).

We find no indication of a finite lifetime of the single soliton states which are stable under this adiabatic procedure (see Fig. 2.4). Moreover, the torsion (1.23) – generally not a conserved quantity of the Heisenberg chain – is conserved in these states, up to numerical accuracy.

We can also examine how the properties of the solitons are modified in the Heisenberg chain. Fig. 2.3 shows that the internal frequency (the frequency with which the in-plane spin-components rotate) and velocity of a Heisenberg soliton are suppressed. The energy (measured in both cases by the Heisenberg Hamiltonian) is only slightly reduced – while the torsion is very slightly higher for the Heisenberg solitons (see also Fig. 2.4). Overall, we note a remarkable similarity between the one-soliton properties in the Ishimori and Heisenberg chains. Differences increase when approaching the boundary of the stability region. i.e., for narrower solitons.

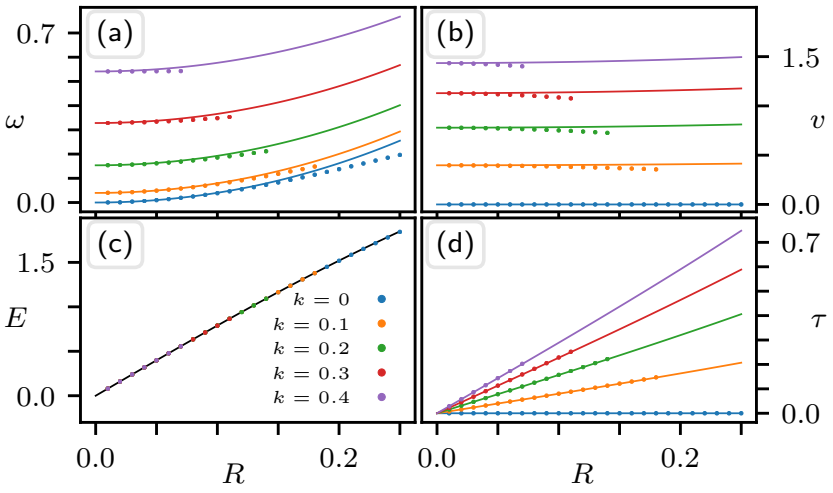

Figure 2.3: Physical properties of the Ishimori solitons (solid lines), compared to Heisenberg solitons (dotted lines – up to the boundary of the existence diagram, Fig. 2.1(a)), shown as a function of inverse-width R, for various values of the wavenumber k. (a), (b), (c), and (d), show, resp., the internal frequency ω, the velocity v, the energy E (measured by the Heisenberg Hamiltonian) and the torsion τ.

2.3.2 Adiabatic stability of the solitons

Let us turn to the question of the stability of the adiabatically constructed solitons, and, in particular, the conditions we use to determine whether the transformation indeed produces a soliton.

The adiabatic time used to calculate the existence diagram (Fig. 2.1(a)) was $t_A = 10^5 J^{-1}$, on a chain of $L = 1024$ sites and periodic boundary conditions (PBCs). The final time of the simulation was $t_f = 2t_A$, i.e., the state was evolved with the Heisenberg equations of motion for a further time of $10^5 J^{-1}$ after the completion of the adiabatic process.

We use the following criteria to assess whether the resultant state is a soliton solution of the Heisenberg chain:

- $\forall\, t$, there is a unique local minimum of z_i, up to a numerical tolerance of 10^{-8}.
- $\forall\ t > t_A$, the unique local minimum propagates with a constant velocity v. More precisely, since the position of the centre can only be measured to integer precision, the condition is: $\exists\, v, x_0 \in \mathbb{R}$ s.t. $\forall t > t_A$, $|\min_i z_i - (x_0 + vt)| < 1$.
- $\forall\ t > t_A$, the torsion $\tau = \sum_i \tau_i$ is constant in time, up to a tolerance of 10^{-8}. The torsion is not a conserved quantity of the Heisenberg chain, but is constant for the solitary wave solutions.

The first condition ensures that no pulses are emitted, as happens if a soliton of the Ishimori/Heisenberg chain is evolved with the other Hamiltonian without an initial adiabatic

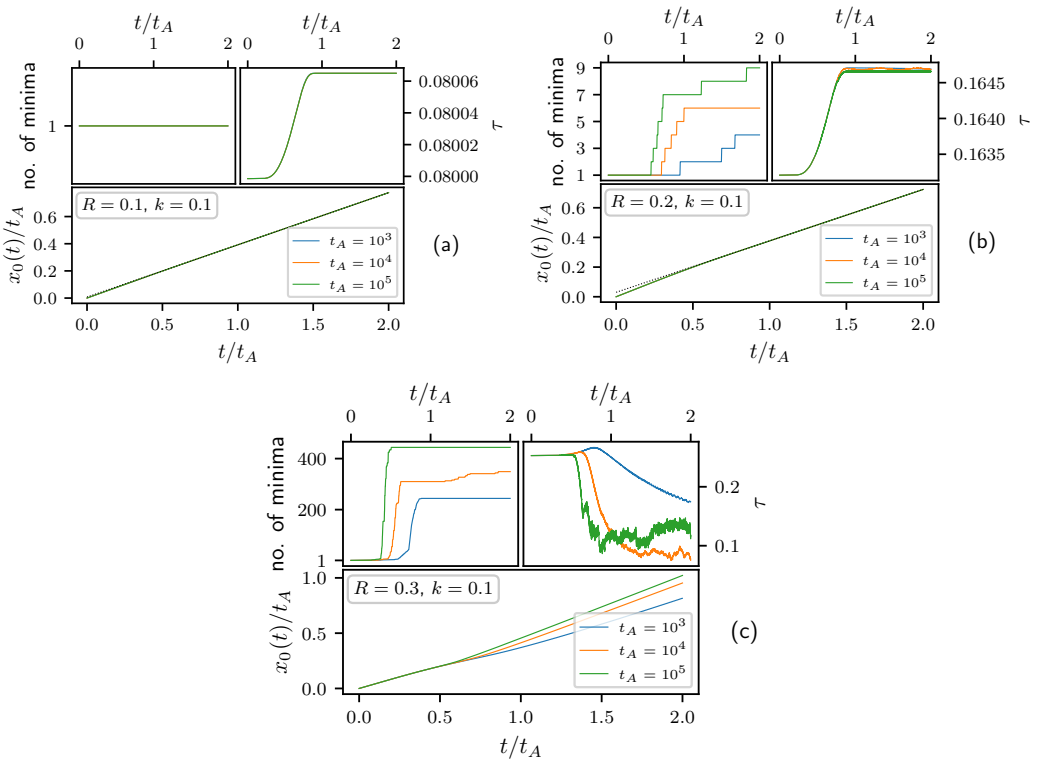

Figure 2.4: Adiabatic stability of the solitons. (a) shows that the Ishimori soliton $R = 0.1, k = 0.1$ is adiabatically connected to a Heisenberg soliton: no additional local minima are generated, the centre propagates with a constant velocity after $t = t_A$, and the profile retains its new shape, as evidenced by the fact that the torsion τ is constant for $t > t_A$. Moreover, these conclusions hold for all three values of t_A, and there is no indication of any instability at $t > t_A$. (b) and (c) show two Ishimori solitons that are not adiabatically connected to Heisenberg solitons, since additional local minima are generated in both cases, and the torsion is not constant (though (b) is very close to the edge of the existence diagram, and so is much more stable than (c)). Increasing t_A by a factor of 100 does not improve the stability of the soliton.

interpolation; the second condition ensures the soliton propagates with a constant velocity; and the third ensures that the soliton is not decaying by slowly spreading out in space.

The numerical values of the tolerances are somewhat arbitrary, but they are necessary to account for numerical errors and finite-size effects (the soliton solutions, even in the Ishimori chain, are only exact in the limit $L \to \infty$).

We examine these conditions for three initial Ishimori solitons in Fig. 2.4; in particular, we show, as an example, that $(R, k) = (0.1, 0.1)$ is connected to a Heisenberg soliton, since the three conditions above are satisfied; and we check that this holds for three different adiabatic times $t_A = 10^3$, 10^4, and 10^5. We also show how the transformation can fail: the

solitons $(R, k) = (0.2, 0.1)$ and $(0.3, 0.1)$ are not adiabatically stable.

2.4 Soliton-soliton scattering

An inherent characteristic of integrable systems is that all scattering is elastic, and solitons (or the quasiparticles, more generally) emerge unscathed from any collisions. To set the stage for soliton interactions in the Heisenberg chain, let us briefly recall the situation in the Ishimori chain.

As a fully integrable model, interactions are completely described by the two-soliton scattering-shift, even for thermal multi-soliton states [16, 17]. When two solitons collide, their asymptotic trajectories are unchanged, except for a displacement by the scattering-shift [16]

$$\Delta(R, k; R', k') = \frac{\mathrm{sgn}(v(R, k) - v(R', k'))}{2R} \log\left[\frac{\cosh(2(R + R')) - \cos(2(k - k'))}{\cosh(2(R - R')) - \cos(2(k - k'))}\right] \tag{2.11}$$

experienced by the soliton (R, k), due to a collision with the soliton (R', k'); that is, the position of the centre of a soliton after a sequence of collisions is

$$x_c(t) = x_c(0) + vt + \sum_{\lambda} \Delta(R, k; R_\lambda, k_\lambda). \tag{2.12}$$

Fig. 2.5 shows the scattering of two moving solitons. The solitons survive scattering essentially unchanged (Fig. 2.5(a)), akin to the fully integrable model. Whilst the collisions do leave the solitons unchanged asymptotically, the magnetisation of a moving soliton is 'screened' during the collision with a larger soliton, as seen in Fig. 2.5(b). Importantly, solitons survive multiple collisions (Fig. 2.5(c)), with the change to their trajectories apparently given by simple consecutive scattering-shifts.

However, there exist some important differences between the Heisenberg and Ishimori cases. First, in the absence of integrability, scattering in the Heisenberg chain is not perfectly lossless; there is some small amount of radiation emitted in the collisions, though this does not destabilise the solitons. Second, the scattering-shift Δ appears not to depend only on the soliton parameters R, k, R', k'. We extract the scattering-shifts in Fig. 2.5(d) by averaging over 10 scattering events; they are also averaged over the relative phase (azimuthal angles) of the solitons at the moment of collision. In the integrable case, this has no effect, as the soliton parameters completely determine the scattering-shift – in the Heisenberg case, however, the scattering-shift appears to fluctuate for different scattering events, apparently as a result of small differences in the initial conditions of the solitons. (Though we note that this dependence vanishes for sufficiently large solitons).

In Fig. 2.6 we examine the dependence of the scattering-shift on the phase of the target soliton – that is, we uniformly rotate the target soliton about the z-axis through some angle ϕ_0 (the incident soliton is not rotated, thus changing the relative phase). Again, since we can only measure the position of the centre of the soliton to an accuracy of one site, the scattering-shifts are calculated by averaging over ten scattering events with the same incident soliton – giving a resolution of 0.1 sites.

We observe in Fig. 2.6(a) that, for sufficiently large target solitons, the scattering-shift exhibits no dependence on ϕ_0. In Fig. 2.6(b) at intermediate widths there is a smooth, periodic variation of the scattering-shift with ϕ_0. Fig. 2.6(c), however, shows that for narrower

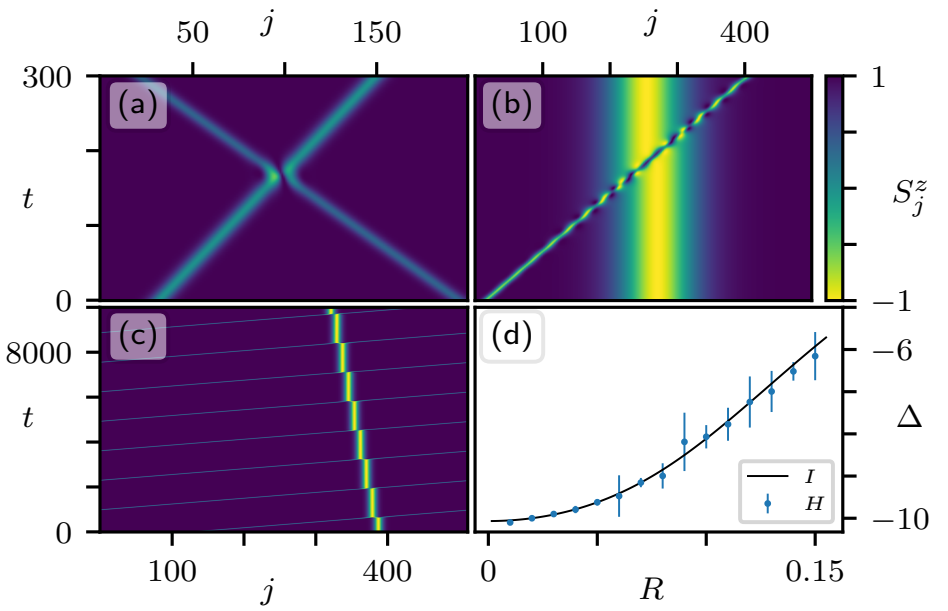

Figure 2.5: Soliton scattering in the Heisenberg chain. Colour-scale shows the z-components, and is the same for (a), (b), and (c). (a) Single scattering event between two solitons with parameters $(R, k) = (0.1, 0.1)$ and $(R', k') = (0.1, -0.15)$. (b) Screening of the magnetisation transported by a narrower soliton as it moves through a wider soliton. (c) Repeated scattering of two solitons $[(R, k) = (0.1, 0.1)$ and $(R', k') = (0.1, 0)]$ under periodic boundary conditions. (d) Comparison of the scattering scattering-shift $\Delta(R, k = 0; 0.1, 0.1)$ in the Ishimori chain (solid line) and in the Heisenberg chain, for stationary target solitons. Scattering-shifts in the Heisenberg chain obtained by averaging over 10 scattering events, cf. (c), and over the relative phases of the solitons – the error bars are the standard deviation w.r.t. the relative phases.

solitons the scattering-shift becomes highly sensitive to the initial conditions determined by the angle ϕ_0.

Despite these differences, collisions over a large parameter regime in the Heisenberg model strongly resemble the scattering in the Ishimori case. Importantly, while the scattering-shift Δ acquires some fluctuations, the velocities of the solitons remain unaffected by the collisions.

To this point we have discussed the scattering in the context of its similarity to the integrable model. We should point out, however, the possibility of more destructive scattering events – collisions with narrow solitons at small k (where the existence diagram is wider in R) can emit significant amounts of radiation. We show the collision of solitons $(R_1 = 0.1, k_1 = 0.1)$ and $(R_2 = 0.25, k_2 = 0)$ in Fig. 2.7. The radiation released by this collision appears to be dissipative, in the sense that it spreads out over the chain with no persistent localised features.

However, whilst the incident solitons are altered by the collision, there are clearly two solitons which emerge from the vertex. These modified solitons are then apparently stable

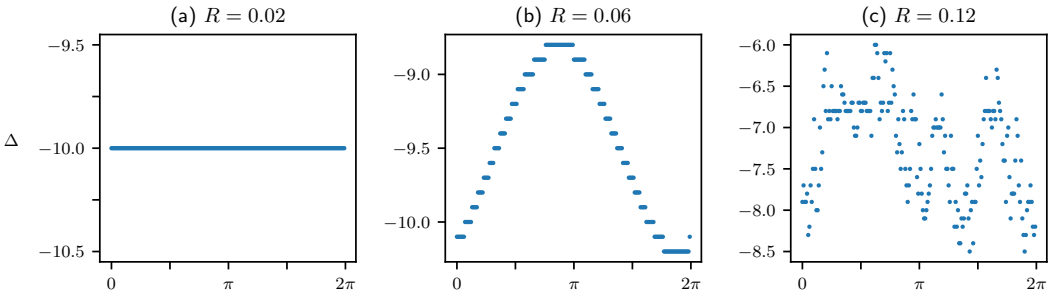

Figure 2.6: Dependence of the scattering-shift $\Delta(R, 0; 0.1, 0.1)$ on the phase difference of the colliding solitons, for different, illustrative values of R. (The actual value of the relative phase is not measured, so the starting point is arbitrary – but a full 2π-sweep is mapped out). In the integrable case, there would be no dependence on ϕ_0. In the Heisenberg case, this remains true for large solitons ($R = 0.02$), but then gives way to a periodic dependence ($R = 0.06$), and finally becomes effectively random as the target soliton becomes narrower ($R = 0.12$). In all cases, however, the soliton never acquires any velocity from the collision (i.e., the collision is elastic), as otherwise Δ would not be measurable.

to further collisions with each other (using PBCs), surviving c. 100 more scattering events, with no sign of further decay, even up to $t = 10^5$ (Fig. 2.7(c)).

Notably, this also indicates that the solitons are stable to (sufficiently) weak fluctuations of the background, suggesting they should remain stable in low-temperature thermal states.

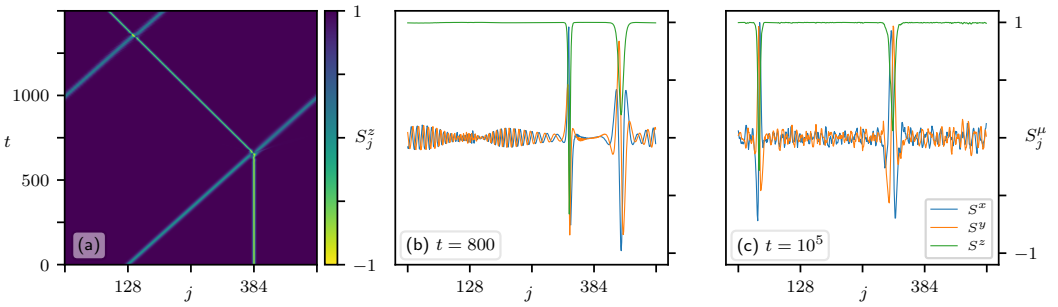

Figure 2.7: A destructive (inelastic) scattering event between solitons with parameters $(0.1, 0.1)$ and $(0.25, 0)$. The colour-scale in (a) shows the z-component. The first scattering event in (a) shows that the initially stationary soliton acquires a velocity, although the moving soliton is relatively well-preserved; at the second scattering event, the two scattered solitons appear to pass through each other without incident. (b) shows the scattered solitons and the decaying pulses emitted from the first collision – on an infinite chain, the pulses would dissipate, but at finite size they become noise. (c) shows the solitons at a much later time, $t = 10^5$ – despite both circling round the chain approximately 100 times, colliding on each pass, and propagating in the noise generated by the first collision, they are remarkably well-preserved.

2.5 Solitons in low-temperature thermal states

Let us therefore turn to that very question: do the solitons of the Heisenberg chain appear in the finite-temperature thermal states? Whilst we have shown that the Heisenberg chain supports solitons as stable solitary waves, which suffer only very weak dissipation in scattering events, the imperfect nature of the scattering implies the existence of a thermal timescale on which they eventually decay. In Part II we will address the question as to what extent these solitons exert their influence on the hydrodynamics and transport properties, but this will rely on at least some sense of stability against thermal fluctuations. Thermal states are not in any sense a dilute soliton gas, and it would not be unreasonable to expect solitons to experience so many scattering events that, unprotected by integrability, they collapse too swiftly to generate any discernible contribution to the dynamics of thermal states.

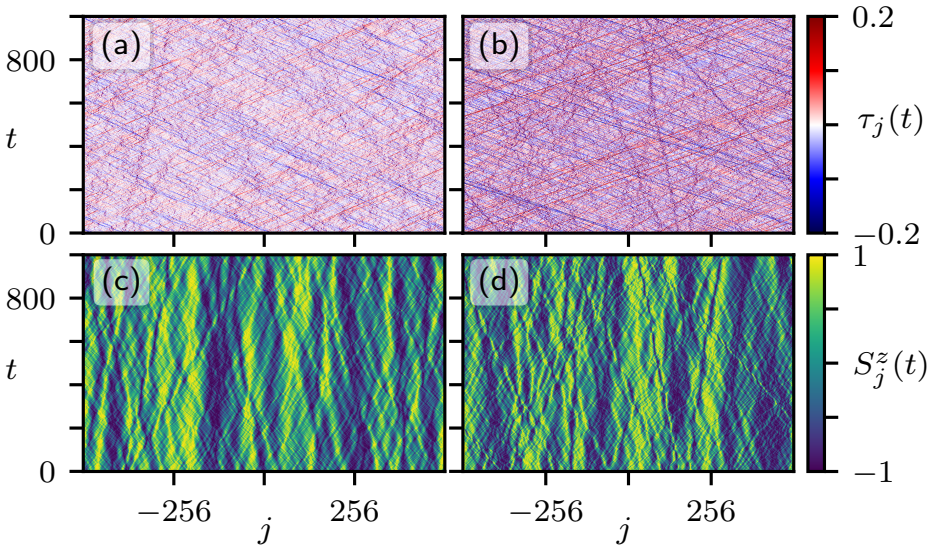

Figure 2.8: Solitons in the thermal state at $T = 0.1J$ for the Heisenberg (left) and Ishimori (right) chains. Upper and lower panels show torsion $\tau_j(t)$, and $S^z_j(t)$ respectively. Ballistic trajectories are clearly visible in the torsion plots, both in the Ishimori and in the Heisenberg chain. These ballistic trajectories can also be seen in the plots of S^z, where the magnetisation carried by a soliton changes as it moves through the chain – the mechanism preventing ballistic spin transport.

2.5.1 Ballistic torsion trajectories

We find that the torsion (1.23) allows us to track the trajectories of solitons through a thermal background: Figs. 2.8(a) and 2.8(b) show the space-time profile of the torsion $\tau(j,t)$ for a low-temperature thermal state of both the Heisenberg and Ishimori chains. The expected ballistic trajectories of the solitons are clearly observed in the Ishimori chain. Remarkably, very long-lived ballistic trajectories are also observed in the Heisenberg chain.

These trajectories can also be seen in the z-spin component $S^z(j,t)$ (Figs. 2.8(c) and 2.8(d)).

2.5.2 Inverse-scattering

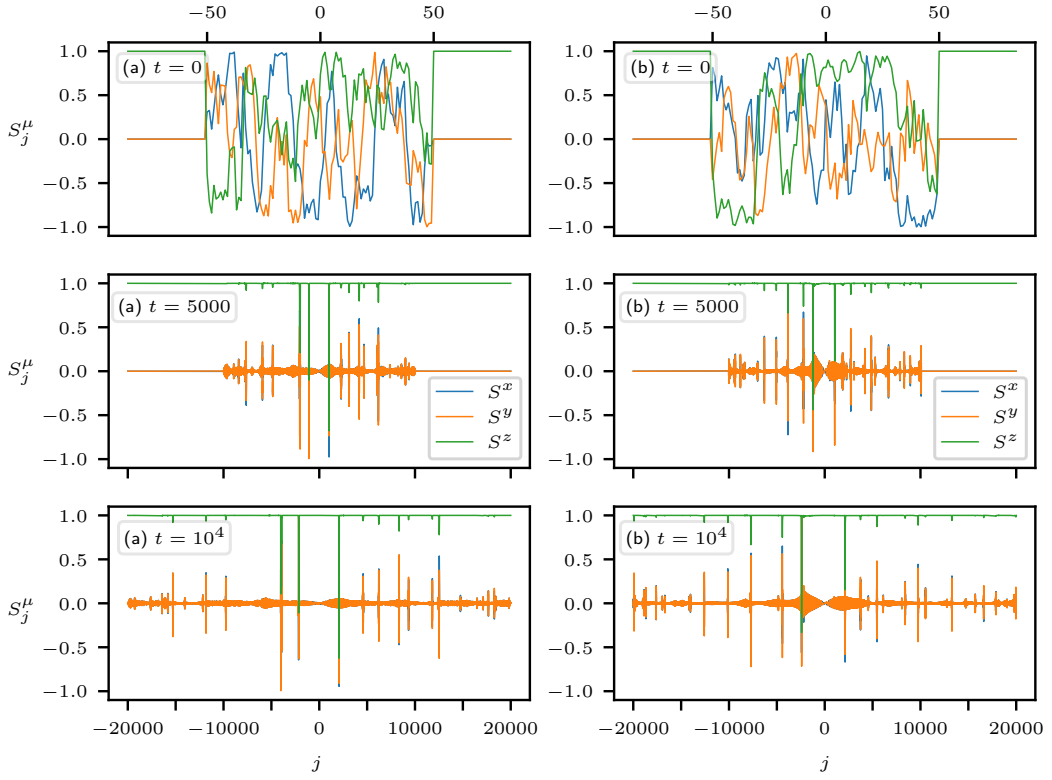

Figure 2.9: Examples of the expansion of a thermal state connected to a fully polarised state (the 'inverse-scattering experiments'). The initial configurations are thermal states on a chain of length $N = 100$ at $T = 0.1$. They are then connected to a fully polarised state – the total length of the system is $L = 4 \times 10^4$. (a) evolves under the Heisenberg chain dynamics; (b) evolves under the Ishimori chain dynamics. The expected inverse-scattering is observed in the Ishimori chain, where the initial thermal region expands into a dilute gas of well-separated solitons. Remarkably, the picture in the Heisenberg chain is, at least qualitatively, strikingly similar. The principal difference is that the Ishimori chain has solitons that are both narrow and fast, cf. the existence diagram (Fig. 1(a)).

We now take a complementary approach to the question of the soliton content of thermal states. In the spirit of the inverse-scattering transform [21] (§1.2), we can isolate the thermal solitons by immersing an initial thermal state in a fully-polarised background $\boldsymbol{S} = \hat{\boldsymbol{z}}$, and allowing the thermal state to expand into this vacuum during the subsequent dynamics. This creates an appealing and direct visual comparison between the Ishimori and Heisenberg chains.

In the integrable case, the thermal state expands into the surrounding quasiparticle (soliton) vacuum, and the solitons, since they have different velocities, become separated in space. If $L \to \infty$ (before $N \to \infty$), this permits a description of the initial thermal state on N sites in terms of the asymptotic trajectories of the solitons. In particular, this is possible since scattering in the integrable case is not *dissipative* and does not change the soliton velocities – thus, the long-time state of well separated solitons is guaranteed to contain the very same solitons as the initial state.

Remarkably, in Fig. 2.9 we observe qualitatively very similar dynamics for the non-integrable Heisenberg chain. Specifically, it appears that during expansion from a thermal state, well-defined spatially localised solitonic excitations emerge that propagate non-dissipatively, at least on numerically accessible length- and timescales, allowing them to become well separated in space. We observe that most of the magnetisation (with respect to the $+\hat{\boldsymbol{z}}$ vacuum) remains bound up in the solitons, not in the dissipative spin waves, suggesting that, at low-temperatures, the thermal states of the Heisenberg chain are – like the integrable Ishimori chain – comprised mainly of solitons.

2.6 Conclusions

Let us take stock of what we have seen in this chapter. We have clearly established the existence of a family of solitons in the non-integrable ferromagnetic Heisenberg chain, in terms of those known to exist in the integrable Ishimori chain. Further, we have shown that these solitons exist in, and are relevant for, the dynamics of thermal low-temperature states of the Heisenberg chain. Looking ahead to Ch. 5, this will be a crucial foundation in explaining the anomalous hydrodynamics; (long-lived) superdiffusion arises as a direct consequence of the nearly integrable scattering behaviour of long-lived solitons, and the screening of magnetisation during collisions.

The fact that these solitons actually survive and determine the hydrodynamic behaviour at finite temperatures, where correlation lengths are only a few lattice sites, seems truly remarkable, in particular considering that, in such a case, the *adiabatically stable solitons are larger than the correlation lengths.*

Chapter 3

Domain wall dynamics in anisotropic spin chains

The work in this chapter has appeared as part of the following article [37]:

Adam J. McRoberts, Thomas Bilitewski, Masudul Haque, & Roderich Moessner
Domain wall dynamics in classical spin chains:
free propagation, subdiffusive spreading, and topological soliton emission
arXiv 2306.15351

Whilst, in Ch. 2, we used a connection to an integrable model to establish solitary excitations, we will, in this chapter, take a different angle of approach to the excitations of spin chains. We broaden our model to allow for anisotropy (though at least one component of spin is always conserved), and simply study the results of exciting the chain directly.

The prototypical setting which we utilise is to take an initial state with two neighbouring regions in different stationary states. A single sharp domain wall between distinct stationary states can move and spread, carrying energy – and, possibly, other conserved quantities. This type of dynamics has been studied in many contexts, including the spin-$\frac{1}{2}$ quantum XXZ chain [38–70], other quantum spin chains [67, 71–75], quantum field theories [76–78], the continuum Landau-Lifshitz model of classical spin densities [67, 79], two-dimensional quantum systems [80, 81], and the simple exclusion process [82].

Here, we examine this setting in a *classical* one-dimensional anisotropic (XXZ) Heisenberg chain. This is, arguably, the simplest incarnation of this problem. As we will show, it is highly tractable, and opens a complementary perspective on the much studied related problems of quantum Heisenberg chains, where signatures of interesting phenomena such as KPZ scaling [62, 83] have been experimentally observed [84, 85].

One particularly surprising finding is that we can describe the domain wall dynamics *quantitatively* using *linear* spin wave theory across a wide range of parameters. At the same time, we also find emission of (possibly multiple) topological solitons, which can only be generated by non-linear scattering processes, and which must be stabilised by non-linear interactions.

We find qualitatively distinct behaviour in the easy-axis, isotropic, and easy-plane cases. Our results and set-up are summarised in Fig. 3.1. For easy-plane anisotropy, the domain

wall splits into two ballistically counter-propagating ones (Fig. 3.1(c)). Since the Hamiltonian is non-integrable and intrinsically non-linear, and since the propagating domain walls have high energy compared to the background, they can, in principle, emit or decay into other excitations — giving the non-equilibrium set-up an inherent non-linear flavour. It is therefore all the more surprising that, over the entire range of easy-plane anisotropy $\Delta \in [0, 1)$, domain walls propagate ballistically. This is reminiscent of the behaviour of quasiparticles in integrable systems [51, 67, 86–96], or that of operator spreading [97–99]. For the latter, ballistic behaviour is accompanied by diffusive broadening [97–99]. More generally, broadening in interacting many-body systems is typically diffusive, with exceptions usually associated with integrability or a lack of interactions.

In sharp contrast to this expectation, we show that the propagating domain walls broaden subdiffusively, as $\sim t^{1/3}$, in the entire easy-plane regime $\Delta \in [0, 1)$. We find that the propagation speed, profile, and $t^{1/3}$ scaling can be quantitatively obtained from *linear* spin wave theory. At the same time, above a critical angle $\varphi_c(\Delta)$ between the domains separated by the propagating domain wall (Fig. 3.1(b)), the linear behaviour of the propagating domain walls coexists with the aforementioned, inherently *non*-linear feature of the emission of topological solitons. We provide a heuristic picture for all of these processes.

At the isotropic Heisenberg point $\Delta = 1$, the domain walls can no longer propagate, and the subdiffusive spreading gives way to a diffusive melting of the original domain wall (Fig. 3.1(c)). Nor can the domain walls propagate in the easy-axis case ($\Delta > 1$), where the melting is fully arrested and a static soliton is approached asymptotically (Fig. 3.1(c)).

The behaviour for $\Delta \geq 1$ is analogous to that known for quantum spin-$\frac{1}{2}$ chains [40, 79] – a classical-quantum analogy which is, in itself, remarkable. By contrast, the $t^{1/3}$ broadening of the domain wall that we find over the entire range $0 \leq \Delta < 1$ appears, in the quantum spin-$\frac{1}{2}$ case, only at the $\Delta = 0$ point [39, 46, 47, 49] or at the light cone of fastest excitations [60, 61, 67, 100], being associated with the non-interacting (free-fermion) nature of these cases. The existence and emission of the solitons have, to the best of our knowledge, not been previously observed – either in the quantum model or in a corresponding continuum Landau-Lifshitz model.

3.1 The classical XXZ spin chain

We consider the classical XYZ spin chain,

$$H = -\sum_i \left(J_x S_i^x S_{i+1}^x + J_y S_i^y S_{i+1}^y + J_z S_i^z S_{i+1}^z \right). \tag{3.1}$$

where the $\boldsymbol{S}_i \in S^2$ are classical $O(3)$ vectors at sites i of a chain. We assume the coupling constants $J_\mu \geq 0$ are all ferromagnetic. The dynamics is given by the classical equations of motion,

$$\dot{S}_i^\mu = -\epsilon^{\mu\nu\lambda} J_\nu (S_{i+1}^\nu + S_{i-1}^\nu) S_i^\lambda, \tag{3.2}$$

which follow from the fundamental Poisson brackets $\{S_i^\mu, S_j^\nu\} = \delta_{ij} \epsilon^{\mu\nu\lambda} S_j^\lambda$.

We set $J_x = J_y = 1$ (which implicitly defines all units), and $0 \leq J_z = \Delta$. The XY-point $\Delta = 0$ corresponds to the free-fermion limit of the quantum spin-$\frac{1}{2}$ chain, but is, in the classical case, an interacting model.

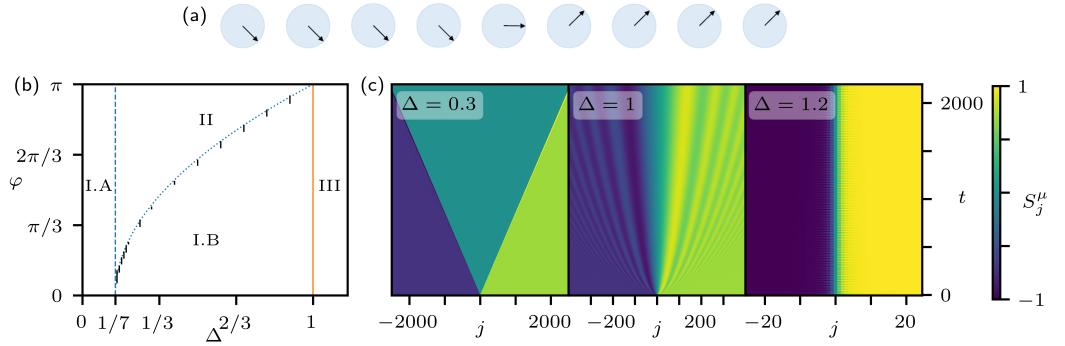

Figure 3.1: (a) Schematic of the initial conditions (3.3), in the xy-plane, shown for $\varphi = \pi/2$. (b) Overview of the different dynamical regimes as a function of the anisotropy Δ and amplitude φ. I.A and I.B are the two linear regimes (distinguished by whether the oscillations are behind or ahead of the counter-propagating domain walls, respectively), where all of the dynamical features are well-described by linear spin wave theory; II is the easy-plane non-linear regime, where topological solitons coexist with the spreading domain walls. III is the easy-axis regime, with a single, static domain wall. The isotropic point $\Delta = 1$ corresponds to the transition between I.B and III, and is well-described by linear spin wave theory with a single, diffusively broadening domain wall. The vertical bars denote the uncertainty in determining the transition between I.B and II from the simulations. (c) Overview of the domain wall dynamics shown for the easy-plane $\Delta = 0.3$, the isotropic point $\Delta = 1$, and the easy-axis $\Delta = 1.2$, respectively. Note the different ranges of the x-axes. $\varphi = \pi/2$ for the easy-plane and the isotropic case, where S^y is plotted. S^z is plotted for the easy-axis case, with $\varphi = \pi$. Ballistic counter-propagation is observed in the easy-plane, diffusive melting of the original domain wall is seen at the isotropic point, whilst the easy-axis approaches a very narrow static soliton.

3.2 Easy-plane: $\Delta < 1$

We take a sharp domain wall in the in-plane components as the initial condition,

$$\begin{aligned} \boldsymbol{S}_{i<0} &= \cos(\varphi/2)\hat{\boldsymbol{x}} - \sin(\varphi/2)\hat{\boldsymbol{y}} \\ \boldsymbol{S}_{i=0} &= \hat{\boldsymbol{x}} \\ \boldsymbol{S}_{i>0} &= \cos(\varphi/2)\hat{\boldsymbol{x}} + \sin(\varphi/2)\hat{\boldsymbol{y}} \end{aligned} \tag{3.3}$$

for some amplitude φ that sets the magnetisation jump across the domain wall as illustrated in Fig. 3.1(a). The $O(2)$ isotropy implies that any choice of φ connects two easy-plane ground states. We set the spin at $i = 0$ to lie halfway between the two domains, $\boldsymbol{S}_{i=0} = \hat{\boldsymbol{x}}$, to ensure that there is some dynamical evolution, even if $\varphi = \pi$.

Numerically integrating the equations of motion (3.2) with initial conditions (3.3) and open boundaries reveals that two counter-propagating domain walls immediately emerge from $i = 0$: a left-moving one connecting the $(-)$-domain to the expanding $\hat{\boldsymbol{x}}$-domain; and a right-moving one connecting the $\hat{\boldsymbol{x}}$-domain to the $(+)$-domain as seen in Fig. 3.1(c).

The size of the $\hat{\boldsymbol{x}}$-domain grows linearly with time, implying ballistic domain wall motion. The underlying velocity $c = \sqrt{2(1-\Delta)}$ does not differ measurably from the group velocity of long-wavelength spin waves, despite the non-linearity of the equations of motion.

To investigate the long-time dynamics of the domain wall numerically, we switch to its co-moving frame. We begin with the sharp domain wall initial conditions (3.3) on a finite chain of length L (with sites $i \in [-\frac{L}{2}, \frac{L}{2}) \cap \mathbb{Z}$) and open boundaries. After a reset time $t_R = L/4c$ (i.e., the time at which the left domain wall reaches site $i = -L/4$, where c is the domain wall speed), we shift the state rightward by $L/4$, i.e., we map $\boldsymbol{S}_i \mapsto \boldsymbol{S}_{i-L/4}$, the rightmost quarter of the state is discarded, and the leftmost quarter is reset to the $(-)$-domain. We store a snapshot of this reset state, and then continue with the numerical time evolution, resetting periodically.

Clearly, resetting the state in this manner induces extra sources of error, viz., any information in the rightmost quarter is lost, and any information which reaches the finite left-boundary will be reflected. The (approximate) locality of the domain walls, however, ameliorates any potential problems here – since their width $w \sim t^{1/3}$ scales slowly with time, only modest system sizes $L \sim 10^4$ are needed to reach long times $t = 10^6$.

Following this procedure, we then find, numerically, that this easy-plane dynamics exhibits three qualitatively distinct regimes, cf. Fig. 3.1(b): two linear regimes, I.A and I.B, so-called because they are well-described by *linear* spin wave theory in their entirety; and a non-linear regime II characterised by an instability to the emission of topological solitons.

Within the linear regimes we find, in addition to the ballistic motion of the domain walls, a subdiffusive spreading, with their width scaling as $t^{1/3}$. We demonstrate this scaling collapse of the full domain wall profiles in Figs. 3.2(a) & 3.2(b). In the non-linear regime we observe the emission of a soliton during domain wall propagation as shown in Fig. 3.2(c), which moves ballistically at a slower speed than the domain wall. We show with a purely ballistic scaling collapse in Fig. 3.2(d) that, indeed, this soliton does not disperse.

3.2.1 Spin-wave theory

We next demonstrate that the spin-wave description of the easy-plane dynamics, remarkably, captures *all* of the relevant features in what we call the linear regimes, and correctly predicts velocity and width-scaling of the domain walls even in the non-linear regime.

To ensure that the Fourier-modes are well-defined, we will work, as an intermediate step, with periodic boundary conditions for a system of size L, and initial conditions

$$\begin{aligned} \boldsymbol{S}_{i=0} &= \hat{\boldsymbol{x}} \\ \boldsymbol{S}_{i=1,\ldots,L/2-1} &= \cos(\varphi/2)\hat{\boldsymbol{x}} + \sin(\varphi/2)\hat{\boldsymbol{y}} \\ \boldsymbol{S}_{i=L/2} &= \hat{\boldsymbol{x}} \\ \boldsymbol{S}_{L/2+1,\ldots L-1} &= \cos(\varphi/2)\hat{\boldsymbol{x}} - \sin(\varphi/2)\hat{\boldsymbol{y}}. \end{aligned} \tag{3.4}$$

We will take the thermodynamic limit when it is explicitly safe to do so. Now, following the usual procedure of classical spin wave theory, we expand each spin about the $\hat{\boldsymbol{x}}$-domain,

$$\boldsymbol{S}_i = \hat{\boldsymbol{x}}\sqrt{1 - l_i^2} + \boldsymbol{l}_i, \tag{3.5}$$

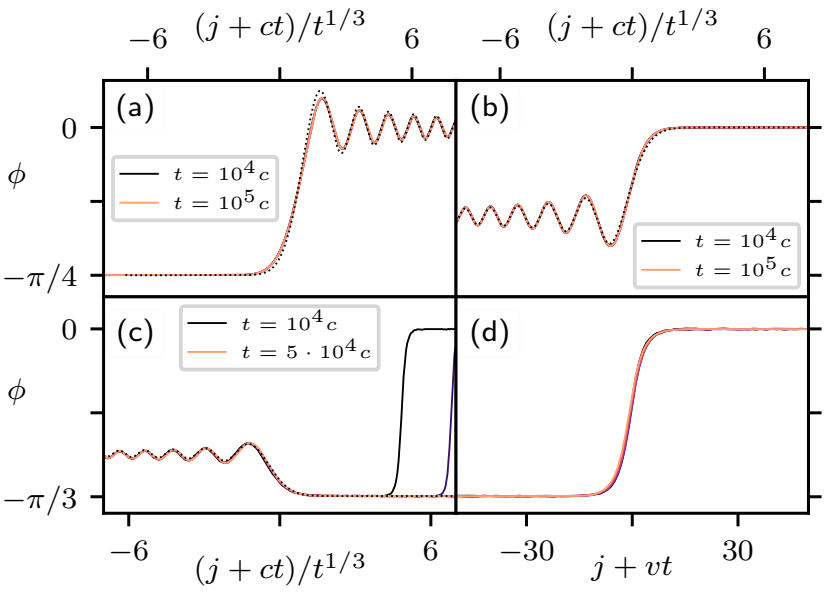

Figure 3.2: Dynamics in the easy-plane case. Dotted lines show spin wave predictions, where relevant. Only the left-moving domain walls are shown. (a) Linear regime I.A ($\Delta = 0$, $\varphi = \pi/2$), showing the ballistic propagation and subdiffusive spreading of the domain wall, with the oscillations trailing. (b) Linear regime I.B ($\Delta = 0.3$, $\varphi = 3\pi/10$), where the oscillations are now ahead of the domain wall. (c) Non-linear regime II ($\Delta = 0.25$, $\varphi = \pi/2$), showing that the domain wall decays by emitting a topological soliton, though its speed and width-scaling are unaffected. (d) Same parameters and times as (c), but in the co-moving frame of the soliton.

and retain only terms linear in $\boldsymbol{l}_i$ in the equations of motion (3.2). We obtain

$$\begin{aligned} \dot{l}_i^x &= 0, \\ \dot{l}_i^y &= 2J_x l_i^z - J_z(l_{i+1}^z + l_{i-1}^z), \\ \dot{l}_i^z &= -2J_x l_i^y + J_y(l_{i+1}^y + l_{i-1}^y). \end{aligned} \tag{3.6}$$

These equations are readily solved by Fourier transformation. Since $l_q^z(0) = 0$, we have

$$l_q^y(t) = S_q^y(t) = \cos(\omega_q t) S_q^y(0), \tag{3.7}$$

where the dispersion is given by

$$\omega_q = 2\sqrt{(1 - \cos q)(1 - \Delta \cos q)}. \tag{3.8}$$

The procedure now is to Fourier transform the initial conditions, apply the time-evolution to each q-mode, and then invert the transform. After some algebra, we obtain

$$S_j^y(t) = \frac{-2i}{L} \sum_{n=1,3,\ldots}^{L-1} e^{2\pi i n j/L} \cot\left(\frac{n\pi}{L}\right) \cos(\omega_q t), \tag{3.9}$$

where $q = 2\pi n/L$. We may now safely pass to the thermodynamic limit $L \to \infty$, which yields

$$S_j^y(t) = -2i \sin\left(\frac{\varphi}{2}\right) \int_{-\pi}^{\pi} \frac{dq}{4\pi} e^{iqj} \cos(\omega_q t) \cot\frac{q}{2}. \tag{3.10}$$

To make further analytic progress, we expand the dispersion in powers of q:

$$\omega_q \sim c|q| - \alpha|q|^3 + \gamma|q|^5 + ..., \quad |q| \sim 0, \tag{3.11}$$

where the coefficients are given as functions of Δ by

$$c = \sqrt{2(1-\Delta)}, \quad \alpha = \frac{1-7\Delta}{12c}, \quad \gamma = \frac{1-62\Delta+\Delta^2}{960(1-\Delta)c}. \tag{3.12}$$

Let us assume, for now, that $\alpha > 0$ (i.e., $0 < \Delta < 1/7$). We insert the expansion of the dispersion at third order, and note that the modulus signs can be ignored because the cosine is even. Then, splitting the cosine to make clear how this separates into left- and right-moving domain walls, we have

$$S_j^y(t) \sim -2i \sin\left(\frac{\varphi}{2}\right) \sum_{\sigma=\pm} \int_{-\pi}^{\pi} \frac{dq}{8\pi} e^{iq(j+\sigma ct) - i\sigma\alpha q^3 t} \cot\frac{q}{2}. \tag{3.13}$$

We make the substitution

$$k^3 = 3\alpha q^3 t \quad \Rightarrow \quad q = \frac{k}{(3\alpha t)^{1/3}}, \tag{3.14}$$

whereupon the integral becomes

$$S_j^y(t) \sim \sum_{\sigma=\pm} \int_{-(3\alpha t)^{1/3}\pi}^{(3\alpha t)^{1/3}\pi} \frac{dk}{4\pi} \exp\left(ik\frac{j+\sigma ct}{(3\alpha t)^{1/3}}\right) \left[\frac{-2i\sin\left(\frac{\varphi}{2}\right) e^{-i\sigma k^3/3}}{2(3\alpha t)^{1/3}} \cot\left(\frac{k}{2(3\alpha t)^{1/3}}\right)\right]. \tag{3.15}$$

We now consider the $t \to \infty$ asymptotics. We send the limits of the integrals to $\pm\infty$, and use the asymptotic equivalence

$$\frac{1}{X}\cot\left(\frac{k}{X}\right) \sim \frac{1}{k}, \quad X \to \infty, \tag{3.16}$$

which yields

$$S_j^y(t) \sim \sin\left(\frac{\varphi}{2}\right) \sum_{\sigma=\pm} \mathcal{F}^{-1}_{[f_\sigma]}\left(\frac{j+\sigma ct}{(3\alpha t)^{1/3}}\right), \tag{3.17}$$

where

$$\mathcal{F}^{-1}_{[f]}(X) := \int_{\mathbb{R}} \frac{dk}{2\pi}\, e^{ikX} f(k), \quad f_\sigma(k) = \frac{-ie^{-i\sigma k^3/3}}{k}. \tag{3.18}$$

The calculation is the same for $\alpha < 0$ ($\Delta > 1/7$), except that an overall minus sign is attached to Eq. (3.17), since we have to flip over the integration limits in Eq. (3.15).

The functions $\mathcal{F}^{-1}_{[f_\sigma]}$ can be explicitly evaluated in terms of the generalised hypergeometric functions ${}_pF_q$, though the full expressions are somewhat unwieldy.

The central result, however, is apparent: the spin-wave calculation correctly predicts two ballistically counter-propagating domain walls which are functions only of the variables $(j \pm ct)/(3\alpha t)^{1/3}$, and, thus, broaden subdiffusively. We also observe good quantitative agreement of the spin-wave prediction (dotted) with the profiles obtained in the full numerical simulation (solid curves) in Fig. 3.2(a,b).

The integral form is different from that appearing in the quantum free-fermion case [38, 49], but has previously been considered in the context of undular tidal bores [101], and more generally in the context of catastrophes in waves at horizons [102]; and related integrals generically describe light cones in quenches in quantum spin chains [102, 103].

Precisely at the point $\Delta = 1/7$, the cubic term vanishes and an analogous calculation would predict that the width should scale as $t^{1/5}$. We do not observe this in the numerical simulations (which use the full equations of motion), presumably due to non-linear interactions between the spin wave modes renormalising the dispersion.

3.2.2 Topological soliton emission

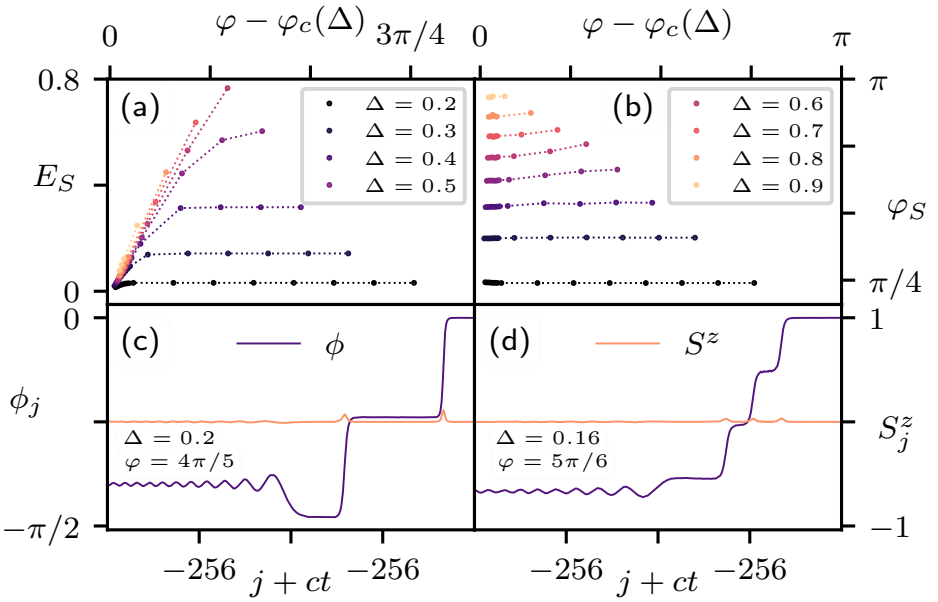

Figure 3.3: Soliton emission in the easy-plane dynamics. (a), (b) Dependence of the soliton energy E_S and soliton amplitude φ_S, respectively, on the initial amplitude φ. We observe that the amplitude of the emitted solitons is almost constant. (c), (d) Two- and three-soliton emission, respectively, when $\varphi >> \varphi_S$.

We next discuss the emission of topological solitons in the easy-plane regime. As we observed in Figs. 3.2(c) & 3.2(d), the moving domain wall can emit a stable (non-dispersing)

ballistically-propagating soliton connecting two ground states. We find that this emission only takes place above a critical, anisotropy-dependent amplitude $\varphi_c(\Delta)$, and, in particular, only in the regime $1/7 < \Delta < 1$, as shown in Fig. 3.1(b). The energy carried by these solitons is seen to depend both on the anisotropy Δ and the initial amplitude of the domain wall φ. Importantly, however, we observe that, at fixed Δ, the angular amplitude φ_S of the emitted soliton (the in-plane angle between the two ground states the soliton connects) does not depend on φ (see Fig. 3.3(b)), and, in fact, is equal to the critical value $\varphi_c = \varphi_S$. Moreover, we observe n-soliton emission if $\varphi > (2n-1)\varphi_S$, as shown in Figs. 3.3(c) & 3.3(d).

Let us try to reason out some explanation of this phenomenology. Taking, for now, the fixed soliton amplitude φ_S as given, a simple energetic argument shows that this *is* the critical amplitude. The domain wall energy depends monotonically on its amplitude, which must, therefore, decrease if soliton emission is to occur. The initial amplitude of the domain wall is $\varphi/2$, and after the emission the new amplitude is $|\varphi_S - \varphi/2|$. Thus, $\varphi_c = \varphi_S$. This also implies that n-soliton emission is possible if $\varphi > (2n-1)\varphi_S$, as observed in Figs. 3.3(c) & 3.3(d).

To explain the uniqueness of the emitted soliton amplitude we propose the following heuristic model of soliton production. We assume that the model supports a two-parameter family of topological soliton solutions (cf. the two-parameter family of non-topological solitons from Ch. 2) characterised by their energy E_S and amplitude φ_S, which determine the other physical properties – in particular, their speed and width. As the interactions are local, and the soliton is observed to be created at the ballistically-moving centre of the domain wall over an extended time, the speed of the soliton must initially be matched to the Δ-dependent domain wall speed so that energy can be efficiently transferred.

Further, since the soliton is seeded by the domain wall, it must begin with zero energy. The condition that the velocities match, combined with the restriction to low-energy solitons $E_S \to 0$, selects a unique soliton from the two-parameter family, with some fixed amplitude $\varphi_S(\Delta)$. As the dynamics proceeds, energy is transferred from the domain wall to the soliton, slowing down the latter and leading to its separation from the domain wall. The amplitude φ_S, however, is topological (in the sense that the soliton connects different boundary conditions), and cannot be changed by local processes.

Finally, there is the question of why soliton production is never observed, for any initial domain wall amplitude φ, when $\Delta < 1/7$. To shed some light on this, let us consider two-magnon scattering, since these are the lowest-order processes which could lead to some dynamic instability.

For two magnons with momenta q_1, q_2, which scatter to two magnons with momenta q_3, q_4, conservation of momentum implies that we may write these as:

$$\begin{aligned} q_1 &= p & q_2 &= p' \\ q_3 &= p' - q & q_4 &= p + q \end{aligned} \tag{3.19}$$

for some momentum transfer q. On the other hand, energy conservation imposes a further constraint:

$$\omega_{p+q} + \omega_{p'-q} = \omega_{p'} + \omega_p. \tag{3.20}$$

Let us assume that all of the magnon momenta have the same sign; for soliton formation we do not consider back-scattering, since any scattering processes must be local, and left and right-movers quickly separate in the sharp domain wall set-up we consider, and would therefore not contribute to the dynamical formation of a soliton.

Now, using the fifth-order expansion of ω_q,

$$\omega_q \sim cq - \alpha q^3 + \gamma q^5, \tag{3.21}$$

and inserting this into Eq. (3.20), yields a quartic equation for the allowed momentum transfers q in terms of p, p', α, and γ (the latter two being functions of Δ). There are two trivial (elastic) solutions,

$$q = 0, \quad q = p' - p, \tag{3.22}$$

and two non-trivial, but potentially complex solutions,

$$q = \frac{p' - p}{2} \pm \frac{\sqrt{5}\sqrt{12\alpha\gamma - 5\gamma^2\left(3p^2 + 2pp' + 3p'^2\right)}}{10\gamma}. \tag{3.23}$$

However, since we are assuming that p, p' have the same sign, these inelastic solutions are never real for $\Delta < 1/7$, where $\alpha > 0$, $\gamma < 0$. For $\Delta > 1/7$ ($\alpha < 0$, $\gamma < 0$), however, there is a range of momenta for which inelastic scattering *is* possible, given by the condition

$$\frac{12}{5}\frac{|\alpha|}{|\gamma|} > 3p^2 + 2pp' + 3p'^2. \tag{3.24}$$

We conjecture that the fact that two-magnon scattering is always elastic for $\Delta < 1/7$ explains why regime I.A (cf. Fig. 3.1(b)) is never observed to emit solitons, for any initial domain wall amplitude φ, since the main dynamical processes that would manifest such an instability are forbidden.

We note, however, that there are some pieces of the puzzle that are not yet in place. Whilst this account provides a plausible explanation of the structure of the different dynamical regimes (Fig. 3.1(b)), it does not explain why there is an apparently generic instability towards topological solitons. Nor does it explain why the solitons themselves are stable – whilst we have dubbed them "topological" solitons, essentially to distinguish them from the non-topological solitons of Ch. 2 which connect the same ground state to itself, these easy-plane solitons are *not* topologically-protected: the set of ground states is not discrete, so the analogous argument to Eq. (1.9) does not apply; indeed, this lack of topological protection is why the spreading of the domain walls is possible in the first place.

3.3 Easy-axis and isotropic dynamics: $\Delta \geq 1$

We briefly remark on the domain wall dynamics at the isotropic point ($\Delta = 1$) and in the easy-axis case ($\Delta > 1$).

At the isotropic point, there can be no propagating domain walls, because all components of the magnetisation are conserved; instead, we observe that the initially sharp domain wall spreads diffusively (Fig. 3.4(a)). This can be understood within the linear spin-wave picture. At $\Delta = 1$, the dispersion switches from an odd-power expansion to the even expansion,

$$\omega_q = 2(1 - \cos(q)) \sim q^2 + ..., \quad q \sim 0. \tag{3.25}$$

There are no linear (dispersionless) terms – so the centre of the domain wall does not move – and the width is now controlled by the quadratic, not cubic, term. The spin-wave calculation

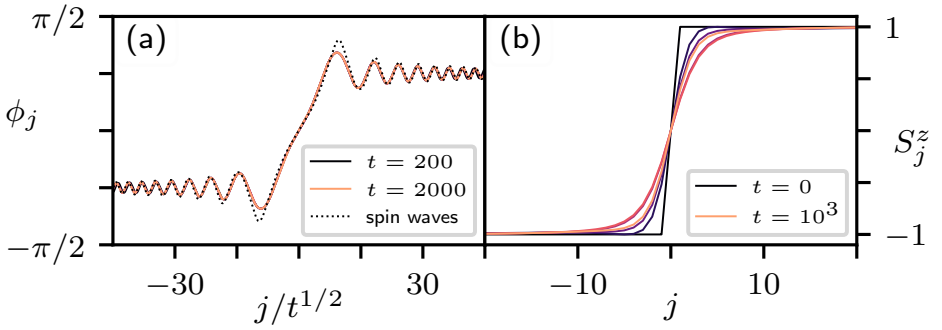

Figure 3.4: Dynamics (a) at the isotropic point, and (b) in the easy-axis regime ($\Delta = 1.2$). There are no propagating domain walls in either case: the initial state spreads diffusively at the isotropic point, whilst it approaches the static soliton in the easy-axis case.

at the isotropic point proceeds with exactly the same steps (initial conditions, equations of motion, Fourier transform, and thermodynamic limit) as the easy-plane case – up to the insertion of the dispersion relation into Eq. (3.10). From this point, we have

$$S^y_j(t) = -2i \sin\left(\frac{\varphi}{2}\right) \int_{-\pi}^{\pi} \frac{dq}{4\pi} e^{iqj} \cos(q^2 t) \cot\frac{q}{2}, \tag{3.26}$$

and we now use the substitution

$$k^2 = 2q^2 t \quad \Rightarrow \quad q = \frac{k}{(2t)^{1/2}}. \tag{3.27}$$

Together with the asymptotic relation (3.16), this yields

$$S^y_j(t) = \sin\left(\frac{\varphi}{2}\right) \mathcal{F}^{-1}_{[g]}\left(\frac{j}{(2t)^{1/2}}\right), \tag{3.28}$$

in the notation of Eq. (3.18), with

$$g(k) = \frac{-2i}{k} \cos\left(\frac{k^2}{2}\right); \tag{3.29}$$

or, in terms of the normalised Fresnel integrals,

$$S^y_j(t) = \sin\left(\frac{\varphi}{2}\right) \left[\mathcal{C}\left(\frac{j}{\sqrt{2\pi t}}\right) + \mathcal{S}\left(\frac{j}{\sqrt{2\pi t}}\right)\right], \tag{3.30}$$

which shows good quantitative agreement with the full solution as seen in Fig. 3.4(a).

For the easy-axis, we change the initial conditions so that the domain wall occurs in the z-components, ensuring that the state has finite energy. Specifically,

$$\boldsymbol{S}_{i<0} = -\hat{\boldsymbol{z}}, \quad \boldsymbol{S}_{i=0} = \hat{\boldsymbol{x}}, \quad \boldsymbol{S}_{i>0} = +\hat{\boldsymbol{z}}. \tag{3.31}$$

Now, since the z-magnetisation is conserved, there can, again, be no propagating domain wall solutions; some dissipative spin-wave radiation escapes, before the state settles down, in an oscillatory manner (Fig. 3.4(b)), to the static soliton

$$S_j^z = \tanh(j \cosh^{-1}(\Delta)), \tag{3.32}$$

which *is* topologically protected.

3.4 Conclusions

In this chapter, we have investigated the non-equilibrium dynamics of a classical anisotropic spin chain with a sharp domain wall as the initial conditions, revealing a phenomenology which is both remarkably rich – particularly in the easy-plane case, with its ballistic propagation and subdiffusive spreading of the domain wall, alongside the existence and emission of solitons – and remarkably tractable, as we have shown that many of these features can be understood within the framework of *linear* spin-wave theory.

This work thus sheds some light on the question of when, and to what extent, classical treatments can account for a priori complex quantum dynamics, by providing closely related instances of where this appears to be (im)possible: while the $\Delta \geq 1$ regimes and the XY point ($\Delta = 0$) appear to be entirely analogous both classically and quantum-mechanically [52, 59, 69, 70, 79], the $0 < \Delta < 1$ regime is qualitatively distinct in the classical case. While reflecting some properties of the quantum $\Delta = 0$ case [46, 47], it exhibits an entirely new phenomenon of soliton emission not found in previous studies of either the $S = \frac{1}{2}$ quantum case or the continuum Landau-Lifshitz model.

This makes a connection to the broader question of under what conditions non-linear settings – e.g. a priori beyond the linear response regime – may still be described by simplified linear theories. This issue has appeared prominently in the study of KPZ dynamics [84, 85, 96] expected for small jumps in the initial condition, but in fact observed for larger ones. How a description of the 'doubly non-linear' phenomenon of the *emission* of (single or even multiple) *stable solitons* can co-exist with a linear description of the propagation of the emitting domain wall is a tantalising open question for future theoretical work.

Part II

Superdiffusion

Chapter 4

Superdiffusion in integrable spin chains

In Part I of this thesis we were concerned with the dynamics of spin systems with single excitations, or perhaps, a small number of them scattering from each other, with the rest of the chain in some ferromagnetic ground state. In Part II, we will go beyond this effectively zero temperature regime and study the hydrodynamics of spin systems at finite temperature.

The principal result, and the subject of Ch. 5, is that anomalously fast – that is, *superdiffusive* – spin transport, over potentially enormously large time-scales, arises in what is arguably the simplest interacting spin model – the classical Heisenberg chain – defying the predictions of standard, diffusive hydrodynamics. We will also observe the same physics in other non-integrable spin chains

We will first, however, use this chapter to review some of the literature on superdiffusion in the context of *integrable* spin chains, where considerable recent progress has greatly advanced our understanding of the underlying physics. It is as this mechanism that the solitary excitations of Part I will re-enter; they are the fundamental reason that superdiffusion exists.

4.1 Diffusion and anomalous diffusion

Before rushing headlong into the subject of anomalous hydrodynamics, however, it may be judicious to pause, and briefly remind ourselves of the generic scenario: ordinary diffusion. Given some general system with a locally-conserved density ϕ, we expect that the (suitably coarse-grained) dynamics of this quantity follows the (stochastic) diffusion equation,

$$\partial_t \phi = D\nabla^2 \phi + \partial_x \xi, \tag{4.1}$$

where ξ is a white-noise field with the correlation function

$$\langle \xi(x,t)\xi(x',t')\rangle = 2D\,\delta(x-x',t-t'), \tag{4.2}$$

which is set by the fluctuation-dissipation theorem. An important conceptual point is that all microscopic details – the dynamics of the non-conserved "fast-modes" – have been washed

away, and enter only by renormalising the diffusion coefficient D and (via the fluctuation-dissipation theorem) the strength of the noise-field. This means that the (connected) correlation function of the slow-mode ϕ has a Gaussian form,

$$\mathcal{C}_\phi(x,t) := \langle \phi(x,t)\phi(0,0)\rangle \sim \frac{1}{(Dt)^{1/2}} \exp\left(-\frac{x^2}{Dt}\right), \tag{4.3}$$

where we have assumed we are in one dimension.

Anomalous hydrodynamics is the name given to any departure from this scenario, though we assume that we may still coarse-grain the system's dynamics and retain only the slow modes. The general form of the correlation functions then, is

$$\mathcal{C}_\phi(x,t) \sim t^{-\alpha}\mathcal{F}(x/t^\alpha), \tag{4.4}$$

for some scaling function $\mathcal{F}$. The dynamical exponent[1] α is most straightforwardly obtained from the autocorrelator,

$$\mathcal{A}(t) := \mathcal{C}(x=0,t) \sim t^{-\alpha} \tag{4.5}$$

where $\alpha = 1/2$ recovers ordinary diffusion, ballistic transport is obtained with $\alpha = 1$, and $1/2 < \alpha < 1$ corresponds to superdiffusion ($0 < \alpha < 1/2$ implies subdiffusion, the subject of Part III).

4.2 The quantum Heisenberg chain

The principal example of an integrable, superdiffusive spin chain is the $S = \frac{1}{2}$ *quantum* Heisenberg chain,

$$\hat{H} = J\sum_j \hat{\boldsymbol{S}}_j \cdot \hat{\boldsymbol{S}}_{j+1}, \tag{4.6}$$

where $\boldsymbol{S}_j^\mu$ is a spin-$\frac{1}{2}$ operator, and J is the coupling strength (since we will be concerned only with infinite-temperature and time-reversal invariant quantities, whether the coupling is ferromagnetic or antiferromagnetic is irrelevant here). To facilitate the discussion, it will be convenient to extend the model and consider the spin-$\frac{1}{2}$ XXZ chain,

$$\hat{H} = J\sum_j \left(\hat{S}_j^x\hat{S}_{j+1}^x + \hat{S}_j^x\hat{S}_{j+1}^x + \Delta\hat{S}_j^z\hat{S}_{j+1}^z\right). \tag{4.7}$$

The Heisenberg chain, of course, is the fully-isotropic point $\Delta = 1$, where the non-abelian $SU(2)$ spin symmetry is intact. At zero temperature, the XXZ chain (4.7) is equivalent, via the Jordan-Wigner transformation [104] and subsequent bosonisation [8] to the sine-Gordon model (1.11), and the Heisenberg point sits at a quantum Kosterlitz-Thouless transition between the easy-plane and easy-axis.

More importantly, in the present context of high-temperature hydrodynamics, is the fact that the $S = \frac{1}{2}$ XXZ chain is fully-integrable, via the Bethe ansatz [105]. Cf. the discussion of the inverse-scattering transform (§1.2), this implies that the model has a complete set of

[1] We will refer to α as the dynamical exponent, though in most of the literature the reciprocal $z = 1/\alpha$ is called the dynamical exponent instead. This is simply a matter of convention.

local quasiparticles (essentially, solitons), which, taking the ferromagnetic ground state as a reference, are bound strings of magnons [106].

Integrability, however, does *not* automatically imply superdiffusive hydrodynamics. Indeed, the generic expectation of an integrable system is that the hydrodynamics is *ballistic*, since any state is composed of freely-propagating quasiparticles carrying the local charges (spin, energy, etc.) of the model.

It has been shown [96] that energy transport in the quantum XXZ chain is ballistic for any Δ. The spin hydrodynamics, however, depend strongly on the anisotropy: ballistic hydrodynamics prevails in the easy-plane case ($\Delta < 1$), but the *diffusive* exponent $\alpha = 1/2$ is observed in the easy-axis ($\Delta > 1$). (Though it should be noted that this is not in the universality class of ordinary diffusion – the full counting statistics, and higher correlation functions, are anomalous [96])

In this case, it is diffusion that is the unexpected outcome. The reason that the ballistic motion of the quasiparticles does not produce ballistic spin transport in the easy-axis is that they are *screened* [106] (cf. Fig. 2.5(b)). When a magnon-string carrying, say, $+s$ units of S^z moves from a spin-down domain into a spin-up domain, it flips over to carrying $-s$ units of S^z. It was shown in Ref. [107], however, that the diffusion constant $D(\Delta)$ diverges as the isotropic point is approached from the easy-axis side,

$$D(\Delta) \sim |1 - \Delta|^{-1/2}, \tag{4.8}$$

Which shows that the isotropic spin hydrodynamics cannot be diffusive, and, since the Drude weight of the spin transport vanishes at the isotropic point [94], it cannot be ballistic either. Numerical evidence [56] supports a superdiffusive exponent $\alpha = 2/3$, and a self-consistent explanation of this finding has been provided [106, 108, 109].

As discussed in these references, the crucial point is that the time-scale over which a string of size s transports spin ballistically scales as $\tau \sim s^3$. This, when applied to the Kubo formula, results in a weak (sub-ballistic) divergence of the a.c. conductivity,

$$\sigma(\omega) \sim \omega^{-1/3}, \tag{4.9}$$

which implies superdiffusion with $\alpha = 2/3$. It is the subtle interplay of the quasiparticle scattering with the non-abelian $SU(2)$ symmetry that results in this transport lifetime, and thus, superdiffusion. It has been shown [110] that other non-abelian global symmetries also give rise to superdiffusion, perhaps lending further credence to this picture. The non-abelian symmetry also limits the rate at which integrability breaking perturbations can scatter the quasiparticles, suggesting that there is some perturbative stability to the superdiffusion [109].

4.3 The Ishimori chain

It would be remiss of us not to include the Ishimori spin chain (1.22) in this discussion, having made such extensive use of it in the generation of the solitons in Ch. 2. Ref. [111] has shown that the Ishimori chain has very similar superdiffusive hydrodynamics to the $S = \frac{1}{2}$ Heisenberg chain.

Moreover, one may generalise the $SO(3)$ symmetric Ishimori chain to include either an easy-plane or easy-axis anisotropy,

$$\begin{aligned}\mathcal{H} = -\sum_j \log \Big| &\cos(\gamma S_j^z)\cos(\gamma S_{j+1}^z) \\ &+ (\cot\gamma)^2 \sin(\gamma S_j^z)\sin(\gamma S_{j+1}^z) \\ &+ (\sin\gamma)^{-2} G_\gamma(S_j^z) G_\gamma(S_{j+1}^z)\left(S_j^x S_{j+1}^x + S_j^y S_{j+1}^y\right)\Big|,\end{aligned} \tag{4.10}$$

where

$$G_\gamma(x) = \left(\frac{\cos(2\gamma x) - \cos(2\gamma)}{1-x^2}\right)^{1/2}, \tag{4.11}$$

and γ is the anisotropy parameter: $\gamma \in \mathbb{R}$ is the easy-plane, $\gamma \in i\mathbb{R}$ is the easy-axis, and the isotropic Ishimori chain is recovered with $\gamma = 0$. Again, it was found that the easy-plane spin hydrodynamics is ballistic, and the easy-axis has diffusive scaling [111]. In this case we know all of the quasiparticles explicitly – they are the solitons (1.24). Fundamentally, the arguments that imply superdiffusion exists in the quantum Heisenberg also apply to the Ishimori chain – the magnetisation carried by a particular soliton is screened on a timescale $\tau \sim R^{-3} \sim s^3$.

4.4 The universality class

Whilst we have discussed the origin of the dynamical exponent $\alpha = 2/3$ in §4.2 and §4.3, this only tells us how the autocorrelator decays with time. To go beyond this, we need to consider the scaling functions. Numerical [67, 94, 96] and experimental [112] evidence shows that the two-point spin correlator of the isotropic integrable spin chains follows the Kardar-Parisi-Zhang (KPZ) scaling form,

$$\mathcal{C}^S(j,t) := \langle \boldsymbol{S}_j(t)\cdot\boldsymbol{S}_0(0)\rangle \sim t^{-2/3}\mathcal{F}_{\mathrm{KPZ}}(j/t^{2/3}), \tag{4.12}$$

where $\mathcal{F}_{\mathrm{KPZ}}$ is the scaling function of the KPZ universality class. This scaling arises from the KPZ equation, a stochastic model describing surface growth,

$$\partial_t h = \nu\partial_x^2 h + \frac{\lambda}{2}(\partial_x h)^2 + \partial_x \xi, \tag{4.13}$$

where $h(x,t)$ is some height field, and ξ is a white-noise field. From this equation we may obtain the stochastic Burgers equation via the substitution $\rho = \partial_x h$,

$$\partial_t \rho + \lambda\rho\partial_x\rho = D\partial_x^2\rho + \partial_x\xi, \tag{4.14}$$

where, λ is a non-linear coupling, D is the diffusion constant, and the strength of the white-noise field ξ is fixed by the fluctuation-dissipation theorem. It is the two-point correlator of ρ which follows the KPZ scaling form [113],

$$\mathcal{C}_\rho(x,t) := \langle \rho(x,t)\rho(0,0)\rangle \sim t^{-2/3}\mathcal{F}_{\mathrm{KPZ}}(x/t^{2/3}). \tag{4.15}$$

Now, the agreement of the scaling functions would suggest that the spin hydrodynamics are in the universality class of the stochastic Burgers equation (identifying $\rho \sim S^z$). However,

as pointed out in Ref. [114], this picture cannot be quite correct, because the KPZ equation and the stochastic Burgers equation are chiral (positive fluctuations of ρ move one way, depending on the sign of λ, negative fluctuations move the other) – but the microscopic spin dynamics are parity-symmetric.

This implies that the full counting statistics of the integrable spin chains and the stochastic Burgers equation disagree [112, 114], implying that, whilst they have the same superdiffusive exponent $\alpha = 2/3$, the spin dynamics are not in the KPZ universality class. For the sake of giving it a name, however, we will refer to the agreement of the two-point spin correlator (4.12) with the KPZ function as KPZ scaling; though we should keep in the back of our minds that not all of the correlation functions are in this class.

4.5 Non-linear fluctuating hydrodynamics

Of course, there remains, then, the question of what the correct hydrodynamic description actually is. Ref. [114] suggests a possible resolution in the form of two coupled equations for the magnetisation density $m(x,t)$ (the quantity in whose hydrodynamics we are primarily interested), and the "quasiparticle imbalance" $\phi(x,t)$,

$$\begin{aligned} \partial_t m + \partial_x \left(\kappa m\phi - D_m \partial_x m - \xi_m\right) &= 0 \\ \partial_t \phi + \partial_x \left(\frac{\kappa}{2} m^2 - D_\phi \partial_x \phi - \xi_\phi\right) &= 0, \end{aligned} \tag{4.16}$$

where D_m and D_ϕ are diffusion constants, and κ is the coupling of these two modes. $\xi_m(x,t)$ and $\xi_\phi(x,t)$ are independent white noise fields.

These non-linear fluctuating hydrodynamics (NFH) equations are derived from the framework of generalised hydrodynamics (GHD), with an appealing physical intuition. The ballistic (Euler scale) term in the m-equation arises because the large, slow-moving quasiparticles (magnon-strings in the quantum Heisenberg chain, solitons in the Ishimori chain), which carry most of the magnetisation, are given an effective non-zero velocity due to their collisions with faster-moving quasiparticles, as the scattering-shifts (cf. Eq. (2.11)) accumulate: if there are, locally, more right-moving quasiparticles than left-movers ($\phi > 0$), the large quasiparticles will, overall, be shifted to the right – and vice-versa.

As was shown in Ref. [114], these NFH equations capture the KPZ scaling of the correlation function, without the issues of chirality intrinsic to the stochastic Burgers equation; though there is potentially still some small disagreement with recent experimental work [112].

4.6 Outlook

In this chapter, we have reviewed the known mechanisms of superdiffusion in spin chains, and discussed how it arises through a combination of the ballistic propagation of excitations (solitons), and the screening of the magnetisation they carry – with the *super*-diffusion, precisely, reliant on the non-abelian symmetry of the model.

All of the models discussed in this chapter were *integrable*, and thus, rather non-generic. If we cast our minds back to Ch. 2, however, we saw that the soliton phenomenology often associated with integrability was, to a substantial extent, present in the non-integrable

classical Heisenberg chain. One might wonder, then[2], as to the extent to which any aspects of anomalous hydrodynamics may persist in non-integrable spin chains: this is the subject of our work in the next chapter.

[2]One may note that the order in which we have presented the solitons and the superdiffusion is quite the reverse of the order in which the relevant papers appeared: we noted first the superdiffusivity of the classical Heisenberg chain, and discovered the solitary excitations subsequently whilst searching for an explanation of the observed superdiffusion. We present an ahistoric progression in this thesis, as we feel that, blessed with retrospective perspicacity, it is the more logically coherent order.

Chapter 5

Superdiffusion in non-integrable spin chains

Some of the work in this chapter has appeared as part of the following article [36]:

Adam J. McRoberts, Thomas Bilitewski, Masudul Haque, & Roderich Moessner
Anomalous dynamics and equilibration in the classical Heisenberg chain
Phys. Rev. B **105**, L100403 (2022)

In Ch. 4, we have reviewed the phenomenology of superdiffusion in integrable spin chains. In non-integrable models, however, the generic expectation is ordinary diffusion.

In this chapter, we will present evidence that, for isotropic spin chains, this generic expectation is not *quite* correct – in the sense that superdiffusion can persist in non-integrable spin chains for extremely long times. The existence of such large intermediate scales is obviously relevant to experiments probing anomalous diffusion – anomalous behaviour might be the only accessible experimental regime even if diffusion is expected at infinite time.

We will first return to the classical Heisenberg chain, which we considered in the context of soliton excitations in Ch. 2. We perform extensive numerical simulations which reveal long-lived superdiffusion in the spin correlations, with the two-point correlator collapsing onto the KPZ scaling function across several decades of time. We are able to extract the dependence of the superdiffusive time-scale on the temperature, and show that it diverges rapidly as the temperature is lowered, implying that the observed superdiffusion becomes arbitrarily long-lived. We discuss a possible explanation of this phenomenology in terms of the solitons studied in Ch. 2, linking the solitary, localised excitations to the thermal hydrodynamics of the Heisenberg chain.

In §5.2 we examine spin superdiffusion in other non-integrable models. In particular, by considering the interpolating Hamiltonian (2.8) (which we used to build the solitons), we can extricate the dependence of the superdiffusive time-scale on the degree of integrability-breaking. We will also show that further-neighbour perturbations, which take us even further from integrability, lead to no loss of anomalous dynamics.

§5.3 asks whether anomalous dynamics, at least on large time-scales, is actually the norm in spin chains. We argue that the antiferromagnetic Heisenberg chain provides an example

of a "generic" spin chain, in that it shows no anomalous dynamics at any temperature. This is consistent with the soliton picture – the antiferromagnet has no solitons, and, hence, no superdiffusion.

5.1 Superdiffusion in the classical Heisenberg chain

As a paradigmatic example of a non-integrable model, we return to the classical Heisenberg chain. Again, the Hamiltonian is

$$\mathcal{H} = -J \sum_i \boldsymbol{S}_i \cdot \boldsymbol{S}_{i+1}, \tag{5.1}$$

where $\boldsymbol{S}_i \in S^2$, and we will use periodic boundary conditions (we have dropped the constant compared to Ch. 2). We set $J = 1$, which implicitly defines units of energy and time. For ease of reference, we repeat here the equations of motion:

$$\dot{\boldsymbol{S}}_i = J\boldsymbol{S}_i \times (\boldsymbol{S}_{i-1} + \boldsymbol{S}_{i+1}) \,. \tag{5.2}$$

Despite the fact that this is, arguably, the simplest interacting many-body spin system, the nature of its hydrodynamics has provoked extensive and long-lasting debate: it has been argued that the lack of integrability necessarily implies ordinary diffusion holds for both spin and energy [25–31]; however, there have also been proposals of anomalous behaviour [32–35], including an argument for logarithmically enhanced diffusion [35]; a claim subsequently contested by Ref. [31], arguing from a theory of non-abelian hydrodynamics that each component of the spin follows a separate, ordinary diffusion equation.

Here, we aim to settle this debate by presenting a systematic numerical study of the dynamical correlations of the classical Heisenberg chain over a wide range of temperatures, $T \ll |J|$ to $T = \infty$. In accordance with the expectation of diffusivity, we find ordinary diffusion of both spin and energy at $T = \infty$, and ordinary diffusion of energy at all (non-zero) temperatures.

We find, however, that the finite temperature spin correlations do not appear to follow this generic expectation. In particular, we find that the spin hydrodynamics is *superdiffusive*, at least over the numerically accessible time-scales. This deviation from diffusivity is apparent even at high temperatures, where the correlation length is less than a single lattice spacing.

The numerically-observed behaviour could be interpreted as anomalous diffusion with a temperature-dependent exponent, or, alternatively, as a crossover at remarkably large time-scales, rendering diffusion in practice prohibitively difficult to observe experimentally below some temperature scale. At low temperatures we observe the KPZ exponent almost perfectly across three decades in time, and the space-time profile of the correlation function closely follows the KPZ scaling form – establishing intermediate-time KPZ scaling at low temperatures in the Heisenberg chain, even if ultimately followed by a crossover to normal diffusion at very long times.

We proceed by first presenting the numerical data for the energy and spin correlations of the classical Heisenberg chain. All of the correlation functions at a given temperature were obtained by averaging over 20 000 initial states drawn from the canonical ensemble via heatbath Monte Carlo [115] (App. A). Each state is evolved in time, cf. (5.2), with snapshots

stored at intervals of $\Delta t = 10J^{-1}$. The correlation function at a fixed time difference t is calculated by averaging over 1000 consecutive snapshots for every initial state. All system sizes are $L = 16384$.

5.1.1 Energy correlations

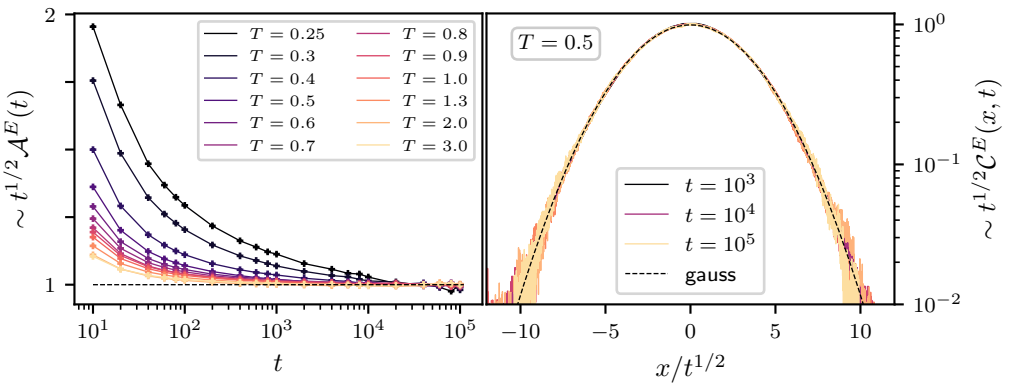

Figure 5.1: Energy diffusion in the classical Heisenberg chain. (Left) Convergence of the energy autocorrelator $\mathcal{A}^E(t)$ to the diffusive power-law $\alpha = 1/2$, at all temperatures. (Right) Diffusive scaling collapse at $T = 0.5$, showing that the Gaussian scaling function is recovered. Note that $T = 0.5$ is a sufficiently low temperature that spin *superdiffusion* is observed (Fig. 5.3), but the energy correlations are perfectly diffusive.

We can dispense relatively briefly with the energy correlations, where the expected results for a non-integrable model are recovered; to wit, ordinary diffusion swiftly prevails.

We show the energy autocorrelator in Fig. 5.1, finding that, for all temperatures, there is convergence towards diffusion over the simulation time, $t = 10^5$. We also show a scaling collapse with the standard diffusive exponent $\alpha = 1/2$, and find excellent agreement, recovering the standard Gaussian scaling function,

$$\mathcal{C}^E(x,t) \sim \frac{1}{(Dt)^{1/2}} \exp\left(-\frac{x^2}{Dt}\right). \tag{5.3}$$

5.1.2 Spin correlations

We turn now to the spin correlations, which, in contrast to the energy, and in apparent defiance of any presumption of ordinary diffusion, show anomalous dynamics at finite temperature.

The numerical data for the spin correlations are consistent with a temperature-dependent dynamical exponent $\alpha(T)$, ranging from $\alpha = 1/2$ (ordinary diffusion) at high temperature to $\alpha = 2/3$ (superdiffusion) at low temperature, obtained by directly fitting the autocorrelator to a power-law,

$$\mathcal{A}^S(t) \sim \kappa t^{-\alpha}, \tag{5.4}$$

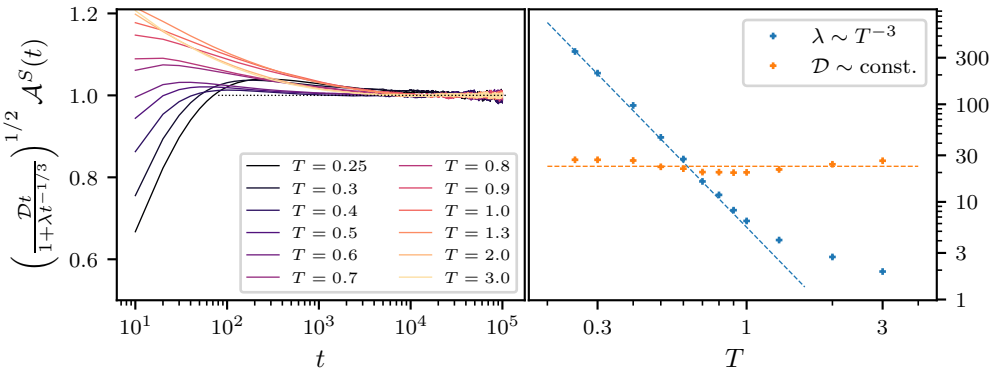

Figure 5.2: Spin superdiffusion in the classical Heisenberg chain: (Left) Convergence of the spin autocorrelator $\mathcal{A}^S(t)$ to the crossover form (5.7); excellent agreement after $t \approx 10^3$ is observed at all temperatures. (Right) Values of the crossover parameters $\mathcal{D}$ and λ obtained by fitting the measured spin autocorrelator to Eq. (5.7), as a function of temperature. The superdiffusion-parameter λ diverges as $\lambda \sim T^{-3}$ for $T \lesssim J$, suggesting that the superdiffusive regime becomes arbitrarily long-lived at low temperatures. There are some fluctuations of the measured diffusion constant $\mathcal{D}$, but overall it is observed to be effectively independent of temperature. Note that $T = 0.1$ and $T = 0.2$ have also been simulated, but it is impossible to extract the crossover parameters, as there is no observable deviation from KPZ-like superdiffusion over the simulation time at these temperatures.

and then using this α in the scaling collapse of the full correlation function $\mathcal{C}^S(x,t)$. In Ref. [36], where we first presented the anomalous dynamics of the classical Heisenberg chain, we suggested this as a possible picture, alongside a competing picture of a crossover from ballistic correlations at short time to diffusion at long times,

$$\mathcal{A}^S(t) \sim (Dt)^{-1/2} + \Lambda t^{-1}. \tag{5.5}$$

We no longer believe that either of these scenarios captures the essential physics of the problem. In light of more recent work on integrable spin chains [35, 96, 106, 114, 116], and our own work on the existence of solitons in non-integrable spin chains [24] (& Ch. 2), we believe that the true description is a crossover from KPZ-like superdiffusion ($\alpha = 2/3$) to ordinary diffusion ($\alpha = 1/2$) as $t \to \infty$, but that the superdiffusive regime becomes parametrically long-lived at low temperature.

We can be somewhat more sophisticated in reasoning out the form of the crossover than we were in Eq. (5.5), as follows: if we have ordinary diffusion, the autocorrelator has the form

$$\mathcal{A}^S(t) = \frac{1}{(Dt)^{1/2}}, \tag{5.6}$$

where D is the diffusion constant. We can describe the crossover by adding time-dependence to the diffusion "constant", $D \mapsto D(t)$. We must have this asymptote to a constant as $t \to \infty$, but recover the $t^{-2/3}$ decay at finite time. The simplest form that satisfies these constraints

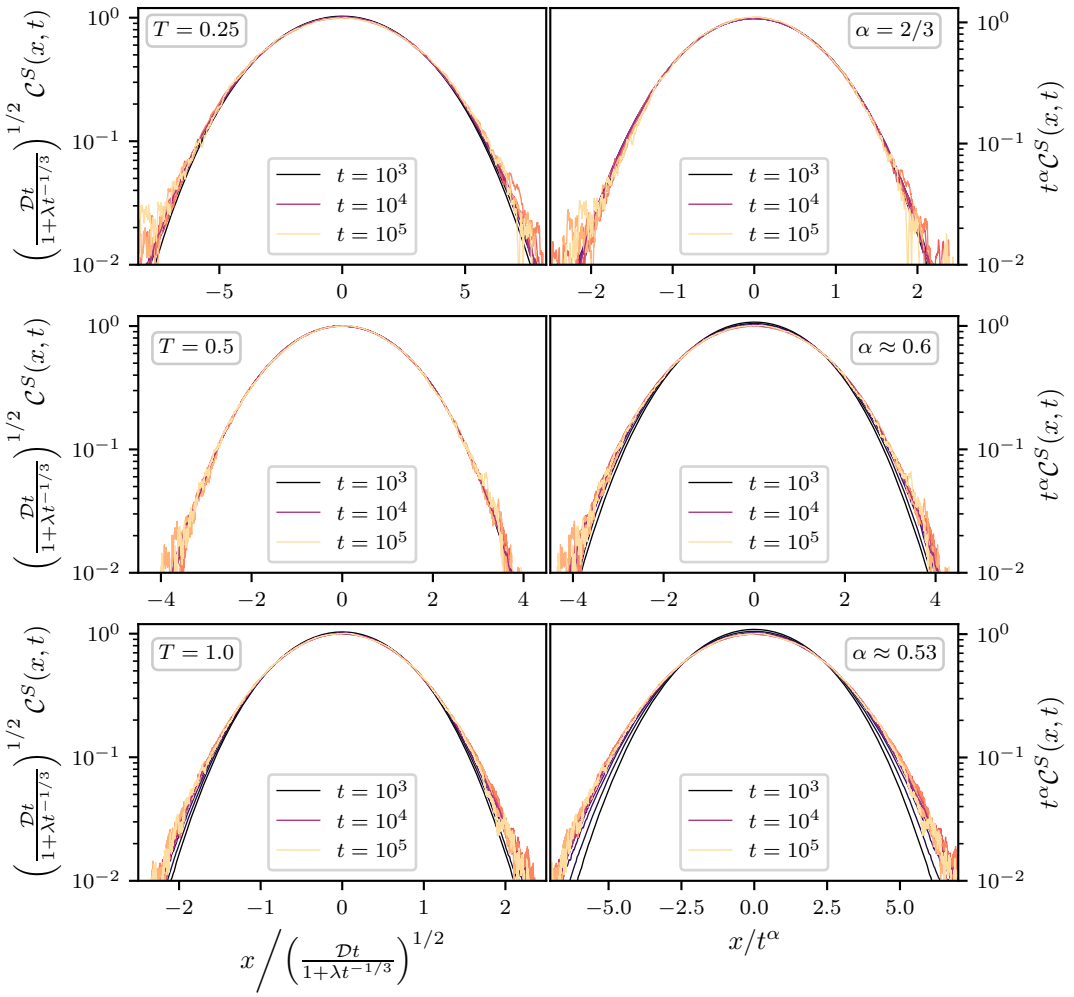

Figure 5.3: Scaling collapses of the spin correlations at various temperatures, showing the anomalous dynamics. (Left column) Scaling collapses using the KPZ-diffusion crossover, Eq. (5.7). (Right column) For comparison, scaling collapses using a direct fit to a power-law with an anomalous exponent, Eq. (5.4). We observe that the anomalous exponent provides good scaling collapses after $t \approx 10^4$, but that the crossover picture collapses the correlations better at both early and late times, which is strong evidence in its favour – a slight exception to this is seen at $T = 0.25$, where the $\alpha = 2/3$ power-law persists over the entire simulation time, and it becomes very difficult to extract the crossover parameters with any reliability below this temperature.

is a two-parameter fit:

$$D(t) \sim \frac{\mathcal{D}}{1 + \lambda t^{-1/3}}. \tag{5.7}$$

This is borne out by the numerical data. In Fig. 5.2 we show that the spin autocorrelator converges to the form predicted by this crossover (5.7) at all temperatures. We plot the scaling collapses derived from the crossover in Fig. 5.3, where we also compare them to scaling obtained from a direct fit to an anomalous power-law (5.4). We find that the crossover picture provides a slightly better collapse across the full range of times – though, at low-temperatures, it becomes difficult to extract the crossover parameters as the $\alpha = 2/3$ regime survives over the entire simulation.

5.1.3 A matter of time(-scale)

We turn now to the temperature-dependence of the time-scale over which the spin superdiffusion we have seen in §5.1.2 is observable.

Asymptotically, Eq. (5.7) predicts ordinary diffusion, but, if $\lambda \gg 1$, a very long time will need to elapse before this becomes apparent. Now, at any moment, an effective dynamical exponent is given by the logarithmic derivative,

$$\alpha(t) = -\frac{d\log \mathcal{A}(t)}{d\log t} = \frac{2}{3} - \frac{1}{6\left(1+\lambda t^{-1/3}\right)}. \tag{5.8}$$

If we define some crossover time $\tilde{t}$ as the time after which $\alpha(t) < \tilde{\alpha}$, for some arbitrary $\tilde{\alpha}$, we find

$$\tilde{t} = \left(\frac{1}{4-6\tilde{\alpha}} - 1\right)^{-3} \lambda^3. \tag{5.9}$$

We show in Fig. 5.2 that, for $T \lesssim J$, the temperature-scaling is $\lambda \sim T^{-3}$. This, in turn, implies that the crossover time has the temperature dependence

$$\tilde{t} \sim T^{-9}, \tag{5.10}$$

which explains why it is impossible to reliably extract $\mathcal{D}$ and λ from the data at $T \lesssim 0.2$; diffusive behaviour does not emerge, at these temperatures, over the length and time-scales that we can simulate.

Indeed, extrapolating the parameters from Fig. 5.2, the crossover times for $\tilde{\alpha} = 0.65$ (i.e., the time at which it becomes clear that $\alpha = 2/3$ is not the true dynamical exponent), are $\tilde{t} \approx 10^6$ and $\tilde{t} \approx 10^8$ for $T = 0.2$ and $T = 0.1$, respectively. The time-scales for recovering ordinary diffusion at these temperatures, say, $\tilde{\alpha} = 0.51$, are $\tilde{t} \approx 10^{12}$ and $\tilde{t} \approx 10^{15}$, respectively.

5.1.4 Role of the solitons

Let us recapitulate the phenomenology of the classical Heisenberg chain we have observed so far. Energy correlations are diffusive, and any ballistic spin-wave regime is short-lived and only occurs at the lowest temperatures we have simulated. This is clearly unlike the integrable spin chains, where energy transport is ballistic even at $T = \infty$.

By contrast, one does not require very low temperatures to observe a long-lived regime of superdiffusion in the spin correlations – indeed, at $T = J$, the correlation length is less than a single lattice spacing, but the time-scale for recovering diffusion is $\tilde{t} \approx 10^7$

($\tilde{\alpha} = 0.51$). Moreover, at low temperatures, the superdiffusive regime is likely to be the only experimentally accessible regime in, say, some cold-atom experiment probing this dynamics.

The question thus arises: Why are the spin correlations of the non-integrable Heisenberg chain similar to those of the integrable chains, but the energy correlations are not?

The answer, we posit, lies in the solitons. Recall that the magnetisation and energy carried by an Ishimori soliton are

$$M = \frac{2\sinh 2R}{\cosh 2R - \cos 2k}, \quad E = 4\tanh 2R. \tag{5.11}$$

Examining the existence diagram (Fig. 2.1), we see that the solitons which do not survive in the Heisenberg chain are those which are narrow and fast (large R, large k) – these are the solitons which carry high amounts of energy, so the excitations responsible for ballistic energy transport in integrable spin chains do not appear in the classical Heisenberg chain.

The solitons which do survive are those at small k and R, which are the solitons that carry large amounts of magnetisation – and are known to be responsible for the superdiffusive spin transport in the Ishimori chain. We have shown in Ch. 2 that the Heisenberg solitons are remarkably similar to the Ishimori solitons – both in their individual properties and in their scattering. And we have shown in Figs. 2.8 and 2.9 that they are present in the low-temperature thermal states. In fact, the inverse-scattering (Fig. 2.9) indicates, albeit qualitatively, that the solitons comprise the main content of low-temperature thermal states of the classical Heisenberg chain.

The eventual crossover to diffusion, however, indicates that the solitons have some finite thermal lifetime, which, presumably, depends both on the inverse-width (how stable the soliton is to collisions) and the temperature (the density of other objects in the state).

Now, consider again the NFH picture (4.16) [114]. In this formulation, the superdiffusion arises due to a ballistic (Euler scale) contribution to the spin-current: large solitons, carrying most of the magnetisation m, are given an effective velocity by their collisions with faster-moving solitons, via the scattering shift (cf. Eq. (2.11)). A local imbalance in the number of left-moving or right-moving solitons, ϕ, causes the large solitons to experience more scattering shifts in the opposite direction.

The magnetisation remains a conserved charge of the non-integrable classical Heisenberg chain, and we have seen that the soliton-scattering is very similar to the integrable case. Moreover, the large solitons are extremely stable [109, 116], since they are related to the Goldstone modes. It seems reasonable, then, that the hydrodynamic equation for m will be unchanged,

$$\partial_t m + \partial_x \left(\kappa m\phi - D_m \partial_x m - \xi_m\right) = 0. \tag{5.12}$$

The "quasiparticle imbalance" ϕ, however, does not refer only to the large solitons. Since the solitons are not perfectly protected, this cannot be a conserved quantity and so does not, formally, constitute a hydrodynamic mode. On the other hand, the long-lived ballistic trajectories (Fig. 2.8) and the long-lived superdiffusion suggest that it is "quasi-conserved" at low temperatures. We therefore conjecture that its hydrodynamic equation may be retained, but with an additional decay term,

$$\partial_t \phi + \partial_x \left(\frac{\kappa}{2} m^2 - D_\phi \partial_x \phi - \xi_\phi\right) = -g\phi, \quad g \geq 0, \tag{5.13}$$

which breaks the conservation of ϕ (Eq. (5.13) does not have the form of a continuity equation for $g > 0$). We note that, while the decay term naturally causes any large imbalance to fall

towards zero, a finite value of g does not mean that $\phi(x, t \to \infty) \to 0$; non-zero values of ϕ are still sourced both by the noise and the coupling to the magnetisation.

A topic for future work is to show that these modified NFH equations actually capture the finite-time behaviour of the classical Heisenberg chain, and evince the same long-lived superdiffusion. It may be seen by inspection, however, that the limiting behaviours ($\alpha = 2/3$ and $\alpha = 1/2$) are captured by this modification: $g = 0$ returns the original NFH equations exhibiting superdiffusion; and, in the limit $g \to \infty$, any non-zero ϕ decays immediately to zero, reducing the m-equation (5.12) to the (noisy) diffusion equation.

5.2 Superdiffusion in other non-integrable spin chains

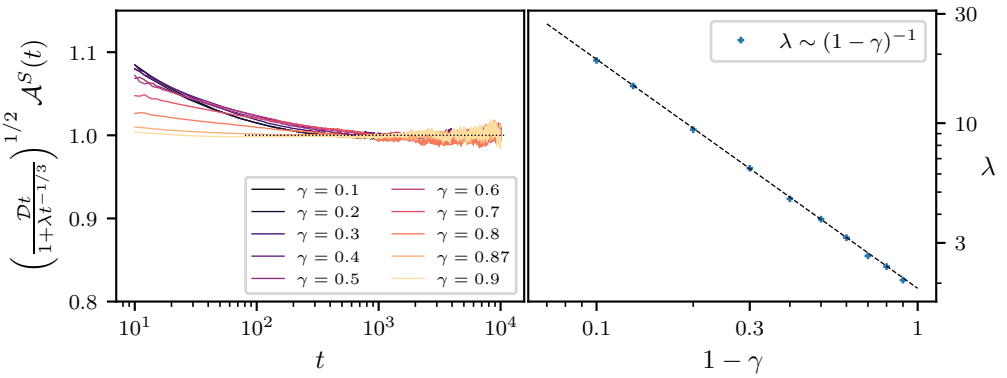

Figure 5.4: Superdiffusion as a function of integrability-breaking, $1-\gamma$. All results obtained at $T = \infty$. (Left) Convergence of the spin autocorrelator to the crossover (5.7), for various degrees of broken integrability. (Right) The superdiffusion parameter λ as a function of $1 - \gamma$, showing a clear scaling dependence $\lambda \sim (1 - \gamma)^{-1}$.

In §5.1 we have shown that the classical Heisenberg chain – a non-integrable spin model – harbours a much richer and more subtle hydrodynamic phenomenology than has previously been appreciated. In this section we ask whether other non-integrable spin chains can exhibit similar long-lived regimes of superdiffusion.

5.2.1 Superdiffusion and the degree of integrability-breaking

We will first consider our interpolating model,

$$\mathcal{H} = -2J\gamma^{-1} \sum_i \log\left(1 + \gamma \frac{\boldsymbol{S}_i \cdot \boldsymbol{S}_{i+1} - 1}{2}\right), \tag{5.14}$$

connecting the Ishimori chain ($\gamma = 1$) to the Heisenberg chain ($\gamma = 0$). It is, of course, not surprising that this model shows the same phenomenology as the Heisenberg chain, due to lying on the direct connection to the integrable case, but this fact allows us to examine the dependence of the superdiffusive timescales on the degree of integrability-breaking.

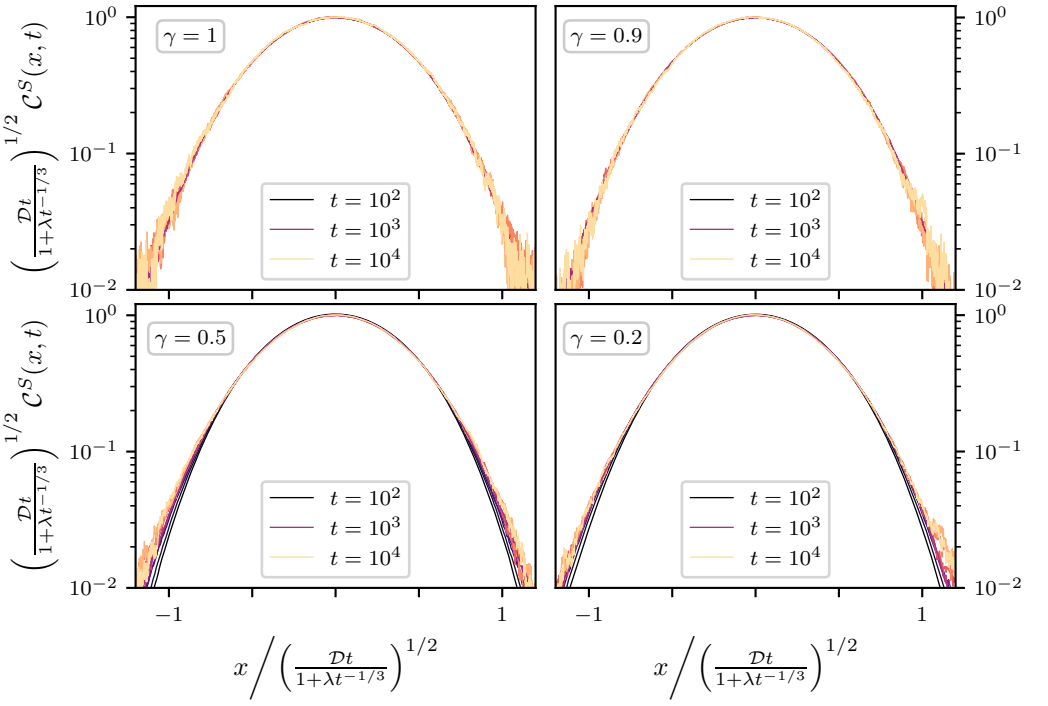

Figure 5.5: Spin scaling collapses (at infinite-temperature) for various degrees of integrability-breaking. We reproduce the known KPZ-scaling of the Ishimori chain ($\gamma = 1$) for longer times than Ref. [111], and show the survival of the superdiffusive regime far from integrability.

We examine the spin correlations of the interpolating Hamiltonian (5.14) at $T = \infty$. The Ishimori chain is believed to be superdiffusive at all temperatures, so working with completely random initial states allows us to investigate the hydrodynamic effects of integrability breaking perturbations to the Hamiltonian, without finite temperatures providing additional stability to the solitonic quasiparticles. The system size used in these simulations was $L = 8192$.

We find that the KPZ-diffusion crossover, Eq. (5.7), again provides a very good description of the dynamical correlations, with the spin superdiffusion persisting for longer times, as expected, when the degree of integrability-breaking, $1 - \gamma$, is small.

We show the dependence of the superdiffusion parameter λ on $1 - \gamma$ in Fig. 5.4. We find the scaling

$$\lambda \sim \frac{1}{1-\gamma}, \tag{5.15}$$

in contrast to this parameter's cubic dependence on the temperature. The superdiffusive time-scale, however, still scales as $\tilde{t} \sim \lambda^3$, so

$$\tilde{t} \sim \frac{1}{(1-\gamma)^3}. \tag{5.16}$$

Fig. 5.5 shows scaling collapses for various values of γ, including the integrable model; again, the crossover (5.7) captures the full two-point correlation function.

5.2.2 Superdiffusion in the $J_1 - J_3$ model

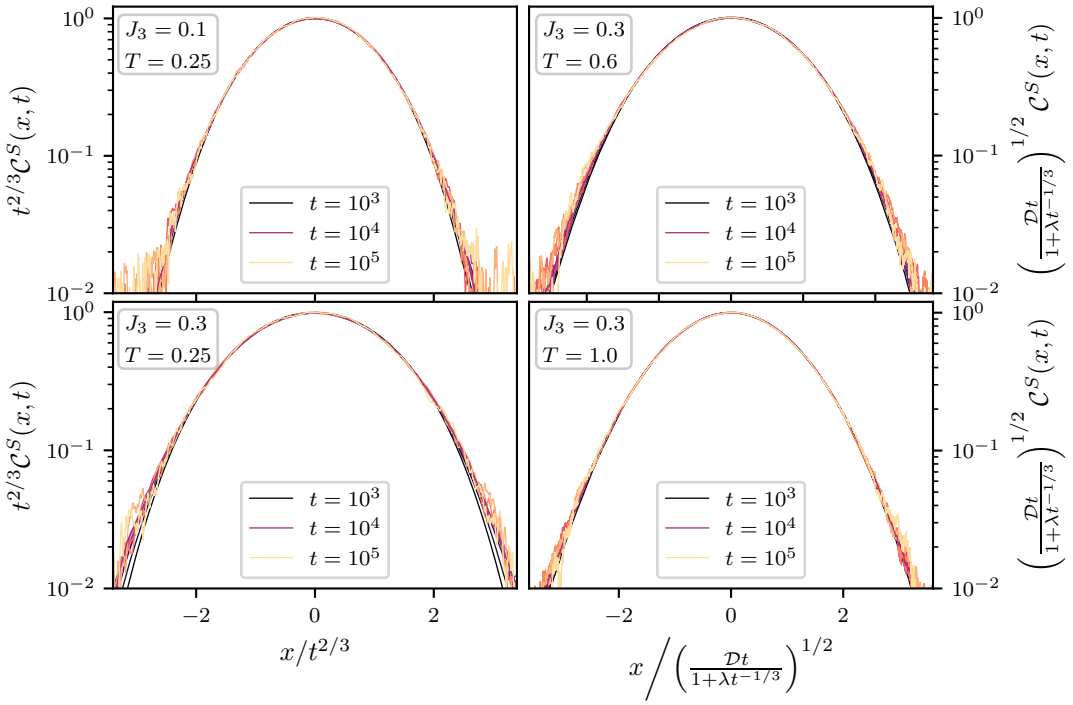

Figure 5.6: Long-lived spin superdiffusion in the $J_1 - J_3$ chain. (Left-column) Low-temperature scaling collapses for $J_3 = 0.1$ and $J_3 = 0.3$ with the superdiffusive exponent $\alpha = 2/3$ directly, establishing the survival of the KPZ-like superdiffusion in this model, and showing that ordinary diffusion does not emerge over the simulation time-scale $t = 10^5 J_1^{-1}$ at $T = 0.25$. (Right column) We show that the long crossover (5.7) provides an excellent scaling collapse at intermediate temperatures. All system sizes $L = 16384$.

We close this section by briefly considering the effect of further neighbour perturbations, and study the spin correlations of the $J_1 - J_3$ spin chain,

$$\mathcal{H} = -J_1 \sum_i \boldsymbol{S}_i \cdot \boldsymbol{S}_{i+1} - J_3 \sum_i \boldsymbol{S}_i \cdot \boldsymbol{S}_{i+3}. \tag{5.17}$$

We use this model instead of the, perhaps, more natural $J_1 - J_2$ model because it is bipartite – which has computational implications (see App. A). The additional perturbation takes us further from integrability than the Heisenberg chain ($J_3 = 0$), but there seems to be no loss of superdiffusive behaviour.

We have not performed a systematic investigation of the superdiffusive time-scale's dependence on J_3, but we do present scaling collapses of the spin correlations which show the same long-lived superdiffusion as in the classical Heisenberg chain ($J_3 = 0$), in Fig. 5.6. At low temperature ($T = 0.25$) we show for both $J_3 = 0.1$ and $J_3 = 0.3$ that the KPZ-like regime survives over the entire simulation, and we show that the crossover continues to provide a good description of the spin correlations at intermediate temperatures.

5.3 Does there exist a generic classical spin chain?

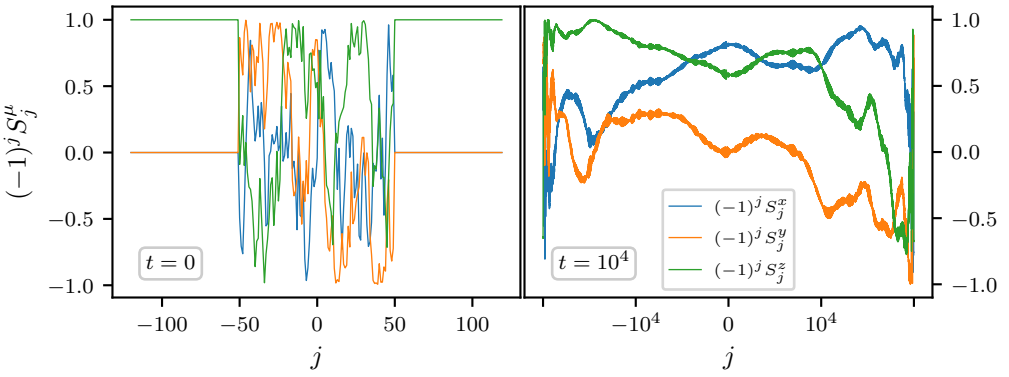

Figure 5.7: Absence of solitary excitations in the antiferromagnetic classical Heisenberg chain. Note that the staggered magnetisation is plotted. The contrast with Fig. 2.9, where many localised excitations (solitons) can be identified, is particularly striking. $T = 0.1$.

Whilst this question is clearly not well-formed, the underlying point is meaningful: in this chapter, we have taken one of the simplest many-body spin models and shown that it exhibits parametrically long-lived anomalous dynamics. Nor is this unique to the Heisenberg chain – we have seen examples of other non-integrable spin chains with the same hydrodynamic phenomenology. Even though ordinary diffusion is expected to *eventually* emerge at all non-zero temperatures, the existence of superdiffusion at all – distinct from a very short-time ballistic (spin wave) regime – is, *a priori*, quite unexpected.

In this light, let us consider the question in the section title. Perhaps we might take "generic" to mean that the only conserved quantities are spin and energy, both of which evince only diffusion (at all temperatures) after a possible ballistic crossover at short times, and that there are no long-lived localised quasiparticles in the thermal states.

One such generic spin model is the classical Heisenberg chain – the *antiferromagnetic* classical Heisenberg chain. Now, the only distinction with the ferromagnet considered in §5.1 is in the distribution of initial states, as both the energy and spin correlators are time-reversal invariant. This is enough, however, to kill the superdiffusive regime at all temperatures, because there are *no solitons on an antiferromagnetic background*, and there are, thus, no excitations to generate the ballistic contribution to the spin current in Eq. 5.12. We show explicitly in Fig. 5.7, by considering the inverse-scattering, that the low temperature antiferromagnetic thermal states are not composed of solitary excitations in the way that the

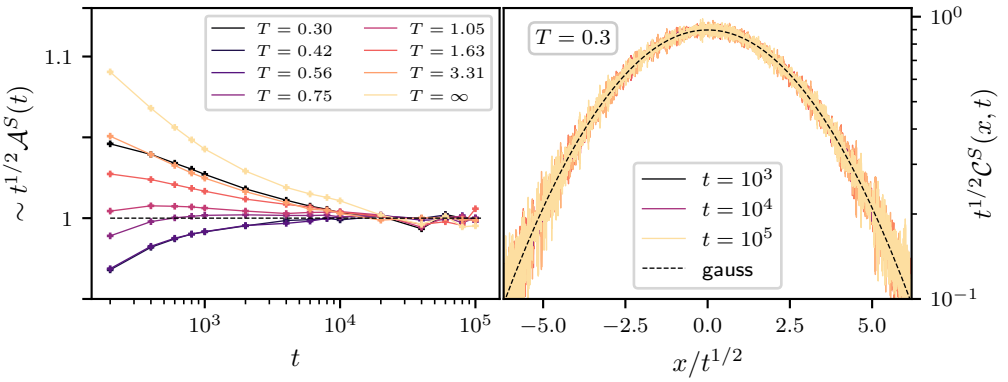

Figure 5.8: Spin diffusion in the antiferromagnetic classical Heisenberg chain. (Left) Convergence of the spin autocorrelator to the diffusive power-law, $\alpha = 1/2$. (Right) Diffusive scaling in the antiferromagnet at $T = 0.3$, at which temperature the ferromagnet evinces superdiffusion up to $\tilde{t} \approx 10^{10}$ ($\tilde{\alpha} = 0.51$).

ferromagnetic states are (cf. Fig. 2.9). We also plot the low-temperature spin correlations of the antiferromagnetic Heisenberg chain in Fig. 5.8, and find no superdiffusive regime.

5.4 Conclusion and outlook

Let us summarise what we have seen in this chapter. We have taken a *non-integrable* model – possibly the simplest spin model – and shown the existence of a parametrically long-lived, KPZ-like superdiffusive regime in the spin correlations. The same phenomenology is apparent in other non-integrable spin chains, indicating that there is some universality to this observation. Further, we have extracted the temperature- and integrability-dependence of the superdiffusive time-scale.

No such superdiffusion is observed for energy correlations, which leads us to posit that the solitons we constructed in Ch. 2 are responsible for the anomalous dynamics – since it is only the solitons which carry large amounts of magnetisation that survive the adiabatic transformation. We have conjectured that a modified set of NFH equations (5.13) may capture the essential physics.

Further credence is lent to this picture by the observation that the antiferromagnetic Heisenberg chain behaves much more generically, displaying only ordinary spin diffusion – since it has no solitons to generate the ballistic contribution to the spin current.

Our work contributes to the broader study of the role of approximate integrability in many-body systems, a question of sustained interest in both quantum [117–123] and classical [124–130] contexts. An obvious further question is to test the extent to which the modified NFH equations (5.13) are consistent with the Heisenberg chain, and to explain the observed temperature-dependence. Nevertheless, the striking absence of diffusion on accessible time-scales at low temperatures certainly illustrates the point that, even in the very simplest settings, many-body dynamics still holds many surprises awaiting discovery.

Part III

Subdiffusion

Chapter 6

Three routes to subdiffusion

In contrast to Parts I & II of this thesis, where we have examined ballistically propagating excitations and superdiffusive hydrodynamics, we concern ourselves now with the opposite scenario – where normal diffusive processes are heavily constrained, and the motion of conserved quantities through the system is strongly suppressed.

This is the realm of *subdiffusion*, where the general hydrodynamic form for the (connected) two-point correlation function of some conserved quantity ϕ is still

$$\langle \phi(x,t)\phi(0,0)\rangle \sim t^{-\alpha}\mathcal{F}(x/t^{\alpha}), \tag{6.1}$$

but where the dynamical exponent is such that $0 < \alpha < \frac{1}{2}$. This is distinct from *localisation*, where $\alpha = 0$.

In this chapter, we will review some of the literature on subdiffusion, and discuss three mechanisms by which it arises. First, and perhaps most straightforwardly – disorder. We will consider the possibility of a sharp diffusion-subdiffusion transition in the random field XXZ model, originally conceived as the lead-up to a many-body localisation (MBL) transition. Though serious doubt as to the existence of the MBL phase has been cast in recent years, the observed subdiffusive phenomenology still merits close attention.

Second – additional conservation laws. We will discuss how the additional constraints imposed on the degrees of freedom by the conservation of additional moments, such as the dipole moment or the centre of mass forbid the processes that drive ordinary diffusion.

Third – kinetic constraints, where certain "matrix elements" corresponding to free random motion (and thus diffusion) vanish, though these models are distinct from those that obtain subdiffusion by additional conservation laws because these constraints do not necessarily imply any additional conserved quantity.

Lastly, we will discuss the extent to which these mechanisms may be connected. *Prima facie*, these appear to be distinct mechanisms, but, ultimately, it may be that subdiffusion is arrived at in a fundamentally similar manner – the basic diffusive processes are parametrically slowed or forbidden altogether. We will look ahead to the next chapter, where we will present our work on the bond-disordered classical Heisenberg chain, providing an analytic example of an interacting subdiffusive model with no additional constraints.

6.1 Disorder

Perhaps the most obvious mechanism by which the transport of conserved quantities can be slowed is the introduction of disorder. In particular, whilst Anderson localisation has long been known to be the generic result for (quenched) disordered non-interacting 1D quantum systems [131], the interplay of many-body interactions with disorder has been the subject of intense study, and the source of much controversy, ever since.

A proper discussion of subdiffusion in disordered systems requires a digression into the history and current state of the many-body localisation transition. One of the canonical models used in this subject is the random-field quantum spin-$\frac{1}{2}$ XXZ chain,

$$\hat{H} = J \sum_j \left(\hat{S}^x_j \hat{S}^x_{j+1} + \hat{S}^y_j \hat{S}^y_{j+1} + \Delta \hat{S}^z_j \hat{S}^z_{j+1} \right) + \sum_j h_j \hat{S}^z_j, \tag{6.2}$$

with anisotropy parameter Δ, and random fields h_j drawn from the uniform distribution on the interval $[-W, W]$, where W is the disorder strength. Through the Jordan-Wigner transformation [104], this is equivalent (up to a constant) to an interacting fermion model with random chemical potentials,

$$\hat{H} = -\frac{J}{2} \sum_j \left(\hat{c}^\dagger_{j+1} \hat{c}_j + \hat{c}^\dagger_j \hat{c}_{j+1} \right) + J\Delta \sum_j \hat{c}^\dagger_{j+1} \hat{c}^\dagger_j \hat{c}_j \hat{c}_{j+1} + \sum_j h_j \hat{c}^\dagger_j \hat{c}_j, \tag{6.3}$$

so Anderson localisation of non-interacting fermions is recovered when $\Delta = 0$. This model is sometimes modified further by breaking the in-plane isotropy (the XYZ chain), which breaks the conservation of the z-magnetisation, or, equivalently, the fermion number.

From the mid-2000s onwards, an accumulation of perturbative [132, 133] and numerical [134–138] evidence suggested that, for sufficiently strong disorder $W > W_c$, a phase of localisation survived in interacting, many-body systems – and was thus dubbed many-body localisation (MBL).

Much of the numerical work – particularly the exact diagonalisation studies – put the MBL transition at a relatively mild critical disorder $W_c \approx 3$. In recent years, however, serious doubt has been cast on whether the critical disorder is not, in fact, much greater ($W_c \approx 100$), whether the MBL regime is numerically accessible [139], or, indeed, whether a many-body localised phase exists at all [140–146]. Particularly challenging to the idea of MBL as a true phase (i.e., in the thermodynamic limit) is the idea of the avalanche instability [144, 147], where rare ergodic sub-regions cause their surrounding, apparently localised regions, to eventually thermalise.

Concomitantly with this development of the field of many-body localisation, it was noted by several authors [148–155] that, in the approach to the apparent MBL transition, a regime of subdiffusion appears to emerge, where, at some lower critical disorder $W_c^<$, the dynamical exponent α departs from $1/2$ and falls continuously towards zero as W increases, terminating at the MBL transition, if it exists.

One proposed mechanism for the subdiffusive regime is that rare-region (Griffiths) effects act as local bottlenecks constraining the transport [148, 156], or, from a different perspective, as part of a resonant cluster that ensures the system is delocalised [149], though Ref. [157] points out a few possible inconsistencies in this picture. Ultimately, whilst the disordered spin-$\frac{1}{2}$ chain shows clear signatures of subdiffusion at finite-size, the curse of dimensionality

coupled with the lack of a convincing analytic picture means that it is not totally clear whether this subdiffusion survives to asymptotic times and system sizes.

6.2 Higher-moment conservation

Ref. [158] has provided a second mechanism by which subdiffusion can arise – namely, the conservation of higher-moments of the charge density whose transport is being probed. These additional conservation laws can give rise to fracton dynamics [159–164] or, in the case of low spin and very short range interactions, fragment the Hilbert space into an exponential number of disconnected sectors, preventing thermalisation and localising the charge [165, 166].

However, by including slightly longer range interactions (still "short-range", in the sense that they have bounded support), or higher-spin representations, or, indeed, using a classical circuit model – while still incorporating these additional conservation laws – a hierarchy of subdiffusive exponents can be obtained.

The simplest classical circuit model in this paradigm consists of four-site gates which can act by hopping one particle to the right by one site, and one other particle to the left by one site – thus conserving the dipole moment $\sum_j j n_j$, where $n_j \in 0, 1$ is the occupancy of the j^{th} site. As shown in Ref. [158], this stochastic model has subdiffusive dynamics with $\alpha = 1/4$.

More generally, if m additional moments (dipole, quadrupole, octupole, etc.) are conserved, the hydrodynamics is governed by the simple equation

$$\partial_t \phi = -(-1)^{m+1} D \, \partial_x^{2(m+1)} \phi, \tag{6.4}$$

where ϕ is the base conserved charge, and D is some constant, which results in subdiffusion with the dynamical exponent

$$\alpha = \frac{1}{2(m+1)}. \tag{6.5}$$

(There is only one hydrodynamic equation – whilst $m+1$ independent charges would result in $m+1$ equations, the hierarchy of moments are clearly not independent of each other). In this way, constructing models with higher-moment conservation allows multiple different subdiffusive regimes to be accessed.

6.3 Kinetic constraints

A third route by which subdiffusion is known to occur is that of "kinetic constraints" – where the hopping processes that would lead to ordinary diffusion are forbidden. Ref. [167] has studied a number of models with various constraints, going under the names of PXYP, $U(1)$-East [168], XNOR, Fredkin, and GLT, and found that the XNOR and Fredkin models are subdiffusive with exponents $\alpha = 1/2$ and $\alpha = 3/8$, respectively. (The PXYP and $U(1)$-East models were found to be localised, and the GLT model is diffusive).

For this exposition, let us focus on the XNOR model, since there is an appealing intuitive explanation of the mechanism in terms of the flux of random walkers. Although the original

study was of a quantum circuit model [167], the same transport phenomenology appears in the classical case, so we will describe it in this manner.

The setup is rather simple. Consider a classical chain with N sites. The state of the system, $\boldsymbol{n}$, is specified by the binary occupancy $n_i \in \{0, 1\}$ of each site i. The occupation of the sites is the locally conserved charge in whose transport we are interested. The model is imbued with stochastic dynamics by the action of four-site gates $\mathcal{G}_i$, acting on sites $i, ..., i+3$, which swaps the occupation of sites $i + 1$ and $i + 2$ if and only if $n_i = n_{i+3}$; that is, both sites on either side of a bond must be either occupied or unoccupied for a hop to occur, hence the name XNOR. A single time-step consists of the application of each gate $\mathcal{G}_i$, once for each i, but in a randomly-determined order.

To give a possible physical context for this[1], at first glance, rather unnatural-looking constraint, we might consider there to be some nearest-neighbour repulsive energy between particles – i.e., the bond $(i, i+1)$ has energy $\mathcal{E}_i = +1$ if $n_i = n_{i+1} = 1$, and $\mathcal{E}_i = 0$ otherwise. The XNOR constraint is then equivalent to imposing energy conservation at each move, though this does lead to the somewhat counter-intuitive outcome that domains of two or more particles are bound together by *repulsion*, since lowering the energy by spontaneously breaking the domain apart is forbidden (there is no kinetic energy term).[2]

Regardless of how we arrive at it, let us now see why this model is subdiffusive. The first key insight is that the XNOR constraint freezes the motion of any string of two or more consecutive particles: only single particles isolated in a domain of holes, or, conversely, a single hole isolated in a domain of particles, can move under the action of the gates $\mathcal{G}$.

This leads us to the notion of quasiparticles in this model – in any given initial state, we can identify the isolated holes and isolated particles, imbued by the gate actions with a naturally diffusive motion (each quasiparticle will perform a random walk), and which are the only directly itinerant degrees of freedom in the state. These quasiparticles are themselves locally conserved, but, crucially, are decoupled from the direct transport of charge because a quasiparticle which moves from a hole domain into a particle domain changes flavour from a particle to a hole, and vice-versa. Each quasiparticle spends half its time as a particle, and half its time as a hole, so its diffusive motion does not directly contribute to the hydrodynamic motion of the charge n_i.

The second key insight, however, is to note that the domains *can* move, but that their motion is tied to the quasiparticles – if a quasiparticle completely crosses a charge domain from left-to-right, the domain is shifted one site to the left, and vice-versa. That is, a domain moves a number of sites equal to the total flux of quasiparticles through it, and it is this motion that leads to subdiffusive charge transport.

Let us put this on a more mathematical footing with a hydrodynamic picture. Suppose we start with a quasiparticle at position $x = x_0$. Since its motion is diffusive by construction, the coarse-grained probability density for this quasiparticle spreads as

$$p(x, t) = \frac{1}{\sqrt{\pi D t}} \exp\left(-\frac{(x - x_0)^2}{Dt}\right). \tag{6.6}$$

[1] As a historical note, this energy-conservation motivation is, in fact, how Chris Hooley, Frank Pollmann, and I first arrived at this model, when we were unaware of the kinetic constraint formalism. The classical circuit results we discuss in this section were obtained independently, but are fundamentally equivalent to the quantum XNOR model of Ref.[167].

[2] Curiously, we obtain the same constraint if we instead introduce some *attraction* between particles, $\mathcal{E}_i = -1$ if $n_i = n_{i+1} = 1$; though the counter-intuitive aspect now is that free particles cannot bind to domains of other particles, even though they are attracted.

Thus, the probability that the quasiparticle is found at $x > x_c$ at time t is

$$P_{x>x_c}(t) = \int_{x_c}^{\infty} \frac{dx}{\sqrt{\pi D t}} \exp\left(-\frac{(x-x_0)^2}{Dt}\right) = \frac{1}{2}\left(1 + \mathrm{Erf}\left(\frac{x_0 - x_c}{\sqrt{Dt}}\right)\right). \tag{6.7}$$

Without loss of generality we will set $x_c = 0$ in what follows. Denote the total quasiparticle density by $\phi(x,t)$. The mean flux through the point $x_c = 0$ is

$$\langle \Phi(t) \rangle = \int_{\mathbb{R}} dx_0 \; \phi(x_0, 0)\mathrm{sgn}(x_0)\mathcal{P}_{x_0}(t) \sim 0, \tag{6.8}$$

where

$$\mathcal{P}_{x_0}(t) = \frac{1}{2}\left(1 + \mathrm{Erf}\left(-\frac{|x_0|}{\sqrt{Dt}}\right)\right) \tag{6.9}$$

is the probability that a quasiparticle which starts at $x = x_0$ has crossed the point $x_c = 0$ at time t. The integral vanishes by symmetry if $\phi(x_0, 0)$ is an even function of x_0, which is true on average. Thus, as expected, the average flux of quasiparticles vanishes.

However, the *variance* of the quasiparticle flux is

$$\begin{aligned} \left\langle \Phi(t)^2 \right\rangle &= \int_{\mathbb{R}} dx_0 \; \phi(x_0,0)^2 \mathrm{sgn}(x_0)^2 \mathcal{P}_{x_0}(t)^2 \\ &\sim \frac{1}{4}\phi_0^2 \int_{\mathbb{R}} dx_0 \; \left(1 + \mathrm{Erf}\left(-\frac{|x_0|}{\sqrt{Dt}}\right)\right) \\ &\sim \phi_0^2 \, \frac{2-\sqrt{2}}{2\sqrt{\pi}} \, (Dt)^{1/2}, \end{aligned} \tag{6.10}$$

where we have neglected fluctuations of the initial quasiparticle density $\phi(x_0, 0) \sim \phi_0$, but which establishes that, to leading order, the variance in the positions of the charge domains scales as $x^2 \sim t^{1/2}$, which corresponds to subdiffusion with $\alpha = 1/4$.

To close this section, let us use these considerations to motivate a set of two hydrodynamic equations which capture the subdiffusive dynamics. Let us first subtract off the average charge density (so that we are only dealing with connected correlators) by defining $\tilde{\rho} = \rho - \langle \rho \rangle$. Now, if we are in a particle domain, the charge current $j_{\tilde{\rho}}$ will oppose the quasiparticle current j_ϕ, and vice-versa if we are in a hole domain. (We neglect the charge of the quasiparticle itself, since on fluid-cell scales it is dwarfed by the charge of the surrounding domain). The current generated by the quasiparticle is also proportional to the total charge of the domain, which is simply $\tilde{\rho}$ on fluid-cell scales. Thus, $j_{\tilde{\rho}} \sim -\tilde{\rho} j_\phi$, and

$$\partial_t \phi + \partial_x \left(-D\partial_x \phi + \xi\right) = 0, \qquad \partial_t \tilde{\rho} + \partial_x \left(\tilde{\rho} D \partial_x \phi - \tilde{\rho}\xi\right) = 0, \tag{6.11}$$

where D is the quasiparticle diffusion constant, and ξ is a phenomenological white noise field which captures the dynamics imparted to the quasiparticles by the gates $\mathcal{G}$.

6.4 Connections and outlook

In this short chapter we have discussed three distinct mechanisms which are known to give rise to subdiffusive dynamics. An outstanding question, and promising direction for future

work, is whether these mechanisms are fundamentally separate, or whether they are, in fact, closely connected.

It is perhaps not so surprising that there may be some connection between the higher-moment conservation and the kinetic constraints – since additional conservation laws, by definition, represent some further limitation on the dynamics. But, as discussed, kinetic constraints do not necessarily imply extra conserved charges; nor does the dipole-conserving model arrive at subdiffusion via a quasiparticle mechanism like the XNOR model, even though they have the same exponent $\alpha = 1/4$.

On the other hand, perhaps the way the disordered XXZ chain (6.2) becomes subdiffusive is that the random fields shut off many of the hopping matrix elements, leaving behind some cluster [149] of allowed moves that is effectively kinetically constrained.

In any case, these ruminations are not well-formed; we have no real hope of answering the question of whether some universal mechanism underlies subdiffusion in this short exposition, after all.

Turning away from such questions, then, one thing which does seem to be missing is an analytic understanding of a model with a tune-able subdiffusive exponent ranging from $\alpha = 1/2$ down to $\alpha = 0$. Whilst we have discussed that there is considerable evidence the disordered XXZ chain (6.2) provides a conceptually simple model satisfying this requirement, the question of whether there is a sharp transition out of the diffusive phase into a subdiffusive phase at some finite critical disorder strength has not been conclusively resolved.

This last point is particularly salient in light of the next chapter, where we report on our contribution to this effort in the form of bond-disordered classical Heisenberg chains. We show that, for many distributions of disorder, the dynamics can appear to be subdiffusive over extremely long time-scales, but cross over to diffusion asymptotically.

Chapter 7

Subdiffusion in bond-disordered classical Heisenberg chains

The work presented in this chapter has appeared as part of the following article [169]:

Adam J. McRoberts, Federico Balducci, Roderich Moessner, & Antonello Scardicchio
Subdiffusive spin transport in bond-disordered classical Heisenberg chains
Phys. Rev. B **108**, 094204 (2023)

In the interests of fairness, I should point out here that the transfer matrix solution of the effective model and the integral equation solution (§7.3 & §7.4) were due mainly to Federico Balducci and Antonello Scardicchio

Ever since the original recognition that diffusion is absent in certain random lattices [131], the study of transport in impure materials has been a rich source of surprising, and often subtle, phenomena. Recently, the study of the mechanism of equilibration in quantum many-body systems has provided an additional impetus, carried by experimental advances [170–172] as well as concomitant conceptual progress [132, 173, 174]. The quantum statistical mechanics of non-equilibrium systems, and of the process of equilibration itself [175, 176], is now reaching the level of detail that classical ergodic theory has reached more than a hundred years after the works of Boltzmann [177, 178].

It is, in particular, the study of systems with both interactions and disorder that has thrown up many puzzles. This is subject to formidable technical difficulties, as exact solutions are generically unavailable, whilst numerics for quantum systems is typically restricted to small system sizes and/or short times. This has led to vigorous debates regarding nature and lifetime of possible intermediate-time dynamical regimes [139–141, 143–146] (and the role of rare events in their genesis [148, 179]), and how to distinguish them from expected or desired long-time behaviour.

One aspect of much recent interest relates to the question of under what conditions, and with what consequences, many-body systems may exhibit neither diffusive nor localised behaviour; much-explored possibilities relate to subdiffusive [152, 153, 155, 180] or (as discussed in Part II) superdiffusive Kardar-Parisi-Zhang [181–185] behaviour.

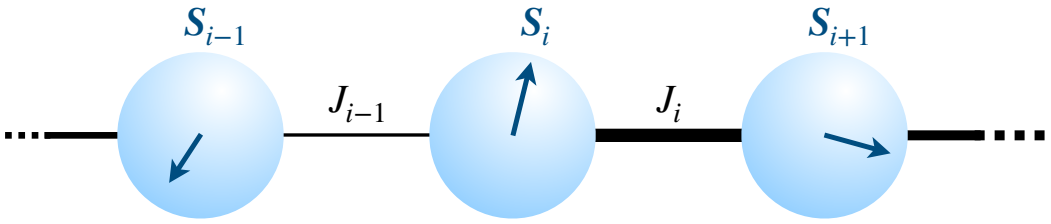

Figure 7.1: Sketch of the spin chain from Eq. (7.1). The spins $\boldsymbol{S}_i$ live on the sphere S^2, and interact via broadly-distributed nearest-neighbour couplings J_i, cf. Eq. (7.2). We use periodic boundary conditions.

In this chapter, we study a family of disordered, classical chains of Heisenberg spins. This picks up the aforementioned threads in the following ways. (i) Such chains are, a priori, generic one-dimensional many-body systems, but, as we have shown in Parts I & II, even the clean (i.e. without disorder) Heisenberg chain is capable of exhibiting extended non-diffusive transport regimes [24, 36, 186, 187] – closing a long-standing debate regarding the nature of its excitations [26, 28, 30, 32, 188–191]. (iii) It is technically possible to simulate large system sizes for long times, and thus there is hope of probing various regimes and their crossovers, all the more as (iv) the tuning parameter distinguishing members of the family of models allows us to access very different behavioural regimes.

In this chapter, we show how this family of disordered Heisenberg chains exhibits a rich set of transport phenomena, comprising standard diffusion as well as tune-able subdiffusion, but, as established in previous work [29], no classical counterpart of many-body localisation. We account for all of these phenomena with a relatively simple treatment, which makes transparent the role of extreme-value statistics and rare phenomena. We also provide detailed insights into the origin and nature of short- to intermediate-time crossovers and corrections, which can be important in the numerics over a broad time window.

Atypical *rare regions* of the system, where, for example, local couplings are much smaller or much larger than their typical value, are suspected to play a significant role in achieving or inhibiting thermalisation in classical and quantum systems. However, their signature in numerical results is often obscured, and can lead to different, contrasting interpretations of finite-size and finite-time numerics on account of the very slow emergence of the true asymptotic behaviour. It is therefore highly desirable to have access to models in which analytical results sufficiently constrain the data analysis to yield a clear interpretation of the numerics.

This study presents one such example. Crucially, our solution of a phenomenological model for transport, in which the local diffusion coefficient is a broadly distributed random variable, provides both leading *and subleading* terms in the large-time expansion of observables. We show how, in the absence of such an analytic prediction for the subleading behaviour, slow diffusion could be mistaken for subdiffusion, the diffusive term achieving dominance for times orders of magnitude larger than those typically reachable in state-of-the-art numerics.

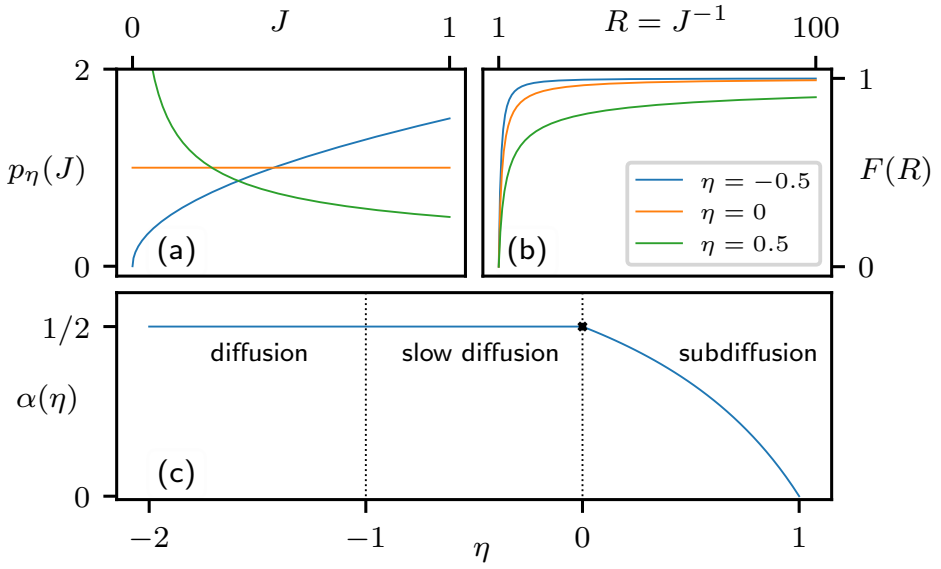

Figure 7.2: (a) Probability density function of the couplings J_i for representative values of η. (b) Cumulative distribution function of the inverse couplings $R = J^{-1}$, showing the fat tails of the distribution for $\eta > 0$. (c) Overview of the dynamical regimes as a function of η. The point at $\eta = 0$ corresponds to logarithmically-suppressed diffusion.

7.1 Model

We consider a bond-disordered version of the classical Heisenberg chain, with the Hamiltonian

$$\mathcal{H} = \sum_{i=1}^{L} J_i \boldsymbol{S}_i \cdot \boldsymbol{S}_{i+1}, \tag{7.1}$$

where $\boldsymbol{S}_i \in S^2$ are classical unit-length spins, and we use periodic boundary conditions. The random couplings J_i are independent and identically distributed (i.i.d.), and drawn from a one-parameter family of power-law distributions. The probability density function,

$$p_\eta(J) = (1-\eta)J^{-\eta}, \qquad J \in [0,1] \tag{7.2}$$

is controlled by an exponent $\eta \in (-\infty, 1)$. We show the distributions $p_\eta(J)$ for representative values of η in Fig. 7.2: for $\eta > 0$, the probability density diverges at $J = 0$; for $\eta < 0$, the weight accumulates around $J = 1$, and approaches the clean model as $\eta \to -\infty$; precisely at $\eta = 0$, the distribution is uniform. Throughout, units are implicitly defined by the maximum coupling $J_{\max} = 1$.

It is, however, the distribution of the *inverse* couplings $R = J^{-1}$ that determines the bare dynamical timescales. Their probability density,

$$q_\eta(R) = (1-\eta)R^{\eta-2}, \qquad R \in [1,\infty), \tag{7.3}$$

is fat-tailed: the first moment $\overline{R}$ diverges for $\eta > 0$; the second moment $\overline{R^2}$ diverges for $\eta > -1$; and so on for the higher moments (we denote the average over disorder by an overline). We will derive the consequences of these divergences in §7.3.

Again, the classical dynamics of the Hamiltonian (7.1) is defined by the fundamental Poisson brackets,

$$\{S_i^\alpha, S_j^\beta\} = \delta_{ij}\epsilon^{\alpha\beta\gamma}S_i^\gamma, \tag{7.4}$$

from which one obtains the equations of motion,

$$\partial_t \boldsymbol{S}_i = (J_{i-1}\boldsymbol{S}_{i-1} + J_i\boldsymbol{S}_{i+1}) \times \boldsymbol{S}_i. \tag{7.5}$$

These equations are manifestly SO(3) invariant: as in the clean model, all three components of the magnetisation are conserved.

7.2 Numerical results for the dynamics

We study the dynamics of the model (7.1) at infinite temperature; in particular, we consider the correlation function of the spins,

$$\mathcal{C}(j,t) := \overline{\langle \boldsymbol{S}_j(t) \cdot \boldsymbol{S}_0(0)\rangle}, \tag{7.6}$$

and the associated autocorrelator $\mathcal{A}(t) := \mathcal{C}(0,t)$, averaged over both realisations of disorder (overline) and a thermal ensemble of initial states (angular brackets), as described below. In the long-time limit, we expect to reach a hydrodynamic regime, wherein the correlation functions of conserved densities approach an asymptotic scaling form,

$$\mathcal{C}(x,t) \sim t^{-\alpha}\mathcal{F}(x/t^\alpha), \tag{7.7}$$

for some universal function $\mathcal{F}$ and scaling exponent α. The latter can also be obtained by fitting the autocorrelator to a power law:

$$\mathcal{A}(t) \simeq \kappa t^{-\alpha}. \tag{7.8}$$

However, the asymptotics – whilst they define the dynamical exponent – capture only the leading behaviour. As we will show, the finite-time corrections to Eq. (7.8) can be quite severe, and persist, at least, to late times $t = 10^6$ (in units with $J_{\max} = 1$).

To evaluate the correlator (7.6) for a given disorder exponent η, we construct an ensemble of 20000 initial states at infinite temperature: each spin is simply, and independently, drawn from the uniform distribution on the sphere. For each state in the ensemble, we draw a distinct realisation of the couplings J_i, and numerically integrate the equations of motion (7.5). Snapshots of the state are stored at intervals of $\Delta t = 10$, with the correlation function at a given time-difference t calculated by averaging over 1000 consecutive snapshots. Data shown are for the system size $L = 8192$ [1].

There are four distinct dynamical regimes. First, in the clean limit ($\eta \to -\infty$), the spin dynamics is diffusive. Even in this limit, however, finite-size and finite-time effects are capable of hiding the asymptotic behaviour, and it has taken modern-day computing

[1] We have simulated system sizes $L = 2048$, 4096, 8192 and found no appreciable differences in the data, indicating that the numerics are principally limited by finite-time effects, not finite-size effects.

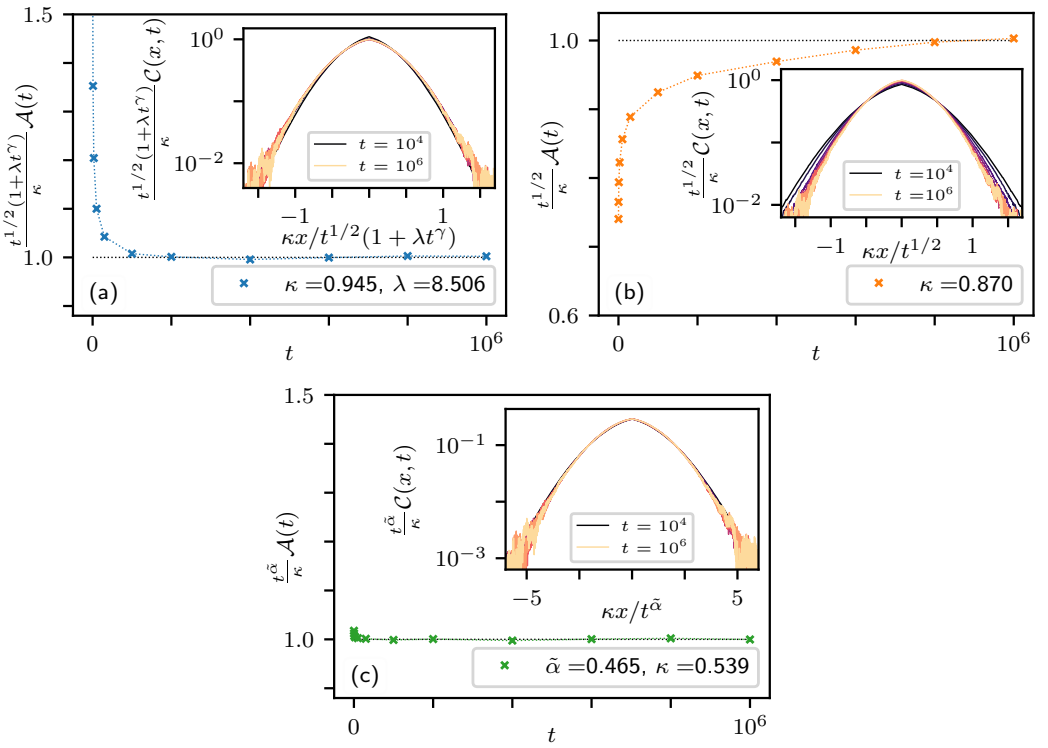

Figure 7.3: Spin dynamics in the "slow diffusion" regime, shown for $\eta = -0.5$. In each panel, the main figure shows the rescaled autocorrelator $\mathcal{A}(t) = \mathcal{C}(x = 0, t)$ (cf. Eq. (7.6)). The insets show the corresponding scaling collapse of the full correlation function $\mathcal{C}(x, t)$. (a) Autocorrelator and scaling collapse from Eq. (7.9), i.e., assuming an asymptotic diffusive behaviour with strong, anomalous corrections. (b) Diffusive scaling without finite-time corrections (i.e., setting $\lambda = 0$, a one-parameter fit), showing that the corrections must be accounted for, at least up to the final time of the simulation, $t = 10^6$. (c) Numerical fit with an anomalous (subdiffusive) exponent, i.e., a direct two-parameter fit to Eq. (7.8). See main text for additional details.

resources [30, 36, 186, 191] to resolve the long-lasting debate on this topic [26, 28, 32, 188–190]. Second, as η becomes finite, and in particular for $-1 \leq \eta < 0$, diffusion persists at extremely large times, but finite-time corrections become increasingly severe. This is due to the existence of local dynamical bottlenecks, which arise from the growing probability of drawing an arbitrarily small coupling. We refer to this regime as "slow diffusion", and study it in detail in §7.2.1. Third, at $\eta = 0$, the probability density $p_\eta(J) = 1$ becomes uniform, and the first moment of the inverse couplings, i.e., $\overline{R}$, diverges logarithmically. Accordingly, the asymptotic spin dynamics shows logarithmically-suppressed diffusion, cf. §7.2.2. Finally, when $0 < \eta < 1$, the spin dynamics is truly subdiffusive, with an exponent (Hurst index) $\alpha < 1/2$, cf. §7.2.3.

In practise, for all the considered cases, the leading corrections to the asymptotics are

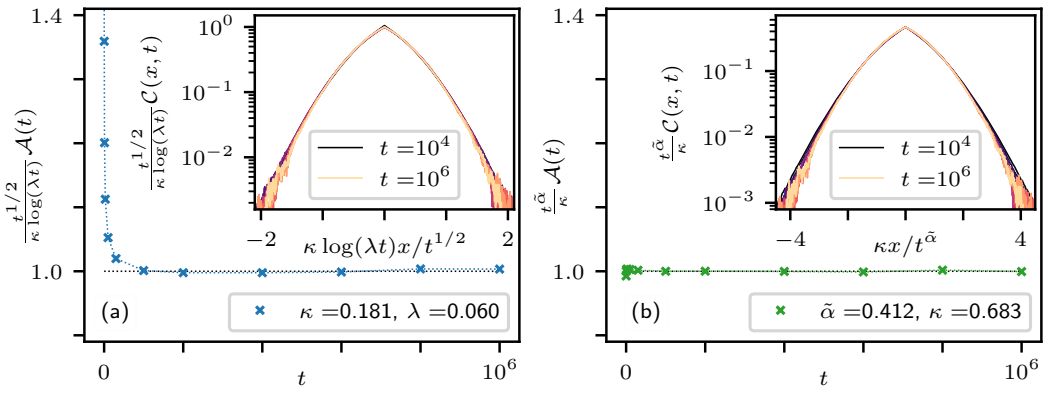

Figure 7.4: Spin dynamics at the slow-diffusion/subdiffusion transition, $\eta = 0$. (a) Rescaled autocorrelator (main panel) and scaling collapse of the correlation function (inset), as predicted by the logarithmic suppression of diffusion, i.e., a two-parameter fit to Eq. (7.11). (b) Same data as panel (a), but fitting with a subdiffusive exponent, i.e., a direct two-parameter fit to Eq. (7.8). Note that the scaling collapse in the tails of the correlations is slightly better using the logarithmic-suppression, indicating that this is the correct picture.

required to obtain the correct scaling exponent α from the numerical data. If the corrections are neglected, one finds an α smaller than the true value. We first present the numerical results, and develop an effective model which accounts for our observations in §7.3.

7.2.1 $-1 \leq \eta < 0$: Slow diffusion

We begin with the regime of slow diffusion, observed when $-1 \leq \eta < 0$. Here, $p_\eta(J)$ is maximal at $J = 1$ and vanishes at $J = 0$ (cf. Fig. 7.2).

In this regime, the average bare timescale $\overline{R}$ remains finite, so the leading behaviour remains diffusive, i.e., $\alpha = 1/2$. Higher moments (e.g. $\overline{R^2}$), however, diverge, giving rise to strong corrections. Correspondingly, the autocorrelator takes the form

$$\mathcal{A}(t) \sim \frac{\kappa}{t^{1/2}(1+\lambda t^\gamma)}, \qquad \gamma = \frac{\eta}{1-\eta} < 0, \tag{7.9}$$

with κ and λ obtained numerically in a two-parameter fit. The subleading exponent γ is fixed by the effective model of §7.3. We show the slow-diffusion dynamics for a representative value $\eta = -0.5$ in Fig. 7.3. We find that the corrections postulated by Eq. (7.9) capture the slow spreading of the correlations, and are necessary to obtain the correct scaling at finite times.

It is interesting to point out that it is also possible to fit the correlations with an anomalous (subdiffusive) exponent, i.e., applying a two-parameter fit to Eq. (7.8) directly. In the slow diffusion regime, this procedure yields a numerical agreement with the simulation data that is comparable to the diffusion-with-strong-corrections hypothesis. We stress, however, that subdiffusion is *not* the correct asymptotic picture; rather, it is an artefact of the corrections taking the form of a sum of (small) power-laws. Indeed, at $\eta = -0.5$, and for the times

accessible by our numerics, a direct power-law fit finds a subdiffusive exponent $\alpha = 0.465$. The effective model we develop in §7.3 instead predicts the form Eq. (7.9) with $\gamma = -1/3$: plugging in the value of λ found from the fits, it holds exactly that

$$\frac{\partial \log \mathcal{A}(t)}{\partial \log(t)} \approx 0.465\ldots \qquad \text{at } t = 10^5. \tag{7.10}$$

Thus, whilst locally, around the largest times we could access, the effective power-law decay is slower than 1/2, our analytical understanding predicts that this is but a crossover, and much longer times ($t \approx 10^8$) are needed for the corrections to become negligible (say, 1% of the leading term).

7.2.2 $\eta = 0$: Logarithmically-suppressed diffusion

At $\eta = 0$ the slow diffusion regime terminates. The distribution of the couplings J_i becomes uniform over $[0, 1]$, and the corrections to the diffusive behaviour are enhanced, fundamentally changing the leading asymptotics. In particular, spin diffusion is now logarithmically suppressed, and one finds

$$\mathcal{A}(t) \sim \frac{\kappa \log(\lambda t)}{t^{1/2}}, \tag{7.11}$$

cf. §7.3.4.

We show the logarithmically-suppressed diffusion in Fig. 7.4. Whilst, again, a direct fit to Eq. (7.8)—i.e., a fit to determine the subdiffusive exponent—is in good agreement with the data (Fig. 7.4(b)), in this case the corresponding scaling collapse is slightly worse in the tails than that provided by the logarithmic-suppression picture (Fig. 7.4(a)). That Eq. (7.11) fits both the centre (the autocorrelator) and the tails of the correlations is strong evidence in favour of the picture predicted by the effective model of §7.3.

7.2.3 $\eta > 0$: Subdiffusion

Finally, we turn to the case $\eta > 0$. The distribution $p_\eta(J)$ now diverges at $J = 0$, which means that a finite fraction of the bonds become arbitrarily small. This leads to truly subdiffusive dynamics, with exponent $\alpha < 1/2$.

However, the fact that corrections in the slow diffusion regime were strong enough that a naive numerical fit to Eq. (7.8) already finds subdiffusion at $\eta < 0$ suggests that, again, there will be strong corrections which hide the correct exponent (the exponent obtained numerically is continuous as a function of η). This is indeed the case, and we find

$$\mathcal{A}(t) \sim \frac{\kappa}{t^\alpha (1 + \lambda t^\gamma)}, \tag{7.12}$$

cf. §7.3.4, with

$$\alpha = \frac{1-\eta}{2-\eta}, \qquad \gamma = 2\alpha - 1 < 0. \tag{7.13}$$

We show the subdiffusive dynamics for $\eta = 0.5$ in Fig. 7.5, again finding that the leading finite-time corrections are required. As was the case at $\eta = 0$, we show that the the form of $\mathcal{A}(t)$ predicted by the effective model, Eq. (7.12), collapses the tails of the correlations slightly better than a direct fit to Eq. (7.8) (compare Figs. 7.5(a) and 7.5(c)).

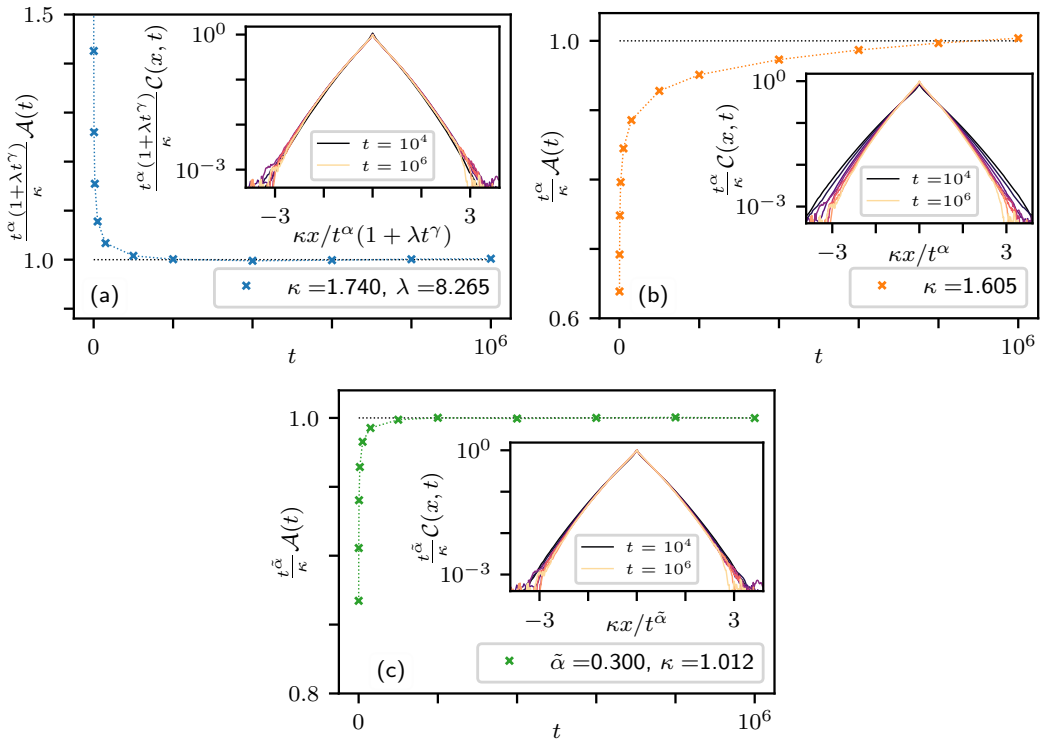

Figure 7.5: Subdiffusive spin dynamics in the strongly-disordered regime, shown for a representative $\eta = 0.5$. Again, each main panel shows the autocorrelator, whilst the insets show the scaling collapse of the correlation function. (a) The autocorrelator and scaling collapse from Eq. (7.12), i.e., a two-parameter fit with the subdiffusive exponent $\alpha = (1-\eta)/(2-\eta) = 1/3$, and with leading corrections included. (b) Subdiffusion with the same exponent as panel (a), but without the corrections, i.e., a one-parameter fit setting $\lambda = 0$. (c) Scaling with an exponent obtained numerically without finite-time corrections, i.e., a direct two-parameter fit to Eq. (7.8). Again, note that the scaling collapse in the tails is better in (a) than in (c), indicating that the finite-time corrections provide the correct picture.

7.3 An effective model for spin transport

Having first presented the numerical data, including, without justification, the forms of the corrections, we now present a phenomenological model of the spin transport which explains, at least qualitatively, the results of §7.2. In particular, in §7.3.1 we introduce the effective model and motivate its form. In §7.3.2 we show how the model can be solved by means of a transfer-matrix technique. Finally, in §7.3.3 we extract the asymptotic scaling via the transfer-matrix trick, whilst in §7.3.4 we address the finite-time corrections to the asymptotics. We present an alternative solution of the effective model in §7.4.

7.3.1 Motivation for the effective model

In order to access the late-time behaviour of the spin-spin correlations, we set ourselves on a hydrodynamic scale, and linearise the microscopic dynamics whilst accounting for the local exchange of energy and spin. By rotational invariance, we consider only the magnetisation density along one axis: whilst one could write down hydrodynamic equations that couple the local magnetisation components along all three axes in an SO(3)-symmetric fashion, we will show that the simplest ansatz of totally decoupled components is sufficient to explain our numerical findings.

Let us denote the magnetisation at the coarse-grained site x by $m_x(t)$. We retain a discretised lattice even on the hydrodynamic scale, because this way it is easier to account for the strong, fat-tailed disorder of Eq. (7.2). The disorder in the couplings J_x suggests that the local diffusion coefficient D_x will vary similarly, giving rise to a local diffusion equation:

$$\partial_t m_x = D_{x-1} m_{x-1} + D_x m_{x+1} - (D_x + D_{x+1}) m_x. \tag{7.14}$$

We argue that this is the correct lattice discretisation of the diffusion equation, since it comes from enforcing Kirchhoff's law at each site, i.e., the inflow and outflow of magnetisation at each site cancel out. In turn, this fact implies that the constant vector $m_x \equiv m$ is a stable solution of Eq. (7.14), and that the magnetisation is locally conserved.

The local, random diffusion coefficients D_x have some unknown distribution function, depending on the underlying J_i's. Interpreting Eq. (7.14) as a coarse graining of Eq. (7.5), the distribution of the D_x's should be obtained, in principle, via some renormalisation procedure (mayhaps akin to the strong-disorder renormalisation group used for quantum disordered spin chains [192–196]). For our purposes, however, it suffices to assume that $1/D_x$ has the same fat tails as $1/J_i$. We thus assume, for simplicity, that D_x has the same probability density function as in Eq. (7.2):

$$p_\eta(D) = (1-\eta) D^{-\eta}, \qquad D \in [0,1]. \tag{7.15}$$

Using a different distribution that shares the same tails leads to equivalent results, as will become clear from the extreme-value analysis below. We have, here, implicitly rescaled the units of time by setting the maximum possible value $D_{\max} = 1$.

In the following, we solve the dynamics described by Eq. (7.14). Before doing so, however, some comments are in order. First, we stress that Eq. (7.14) was already known to approximate the dynamics of the classical Heisenberg model *near zero temperature* [197–199]. Indeed, a spin-wave expansion of the equations of motion (7.5) leads to a copy of Eq. (7.14), if the interactions among spin waves are neglected. Our new contribution is to show that this linearised equation is also capable of describing the dynamical scaling of space and time *at infinite temperature*.

Second, we remind the reader that Eq. (7.14) has been the subject of a vast literature, pioneered by Dyson [200] (see also the reviews [197–199]), and sometimes goes by the name of "random barrier model". The long-time behaviour of $m_x(t)$ can be obtained by various methods: an integral equation that leads to the exact solution [200–202], small-disorder expansions [203, 204], an effective-medium theory [197], and renormalisation-group approaches [205–208]. Here, we solve the model by yet another technique—a series expansion of a transfer-matrix representation—for two reasons: first, we find it faster, and more transparent from a physical standpoint; second, it allows us to access the subleading terms,

which, as noted in §7.2, must be taken into account. In the following sections, we describe in detail the transfer-matrix method, and then extract the scaling in the different dynamical regimes. We benchmark our solution against the integral equation method in §7.4.

7.3.2 Transfer matrix representation, and solution in the clean case

The exact solution of Eq. (7.14) can be obtained only numerically, owing to the random nature of the D_x's. However, the dynamical behaviour of the solution can be accessed with a clever transfer-matrix trick, borrowed from the problem of Anderson localisation [209, 210]. Let us first pass to the Fourier transform in time, $\tilde{m}_x(\omega) = \int dt\, e^{-i\omega t} m_x(t)$, which yields

$$i\omega\tilde{m}_x(\omega) = D_{x-1}\tilde{m}_{x-1}(\omega) + D_x\tilde{m}_{x+1}(\omega) - (D_{x-1} + D_x)\tilde{m}_x(\omega). \tag{7.16}$$

We now rewrite this equation in transfer matrix form:

$$\begin{pmatrix} \tilde{m}_{x+1} \\ \tilde{m}_x \end{pmatrix} = \begin{pmatrix} \frac{D_{x-1}+D_x+i\omega}{D_x} & -\frac{D_{x-1}}{D_x} \\ 1 & 0 \end{pmatrix} \begin{pmatrix} \tilde{m}_x \\ \tilde{m}_{x-1} \end{pmatrix}, \tag{7.17}$$

which can be recast in a more compact notation,

$$M_{x+1} = T_x(\omega) M_x, \tag{7.18}$$

where we have introduced the vector of the two magnetisations M_x, and the 2×2 transfer matrix $T_x(\omega)$. Iterating, one finds

$$M_{x+1} = T_x(\omega) T_{x-1}(\omega) \cdots T_1(\omega) M_1, \tag{7.19}$$

which expresses m_{x+1} for any x in terms of m_0 and m_1.

Equation (7.19) does not admit a solution any more than the original form, but it does bring the problem into the realm of products of random matrices—a classic topic in statistical physics dating back to the works of Furstenberg [211, 212]. Now, to get an idea of the nature of the product, let us consider the clean case,

$$T = \begin{pmatrix} 2 + \frac{i\omega}{D} & -1 \\ 1 & 0 \end{pmatrix}. \tag{7.20}$$

Even though T is not Hermitian, it is diagonalisable and has eigenvalues

$$\lambda_{1,2} = \frac{2D + i\omega \pm \sqrt{4iD\omega - \omega^2}}{2D}. \tag{7.21}$$

Notice that, since $\det(T) = 1$, it holds that $\lambda_1 = 1/\lambda_2$; we choose the labels such that $|\lambda_1| \geq 1 \geq |\lambda_2|$. Now, an n-fold application of T to a generic vector corresponds (approximately) to a rotation plus an enlargement by a factor $|\lambda_1|$. This represents a vector localised *away* from the left boundary—ideally, on the right boundary. By, instead, fine-tuning the initial vector to the right eigenvector corresponding to λ_2, one finds a vector localised on the left boundary, which corresponds to the propagation of a disturbance created on the site $y = 0$.

The long-time dynamics corresponds to small values of ω, for which

$$\lambda_{1,2} = 1 \pm \sqrt{\frac{i\omega}{D}} + \frac{i\omega}{2D} + \cdots. \tag{7.22}$$

Therefore, for a disturbance localised on $y = 0$, one finds

$$\tilde{m}_y(\omega) \simeq \left(1 - \sqrt{i\omega/D} + \cdots\right)^y = e^{-y\sqrt{i\omega/D}}, \tag{7.23}$$

whilst the other eigenvalue corresponds to a disturbance localised at $y \to \infty$,

$$\tilde{m}_y(\omega) \simeq \left(1 + \sqrt{i\omega/D} + \cdots\right)^y = e^{+y\sqrt{i\omega/D}}. \tag{7.24}$$

Above, we have set the values of the initial seed to $M_1 \approx 1$. The dispersion relation $y^2 \sim Dt$ is immediately apparent from Eqs. (7.23)–(7.24), since y and ω appear only in the combination $y\omega^{1/2} \sim y/t^{1/2}$. Then, selecting the decaying exponential, the inverse transform is

$$m_y(t) \approx \int_{-\infty}^{+\infty} \frac{d\omega}{2\pi} e^{-\sqrt{i\omega/D}y + i\omega t}. \tag{7.25}$$

If both y and t are large, this integral is dominated by the saddle point,

$$0 = \partial\omega \left(-\sqrt{\frac{i\omega}{D}}y + i\omega t\right) \quad \Longrightarrow \quad \omega = -i\frac{y^2}{4Dt^2}, \tag{7.26}$$

and, substituting this back in, one finds

$$m_y(t) \sim e^{-\frac{y^2}{4Dt}}, \tag{7.27}$$

i.e., diffusive behaviour $y^2 \approx 2Dt$. Note also that the gaussian tails of diffusion are correctly reproduced.

Let us now see how one can get the same results by expanding the product of transfer matrices, $T_x(\omega)T_{x-1}(\omega)\cdots T_1(\omega)$, in powers of ω. This will be useful for the disordered case, as the eigenvalue of the product of the random transfer matrices cannot be obtained from the eigenvalues of the separate T_x's. We consider the action of $T_x(\omega)T_{x-1}(\omega)\cdots T_1(\omega)$ on the trial vector $M_1 = (1, 1)^T$, which represents a good starting guess for a long-wavelength vector. Order-by-order in ω, one finds (re-introducing the index on D for future reference, although $D_x \equiv D$ in the clean case):

$$\begin{aligned}\tilde{m}_{y+1}(\omega) = 1 + i\omega \sum_{x_1 \le y} \frac{x_1}{D_{x_1}} + (i\omega)^2 \sum_{x_1 < x_2 \le y} \frac{x_1(x_2 - x_1)}{D_{x_1} D_{x_2}} \\ + (i\omega)^3 \sum_{x_1 < x_2 < x_3 \le y} \frac{x_1(x_2 - x_1)(x_3 - x_2)}{D_{x_1} D_{x_2} D_{x_3}} + \cdots .\end{aligned} \tag{7.28}$$

The terms in the expression above are reminiscent of the locator expansion, which is a useful tool when studying the physics of localisation [131, 213, 214].

The sums over $x_1, x_2, \ldots$ in Eq. (7.28), when the uniform D is factored out, reduce to

$$\sum_{x_1 < \cdots < x_n \le y} x_1(x_2 - x_1)\cdots(x_n - x_{n-1}) = \frac{(y+n)!}{(2n)!(y-n)!}. \tag{7.29}$$

The first terms in the large-y expansion read

$$\frac{(y+n)!}{(2n)!(y-n)!} = \frac{y^{2n}}{(2n)!}\left(1+\frac{n}{y}+\cdots\right). \tag{7.30}$$

Thus, in the limit of large y, one finds the approximate solution

$$\begin{aligned}\tilde{m}_y(\omega) &\approx \sum_{n=0}^{\infty}\frac{(i\omega)^n}{D^n}\frac{y^{2n}}{(2n)!} = \cosh\left(\sqrt{\frac{i\omega}{D}}y\right)\\ &= \frac{1}{2}\left(e^{\sqrt{\frac{i\omega}{D}}y}+e^{-\sqrt{\frac{i\omega}{D}}y}\right),\end{aligned} \tag{7.31}$$

the two terms corresponding exactly to the two eigenvalues of the transfer matrix. Again, selecting the decaying exponential and inverting the Fourier transform yields the diffusion profile and the Brownian dispersion relation.

To summarise, one can obtain the dispersion relation from the dependence of the series (7.28) on the combination of ω and y, whilst access to the functional form requires the coefficients of the series.

Crucially, this solution strategy can be transposed to the disordered case, as we now move to show in the following sections.

7.3.3 Scaling in the disordered model

We now use the transfer-matrix method to solve the disordered chain, in which the D_x's are i.i.d. random variables distributed according to $p_\eta(D)$. Note that, if the average $\overline{1/D}$ exists (i.e. $\eta < 0$), then $\overline{m_y}$ behaves diffusively, with an effective diffusion coefficient $D_{\mathit{eff}} = (\overline{1/D})^{-1}$. We stress that the effective diffusion coefficient is not given by $\overline{D}$, since the resistances $\sim 1/D_x$ are additive but the conductances $\sim D_x$ are not [215].

The only case we need to treat, therefore, is when the moment $\overline{1/D}$ is infinite, i.e., $\eta \geq 0$. We will focus, however, on $\eta > 0$, leaving the limiting case $\eta = 0$ to §7.3.4.

When $\eta > 0$, one must retain the explicit sums in Eq. (7.28). Now, since $1/D_x$ has a fat-tailed distribution, the (finite) sums are dominated by the maximum—in particular,

$$\sum_{x_{i-1}\leq x_i}\frac{x_{i-1}}{D_{x_{i-1}}} \simeq \max_{x_{i-1}<x_i}\frac{x_{i-1}}{D_{x_{i-1}}}. \tag{7.32}$$

For $\eta > 0$ the numerator is irrelevant—it is just a random number uniformly distributed in $[0, x_i]$, which we write as $c_i x_i$ with $c_i \in [0,1]$. Thus, simplifying further, one has

$$\sum_{x_{i-1}\leq x_i}\frac{x_{i-1}}{D_{x_{i-1}}} \simeq c_i x_i \max_{x_{i-1}<x_i}\frac{1}{D_{x_{i-1}}}. \tag{7.33}$$

The maximum, over a large number of instances x_i, of the i.i.d. random variables $1/D_{x_{i-1}}$ is a random variable of typical value $x_i^{1/(1-\eta)} \gg x_i$, owing to $\eta > 0$. Consequently, the whole sum is approximately

$$\sum_{x_{i-1}\leq x_i}\frac{x_{i-1}}{D_{x_{i-1}}} \simeq b_i x_i^{1+\frac{1}{1-\eta}}, \tag{7.34}$$

where b_i is another random variable of $O(1)$. Therefore:

$$\sum_{x_1 \le y} \frac{x_1}{D_{x_1}} \simeq b^{(1)} y^{1+\frac{1}{1-\eta}}, \tag{7.35}$$

$$\sum_{x_1 < x_2 \le y} \frac{x_1(x_2 - x_1)}{D_{x_1} D_{x_2}} \simeq b^{(2)} y^{2+2\frac{1}{1-\eta}}, \tag{7.36}$$

and so on.

We have now all the tools to evaluate the random series, Eq. (7.28):

$$\begin{aligned} \tilde{m}_y(\omega) = 1 &+ i\omega b^{(1)} y^{1+\frac{1}{1-\eta}} \big[1 + o(y^0)\big] \\ &+ (i\omega)^2 b^{(2)} y^{2+2\frac{1}{1-\eta}} \big[1 + o(y^0)\big] \\ &+ (i\omega)^3 b^{(3)} y^{3+3\frac{1}{1-\eta}} \big[1 + o(y^0)\big] + \cdots \\ &= f_\eta(\omega y^{\frac{2-\eta}{1-\eta}}) \big[1 + o(y^0)\big]. \end{aligned} \tag{7.37}$$

The neglected terms of $o(y^0)$ represent finite-time corrections, and they will be the object of the next section. The functional form of $f_\eta(x)$ cannot be evaluated at this coarse level of calculation, since it requires the knowledge of the coefficients $b^{(n)}$ at every order: for example, in the clean case one has $b^{(n)} = 1/(2n)!$, and thus it simplifies to $f_\eta(x) = \cosh(\sqrt{ix})$ when $\eta \to -\infty$.

Even if f_η is left undetermined, the dispersion relation is found from the scaling

$$t \sim \omega^{-1} \sim y^{(2-\eta)/(1-\eta)} \tag{7.38}$$

or, equivalently,

$$y \sim t^{(1-\eta)/(2-\eta)}. \tag{7.39}$$

We conclude that, in the region $0 < \eta < 1$, the scaling is subdiffusive, with an exponent (Hurst index)

$$\alpha = \frac{1-\eta}{2-\eta} < \frac{1}{2}. \tag{7.40}$$

This is exactly the subdiffusive exponent used in §7.2.3 (see Eq. (7.12) in particular) to fit the numerical data.

7.3.4 Finite-time corrections to the scaling

As can be seen from the numerical data of §7.2, sizeable corrections to the asymptotic scaling persist until very long times in the bond-disordered Heisenberg chain, Eq. (7.1). This feature is shared by the phenomenological model, Eq. (7.14), as we now show. We will split the discussion for the regimes of diffusion, slow diffusion, and subdiffusion; the logarithmically-suppressed diffusion will follow as a limiting case.

Diffusion. To set the stage, let us first address the finite-time corrections in the clean case $D_x \equiv D$ (i.e. $\eta \to -\infty$). The same features are shared by the whole region $-\infty < \eta < -1$,

as will become clear. Retaining the first-order corrections in Eq. (7.30), one can resum the series in Eq. (7.28) to

$$\tilde{m}_{y+1}(\omega) = \cosh\left(\sqrt{\frac{i\omega}{D}}y\right) + \frac{1}{2}\sqrt{\frac{i\omega}{D}}\sinh\left(\sqrt{\frac{i\omega}{D}}y\right) + \cdots \tag{7.41}$$

The second term, upon taking the inverse Fourier transform, is dominated by the same saddle as the first, and one finds

$$m_{y+1}(t) = e^{-\frac{y^2}{4Dt}}\left(\frac{1}{2} + \frac{y}{8Dt} + \cdots\right). \tag{7.42}$$

Again, the overall constant needs to be fixed by normalisation, since the initial guess for m was not normalised. What counts for our purposes is the relative size of the first two terms: using $y \sim t^{1/2}$ from the scaling, the second term is seen to be of order $t^{-1/2}$ w.r.t. the first.

Upon reintroducing the disorder, finding the explicit first-order corrections to Eq. (7.37) is more difficult, and a careful study of the random sums in Eq. (7.28) at all orders of ω is needed. Indeed, $\tilde{m}_y(\omega)$ is itself a random variable, and the large-space and long-time behaviour of $m_y(t)$ should be inspected by considering not only the average, $\overline{m_y(t)}$, but also its moments—or, equivalently, the average of quantities such as $\overline{\log m_y(t)}$. For this reason, we find it convenient to pass to the logarithm *at the level of the Fourier transform*:

$$\log\tilde{m}_{y+1}(\omega) = i\omega\sum_{x_1\le y}\frac{x_1}{D_{x_1}} + (i\omega)^2\left[\sum_{x_1\le y}\frac{x_1^2}{D_{x_1}^2} + 2\sum_{x_1<x_2\le y}\frac{x_1^2}{D_{x_1}D_{x_2}}\right] + \cdots \tag{7.43}$$

The equation above has the useful property that, at each order ω^n, there is one term $\propto 1/D_{x_1}^n$, followed by less singular terms $1/D_{x_1}^{n-1}D_{x_2}$, $1/D_{x_1}^{n-2}D_{x_2}D_{x_3}$, and so on. When the moment $\overline{1/D^n}$ does not exist, but all the moments $\overline{1/D^m}$ with $m < n$ exist (i.e. for $\eta \le -n+1$), an anomalous contribution to $\tilde{m}_y(\omega)$ appears—influencing the finite-time dynamics at order ω^n. As long as $\eta < -1$, both the terms of order ω and ω^2 are regular, and thus we expect moderately long times to suffice to make diffusion manifest. On the other hand, when η crosses -1, the first correction $O(\omega^2)$ gains an anomalous power, and signatures of slow diffusion are found. We detail this fact in the next paragraph.

Slow diffusion. Let us focus again on Eq. (7.43). By using the same analysis as §7.3.3 for the sums of random variables, one finds, in the region $-1 \le \eta < 0$,

$$\sum_{x_1\le y}\frac{x_1}{D_{x_1}} \sim \overline{1/D}\,y^2, \tag{7.44}$$

$$\sum_{x_1\le y}\frac{x_1^2}{D_{x_1}^2} \sim y^{2(2-\eta)/(1-\eta)}, \tag{7.45}$$

$$\sum_{x_1<x_2\le y}\frac{x_1^2}{D_{x_1}D_{x_2}} \sim \overline{1/D}^2 y^4, \tag{7.46}$$

and similarly for higher moments. By looking at the expression above, one recognises that the terms (7.44) and (7.46) combine to form a regular function of ωy^2. Indeed, similarly to

the subdiffusive case (see Eq. (7.37)), one can group terms and find

$$\log \tilde{m}_{y+1}(\omega) = \log f_\eta(\omega y^2) + c^{(1)}\omega^2 y^{2(2-\eta)/(1-\eta)} + \cdots \tag{7.47}$$

with $c^{(1)}$ being a constant of $O(1)$. This has to be interpreted in the same way as an anomalous scaling of the free energy at a critical point: the analytic part is represented by the first term and it is followed by a series of anomalous corrections, beginning with $\omega^2 y^{2(2-\eta)/(1-\eta)} \sim t^{\eta/(1-\eta)}$ (having used the scaling of the dominant term $y^2 \sim t$).

We remark that the subleading terms are very important when one wants to extract the scaling exponents from the numerics, as we already showed in §7.2. If they are not properly accounted for, the errors are rather large and the determination of the onset of subdiffusion is misplaced. The reason is that the subleading term $t^{\eta/(1-\eta)}$ has to be much smaller than unity if one wants to extract the leading exponent $1/2$ with some accuracy: this requires extremely long times for $|\eta| < 1$, and is a major source of obfuscation in the analysis of numerical data as shown in the previous sections.

Subdiffusion. We now consider the case $\eta > 0$, where not even the first moment of the random variable $1/D$ exists. Extreme-value statistics tells us that all the sums in Eqs. (7.28) or (7.43) become anomalous, giving rise to the expression in Eq. (7.37). Here, we argue that the corrections left out in Eq. (7.37) involve *regular* powers of y, as we illustrate with a very simple example. Consider the first-order term $i\omega \sum_{x_1 \le y} x_1/D_{x_1}$. Let us split the sum according to whether $D_{x_1} > D_\star$ or $D_{x_1} < D_\star$, where the value $D_\star$ is fixed so that the probability $D < D_\star$ is $p = 1/2$ (any other finite value of p would lead to the same conclusion). Then, one recognises that the random variable

$$\psi := \sum_{x_1 \le y} \frac{x_1}{D_{x_1}} \tag{7.48}$$

has a broad probability distribution peaked at a value $\psi \sim y^{(2-\eta)/(1-\eta)}$, but with non-zero weight down to $\psi \sim y^2$: this latter value comes from the regular sum of the terms involving $D_{x_1} > D_\star$, whilst the former represents the anomalous contribution of the very small instances $D_{x_1} < D_\star$. So, with a slight abuse of notation, one can say that

$$\sum_{x_1 \le y} \frac{x_1}{D_{x_1}} \sim y^{(2-\eta)/(1-\eta)} + cy^2, \tag{7.49}$$

in the sense that all functions of this random variable may be expanded, at large y, in these two (leading and subleading) terms.

A careful treatment of the random sums thus leads to two families of terms: those involving regular powers of y, and those involving anomalous powers. These two families receive contributions from all orders in ω, and a resummation of all the terms is beyond the scope of this work. We will content ourselves with the following simple scaling analysis: the combination of ω and y which appears is

$$\omega(y^{(2-\eta)/(1-\eta)} + cy^2) \sim 1, \tag{7.50}$$

from which it follows that

$$y \sim t^\alpha (1 + c' t^{2\alpha - 1}), \tag{7.51}$$

which is the form of the autocorrelator (7.12) used to fit the numerical data. The constants c and c' cannot be fixed at this rough level of calculation; thus, in §7.2, some fitting was still required.

Logarithmically-suppressed diffusion.
We finally consider how logarithmically-suppressed diffusion emerges. Being the limiting case between subdiffusion and slow diffusion, it can be understood from both sides. From the slow-diffusion side, one can see that the corrections to the asymptotic (diffusive) scaling tend to become of the same order of the leading term as $\eta \to 0^-$: this is because $(2-\eta)/(1-\eta) \to 2$, and the two terms on the r.h.s. of Eq. (7.47) coalesce, forming a logarithm. The same happens from the subdiffusive side, where the dominant term is now $y^{(2-\eta)/(1-\eta)}$, whilst the corrections are given by y^2: the mechanism is the same, though the role of the two terms is exchanged. We stress that this coalescence of power-laws can be understood from a complementary perspective via the integral-equation solution, see §7.4.

7.4 Integral equation solution of the effective model

In this section we present a different method for solving the effective model, Eq. (7.14), taking inspiration from the calculations of Ref. [201], but employing a simpler strategy – against which we will compare our transfer matrix solution. We start by rewriting Eq. (7.14) as

$$\partial_t m_x(t) = -(Hm)_x(t), \tag{7.52}$$

where

$$H = \sum_x \big[(D_x + D_{x-1})|x\rangle\langle x| - D_x(|x+1\rangle\langle x| + \text{h.c.})\big], \tag{7.53}$$

and the state $|x\rangle$ represents a particle located at position x on the chain. We now introduce the diagonal element of the resolvent of H, namely,

$$G_{00} := \langle 0|\frac{1}{\omega - H}|0\rangle. \tag{7.54}$$

Notice that here the frequency ω is obtained via a Laplace transform instead of a Fourier transform, so there is an imaginary unit of difference w.r.t. §7.3.

Using standard methods for tridiagonal matrices—or, equivalently, a locator expansion [131, 213, 214]—Eq. (7.54) can be recast in the form

$$G_{00}(\omega) = \frac{1}{G_+ + G_- + \omega}, \tag{7.55}$$

with the random variables D_x to the right of site 0 appearing in

$$G_+ = \frac{1}{D_1^{-1} + \frac{1}{\omega + \frac{1}{D_2 + \cdots}}}, \tag{7.56}$$

and those to the left appearing in

$$G_- = \frac{1}{D_0^{-1} + \frac{1}{\omega + \frac{1}{D_{-1} + \cdots}}}. \tag{7.57}$$

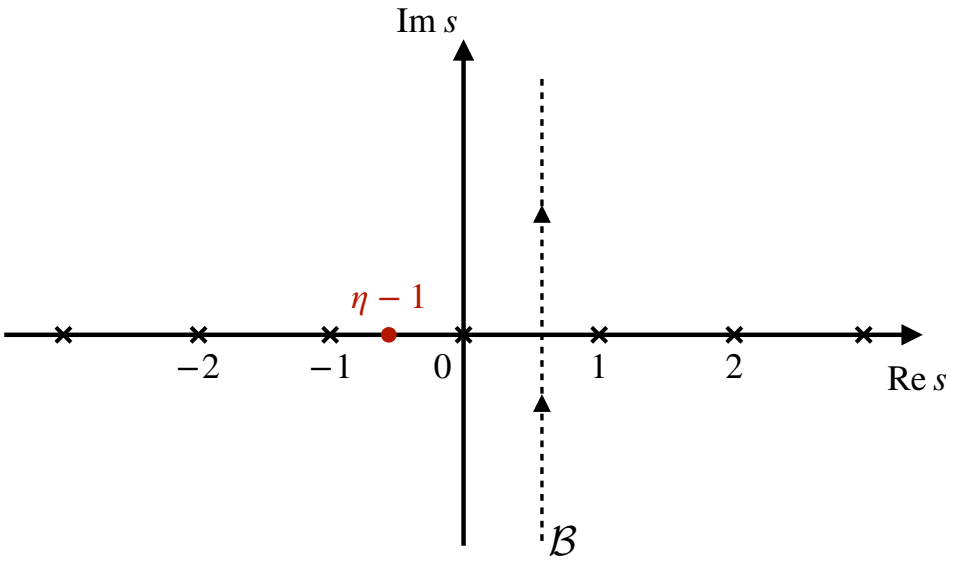

Figure 7.6: Bromwich contour for the inversion of the Mellin transform, Eq. (7.62). The poles at integer-values (black crosses) are responsible for a regular scaling of time and space, whilst the pole at $s = \eta - 1$ (red dot) is responsible for subdiffusion when $\eta > 0$, and for the anomalous corrections to diffusion when $-1 < \eta < 0$.

Now, $G_\pm$ are themselves random variables, and their distribution can be found in an iterative way. In fact, the relation

$$G_{\pm,x} = \frac{1}{D_x^{-1} + 1/(\omega + G_{\pm,x-1})} \tag{7.58}$$

is a sort of recursion equation familiar from the theory of Anderson localisation [213, 214, 216], and that of spin glasses [217–219]. The limiting distribution of G must be invariant under the iteration

$$f(g) = \int dg' f(g') \int dD\, \rho(D)\, \delta\left[g - \left(D^{-1} + (\omega + g)^{-1}\right)^{-1}\right]. \tag{7.59}$$

The scaling form at small ω can be recovered by looking at the first moment $\overline{g} = \int dg\, g\, f(g)$:

$$\begin{aligned} \overline{g} &= \int dg' f(g') \int dD\, \rho(D) \left[D^{-1} + (\omega + g)^{-1}\right]^{-1} \\ &= \int dg' f(g')(\omega + g') F(\omega + g'), \end{aligned} \tag{7.60}$$

where

$$\begin{aligned} F(s) &= \int dD\, \rho(D) \frac{1}{1 + s/D} \\ &= (1 - \eta) \int_1^\infty dR\, R^{-2+\eta} \frac{1}{1 + sR}, \end{aligned} \tag{7.61}$$

having passed to the variable $R := 1/D$. Notice that $F(0) = 1$, but one needs also the corrections at small $s = \omega + g'$. Going to the Mellin transform, one can write

$$F(s) = \int_{\mathcal{B}} \frac{dz}{2\pi i} \frac{\pi s^{-z}}{\sin \pi z} \frac{1-\eta}{z+1-\eta}, \tag{7.62}$$

where $\mathcal{B}$ is the Bromwich path from $-i\infty$ to $+i\infty$ with $0 < \Re(z) < 1$, see Fig. 7.6. The function $F(s)$ in the complex s plane contains poles at all the integers $s \in \mathbb{Z}$ and at $s = \eta - 1 < 0$, see again Fig. 7.6. In order to find the small-s behaviour, one can move the contour to the left, picking up as many poles as terms required. For $\eta > 0$, one finds

$$F(s) = 1 - \frac{\pi(1-\eta)}{\sin \pi(1-\eta)} s^{1-\eta} + O(s). \tag{7.63}$$

Inserting the relation above in Eq. (7.60), we have

$$\begin{aligned} \overline{g} &= \int dg' f(g')(\omega + g') \left[1 - \frac{\pi(1-\eta)}{\sin \pi(1-\eta)} (\omega + g')^{1-\eta} \right] \\ &= \omega + \overline{g} - \frac{\pi(1-\eta)}{\sin \pi(1-\eta)} \overline{(\omega + g)^{2-\eta}}, \end{aligned} \tag{7.64}$$

with the promised small s corrections. Neglecting, self-consistently, ω w.r.t. g, one obtains

$$\omega = \frac{\pi(1-\eta)}{\sin \pi(1-\eta)} \overline{g^{2-\eta}}, \tag{7.65}$$

and so

$$\overline{g^{2-\eta}} \sim \omega. \tag{7.66}$$

Analogously, for all $n \geq 2$ one can prove that $\overline{g^{n-\eta}}/\overline{g^{n-2}} \sim \omega$. Therefore, the typical value of $g \sim \omega^{1/(2-\eta)}$ which, when inserted in Eq. (7.55), gives

$$\mathcal{A}(t) \sim \int d\omega \frac{e^{i\omega t}}{\omega^{\frac{1}{2-\eta}} + O(\omega)} \sim t^{-\frac{1-\eta}{2-\eta}}. \tag{7.67}$$

This is consistent with the result obtained in §7.3.

From the Mellin transform formalism one can also get a complementary understanding of the subleading terms. Looking at Eq. (7.62) or Fig. 7.6, one can see that the function $F(s)$ receives contributions from two kinds of poles: those at integer-values, and an anomalous pole at $s = \eta - 1$. This last pole moves as the disorder strength η is tuned, and, depending on the relative position of the anomalous pole $s = \eta - 1$ and the pole at $s = -1$, the asymptotic behaviour changes from diffusion to subdiffusion: indeed, it is the first pole to the left of $s = 0$ that determines the asymptotics. One can see that the two poles coalesce precisely at $\eta = 0$, in accordance with the power series treatment of §7.3.

The poles at $s = -2$, $s = -3$, etc., represent subleading corrections to the scaling of $\overline{g}$ w.r.t. ω. When $-1 < \eta < 0$, i.e., in the slow diffusion regime, all such poles are subleading; the anomalous pole is the first to be encountered to the left of $s = -1$, and thus provides the leading finite-time corrections to the asymptotic scaling. When, instead, $\eta < -1$, it is the pole at $s = -2$ that dominates the corrections, and standard diffusion is recovered to a very good approximation.

7.5 Conclusions

We have shown that the dynamics of a classical Heisenberg chain with broadly-distributed couplings J_i, specifically $p_\eta(J) \sim J^{-\eta}$, goes through various dynamical phases as η is increased from very negative to its maximum achievable value, $\eta = 1$. For $\eta < -1$ the correlation functions are diffusive (data not presented, though see, e.g., the supplementary material of Ref. [36]). For $-1 < \eta < 0$, we have shown that, whilst the asymptotic behaviour is still diffusive, there are strong finite-time corrections which can be mistaken as signs of subdiffusive transport. True subdiffusion sets in only when $\eta > 0$, with the subdiffusive exponent matching the analytic prediction of a phenomenological model in which a local diffusion coefficient is assumed to be a random variable, also broadly-distributed, with the same exponent η as the local couplings J.

We point out that the quantum version of the model considered here (7.1) was the subject of recent works [220, 221], in which it was argued that a regime intermediate between many-body localisation and thermalisation persists in the thermodynamic limit. Such a regime is found in a range of parameters equivalent to our $0 \leq \eta < 1$, i.e., when the classical model shows subdiffusive transport. It may be interesting to consider whether a semi-classical treatment of the quantum model could link these findings.

Our work, we believe, settles the question about the onset of diffusion and subdiffusion in classical Heisenberg chains with random couplings, in part already considered in Refs. [28, 30]. It also presents yet another cautionary tale for efforts to extract potentially anomalous dynamical exponents, and identify possible dynamical phase transitions based on short-time, small-system numerics. Indeed, the discrepancy between exponents obtained from different but, visually, similarly good fits on system sizes of several thousand spins at times of a million $J_{\max}^{-1}$, gives a quantitative indication of just how challenging it is to estimate "systematic" error bars.

To conclude, leaving aside the considerations of a largely technical nature, the family of models we have studied provides a window on the physics of how rare (or not-so-rare) local fluctuations manifest themselves at long length- and time-scales. Our work, in this sense, is a classical counterpart to the strong-disorder renormalisation group treatments [192–196] which have been so influential for the study of quantum models in the last few decades. The question of which regimes still await discovery, in addition to those found and referenced in this chapter, strikes us as a subject of study likely to hold more than one surprise in store.

Part IV

Spin dynamics out-of-equilibrium

Chapter 8

The boundary-driven Floquet XXZ chain

Parts I – III of this thesis have been focused on either single excitations above the ground state – an effectively zero temperature regime – or the dynamics of spin systems in thermal equilibrium. In this last part, however, we forsake the embrace of the canonical ensemble, and study the dynamics of spin systems out of equilibrium. In the next chapter, we will investigate the stability of spin dynamics under non-reciprocal interactions, where the canonical ensemble is not even (in principle) well-defined; in this chapter, we consider the transport of magnetisation across a boundary-driven Floquet (periodic) XXZ spin chain (8.1).

The far-from-equilibrium nature of the setup results in vastly different transport phenomenology from what would be predicted by the equilibrium hydrodynamics of parts II & III. We will show, both numerically and analytically that, for the easy-plane, isotropic, and easy-axis cases we obtain, respectively, magnetisation transport which is ballistic, subdiffusive (with $\alpha = 1/3$), and localised. Further, we will demonstrate that this phenomenology is extremely robust to the introduction of (quenched) bond disorder.

This study of the classical model is partly motivated by the recent Google Quantum AI experiments on its direct quantum counterpart [222]. Remarkably, the fundamental results – in particular, the asymptotic transport regimes as a function of anisotropy – are the same in both cases. We point out that, *a priori*, there is no reason to expect the quantum and classical models to show the same phenomenology, especially since the infinite-frequency limit of the quantum case is integrable, and the classical model, as we have repeatedly pointed out, is not. In this light, the driven classical spin chain (8.1) serves as another elucidating example of an integrable–non-integrable and quantum-classical correspondence; and, moreover, whereas the superdiffusion of Ch. 5 was ultimately limited by some (extremely long) finite time-scale, the anomalous transport regimes we present in this chapter *are* the asymptotic, infinite-time results. And, as always, the intrinsic advantage of classical models – that larger systems and longer times can be utilised – still applies.

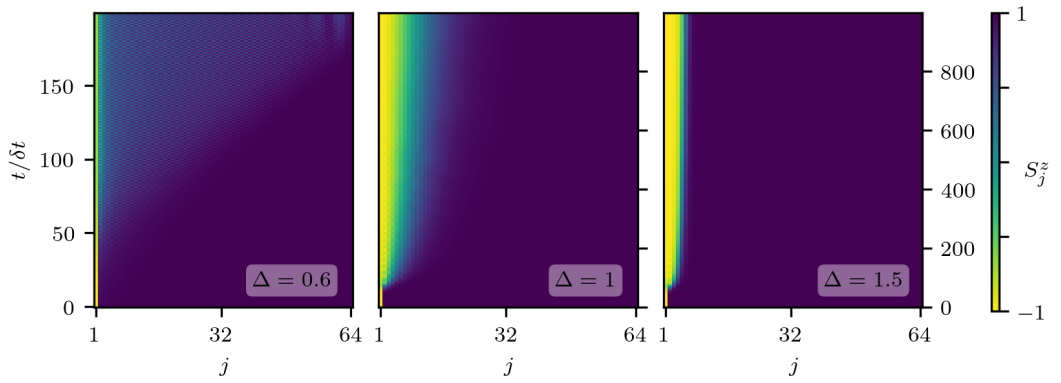

Figure 8.1: Overview of the different dynamical regimes. From left to right: easy-plane ($\Delta = 0.6$), isotropic ($\Delta = 1$), and easy-axis ($\Delta = 1.5$). Value of $S^z(j,t)$ is shown in each case. The easy-plane features a front which spreads ballistically across the chain. There is no transport across the chain in the easy-axis case: a domain wall (which is stable under these dynamics) is formed. In the isotropic case, the spin excitations can only move subdiffusively, but will eventually reach the other side. In these figures, the system size is $L = 64$.

8.1 Classical model

The classical model we consider here is the direct counterpart of the boundary-driven Floquet XXZ spin chain which was the subject of a recent study by Google Quantum AI [222]. For ease of reference, we repeat here the Hamiltonian of the classical XXZ spin chain,

$$\mathcal{H} = -J \sum_{i=1}^{L} \left(S_i^x S_{i+1}^x + S_i^y S_{i+1}^y + \Delta S_i^z S_{i+1}^z \right), \tag{8.1}$$

where the $\boldsymbol{S}_i \in S^2$ are classical unit-length vectors at sites i of the chain. We set $J = 1$, which defines units of energy and time throughout.

We imbue the chain with boundary-driven Floquet dynamics. A single time-step $t \mapsto t + \delta t$ consists of the following:

- The boundary spins are reset, $\boldsymbol{S}_1 = -\hat{\boldsymbol{z}}$, $\boldsymbol{S}_L = +\hat{\boldsymbol{z}}$ (cf. the iSWAP($\pi/2$) gates of the quantum experiment [222]). Note that the boundary spins *are* allowed to evolve in the following sub-steps.

- The odd bonds, $(1,2)$, $(3,4)$, ..., $(L-1, L)$, evolve between times t and $t + \delta t/2$ (cf. the fSim gates, $\delta t/2 = \pi/4$).

- The even bonds, $(2,3)$, $(4,5)$, ..., $(L-2, L-1)$, evolve between times $t + \delta t/2$ and $t + \delta t$ (cf. the fSim gates, $\delta t/2 = \pi/4$).

It is assumed in the above that L is even, but this is not important. The two-site dynamics on a given bond is the classical dynamics which follows from the XXZ Hamiltonian (8.1)

restricted to the two sites in question, and the fundamental spin Poisson brackets. Explicitly, denoting the sites by l and r, the equations of motion are

$$\begin{aligned} \dot{S}_l^x &= -S_r^y S_l^z + \Delta S_r^z S_l^y, & \dot{S}_r^x &= -S_l^y S_r^z + \Delta S_l^z S_r^y, \\ \dot{S}_l^y &= -\Delta S_r^z S_l^z + S_r^x S_l^z, & \dot{S}_r^y &= -\Delta S_l^z S_r^x + S_l^x S_r^z, \\ \dot{S}_l^z &= -S_r^x S_l^y + S_r^y S_l^x, & \dot{S}_r^z &= -S_l^x S_r^y + S_l^y S_r^x. \end{aligned} \tag{8.2}$$

For book-keeping purposes we will generally label bonds with the left site index. By construction, the z-magnetisation is locally conserved in the bulk, and we can define the discrete-time ($t \mapsto t + \delta t$) spin current across the bond $(i, i+1)$:

$$\begin{cases} j_i(t) = -S_i^z(t + \delta t/2) + S_i^z(t) & i \text{ even} \\ j_i(t) = -S_i^z(t + \delta t) + S_i^z(t + \delta t/2) & i \text{ odd.} \end{cases} \tag{8.3}$$

Note, however, that magnetisation can flow into and out-of the system at the boundaries, at the moment when the boundary spins are reset.

The only place where we must explicitly depart (slightly) from the quantum case is in the initial state. The quantum experiment begins with the system prepared in the state

$$|\psi\rangle = |\downarrow\uparrow\uparrow \ldots \uparrow\uparrow\rangle, \tag{8.4}$$

which, since $|\downarrow\uparrow\rangle$ is not an eigenstate of the two-site $S = \frac{1}{2}$ XXZ Hamiltonian, evolves non-trivially with time. In the classical case, however, since anti-parallel spins do not evolve, we need to slightly perturb this state to seed the dynamics. In the simulations presented here, we use the initial state

$$\boldsymbol{S}_0 = -\hat{\boldsymbol{z}}, \quad \boldsymbol{S}_1 = \chi\hat{\boldsymbol{x}} + \sqrt{1-\chi^2}\hat{\boldsymbol{z}}, \quad \boldsymbol{S}_2 = \ldots = \boldsymbol{S}_{L-1} = +\hat{\boldsymbol{z}}. \tag{8.5}$$

This does still lead to one of the few noticeable differences between the quantum and classical models: a large value of χ will generate an initial pulse of spin waves that does not appear in the quantum experiment. We can sidestep this issue by using a small value, say, $\chi \approx 0.01$ (used in all of the results presented here). This suppresses the spin wave pulse, but there is a noticeable delay in the onset of the dynamics – the injected current rises exponentially from an extremely small value up to some time $t \approx 10^2 \delta t$ (see Fig. 8.4). From this point, however, the dynamics appears to proceed in the same manner as in the quantum case, and, in particular, the asymptotics are fundamentally equivalent.

8.2 Non-equilibrium spin transport

Let us first present the results of classical model before turning to the explanation of the various transport regimes in §8.3. (Note that there is no need to average over initial states here; this section is entirely deterministic).

The behaviour of the model is fundamentally determined by the anisotropy Δ. We give an overview of the different regimes (easy-plane $\Delta < 1$, isotropic $\Delta = 1$, and easy-axis $\Delta > 1$) in Fig. 8.1, by plotting the space-time dependence of S^z. The classical pictures are, qualitatively, very similar to the different quantum mechanical regimes (cf. Fig. 5(b)

of [222]). In the easy-plane, we have a ballistic transfer of spin from the left- to the right-boundary; in the easy-axis, spin cannot be transported across the chain because a domain wall (the topological soliton (3.32)) is quickly established. The isotropic point sits between these cases; the magnetisation injected at the left-boundary can only move subdiffusively to the right-boundary, but is not localised.

Now, given that dissipation is built into the model by virtue of the connection to the magnetisation reservoirs at the boundaries, we will, quite generically, approach some non-equilibrium steady state (NESS). We find, from the numerical simulations, that the easy-plane NESS supports a spatially-uniform, non-zero spin current through the bulk; the spin profile symmetrises between the $-\hat{\boldsymbol{z}}$ and $+\hat{\boldsymbol{z}}$ boundaries, and oscillates around $S^z = 0$ near the middle of the chain.

In the easy-axis, the domain wall (topological soliton) develops quickly, and is then, as far as can be detected numerically, static, with the centre of the domain wall close to the left-boundary. This NESS has no current through the bulk of the chain. Whilst we do expect that this is not the *true* steady state (see §8.3) – the centre of the domain wall should move exponentially slowly (in the system size) to the centre of the chain – any residual current is still exponentially suppressed in the system size.

The isotropic point is the transition between these ballistic and localised regimes. The magnetisation profile slowly builds up until the cosine-profile steady-state (§8.3) is attained.

These results are summarised in Fig. 8.2, where we show the spin S^z_j in the NESS, along with the corresponding current profile, for various values of the anisotropy. We plot the NESS value of the central spin $S^z_{L/2}$ and the corresponding bulk-current $j_{L/2}$ as a function of the anisotropy in Fig. 8.3, which shows the presence of a ballistic transport regime in the easy-plane case, with the asymptotic current scaling linearly in the deviation from isotropy $(1-\Delta)$ near $\Delta = 1$. It is also clear that the easy-axis case is localised, with essentially zero spin current flowing in the NESS.

These plots, however, do not tell us much about what is going on at the isotropic point, nor do they suffice to properly measure the dynamical exponents. These we extract by considering the time-dependence of the current injected into the system from the left-boundary.

We plot the time-dependence of the injected spin current for three representative anisotropies in Fig. 8.4. As we have noted when discussing the initial state, there is in all cases an initial (exponential) ramp as the system moves away from the unstable steady state $(-\hat{\boldsymbol{z}}, +\hat{\boldsymbol{z}}, +\hat{\boldsymbol{z}}, ...)$. This initial time-lag is not present in the quantum experiments, but the asymptotic decay of the injected current is the same in both the quantum and classical cases (cf. Fig. 5(d) of [222]): in the easy-plane case, the injected current does not decay; whereas the isotropic case shows a clear $t^{-2/3}$ decay, which is enhanced to t^{-1} in the easy-axis. In summary, we have the three different dynamical regimes:

$$\begin{cases} j_1(t) \sim \text{const.} & \Delta < 1 \\ j_1(t) \sim t^{-2/3} & \Delta = 1 \\ j_1(t) \sim t^{-1} & \Delta > 1. \end{cases} \tag{8.6}$$

To understand why the temporal decay of the injected current is related to the dynamical exponents, consider the following heuristic argument. In the hydrodynamic limit, the boundary drive is, essentially, attempting to inject magnetisation through the edge of the system at a constant rate, but will be slowed by the build-up of magnetisation near the edge.

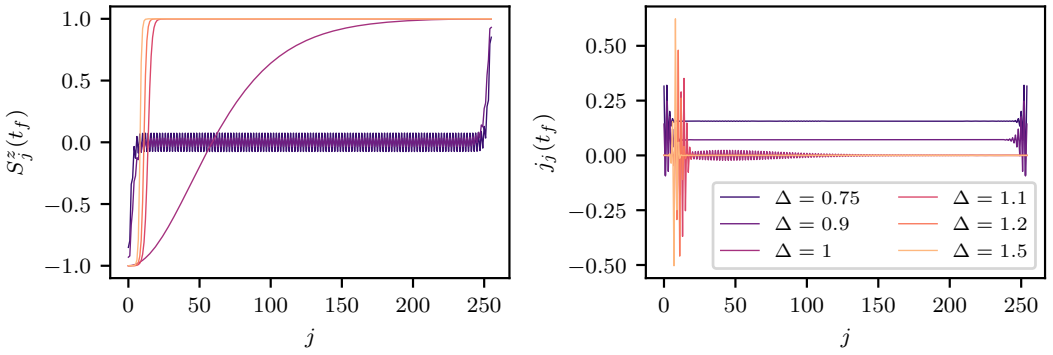

Figure 8.2: Spin and current profiles for various anisotropies in the NESS. Left: the z-components of the spin. Right: the spin current j. In the easy-axis case, the domain walls are clear; there is still some "a.c." current near the left-boundary as the xy-components rotate, but there is no current in the bulk of the chain or over towards the right-boundary. In the isotropic case there is a small current (almost averaging to zero over space) associated with the slow spreading of the magnetisation. The easy-plane supports nonzero, spatially-uniform currents across the bulk of the chain. $L = 256$.

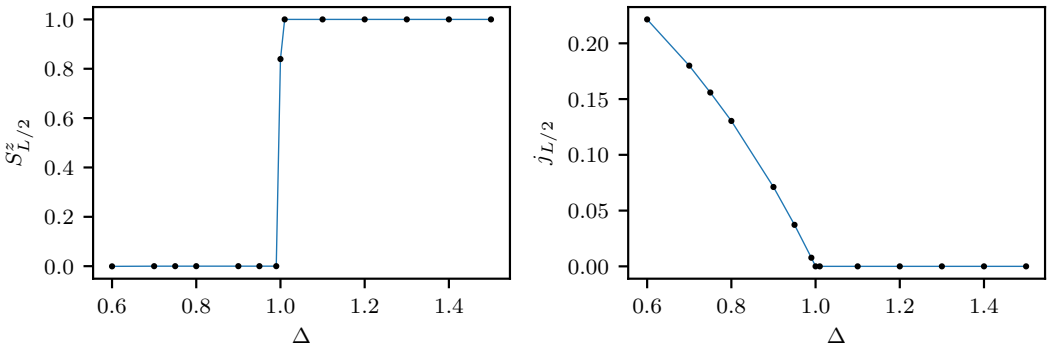

Figure 8.3: Spin and current in the bulk of the NESS as a function of anisotropy Δ (measured as an average across the two middle sites to remove the spatial oscillation in the easy-plane case). There is a very sharp change across the transition. System size $L = 256$.

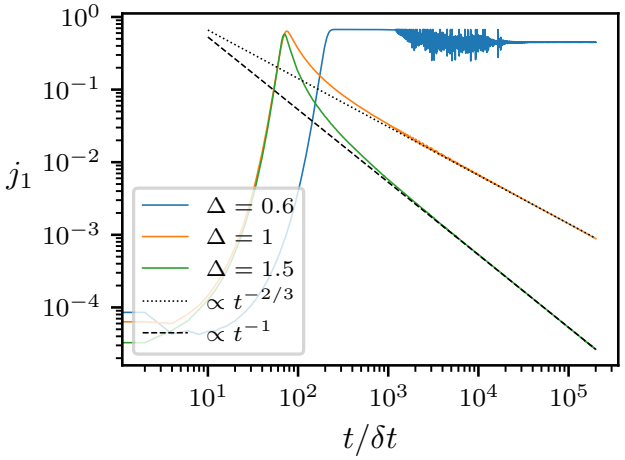

Figure 8.4: Transport exponents measured by the injected current as a function of time. The different regimes are clearly visible after the dynamics sets in, following an initial exponential ramp of injected current.

Now, from the scaling relation $x \sim t^\alpha$, and the fact that magnetisation is not driven across in the bulk, we know that, by time t, the magnetisation spreads into the bulk a distance $x \sim t^\alpha$, by definition; that is, the charge moves away from the edge at an effective rate t^α/t, which is precisely the current we can inject at time t.

It follows, then, that $j_1(t) \sim t^{\alpha-1}$, which returns:

$$\begin{cases} \alpha = 1 & \Delta < 1 \quad \text{(ballistic)} \\ \alpha = 1/3 & \Delta = 1 \quad \text{(subdiffusive)} \\ \alpha = 0 & \Delta > 1 \quad \text{(localised).} \end{cases} \tag{8.7}$$

8.3 Origin of the dynamical exponents

Having clearly observed the different dynamical exponents associated to the different regimes in Fig. 8.4, we now explain their origin.

The transport exponents can be obtained directly from the NESS. At late times, and under the Floquet dynamics of Eq. (8.2), we approach a steady-state which satisfies the stroboscopic condition

$$\boldsymbol{S}_i(t) = \boldsymbol{S}_i(t + \delta t), \quad \forall i, \tag{8.8}$$

though note that $\boldsymbol{S}_i(t) \neq \boldsymbol{S}_i(t + \delta t/2)$ is allowed, and, in fact, always occurs. Now, consider the $\delta t \to 0$ (or infinite-frequency, $\omega \to \infty$) limit. This is well-defined, and corresponds to the continuous-time dynamics of the XXZ Hamiltonian (8.1), subject to the boundary conditions $\boldsymbol{S}_1 = -\hat{\boldsymbol{z}}$, $\boldsymbol{S}_L = +\hat{\boldsymbol{z}}$. The steady-state condition becomes

$$\dot{\boldsymbol{S}}_i(t) = 0, \quad \forall i, \quad \omega \to \infty. \tag{8.9}$$

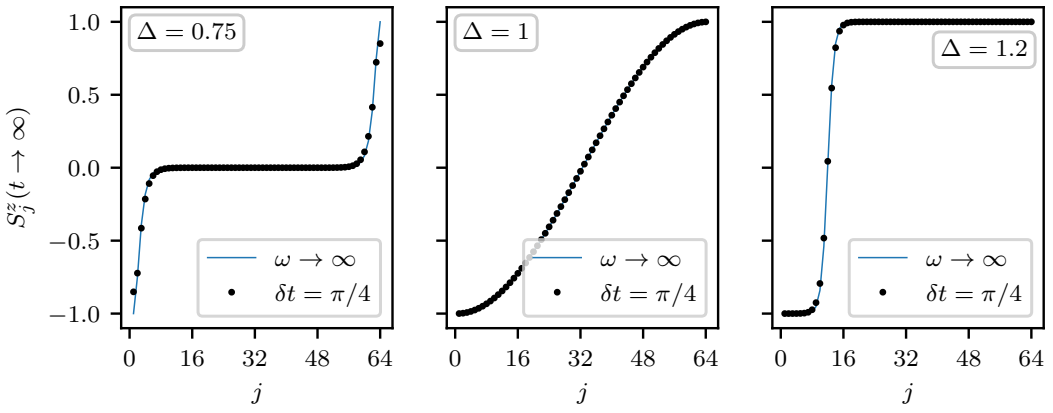

Figure 8.5: Comparison of the NESS obtained from the simulations (black dots, $n_t = 10^5$) and the $\omega \to \infty$ limit, Eq. (8.10) (blue lines), for the different dynamical regimes. In the easy-plane case the simulation data have been averaged over the full- and half-timestep to remove the spatial oscillations (cf. Fig. 8.2). The agreement is particularly striking at the isotropic point.

These equations may be solved to arbitrary precision: they are the same consistency equations that built the static solitons of the classical Heisenberg chain, all the way back in Ch. 2 – though they appear now with different boundary conditions. Explicitly, the z-components $S^z_i = z_i$ satisfy

$$\frac{z_i}{\sqrt{1-z_i^2}} = \Delta \frac{z_{i+1} + z_{i-1}}{\sqrt{1-z_{i+1}^2} + \sqrt{1-z_{i-1}^2}}, \quad z_1 = -1, \quad z_L = +1, \tag{8.10}$$

and the in-plane components have a constant azimuthal angle, i.e., $S^x_i = \cos\varphi\sqrt{1-z_i^2}$, $S^y_i = \sin\varphi\sqrt{1-z_i^2}$, for some arbitrary φ. An example steady-state solution for each of the dynamical regimes is shown in Fig. 8.5.

Now, the infinite-frequency NESS obviously has no currents, and the finite-frequency NESS is defined by the stroboscopic condition (8.8) and is, thus, different. It suffices, however, to consider the small ω limit to obtain the dynamical exponents. We assume that the finite-frequency NESS may be approximated by the infinite-frequency NESS (cf. Fig 8.5), but we apply the finite-ω dynamics to this state to obtain the asymptotic value of the current, $j_i(t \to \infty; L)$, for a given system size L. Without loss of generality, we may assume $\varphi = 0$, i.e., $\boldsymbol{S}_i = z_i\hat{\boldsymbol{z}} + \sqrt{1-z_i^2}\hat{\boldsymbol{x}}$.

In particular, we are interested in the asymptotic value of the *extracted* current, $j_{L-1}(t \to \infty; L)$, at the right-boundary; since we are considering a boundary drive, i.e., magnetisation is not forced across through the bulk, this residual current is directly proportional to the conductance $G(L)$.

To obtain the extracted current, we need the two-spin dynamics on the final bond. For $\Delta = 1$, the exact solution of the two-spin dynamics may be obtained by rotations about the

total, conserved effective field on the bond, $\boldsymbol{S}_{L-1} + \boldsymbol{S}_L$. It follows:

$$\begin{aligned}
\boldsymbol{S}_L(t+\delta t/2) &= \left(\sqrt{1-z_{L-1}^2}\sin^2\frac{\delta t}{4}\right)\hat{\boldsymbol{x}} + \left(\frac{-\sqrt{1-z_{L-1}}}{\sqrt{2}}\sin\frac{\delta t}{2}\right)\hat{\boldsymbol{y}} \\
&\quad + \frac{1}{2}\left(1+z_{L-1}+(1-z_{L-1})\cos\frac{\delta t}{2}\right)\hat{\boldsymbol{z}}, \\
\boldsymbol{S}_{L-1}(t+\delta t/2) &= \left(\sqrt{1-z_{L-1}^2}\cos^2\frac{\delta t}{4}\right)\hat{\boldsymbol{x}} + \left(\frac{\sqrt{1-z_{L-1}}}{\sqrt{2}}\sin\frac{\delta t}{2}\right)\hat{\boldsymbol{y}} \\
&\quad + \left(\frac{z_{L-1}}{2}\left[1+z_{L-1}+(1-z_{L-1})\cos\frac{\delta t}{2}\right] + [1-z_{L-1}^2]\sin^2\frac{\delta t}{4}\right)\hat{\boldsymbol{z}} \qquad (8.11)
\end{aligned}$$

This last step is exact (assuming we could exactly obtain the finite-frequency value of z_{L-1}). It follows that the current is given by

$$j_{L-1}(t\to\infty; L) = \frac{1}{2}\left(1+\frac{1}{\sqrt{2}}\right)(1-z_{L-1}). \qquad (8.12)$$

We need only the proportionality, $j_{L-1}(t\to\infty; L) \sim 1 - z_{L-1}$, which holds for any Δ, in what follows.

Now that we have this relation, we need only calculate the steady-states from Eq. (8.10) to find the conductances $G(L)$. We begin with the easy-plane case, where we find from the numerically-exact solutions to the consistency equations (8.10) that $z_{L-1} \sim \Delta$, $L\to\infty$, and thus

$$j_{L-1}(t\to\infty; L) \sim 1 - z_{L-1} \sim G(L) \sim 1-\Delta. \qquad (8.13)$$

The conductance does not decay with system size, implying ballistic transport ($\alpha = 1$), and depends linearly on the deviation from isotropy. This latter prediction is also supported by the numerics; a linear dependence at small $|1-\Delta|$ may be observed in Fig. 8.3. The curvature is a finite-frequency effect.

Now, at the isotropic point, the exact solution of the consistency equations (8.10) is

$$z_n = \sin\left(\frac{\pi}{L}\left[n - \frac{(L+1)}{2}\right]\right). \qquad (8.14)$$

This implies

$$z_{L-1}(L) \sim 1 - \frac{\pi^2}{8}L^{-2} + \frac{\pi^4}{384}L^{-4} - ..., \quad L\to\infty, \qquad (8.15)$$

and thus, at the isotropic point $\Delta = 1$, we have

$$j_{L-1}(t\to\infty; L) \sim 1 - z_{L-1} \sim G(L) \sim L^{-2}. \qquad (8.16)$$

That is, the conductance decays with a power-law faster than $1/L$, implying subdiffusion; explicitly, the scaling of the conductance is generally related to the dynamical exponent by $G(L) \sim L^{1-1/\alpha}$, so we have precisely recovered $\alpha = 1/3$ at the isotropic point. We show explicitly in Fig. 8.6 that this prediction is borne out by the finite-frequency simulations.

Finally, in the easy-axis case, the steady-state solution to Eqs.(8.10) is asymptotically given by the topological soliton,

$$z_n \sim \tanh\left(\left(n - \frac{L+1}{2}\right)\cosh^{-1}\Delta\right), \quad L\to\infty, \qquad (8.17)$$

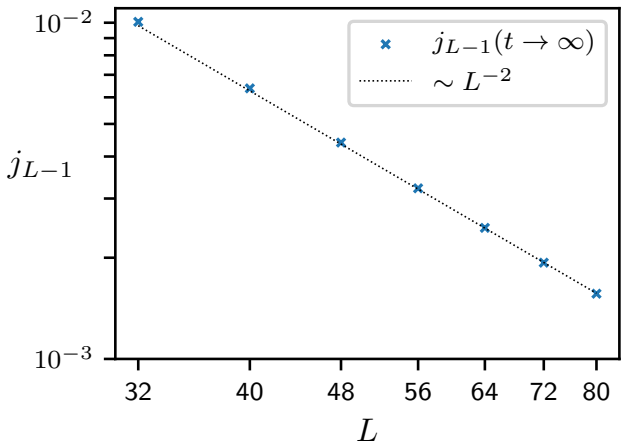

Figure 8.6: Scaling of the extracted current with system size at the isotropic point, showing a clear subdiffusive scaling of the conductance, $G(L) \sim L^{-2}$. We use a final time of $t = 10^5 \delta t$, and measure for system sizes small enough that the current on the final bond has ceased to change with time by the end of the simulation (i.e., for which the NESS is attained).

with only exponentially small deviations necessary to fulfil the boundary conditions at finite size. To actually attain this NESS will require an exponentially long time, since the system reaches a very good approximation of a steady-state (as measured by Eqs. (8.10), cf. Fig. 8.1(right)) as soon as the centre of the soliton has moved a few sites away from the edge. In any event, we have

$$j_{L-1}(t \to \infty; L) \sim 1 - z_{L-1} \sim G(L) \sim e^{-L}, \tag{8.18}$$

and the conductance is suppressed exponentially in the system size, which returns $\alpha = 0$. The NESS formalism, via the consistency equations (8.10), has successfully predicted all of the dynamical exponents found in Fig. 8.4 (and Fig. 5(c) of the quantum experiment [222]).

8.4 Effects of disorder

Having shown that the equivalent classical model captures the non-equilibrium transport features of the quantum-mechanical experiment [222], let us now go slightly further and see how the spin dynamics is affected by the introduction of random couplings. Whilst the fact that this phenomenology appears in a real experiment implies that it must be stable to (sufficiently) weak external noise, there is no guarantee of non-perturbative stability against quenched randomness.

8.4.1 Random coupling model

To investigate the stability of, particularly, the ballistic regime, let us modify the Hamiltonian (8.1) on which the Floquet dynamics is based by randomising the couplings. Since

we are considering a boundary drive, however, we will treat the first and final bonds as connections to external reservoirs, not subject to disorder. That is, we have

$$\mathcal{H} = -\sum_{i=1}^{L-1} J_i \left(S_i^x S_{i+1}^x + S_i^y S_{i+1}^y + \Delta S_i^z S_{i+1}^z \right), \tag{8.19}$$

with each J_i (except J_1 and J_{L-1}) drawn independently from the uniform distribution over the interval $[1 - W, 1]$, where W is the disorder strength. Apart from this change, the dynamical protocol is still that specified in §8.1. We use the same initial state (8.5) as in the clean model, though now we need to average over the different realisations of the coupling strengths J_i. The primary parameter which controls the different dynamical responses is still the overall anisotropy Δ.

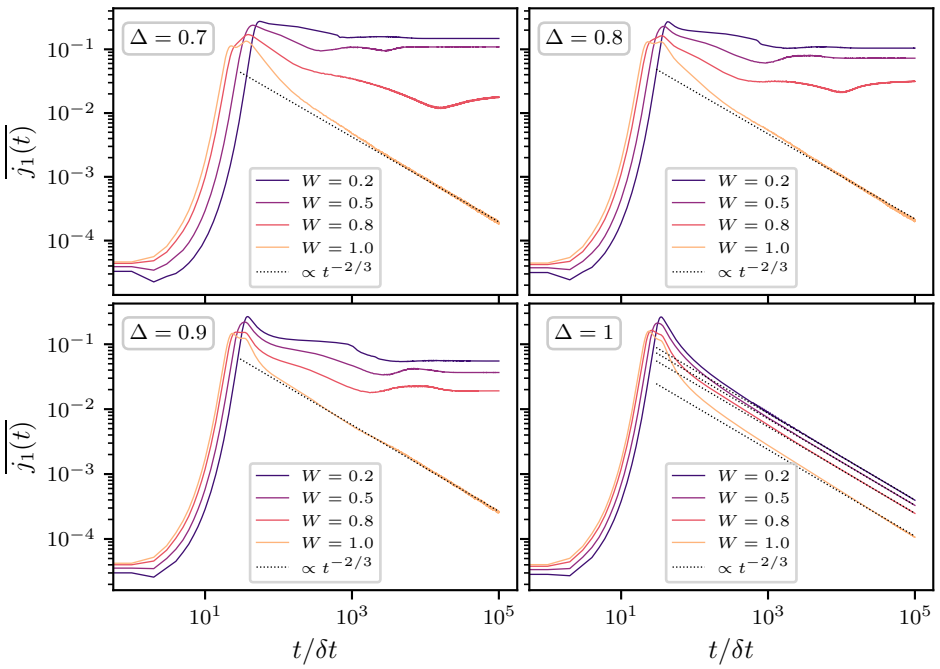

Figure 8.7: Time-dependence of the disorder-averaged injected current, $\overline{j_1(t)}$, shown for various anisotropies and disorder strengths. The ballistic transport regime is shown to survive if $\Delta < 1$, $W < 1$. At strong disorder $W = 1$, the easy-plane ballistic regime gives way to a regime of subdiffusive transport with $\alpha = 1/3$, which is also observed at all disorder strengths at the isotropic point $\Delta = 1$. The averages are taken over 10^4 independent realisations of disorder, at $L = 256$.

The principal diagnostic of the dynamical exponent remains the time-dependence of the injected current, or, rather, its disorder average $\overline{j_1(t)}$; each sample is allowed to evolve in time independently, the injected current $j_1(t)$ is calculated, and the arithmetical mean is then taken. All of the results in this section are averaged over 10^4 independent realisations of disorder.

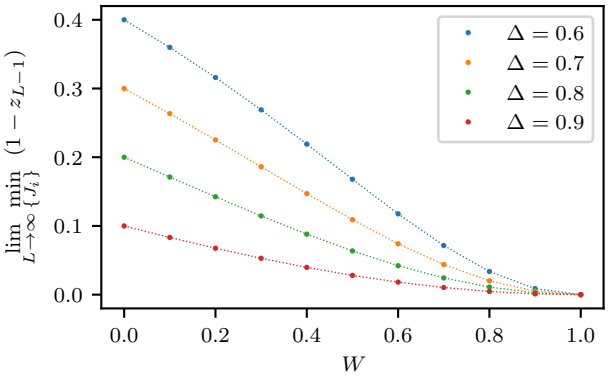

Figure 8.8: Minimum value, as a functional of the disorder realisation, of the difference $1 - z_{L-1} \propto G(L)$ in the steady state, shown for various overall anisotropies Δ and as a function of the disorder strength W. So long as $W < 1$ and $\Delta < 1$, this is a finite value, showing the stability of the easy-plane ballistic transport regime to disorder in the coupling strengths. The values shown were obtained using $L = 128$ from the numerically exact solution to the consistency equations (8.20) with the disorder realisation $J_1 = J_{L-1} = 1$, $J_2 = ... = J_{L-2} = 1 - W$ (which minimises the conductance). There is no observable difference (up to machine precision) if one were to use $L = 64$ or $L = 256$ instead.

We show in Fig. 8.7 that, though the steady-state current does depend on the disorder strength, the easy-plane spin transport remains *ballistic* in the presence of random couplings, apparently for any $W < 1$; that is, as long as there is some lower bound to the coupling strength, the ballistic transport survives. We show also that when $W = 1$, the easy-plane transport transitions to the subdiffusive $\alpha = 1/3$ regime observed in the clean isotropic model. Fig. 8.7 also shows that the isotropic case is similarly stable – the $\alpha = 1/3$ subdiffusive regime is observed for all values of W. The easy-axis case is not particularly interesting: it is localised in the clean case, and, unsurprisingly, it is also localised in the disordered case.

The fact that the transport asymptotics appear to be barely affected by the disorder – particularly the fact that a *ballistic* regime survives the introduction of random couplings until the disorder is strong enough to cut the chain – is a remarkable result. Ballistic transport in interacting, many-body models is often associated with integrability – which is conspicuously absent here – and its survival to asymptotic times usually indicates that there is something protecting it.

To try to make sense of this, let us attempt the same analysis that successfully explained the clean case. The infinite-frequency steady-state condition is still $\dot{\boldsymbol{S}}_i = 0 \; \forall i$, but, of course, the consistency equations are modified to account for the random couplings:

$$\frac{z_i}{\sqrt{1 - z_i^2}} = \Delta \frac{J_i z_{i+1} + J_{i-1} z_{i-1}}{J_i \sqrt{1 - z_{i+1}^2} + J_{i-1} \sqrt{1 - z_{i-1}^2}}, \quad z_1 = -1, \quad z_L = +1. \tag{8.20}$$

This remarkably simple set of equations will again explain all of the non-equilibrium transport results: the extraordinary stability of the dynamical regimes is derived from the fact

that the disordered consistency equations (8.20) are fundamentally limited in the extent to which they can modify the NESS of the clean model – the (infinite-frequency) NESS is monotonic in z_i, and this property is preserved by the introduction of bond disorder.

That monotonicity holds for any realisation of the couplings $J_i > 0$ can be proven inductively, though some care needs to be taken in dealing with the various cases. Let us assume $z_{i-1} < z_i$, and show that this implies $z_i < z_{i+1}$. That $z_1 < z_2$ is guaranteed by the boundary conditions. We will assume $\Delta \leq 1$ to facilitate the proof – we are not interested in the easy-axis case, since it is always localised[1].

The first case to consider is where $z_i > z_{i-1} > 0$. Now, using the inductive assumption, we have the inequality

$$\frac{z_i}{\sqrt{1-z_i^2}} < \Delta \frac{J_i z_{i+1} + J_{i-1} z_i}{J_i \sqrt{1-z_{i+1}^2} + J_{i-1}\sqrt{1-z_i^2}}, \tag{8.21}$$

which is clearly true (cf. Eq. (8.20)) since the replacement $z_{i-1} \mapsto z_i$ both increases the numerator and decreases the denominator of the right hand side (and both sides are positive). If we now assume, for contradiction, that $z_{i+1} < z_i$, we would obtain, for the same reasons, the further inequality

$$\frac{z_i}{\sqrt{1-z_i^2}} < \Delta \frac{J_i z_{i+1} + J_{i-1} z_i}{J_i \sqrt{1-z_{i+1}^2} + J_{i-1}\sqrt{1-z_i^2}} < \Delta \frac{J_i z_i + J_{i-1} z_i}{J_i \sqrt{1-z_i^2} + J_{i-1}\sqrt{1-z_i^2}} = \frac{\Delta z_i}{\sqrt{1-z_i^2}}, \tag{8.22}$$

which is a contradiction, since we have assumed $\Delta \leq 1$. Thus, $z_{i+1} > z_i$.

The opposite case, when $0 < z_{i-1} < z_i$, holds *mutatis mutandis*. The edge case to consider is what happens when $z_{i-1} < 0 \leq z_i$. If it holds precisely that $z_i = 0$, then, clearly, $z_{i+1} = -\frac{J_{i-1}}{J_i} z_{i-1} > 0$. Otherwise, since $z_{i-1} < 0$, it is clear that

$$\frac{z_i}{\sqrt{1-z_i^2}} = \Delta \frac{J_i z_{i+1} + J_{i-1} z_{i-1}}{J_i \sqrt{1-z_{i+1}^2} + J_{i-1}\sqrt{1-z_{i-1}^2}} < \Delta \frac{J_i z_{i+1}}{J_i \sqrt{1-z_{i+1}^2}}, \tag{8.23}$$

which returns $z_{i+1} > z_i$ because we have assumed $\Delta \leq 1$. Thus, in all cases – and independently of the realisation of disorder – the infinite-frequency steady-state is monotonic increasing in z_i.

Of course, whilst this establishes one limitation of the ability of disorder to affect the transport relative to the clean case, it does not quite fully establish the stability of the ballistic transport regime. To do this, we need to show that there remains a finite, length-independent gap between $z_L = 1$ and z_{L-1}, since, cf. §8.3, this difference is proportional to the conductance $G(L)$.

We conjecture that the minimum conductance $G(L) \sim 1 - z_{L-1}$ (as a functional of the disorder realisation) is obtained from the couplings $J_1 = J_{L-1} = 1$, $J_2 = ...J_{L-2} = 1 - W$, and that this, indeed, corresponds to a finite, length-independent lower bound on $G(L)$, establishing the survival of the ballistic transport regime. We show this minimum

[1] It does appear, however, that the easy-axis case also follows the monotonicity condition on the NESS, suggesting the assumption $\Delta \leq 1$ may not be truly necessary – but I have not been able to construct the proof without it.

conductance as a function of the disorder strength W, for various anisotropies $\Delta < 1$, in Fig. 8.8.

In lieu of actually proving that this is the minimum, however, we have to resort to brute force: for any randomly chosen set of couplings J_i, the consistency equations (8.20) can be solved to arbitrary precision, and the distribution of conductances $G(L)$ is then essentially specified by the distribution of the values of z_{L-1}. We plot some histograms of the probability density of $1 - z_{L-1}$ for selected Δ and W in Fig. 8.9, lending some numerical credence to our assertion that the conductance $G(L)$ has a finite lower bound in the easy-plane – none of the 3×10^5 randomly drawn sets of couplings are found to violate the conjectured bound.

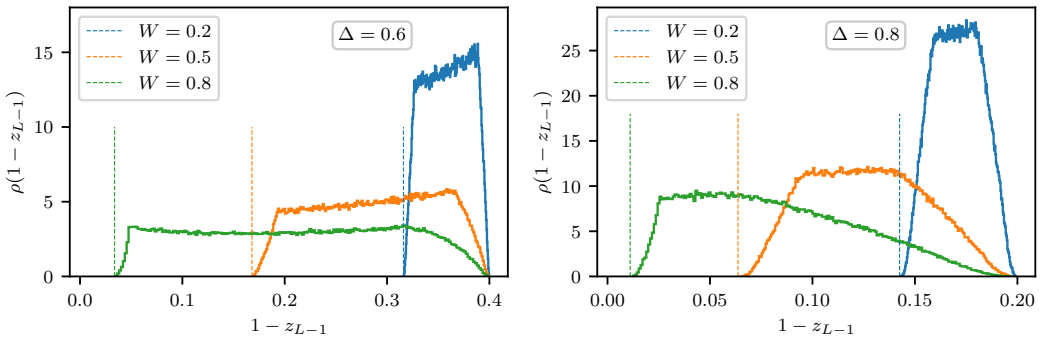

Figure 8.9: Probability density of the steady-state boundary-difference $1 - z_{L-1}$ (as a functional of the random couplings), for various disorder strengths and two different easy-plane anisotropies. The vertical lines denote the (conjectured) minimum possible value, cf. Fig. 8.8, with no sets of random couplings found to violate the bound. The upper bound in all cases is $1 - \Delta$. Each histogram is drawn using 3×10^5 independent realisations of disorder, with $L = 128$.

8.4.2 Sample-to-sample fluctuations

What we have shown, both numerically and (semi-)analytically, is that the ballistic transport regime observed in the easy-plane boundary-driven clean XXZ model (8.1), and in the quantum experiments [222], survives the introduction of random couplings, in the sense that the average current driven through the steady-state is independent of the size of the system.

In fact, we have shown something slightly stronger than this – a finite, length-independent current will be driven through the steady-state for *any* set of random couplings – though there is some probability distribution for the conductance of any particular sample.

What this suggests is that the steady-state current is primarily determined by the couplings near the edges of the chain – there is no "self-averaging" as the chains get longer, and, as indicated by the histograms of $1 - z_{L-1}$ (Fig. 8.9), we have strong sample-to-sample fluctuations.

This is, perhaps, not *so* surprising, since the boundary is clearly distinguished from the bulk by the nature of the drive; but it is worth remarking upon – in particular, this is quite

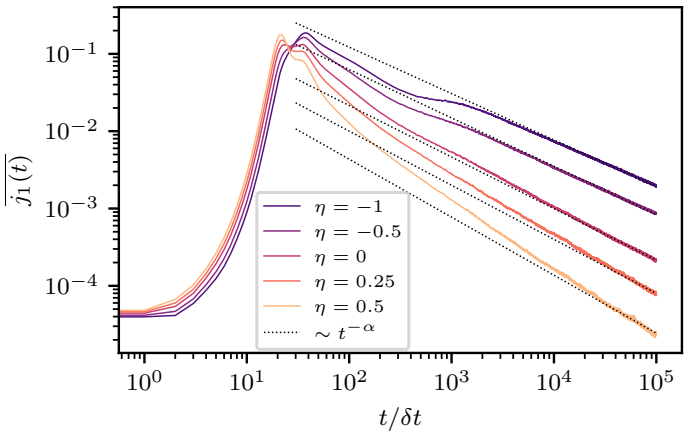

Figure 8.10: Time-dependence of the disorder-averaged injected current $\overline{j_1(t)}$, for the power-law distributions of disorder, Eq. (8.24). The power-law asymptotes use the subdiffusive exponent $\alpha(\eta)$ predicted by Eq. (8.26). Again, 10^4 realisations of disorder have been averaged over. $L = 1024$.

unlike the hydrodynamic subdiffusive spin transport of Ch. 7, where a rare-region of very slow spin diffusion could be averaged with a comparatively faster region in the same chain.

8.4.3 Transport in the strongly-disordered case

To end this chapter, let us turn our attention to the nature of the transition away from the ballistic transport regime at strong disorder. The arguments of §8.4.1, showing the survival of ballistic spin transport in the presence of random couplings, do not apply if there is not some finite lower bound to the coupling strengths, i.e., $J_i \geq J_{\min} > 0$.

Indeed, as briefly remarked in §8.4.1, the nature of the easy-plane spin transport appears to flip from ballistic to subdiffusive ($\alpha = 1/3$) when $W = 1$.

However, the story does not appear to be as simple as noting that there is no longer any minimum gap between z_{L-1} and z_L in the steady-state. Simply trying a few realisations of disorder in the consistency equations (8.20), and looking at the steady-states which result, indicates that, typically, there is no dramatic change to the NESS when we reach $W = 1$.

What the steady-state analysis has neglected, however, is that, regardless of the NESS, a very small coupling J_i in the bulk can constrain the total current. We were able to neglect this when $W < 1$ because the lower bound to J_i ensured that each bond supported some minimum current, and we were primarily interested in showing only that the spin transport remained ballistic.

To try to gain some further insight into the nature of the strongly disordered transport, let us generalise the disorder distribution to the power-laws used in Ch. 7 (7.2),

$$p_\eta(J) = (1-\eta)J^{-\eta}, \qquad J \in [0,1], \tag{8.24}$$

with the exponent $\eta \in (-\infty, 1]$. The uniform distribution (with $W = 1$) is recovered by setting $\eta = 0$. We plot the disorder-averaged injected current as a function of time for a few

different values of η in Fig. 8.10, and observe subdiffusive regimes with different exponents $\alpha(\eta) < 1/2$, which apparently approach the diffusive limit $\alpha = 1/2$ as $\eta \to -\infty$. We do not observe superdiffusive spin transport at any η.

We do not have a full understanding of the dependence of the observed α on the disorder exponent η, but we may be able to gain some insight by assuming that the current is limited principally by the smallest coupling.

Given a sample of L couplings drawn independently from the distribution Eq. (8.24), the expected value of the minimum has the scaling

$$\overline{\min_{i=1,\ldots,L} J_i} \sim L^{-\frac{1}{1-\eta}}. \tag{8.25}$$

If we assume this represents a global bottleneck and is thus proportional to the *conductivity* (not directly the conductance), we obtain

$$G(L) \sim L^{-\frac{1}{1-\eta}-1} \quad \Rightarrow \quad \alpha = \frac{1}{2+\frac{1}{1-\eta}}, \tag{8.26}$$

which correctly returns $\alpha = 1/3$ at $\eta = 0$, and is in good agreement with the numerical simulations (Fig. 8.10), though, admittedly, the results at $\eta = 0.5$ are not entirely conclusive. Nonetheless, this appears to show that we may, by tuning the distribution of disorder, access all of the subdiffusive exponents $0 < \alpha < 1/2$.

An obvious point which we must address is the nature of the limit $\eta \to -\infty$. Eq. (8.26) claims that this limit is diffusive – but this is the clean limit, where ballistic spin transport has been clearly established.

The resolution of this apparent contradiction is in the order of limits: if the clean limit $\eta \to -\infty$ is taken *before* the thermodynamic limit $L \to \infty$, ballistic transport prevails; if this order is reversed, diffusion is approached instead. What this means, practically, is simply that, as η becomes smaller, the spin transport will appear to be ballistic for larger-and-larger system sizes – because the chance of any particular finite-size sample actually drawing a very small coupling becomes very unlikely.

We re-iterate that this non-commutativity of the limits applies to the power-law distributions (8.24); for the bounded-below uniform distributions of §8.4.1, the spin transport is truly ballistic in the thermodynamic limit.

8.5 Conclusions

Let us recapitulate what we have seen in this chapter. In this first part of our foray into non-equilibrium dynamics we have shown that we can capture, entirely classically, the phenomenology of a recent quantum mechanical experiment, and we have shown that the ballistic spin transport found in the easy-plane survives the introduction of disorder. This further illustrates one of the general points we have been making: that much of the phenomenology often ascribed to the quantum nature of spin dynamics is not, in fact, necessarily non-classical. And it demonstrates that moving away from thermal equilibrium can conjure new and qualitatively different physics – ballistic transport in a disordered model, whilst not unheard of [223], is not exactly a common expectation.

Chapter 9

Non-reciprocal periodically driven spin dynamics

The work in this chapter has appeared as part of the following article [187]:
Adam J. McRoberts, Hongzheng Zhao, Roderich Moessner, & Marin Bukov
Prethermalization in periodically-driven nonreciprocal many-body spin systems
Phys. Rev. Research **5**, 043008 (2023)

In this, the last of the main chapters of this thesis, we continue our sortie through out-of-equilibrium dynamics. Here, we will depart momentarily from the subject of transport, and consider the implications of *non-reciprocity* for spin dynamics.

Systems exhibiting non-reciprocal interactions evade Newton's third law, and are intrinsically out-of-equilibrium due to the absence of energy conservation. As an effective description of physical systems, non-reciprocity finds a plethora of applications [224], underlying flocking phenomena in active matter [225, 226], interactions between micro-particles in an anisotropic plasma [227], and the formation of active chiral matter in starfish embryos. Outwith biophysics, such interactions arise naturally in systems of colloidal particles interacting through non-reciprocal electrostatic torques, tune-able by changing either the salt concentration or the external electric field [228, 229]; moreover, non-reciprocal interactions have been shown to exhibit out-of-equilibrium phase transitions [230] and non-Hermitian topology [231], and have recently been emulated between robots in a programmable way [232].

In this chapter, we investigate the consequences of non-reciprocity for the dynamics of spin systems subject to a time-periodic drive. This question arises naturally from the main numerical method for integrating the spin dynamics that we have used in the previous chapters (see also App. A) – as, whilst it provides an excellent approximation of continuous-time spin dynamics in the limit of small time-steps, we are perfectly at liberty to investigate its dynamics at finite-frequency.

Now, Floquet-driven (periodic), *Hamiltonian*, closed, many-body systems generically feature long-lived meta-stable states in the high-frequency regime, when drive frequencies are much larger than the local bandwidth [233, 234]. For sufficiently short-ranged interactions, such systems feature exponentially long-lived prethermal plateaus, where energy

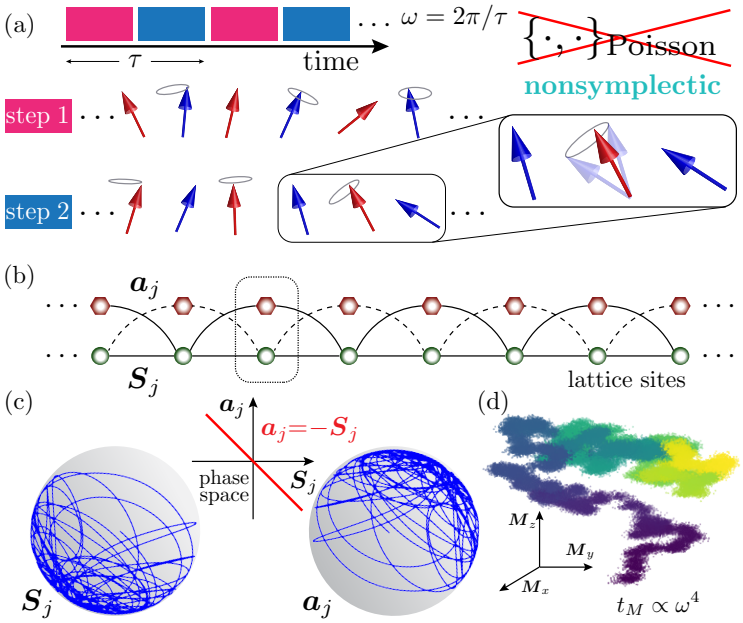

Figure 9.1: (a) An interacting non-integrable spin chain is subject to time-periodic two-step dynamics that breaks the reciprocity of the interactions and the symplectic structure of phase space. In the first half-cycle spins on one sublattice are held fixed, while the other spins precess in the exchange field of their neighbours, and vice-versa during the second half-cycle. (b) The spin chain can be embedded in a larger Hamiltonian system comprised of two interacting dynamical spin degrees of freedom $\boldsymbol{S}_j$ and $\boldsymbol{a}_j$, which restores symplecticity. (c) The initial condition $\boldsymbol{a}_j = -\boldsymbol{S}_j$ confines the phase space dynamics of the $(\boldsymbol{S}, \boldsymbol{a})$-system to a subspace for all time; the $\boldsymbol{S}$-subsystem is exactly described by the non-symplectic drive from (a). (d) The non-reciprocal drive breaks magnetisation conservation: at large drive frequencies ω, the magnetisation of an initial ensemble (shown by collection of points) exhibits a prethermal plateau whose lifetime scales as $t_M \sim \omega^4$, before it relaxes in a diffusion-like process (colour-code shows arrow of time from purple to yellow).

absorption is severely constrained and slowed down, as higher-order interaction processes are required [235–241]. Experimentally, Floquet prethermalisation has been instrumental for the realisation of novel engineered properties [242–246], such as artificial gauge fields for neutral particles [247–249]; discrete time crystalline [250–254] or topologically-ordered [255–257] phases of matter without equilibrium counterparts; as a stabilisation mechanism to create long-lived coherent dynamics [258–263]; and in providing a long time-window to realise Trotterised dynamics on digital quantum processors [264]. For all these reasons, Floquet drives offer a highly versatile toolbox; however, the extent to which *non-reciprocal* systems are amenable to Floquet engineering remains unclear [265, 266].

The combination of non-reciprocity and periodicity inherent in our spin model (9.1) provides a propitious stage to ask the fundamental question of this chapter: can non-reciprocal systems offer a suitable framework to implement ideas from Floquet engineering?

More precisely, can closed, *non-reciprocal* many-body systems, subject to a periodic, conservative (i.e., phase-space-volume-preserving) drive, exhibit long-lived prethermalisation?

We give an affirmative answer by investigating the magnetisation relaxation of a spin chain [267–274] exposed to such a drive (Fig. 9.1(a)). Unlike their Hamiltonian Floquet counterparts [268, 275], non-reciprocal periodically-driven equations of motion (EOM) cannot be derived from any time-dependent Hamiltonian, and, therefore, possess no well-defined quasi-energy. As a consequence, they cannot, *a priori*, exhibit energy prethermalisation and are not described by an effective Hamiltonian, even in the high-frequency regime.

Nevertheless, we will show that non-reciprocal time-periodic dynamics can exhibit quasi-conserved quantities which relax through a parametrically controlled long-lived prethermal plateau, the duration of which scales as the *fourth power* of the drive frequency. We derive an effective stroboscopic EOM in the high-frequency regime, by considering the spin chain as a subsystem of a larger Hamiltonian system (Fig. 9.1(b)); the leading-order inverse-frequency correction is sufficient to capture the magnetisation relaxation process (Fig. 9.1(d)). Moreover, the non-reciprocal periodic drive we investigate is quite general, and directly applicable to various classical spin models, irrespective of their dimensionality, support of interactions, and lattice geometry, and thus defines a new and distinct class of prethermal states.

9.1 Non-reciprocal spin model

We consider a bipartite lattice of interacting classical spins $\boldsymbol{S}_j$, governed by the time-periodic equations of motion:

$$\begin{cases} \dot{\boldsymbol{S}}_j^\mu = \epsilon^{\mu\nu\lambda} \left(\sum_i J_{ij}^\nu \boldsymbol{S}_i^\nu \right) \boldsymbol{S}_j^\lambda, & j \in \mathcal{A} \\ \dot{\boldsymbol{S}}_j^\mu = 0, & j \in \mathcal{B} \end{cases}; \quad \text{for } t \in \left[0, \tfrac{\tau}{2}\right), \\ \begin{cases} \dot{\boldsymbol{S}}_j^\mu = 0, & j \in \mathcal{A} \\ \dot{\boldsymbol{S}}_j^\mu = \epsilon^{\mu\nu\lambda} \left(\sum_i J_{ij}^\nu \boldsymbol{S}_i^\nu \right) \boldsymbol{S}_j^\lambda, & j \in \mathcal{B} \end{cases}; \quad \text{for } t \in \left[\tfrac{\tau}{2}, \tau\right), \tag{9.1}$$

where $J_{ij}^\nu = J_{ji}^\nu$ denotes the interaction strength[1], i, j label the lattice sites, and $\mathcal{A}, \mathcal{B}$ are the two sublattices; in all simulations, we use periodic boundary conditions.

During the first (second) half-cycle, the spins on the $\mathcal{B}$ ($\mathcal{A}$) sublattice are kept frozen, and produce an effective constant field in which their neighbouring spins precess (Fig. 9.1(a)); the roles of the two sublattices are then flipped, and the protocol repeats. Since the rotation axis depends on the neighbouring spins – the directions of which keep changing – this protocol gives rise to chaotic non-linear dynamics over many drive periods τ; the frequency of switching is $\omega = 2\pi/\tau$.

We define the infinite-frequency limit by fixing a physical time in units of J^{-1}, and solving the equations of motion up to that time as $\tau \to 0$. In this limit, averaging over a period reduces Eq. (9.1) to the continuous-time spin dynamics, $\dot{\boldsymbol{S}}_j^\mu = \{\boldsymbol{S}_j^\mu, H_\infty\}$, generated by the Hamiltonian,

$$H_\infty = \frac{1}{2} \sum_{i,j} J_{ij}^\mu \boldsymbol{S}_i^\mu \boldsymbol{S}_j^\mu. \tag{9.2}$$

[1]Despite the symmetry of the interaction coupling, $J_{ij}^\nu = J_{ji}^\nu$, the interactions between the spins are nonreciprocal during each half-step by construction.

In all cases, we assume, at least, an O(2) isotropy, $J^x_{ij} = J^y_{ij}$. The infinite-frequency dynamics is thus Hamiltonian, and conserves both the magnetisation $\boldsymbol{M}_z = \sum_j \boldsymbol{S}^z_j$ and the infinite-frequency energy H_∞. At finite frequency, H_∞ remains conserved, but the magnetisation does not.

A key feature of Eq. (9.1) is that, for finite drive frequencies, it cannot be derived from *any* Hamiltonian, time-dependent or static, since the non-reciprocity breaks the symplectic structure (App. B.1.1). Nevertheless, it is curious to note that Eq. (9.1) still preserves the phase space volume[2], and hence the dynamics remains incompressible at all frequencies.

The lack of a Hamiltonian implies that the dynamics of Eq. (9.1) is not directly amenable to Floquet theory (though see Ref. [275]). This raises two questions: (i) what are the similarities and differences between non-reciprocal and Hamiltonian Floquet systems, and (ii) how can we effectively describe their thermalising dynamics?

9.2 Long-lived meta-stable plateau

We address these questions numerically before presenting a theoretical description. We initialise the chain in a canonical ensemble at temperature β^{-1}, magnetised along the z-direction; specifically, this ensemble is thermal with respect to the Hamiltonian

$$\tilde{H} = 2H_\infty + h\sum_j \boldsymbol{S}^z_j, \tag{9.3}$$

at $h/|J| = 0.7$. We then evolve each state in the ensemble up to a sufficiently long time, and measure the expectation value (ensemble-average) of the magnetisation.

Now, since H_∞ is conserved for each state in the ensemble, the system cannot heat with respect to H_∞ – nevertheless, it can still absorb energy with respect to the Hamiltonian $\tilde{H}$ that generated the initial ensemble; this gives rise to magnetisation relaxation, and we therefore, somewhat colloquially, refer to the dynamics as "thermalising".

To quantify the rate at which this happens as a function of ω, we study the magnetisation relaxation for several spin models: the XXZ spin chain (J^x=J^y=1, J^z=Δ), for both easy-axis and easy-plane anisotropy, and the nearest-neighbour isotropic Heisenberg model (J^x=J^y=J^z=1) on the chain, square lattice, and triangular lattice. Fig. 9.2 (inset) shows the time evolution of $\langle \boldsymbol{M}_z \rangle$ for different values of the drive frequency. Despite the lack of symplecticity in Eq. (9.1), the overall behaviour appears similar to Hamiltonian-Floquet drives in the following aspect: the system first prethermalises to a frequency-dependent plateau above the infinite-frequency magnetisation value, which lasts until a time t_M, parametrically controlled by ω, when the ensemble starts approaching the $\langle \boldsymbol{M}_z \rangle = 0$ state. However, since no effective Hamiltonian exists that describes the prethermal plateau, there exists no canonical ensemble description of the state and no effective temperature can be assigned to it. Therefore, non-reciprocal prethermal states should be understood within the microcanonical ensemble as maximum-entropy states on the accessible phase-space manifold. Curiously, moreover, we observe a power-law scaling $t_M \propto \omega^\alpha$ with $\alpha = 4$, *independently of the particular spin model*. This is in stark contrast to both the exponential scaling in locally-interacting Hamiltonian-Floquet systems [268], and the $\alpha = 2$ Fermi's Golden rule

[2]The phase space volume is preserved independently during each half-cycle, and hence also by the entire dynamics.

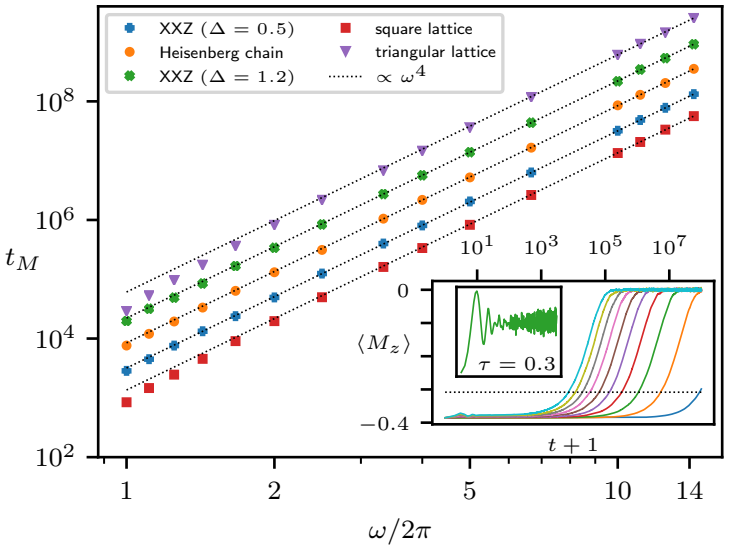

Figure 9.2: Magnetisation relaxation in the non-reciprocal drive, Eq. (9.1), occurs via a prethermal plateau whose lifetime is controlled by the drive frequency ω. The models shown are the XXZ spin chain ($J^x{=}J^y{=}1$, $J^z{=}\Delta$) and the Heisenberg model ($J^x{=}J^y{=}J^z{=}1$) on the chain, square lattice, and triangular lattice. The inset shows the relaxation curves for the Heisenberg chain for drive periods $\tau = 0.1$ (blue, rightmost) to 1.0 (cyan, leftmost), in steps of 0.1 – their intersection with the horizontal line defines t_M. The main plot shows that the relaxation timescale $t_M \sim \omega^4$ scales with the fourth power of the drive frequency (dotted lines), regardless of the particular spin model (the data have been shifted vertically to clarify the scaling). All ensemble averages are taken over 2000 initial states, at temperature $\beta = 1$ and initial applied field $h_z = 0.7$. The system size for the chains is $L = 128$, and the linear sizes for the 2D lattices are $L = 16$ (square) and $L = 15$ (triangular). The non-reciprocal drive for the triangular lattice does not follow Eq. (9.1) (it is not bipartite), but follows an analogous three-step protocol (App. B.3).

regime characteristic of long-range systems [237]. We emphasise that the proofs of rigorous upper bounds on energy absorption explicitly use the Hamiltonian formalism [233, 234, 276], and hence do not apply to non-reciprocal dynamics.

To contrast the non-reciprocal drive from its reciprocal counterpart, we can specialise to the isotropic Heisenberg chain, $H_\infty = \frac{J}{2}\sum_j \boldsymbol{S}_j \cdot \boldsymbol{S}_{j+1}$, and consider the Hamiltonian Floquet drive $H(t){=}\sum_j J_j(t)\boldsymbol{S}_j{\cdot}\boldsymbol{S}_{j+1}$ with $J_j(t){=}J/2\left[1{+}(-1)^j \mathrm{sgn}\,(\sin\omega t)\right]$. Both drives share the same infinite-frequency Hamiltonian H_∞ – at finite frequency, however, the Hamiltonian structure implies the heating timescale is exponentially suppressed (App. B.2), in accordance with the theorem of Ref. [268].

9.3 Extended Hamiltonian system

These numerical observations call for a theoretical description; we are confounded, however, by the fact that non-reciprocity precludes the description of the spin dynamics using an effective Floquet Hamiltonian. We sidestep this issue by explicitly constructing a larger, Hamiltonian (i.e., reciprocal) system, of which the original spins constitute an open, but non-dissipative, subsystem.

Each half-cycle of the dynamics governed by Eq. (9.1) can be realised in the presence of local external magnetic fields that cancel the precession of the static spins. For this to happen during both half-cycles, the external fields have to change both their direction and lattice support in time, but without simply measuring half of the spins and applying a site-dependent field (which would obviously not be a Hamiltonian); we thus need to promote them to dynamical degrees of freedom. We introduce an auxiliary spin $\boldsymbol{a}_j$ on every lattice site, with the canonical Poisson brackets $\{\boldsymbol{a}_i^\alpha, \boldsymbol{a}_j^\beta\} = \varepsilon^{\alpha\beta\gamma}\boldsymbol{a}_j^\gamma\delta_{ij}$ and $\{\boldsymbol{a}_i^\alpha, \boldsymbol{S}_j^\beta\} = 0$, cf. Fig. 9.1(b). Each $\boldsymbol{a}_j$ couples periodically to the neighbours of $\boldsymbol{S}_j$, giving rise to the Hamiltonian

$$\mathcal{H}(t) = \sum_{i,j} J_{ij}^\mu \boldsymbol{S}_i^\mu \boldsymbol{S}_j^\mu + \left[\frac{1}{2} + g(t)\mathrm{sgn}(j)\right] J_{ij}^\mu \boldsymbol{S}_i^\mu \boldsymbol{a}_j^\mu, \tag{9.4}$$

where $g(t) = \mathrm{sgn}(\sin\omega t)/2$ is, again, the τ-periodic step-drive, and $\mathrm{sgn}(j)$ takes different signs on the two sublattices.

In general, the chaotic dynamics generated by the total Hamiltonian (9.4) differs from Eq. (9.1). We will show, however, that an initial condition of the form $\boldsymbol{a}_j(0) = -\boldsymbol{S}_j(0)$ is preserved, i.e., $\boldsymbol{a}_j(t) = -\boldsymbol{S}_j(t)$, and that, under these conditions, we recover exactly the original non-reciprocal dynamics (9.1).

The Hamiltonian (9.4) sheds new light on our problem, as it allows us to think of the $\boldsymbol{S}$-spins as an open system. Note, however, that the dynamics described by Eq. (9.1) is conservative, since the Poincaré recurrence theorem is satisfied[3].

Adopting this view, we find that, for $\boldsymbol{a}_j(t) = -\boldsymbol{S}_j(t)$, the total energy of the system vanishes identically, $\mathcal{H}(t) \equiv 0$. Since the energy of the $\boldsymbol{S}$-spin subsystem is independently conserved, it follows that the energy absorbed from the periodic drive in the total system remains trapped in the interaction term between the two subsystems. Moreover, the magnetisation of the total system also vanishes identically, $\sum_j \boldsymbol{S}_j + \boldsymbol{a}_j \equiv 0$. Thus, we can interpret the slow magnetisation relaxation in the high-frequency limit as scrambling dynamics within the $\boldsymbol{M} = 0$ shell of the full system.

Let us emphasise that the specific choice of initial condition for the total system should not be viewed as fine-tuning. Indeed, we are interested in the dynamics of the $\boldsymbol{S}$-subsystem, for which the initial condition is arbitrary; the $\boldsymbol{a}$-subsystem helps us to make analytic progress in a familiar and structured way. Due to the non-linearity of the EOM generated by Eq. (9.4), we expect that small deviations from this initial condition lead to unstable dynamics that leaves the $\boldsymbol{a} = -\boldsymbol{S}$ manifold and features fundamentally different properties.

[3]One can convince oneself that both conditions for Poincaré's recurrence theorem are met for any fixed number of spins: the phase space flow is incompressible, cf. App. B.1.1 and all orbits are bounded since the spin phase space is compact.

9.3.1 Equations of motion for the extended system

Let us now show how the extended Hamiltonian (9.4) reproduces the non-reciprocal dynamics. For convenience, we specialise to the isotropic Heisenberg chain, though the derivation in the general case follows analogously. In this case, the Hamiltonian of the extended system is

$$\mathcal{H} = J\sum_j \boldsymbol{S}_j \cdot \boldsymbol{S}_{j+1} + J\sum_j \left(\frac{1}{2} + g(t)(-1)^j\right) \boldsymbol{a}_j \cdot (\boldsymbol{S}_{j-1} + \boldsymbol{S}_{j+1}). \tag{9.5}$$

We emphasise again that we do not fix the dynamics of the $\boldsymbol{a}$ spins – they evolve as unit-length spins under the above Hamiltonian dynamics with their own equations of motion, $\dot{\boldsymbol{a}} = (\partial\mathcal{H}/\partial\boldsymbol{a}) \times \boldsymbol{a}$. We will, however, impose a particular set of initial conditions. Setting $f_j(t) = \frac{1}{2} + g(t)(-1)^j$, the Hamiltonian equations of motion are:

$$\begin{aligned} \dot{\boldsymbol{S}}_j &= J\left(\boldsymbol{S}_{j-1} + \boldsymbol{S}_{j+1} + f_{j-1}(t)\boldsymbol{a}_{j-1} + f_{j+1}(t)\boldsymbol{a}_{j+1}\right) \times \boldsymbol{S}_j \\ \dot{\boldsymbol{a}}_j &= J f_j(t)(\boldsymbol{S}_{j-1} + \boldsymbol{S}_{j+1}) \times \boldsymbol{a}_j. \end{aligned} \tag{9.6}$$

We fix the initial conditions as $\boldsymbol{a}_j(0) = -\boldsymbol{S}_j(0)$. Now, over the first half-period, $0 < t < \tau/2$, we have $g(t) = +1/2$, which implies

$$\dot{\boldsymbol{a}}_j = \begin{cases} J(\boldsymbol{S}_{j-1} + \boldsymbol{S}_{j+1}) \times \boldsymbol{a}_j, & j \text{ even} \\ 0, & j \text{ odd} \end{cases} \tag{9.7}$$

and

$$\dot{\boldsymbol{S}}_j = \begin{cases} J\left(\boldsymbol{S}_{j-1} + \boldsymbol{S}_{j+1}\right) \times \boldsymbol{S}_j, & j \text{ even} \\ J\left(\boldsymbol{S}_{j-1} + \boldsymbol{S}_{j+1} + \boldsymbol{a}_{j-1} + \boldsymbol{a}_{j+1}\right) \times \boldsymbol{S}_j, & j \text{ odd} \end{cases} \tag{9.8}$$

Now, observe that for even j, $\boldsymbol{S}_j$ and $-\boldsymbol{a}_j$ have the same equation of motion with the same initial condition. Thus $\boldsymbol{S}_j(t) = -\boldsymbol{a}_j(t)$ for even j. This then implies that, for odd j, the effective field seen by $\boldsymbol{S}_j$ vanishes at all times in the half-period, and thus $\dot{\boldsymbol{S}}_j = 0$ for all odd j. The equations of motion directly establish $\dot{\boldsymbol{a}}_j = 0$ for odd j, and so the initial conditions are preserved in the sense that $\forall j,\ \forall t : \boldsymbol{S}_j(t) = -\boldsymbol{a}_j(t)$.

This argument is clearly symmetric with respect to the parity of j, and so the opposite situation holds over the next half-period. Since the initial condition is preserved throughout, the Hamiltonian (9.4) exactly reproduces the non-reciprocal drive.

9.4 Floquet-Magnus expansion and effective stroboscopic dynamics

The advantage of having derived the extended system Hamiltonian (9.4) is that it enables the application of the standard techniques of Floquet theory; in particular, let us consider the inverse-frequency expansions (IFE). For the purpose of deriving effective high-frequency EOM, it suffices to focus on the stroboscopic dynamics which governs the motion of the slow degrees of freedom. Out of the different variants, we choose the Floquet-Magnus expansion since it does not require kick operators that modify the initial conditions [4].

[4] Classically, kick operators give rise to canonical transformations that are more difficult to apply, as compared to unitary change of basis in quantum mechanics. The latter is the case for the van-Vleck expansion [243].

9.4.1 Derivation of the Floquet-Magnus Hamiltonian

Our goal here is to find the time-independent Floquet Hamiltonian $\mathcal{H}_F[t_0]$ which governs the stroboscopic dynamics of the combined system consisting of the original spins $\boldsymbol{S}$ and the auxiliary spins $\boldsymbol{a}$. Note that $\mathcal{H}_F[t_0]$ depends explicitly on the initial choice for the phase of the drive or, equivalently, on the initial time t_0, and we keep track of this dependence below.

Now, using the Floquet-Magnus expansion [243], we can construct the Floquet Hamiltonian as a series in the drive-period τ:

$$\mathcal{H}_F[t_0] = \sum_{n=0}^{\infty} \mathcal{H}_F^{(n)}[t_0], \tag{9.9}$$

where the superscript (n) means $\mathcal{H}_F^{(n)} \propto \mathcal{O}(\tau^n) = \mathcal{O}(\omega^{-n})$. The lowest-order contributions to the Floquet Hamiltonian are, explicitly,

$$\mathcal{H}_F^{(0)} = \frac{1}{1!\tau}\int_{t_0}^{\tau+t_0} dt_1 H(t_1) \equiv \mathcal{H}_0 \tag{9.10}$$

$$\mathcal{H}_F^{(1)}[t_0] = \frac{1}{2!\tau}\int_{t_0}^{\tau+t_0} dt_1 \int_{t_0}^{t_1} dt_2 \{H(t_1), H(t_2)\} \tag{9.11}$$

$$\mathcal{H}_F^{(2)}[t_0] = \frac{1}{3!\tau}\int_{t_0}^{\tau+t_0} dt_1 \int_{t_0}^{t_1} dt_2 \int_{t_0}^{t_2} dt_3 \Big(\{H(t_1), \{H(t_2), H(t_3)\}\} + \{H(t_3), \{H(t_2), H(t_1)\}\} \Big). \tag{9.12}$$

The zeroth-order term is the period-averaged Hamiltonian, and includes static interactions between the original and the auxiliary spins. In the subsequent discussion, it will be convenient to separate out the time-averaged term $\mathcal{H}_0$ and the time-dependent term $\mathcal{V}$,

$$\begin{aligned}\mathcal{H}(t) &= J\sum_j \left[\boldsymbol{S}_j \cdot \boldsymbol{S}_{j+1} + \frac{1}{2}\boldsymbol{a}_j \cdot (\boldsymbol{S}_{j-1} + \boldsymbol{S}_{j+1}) \right] + g(t) J \sum_j (-1)^j \boldsymbol{a}_j \cdot (\boldsymbol{S}_{j-1} + \boldsymbol{S}_{j+1}) \\ &= \mathcal{H}_0 + g(t)\mathcal{V}. \end{aligned} \tag{9.13}$$

The explicit time-dependence is now only carried by the function $g(t)$, and the first-order term becomes

$$\mathcal{H}_F^{(1)}[t_0] = \frac{1}{2!\tau}\int_{t_0}^{\tau+t_0} dt_1 \int_{t_0}^{t_1} dt_2 \left(g(t_1) - g(t_2)\right) \{\mathcal{V}, \mathcal{H}_0\} = \left(\frac{t_0}{2} - \frac{\tau}{8}\right) \{\mathcal{V}, \mathcal{H}_0\}. \tag{9.14}$$

A straightforward calculation yields the required Poisson bracket,

$$\{\mathcal{V}, \mathcal{H}_0\} = J^2 \sum_j (-1)^j \varepsilon^{\mu\nu\lambda} \left(\boldsymbol{a}_j^{\mu} + \boldsymbol{a}_{j-2}^{\mu}\right) \left(\boldsymbol{S}_j^{\nu} + \boldsymbol{S}_{j-2}^{\nu}\right) \boldsymbol{S}_{j-1}^{\lambda}. \tag{9.15}$$

Rewriting this in terms of dot and cross products, and shifting some site labels, we arrive at the first-order term,

$$\mathcal{H}_F^{(1)}[t_0] = \left(\frac{t_0}{2} - \frac{\tau}{8}\right) J^2 \sum_j (-1)^j \boldsymbol{a}_j \cdot \left[(\boldsymbol{S}_j + \boldsymbol{S}_{j-2}) \times \boldsymbol{S}_{j-1} + (\boldsymbol{S}_{j+2} + \boldsymbol{S}_j) \times \boldsymbol{S}_{j+1} \right], \tag{9.16}$$

which contains $\boldsymbol{a}_j$-mediated nearest-neighbour interactions between the spins $\boldsymbol{S}_j$, and breaks time-reversal symmetry.

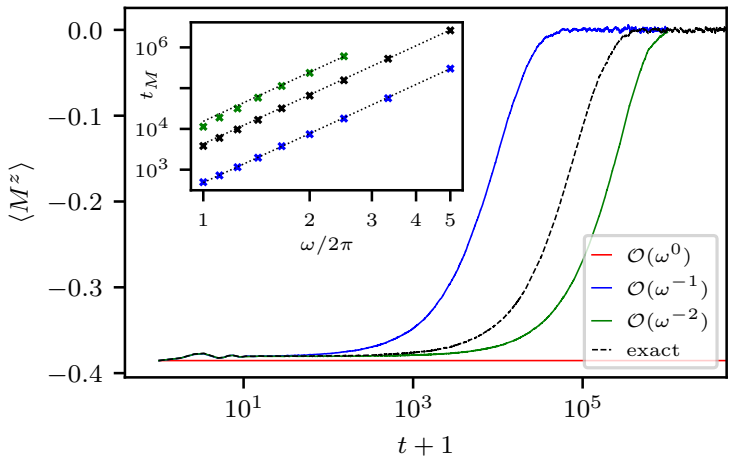

Figure 9.3: Comparison between the effective stroboscopic dynamics and the exact dynamics in the isotropic Heisenberg chain. Main figure shows the magnetisation dynamics within the first three orders of the inverse-frequency expansion (IFE): $\boldsymbol{M}_z$ is conserved at zeroth-order; the first-order curve relaxes faster than the exact curve; whilst the second-order curve takes longer, hinting at a possible oscillatory convergence. Even at first-order, the IFE captures the short-time quenched dynamics that drives the state into the 'prethermal' plateau. The inset shows that the power-law scaling of the relaxation time, $t_M \sim \omega^4$, (dotted lines) is also captured at first-order in the IFE. Simulation parameters are the same as in Fig. 9.2, with $\beta = 1$. The curves in the main figure correspond to $\tau = 0.8$.

9.4.2 Effective Stroboscopic Dynamics

Now that we have it, the Floquet-Magnus Hamiltonian permits the derivation of the effective stroboscopic equations of motion. At first-order, and fixing the Floquet-gauge by setting $t_0 = 0$, we have

$$\begin{aligned}\dot{\boldsymbol{a}}_j &= \frac{\partial \mathcal{H}_F^{(0)}}{\partial \boldsymbol{a}_j} \times \boldsymbol{a}_j + \frac{\partial \mathcal{H}_F^{(1)}}{\partial \boldsymbol{a}_j} \times \boldsymbol{a}_j \\ &= \Big(\frac{J}{2} \left(\boldsymbol{S}_{j-1} + \boldsymbol{S}_{j+1} \right) - \frac{\tau J^2}{8} (-1)^j \Big[\left(\boldsymbol{S}_j + \boldsymbol{S}_{j-2} \right) \times \boldsymbol{S}_{j-1} + \left(\boldsymbol{S}_{j+2} + \boldsymbol{S}_j \right) \times \boldsymbol{S}_{j+1} \Big] \Big) \times \boldsymbol{a}_j . \end{aligned} \tag{9.17}$$

Then, using the condition $\boldsymbol{a}_j(t) = -\boldsymbol{S}_j(t)$, we find

$$\dot{\boldsymbol{S}}_j = \frac{J}{2} \left(\boldsymbol{S}_{j-1} + \boldsymbol{S}_{j+1} \right) \times \boldsymbol{S}_j + \frac{\tau J^2}{8} (-1)^j \Big[\left(\boldsymbol{S}_j + \boldsymbol{S}_{j-2} \right) \times \boldsymbol{S}_{j-1} + \left(\boldsymbol{S}_{j+2} + \boldsymbol{S}_j \right) \times \boldsymbol{S}_{j+1} \Big] \times \boldsymbol{S}_j . \tag{9.18}$$

Showing that the initial condition $\boldsymbol{a}_j(0) = -\boldsymbol{S}_j(0)$ is conserved by the effective dynamics is a simple matter of deriving the general equation of motion for the $\boldsymbol{S}$-spins directly, and checking that we obtain the same effective equation of motion (9.18). We have, to first

order,

$$\begin{aligned}\dot{\boldsymbol{S}}_j &= \frac{\partial \mathcal{H}_F^{(0)}}{\partial \boldsymbol{S}_j} \times \boldsymbol{S}_j + \frac{\partial \mathcal{H}_F^{(1)}}{\partial \boldsymbol{S}_j} \times \boldsymbol{S}_j \\ &= \Big(J\left(\boldsymbol{S}_{j-1} + \boldsymbol{S}_{j+1}\right) + \frac{J}{2}\left(\boldsymbol{a}_{j-1} + \boldsymbol{a}_{j+1}\right) + \frac{\tau J^2}{8}(-1)^j \Big[\left(\boldsymbol{a}_j + \boldsymbol{a}_{j-2}\right) \times \boldsymbol{S}_{j-1} \\ &\qquad + \left(\boldsymbol{a}_{j+2} + \boldsymbol{a}_j\right) \times \boldsymbol{S}_{j+1} + \left(\boldsymbol{a}_{j+1} + \boldsymbol{a}_{j-1}\right) \times + \left(\boldsymbol{S}_{j+1} + \boldsymbol{S}_{j-1}\right) \Big] \Big) \times \boldsymbol{S}_j, \end{aligned} \tag{9.19}$$

which, upon inserting the condition $\boldsymbol{a}_j = -\boldsymbol{S}_j$, may be readily seen to reduce to the same effective equation of motion, Eq. (9.18).

In a similar manner, we derive the second-order contribution to the Floquet-Hamiltonian, $\mathcal{H}_F^{(2)}$. Setting $t_0 = 0$, the effective equations of motion are, to second-order,

$$\begin{aligned}\dot{\boldsymbol{S}}_j &= \frac{J}{2}\left(\boldsymbol{S}_{j-1} + \boldsymbol{S}_{j+1}\right) \times \boldsymbol{S}_j \\ &\quad - \frac{J^2\tau}{8}(-1)^j \left[\left(\boldsymbol{S}_j + \boldsymbol{S}_{j-2}\right) \times \boldsymbol{S}_{j-1} + \left(\boldsymbol{S}_j + \boldsymbol{S}_{j+2}\right) \times \boldsymbol{S}_{j+1}\right] \times \boldsymbol{S}_j \\ &\quad + \frac{J^3\tau^2}{96}\Big(2\left[\boldsymbol{S}_{j-1} \cdot \boldsymbol{S}_{j-2}\right]\ \boldsymbol{S}_{j-3} \\ &\qquad\qquad + \left[\boldsymbol{S}_{j-1} \cdot \left(\boldsymbol{S}_{j+1} + \boldsymbol{S}_j + \boldsymbol{S}_{j-2} - 2\boldsymbol{S}_{j-3}\right) - 1\right] \boldsymbol{S}_{j-2} \\ &\qquad\qquad + \left[\boldsymbol{S}_j \cdot \left(\boldsymbol{S}_{j+1} + \boldsymbol{S}_{j-1} - \boldsymbol{S}_{j-2}\right) + \boldsymbol{S}_{j-2} \cdot \left(\boldsymbol{S}_{j-1} - \boldsymbol{S}_{j+1}\right) - 2\right] \boldsymbol{S}_{j-1} \\ &\qquad\qquad + \left[\boldsymbol{S}_j \cdot \left(\boldsymbol{S}_{j-1} + \boldsymbol{S}_{j+1} - \boldsymbol{S}_{j+2}\right) + \boldsymbol{S}_{j+2} \cdot \left(\boldsymbol{S}_{j+1} - \boldsymbol{S}_{j-1}\right) - 2\right] \boldsymbol{S}_{j+1} \\ &\qquad\qquad + \left[\boldsymbol{S}_{j+1} \cdot \left(\boldsymbol{S}_{j-1} + \boldsymbol{S}_j + \boldsymbol{S}_{j+2} - 2\boldsymbol{S}_{j+3}\right) - 1\right] \boldsymbol{S}_{j+2} \\ &\qquad\qquad + \left[2\boldsymbol{S}_{j+1} \cdot \boldsymbol{S}_{j+2}\right]\ \boldsymbol{S}_{j+3} \Big) \times \boldsymbol{S}_j \\ &\quad + \mathcal{O}(\tau^3). \end{aligned} \tag{9.20}$$

As expected, the zeroth-order term corresponds to the time-averaged Heisenberg dynamics, Eq. (9.2). More interestingly, the first-order terms $(\boldsymbol{S}_j \times \boldsymbol{S}_{j\pm1}) \times \boldsymbol{S}_j$ represent non-Hamiltonian corrections; they cannot be derived from any $\boldsymbol{S}$-subsystem Hamiltonian H_{eff} via $\frac{\partial H_{\text{eff}}}{\partial \boldsymbol{S}_j} \times \boldsymbol{S}_j$. To see this, note that for a term of the form

$$\dot{\boldsymbol{S}} = (\boldsymbol{S} \times \boldsymbol{h}) \times \boldsymbol{S} + ... \tag{9.21}$$

to arise from Hamilton's equations, $\dot{\boldsymbol{S}} = \frac{\partial H}{\partial \boldsymbol{S}} \times \boldsymbol{S}$, would require a Hamiltonian H containing a term K such that

$$\frac{\partial K}{\partial S^\mu} = \epsilon^{\mu\nu\lambda} S^\nu h^\lambda. \tag{9.22}$$

Up to an irrelevant constant, such a K would have to be quadratic in $\boldsymbol{S}$ and linear in $\boldsymbol{h}$, for which the most generic possibility is

$$K = A^{\mu\nu\lambda} S^\mu S^\nu h^\lambda, \tag{9.23}$$

for some arbitrary rank-3 tensor A. But now we obtain

$$\frac{\partial K}{\partial S^\mu} = (A^{\mu\nu\lambda} + A^{\nu\mu\lambda}) S^\nu h^\lambda, \tag{9.24}$$

and since $A^{\mu\nu\lambda}+A^{\nu\mu\lambda} = \epsilon^{\mu\nu\lambda}$ is a contradiction, we conclude that such terms as (9.21) cannot be obtained from a Hamiltonian, and, thus, the symplectic structure is already broken at leading order in ω^{-1}. On the other hand, at least up to second order, the effective dynamics conserves the infinite-frequency energy H_∞. Since the exact dynamics also conserves H_∞, we conjecture that this is true at all orders in inverse-frequency.

However, magnetisation conservation is broken by the $\mathcal{O}(\omega^{-1})$ terms. Fig. 9.3 shows a comparison between the exact and effective dynamics up to and including $\mathcal{O}(\omega^{-2})$. Note that magnetisation relaxation, including the prethermal plateau, is already captured by the $\mathcal{O}(\omega^{-1})$ terms; this contrasts with energy relaxation in Hamiltonian-Floquet systems, where the effective dynamics does not capture heating to infinite temperature at any order [277], and the Floquet-Magnus expansion diverges [234].

Curiously, we find that the $\mathcal{O}(\omega^{-1})$ dynamics relaxes the magnetisation faster than the exact dynamics. This is peculiar, since taking into account all higher-order corrections (i.e., considering the exact dynamics) adds more long-range and multi-body terms to the effective EOM, which one would expect to lead to faster relaxation.

At the same time, our analysis reveals that the scaling of the relaxation time is $t_M \sim \omega^4$ in both the first- and second-order effective EOM (Fig. 9.3(inset)); the differences in relaxation times are, therefore, caused by some non-universal truncation-order-dependent prefactor $c^{(n)}$: $t_M^{(n)} = c^{(n)}\omega^4$. Moreover, the observation that the second-order dynamics leads to magnetisation relaxation that is slower than the exact dynamics hints at the possibility of an oscillatory convergence to the exact magnetisation curve as we include higher-order terms of the IFE [5].

We mention that a Hamiltonian description is not required to derive the effective EOM (see App. B.1.2). We have independently derived Eq. (9.18) by using two-times perturbation theory and the phase-space density approach. We believe that an alternative Lagrangian description exists as well [278].

9.4.3 Origin of the exponent

The origin of the particular exponent, $\alpha = 4$, governing the prethermal lifetime remains unclear; we do know, however, that it cannot arise perturbatively from the IFE. One might consider a Fermi's golden rule-type argument, where, at high-frequency, the corrections play the role of a weak $\boldsymbol{S}$-magnetisation breaking perturbation, but since we have $\mathcal{O}(\omega^{-1})$ corrections, this would give a magnetisation relaxation rate $\Gamma_M \sim (\omega^{-1})^2$, the inverse of which defines the prethermal lifetime (and, indeed, this *is* the heating rate observed in long range interacting Hamiltonian-Floquet systems [237]).

One might object that the corrections depend on the Floquet gauge – the initial time t_0 – and instead consider the van Vleck IFE [243], which is manifestly t_0-independent. For a linearly polarised, real-valued Hamiltonian $\mathcal{H}(t)$, a straightforward calculation shows that the $\mathcal{O}(\omega^{-1})$ terms vanish, and hence $\mathcal{H}_{\text{eff}} \sim \mathcal{H}_{\text{eff}}^{(0)} + \mathcal{H}_{\text{eff}}^{(2)}$ (another way of seeing this is to note that there is a time $t_0 = \tau/4$ for which $\mathcal{H}_F^{(1)}[t_0] = 0$); this would appear to resolve the issue.

This perturbative argument, however, cannot be correct; it is contradicted by the tripartite non-reciprocal drive for the triangular lattice model (cf. Fig. 9.2). This drive manifestly

[5] Fewer data points are available at second-order, since the slower relaxation makes determining t_M infeasible for $\omega/2\pi \gtrsim 3$ over the accessible timescales $t \sim 10^6$.

breaks time-reversal symmetry, which implies a non-vanishing correction $\mathcal{H}_{\text{eff}}^{(1)} \in \mathcal{O}(\omega^{-1})$ (see App. B.3 for the explicit proof). Regardless, the ω^4-scaling is unambiguously evinced.

9.5 Discussion and Outlook

Let us take stock. In this chapter, we have identified a novel class of prethermalising dynamics in classical, periodically-driven spin systems, characterised by conservative, non-reciprocal chaotic dynamics; the systems we have studied thus differ from conventional periodically-driven *dissipative* systems. The long-time behaviour of the magnetisation dynamics features a prethermal plateau, whose lifetime scales as the fourth power of the drive frequency. By considering the spins to be part of a larger system, we have derived an approximate description for the effective dynamics using the inverse-frequency expansion, which captures this magnetisation relaxation.

Our extended model $\mathcal{H}(t)$ could be viewed as an example of non-ergodic scarred dynamics [279–282] in classical many-body systems: the attainable phase space of the total $(\boldsymbol{S}, \boldsymbol{a})$-system is constrained via the initial condition for all time (Fig. 9.1(c)). An intriguing future direction may be to explore the information spreading in such constrained systems [166, 283–286]. Other interesting directions that go beyond the strict periodicity of the drive include generalisations to random multi-polar driving and quasi-periodic extensions [239, 287–289].

Further, our analysis is, of course, directly related to classical ODE solvers designed to conserve integrals of motion exactly, and of which we have made extensive use throughout this thesis. Prethermalisation establishes the parametric stability of symplectic integrators [290, 291], which conserve certain quantities exactly [292]; however, energy conservation is usually lost [293]. While non-symplectic, energy-conserving integration schemes can be implemented instead [294], the analysis of their stability is confounded by the absence of conjugate variables and Poisson brackets – conventionally required to apply the high-frequency expansion in the analysis of higher-order heating processes. Similar to recent work on Floquet Trotterisation in quantum systems [264], the analysis of prethermal plateaus can improve the techniques for simulating equations of motion, which has allowed us to probe the hydrodynamic regimes of these systems with simulations of larger systems and longer times than would otherwise be practicable.

Finally, we have demonstrated that Floquet engineering can be used beyond Hamiltonian systems. Particularly interesting in this context is the possibility to suppress leading-order non-Hamiltonian corrections using model parameters, and engineer quasi-conservation laws in non-reciprocal dynamical systems. This sheds new light on the applicability of the Floquet toolbox to, e.g., biophysics, where systems without a Hamiltonian description are abundant.

Epilogue

For the sake of symmetry, if nothing else, it may be useful to very briefly re-summarise the content of the thesis all at once.

We began, in Part I, with the topic of solitons, where we showed that a non-integrable spin chain – and the simplest interacting spin model – harbours a family of apparently perfectly stable solitary excitations, despite there being no obvious protection afforded by either integrability or topology. We showed also, by considering the spreading of domain walls in an anisotropic spin chain, that a striking co-existence of linear and non-linear phenomena results in an apparent instability to soliton production.

We argued that these solitons have hydrodynamic consequences in Part II, where we showed that anomalous spin hydrodynamics – superdiffusion – can persist in the classical Heisenberg chain for enormously large time-scales.

After reviewing some mechanisms of subdiffusion, we analysed a bond-disordered Heisenberg chain in Part III, finding a tune-able subdiffusive exponent, and showing, again, that corrections to the asymptotic regimes often leave strong imprints for large time-scales, and must be captured if the physics are to be adequately described.

In Part IV, we left the thermal ensemble behind, and studied another example of a classical model exhibiting the same phenomenology as a quantum model – with both ballistic and subdiffusive spin transport accessible in the non-equilibrium steady state. We then examined the consequences of non-reciprocity, finding a new class of prethermal state in periodically-driven spin systems.

What links all of this together is that, out of the relative simplicity of the systems we have studied, exciting and unexpected phenomena emerge. Solitons, in a non-integrable lattice model, are stable without any of their usual protections; the simplest possible spin chain exhibits anomalous hydrodynamics that was expected only if integrability was intact, and for time-scales $t \sim 10^{15} J^{-1}$ at the temperatures we have probed. Corrections to the asymptotic scaling can make a disordered spin chain appear to be subdiffusive at finite time; a prethermal plateau can exist outside of Hamiltonian-Floquet dynamics. And all of the non-equilibrium transport regimes in a driven quantum spin chain can be reproduced classically.

If I might be permitted to make a personal reflection, almost everything I have tested thinking it would be generic has thrown up some unexpected or anomalous phenomenon. The very simplest settings can still be surprising. Many-body dynamics will, doubtless, reveal many more surprises in future.

Acknowledgements

I wish to end (well, the appendices follow, so there goes that idea) with notes of gratitude to those who have had some hand in my getting to this point.

I must admit that I am not particularly good at writing such reflective paragraphs as these. I fear I oft have the tendency to be a somewhat reserved fellow – emotions are dangerous things, after all, and rather than face them directly I am wont to drown them in quite sesquipedalian prose.

Nevertheless, I shall try to be blunt. Doubtless I shall only partially succeed.

I should first thank my supervisor, Roderich Moessner, for his expert guidance in scientific matters, and without whom I would not have produced any of the substance of this thesis. My thanks are also due to all of the collaborators, both at PKS and elsewhere, with whom I have had the pleasure of working: Masud Haque, Thomas Bilitewski, Debanjan Chowdhury, Felipe Méndez-Valderrama, Federico Balducci, Antonello Scardicchio, Marin Bukov, Hongzheng Zhao; and to various other collaborators and interlocutors, Owen Benton, Pieter Claeys, Benoît Douçot, Dmitry Kovrizhin, and Chris Hooley, and my most immediate contemporaries in Benedikt Placke, Jonathan Hallén, and Philippe Suchsland, among others.

Particular thanks are due to Anna Burger, for her invaluable help in navigating the vagaries of the TU Dresden administration, and without whom, it often feels, PKS might cease to function.

Though it is a cliché, I must record heartfelt thanks to those who have believed in me the longest – Mum, Dad, Lucy, and Molly. And Granny and Granda, and Grandma and Granddad, and I won't continue the list because it will go on for quite some time. Though I have just remembered the day my high school physics teacher Mr. Smith spent five hours driving me back and forth to St Andrews to complete my advanced higher project. It's strange the way memories sometimes bubble up, I suppose.

Alas, four years is far too short a time to spend among such excellent and admirable friends as I have met here; with whom I have been fortunate to enjoy both physics and the lack-of-physics, and whom I hesitate now to name for fear that one shall slip the page. I trust and hope those whom I count as friends know I hold them in such regard.

I did say I would fail to be blunt. But anyone who has read thus far must by now realise I am incapable of personal writing that does not descend into self-indulgent elegiacs. This moment feels at once both strange and familiar, as I am reminded of the time I left St Andrews and Scotland for Dresden. Now it must be done again.

The Road goes ever on and on.

Bibliography

[1] S. Coleman, New Phenomena in Subnuclear Physics: Part A , 297 (1977).

[2] J. S. Russell, Report of the fourteenth meeting of the British Association for the Advancement of Science held at York in September 1844 , 311 (1845).

[3] D. J. Korteweg and G. De Vries, The London, Edinburgh, and Dublin Philosophical Magazine and Journal of Science **39**, 422 (1895).

[4] H. Bazin, CR Séances Acad. Science. Paris **55**, 353 (1862).

[5] J. Boussinesq, CR Acad. Science. Paris **72**, 755 (1871).

[6] L. Rayleigh, Philosophical Magazine **Series 5, 1 (4)**, 257 (1876).

[7] J. V. Boussinesq, *Essai sur la théorie des eaux courantes* (Impr. nationale, 1877).

[8] T. Giamarchi, *Quantum physics in one dimension*, Vol. 121 (Clarendon press, 2003).

[9] L. Takhtajan, Physics Letters A **64**, 235 (1977).

[10] L. Faddeev and L. Takhtajan, *Hamiltonian Methods in the Theory of Solitons* (Springer, 1987).

[11] M. Toda, Journal of the Physical Society of Japan **22**, 431 (1967).

[12] M. Henón, Phys. Rev. B **9**, 1921 (1974).

[13] H. Flaschka, Phys. Rev. B **9**, 1924 (1974).

[14] G. Berman and F. Izrailev, Chaos: An Interdisciplinary Journal of Nonlinear Science **15** (2005).

[15] Y. Ishimori, Journal of the Physical Society of Japan **51**, 3417 (1982).

[16] N. Theodorakopoulos, Phys. Rev. B **52**, 9507 (1995).

[17] N. Theodorakopoulos, Physics Letters A **130**, 249 (1988).

[18] E. K. Sklyanin, Journal of Soviet Mathematics **40**, 93 (1988).

[19] E. K. Sklyanin, Functional Analysis and Its Applications **16**, 263 (1982).

[20] T. Prosen and B. Žunkovič, Phys. Rev. Lett. **111**, 040602 (2013).

[21] B. Doyon, SciPost Physics Lecture Notes , 018 (2020).

[22] H. Spohn, arXiv:2301.08504 (2023).

[23] S. Flach and A. V. Gorbach, Physics Reports **467**, 1 (2008).

[24] A. J. McRoberts, T. Bilitewski, M. Haque, and R. Moessner, Phys. Rev. E **106**, L062202 (2022).

[25] R. W. Gerling and D. P. Landau, Phys. Rev. Lett. **63**, 812 (1989).

[26] R. W. Gerling and D. P. Landau, Phys. Rev. B **42**, 8214 (1990).

[27] M. Böhm, R. W. Gerling, and H. Leschke, Phys. Rev. Lett. **70**, 248 (1993).

[28] N. Srivastava, J.-M. Liu, V. Viswanath, and G. Müller, Journal of Applied Physics **75**, 6751 (1994).

[29] V. Oganesyan, A. Pal, and D. A. Huse, Phys. Rev. B **80**, 115104 (2009).

[30] D. Bagchi, Phys. Rev. B **87**, 075133 (2013).

[31] P. Glorioso, L. V. Delacrétaz, X. Chen, R. M. Nandkishore, and A. Lucas, SciPost Phys. **10**, 15 (2021).

[32] G. Müller, Phys. Rev. Lett. **60**, 2785 (1988).

[33] O. F. de Alcantara Bonfim and G. Reiter, Phys. Rev. Lett. **69**, 367 (1992).

[34] O. F. de Alcantara Bonfim and G. Reiter, Phys. Rev. Lett. **70**, 249 (1993).

[35] J. De Nardis, M. Medenjak, C. Karrasch, and E. Ilievski, Phys. Rev. Lett. **124**, 210605 (2020).

[36] A. J. McRoberts, T. Bilitewski, M. Haque, and R. Moessner, Phys. Rev. B **105**, L100403 (2022).

[37] A. J. McRoberts, T. Bilitewski, M. Haque, and R. Moessner, arXiv:2306.15351 (2023).

[38] T. Antal, Z. Rácz, A. Rákos, and G. M. Schütz, Phys. Rev. E **59**, 4912 (1999).

[39] V. Hunyadi, Z. Rácz, and L. Sasvári, Phys. Rev. E **69**, 066103 (2004).

[40] D. Gobert, C. Kollath, U. Schollwöck, and G. Schütz, Phys. Rev. E **71**, 036102 (2005).

[41] T. Antal, P. L. Krapivsky, and A. Rákos, Phys. Rev. E **78**, 061115 (2008).

[42] J. Lancaster and A. Mitra, Phys. Rev. E **81**, 061134 (2010).

[43] J. Mossel and J.-S. Caux, New Journal of Physics **12**, 055028 (2010).

[44] L. F. Santos and A. Mitra, Phys. Rev. E **84**, 016206 (2011).

[45] T. Sabetta and G. Misguich, Phys. Rev. B **88**, 245114 (2013).

[46] V. Eisler and Z. Rácz, Phys. Rev. Lett. **110**, 060602 (2013).

[47] V. Eisler, Phys. Rev. Lett. **111**, 080402 (2013).

[48] V. Alba and F. Heidrich-Meisner, Phys. Rev. B **90**, 075144 (2014).

[49] J. Viti, J.-M. Stéphan, J. Dubail, and M. Haque, EPL (Europhysics Letters) **115**, 40011 (2016).

[50] J. L. Lancaster, Phys. Rev. E **93**, 052136 (2016).

[51] B. Bertini, M. Collura, J. De Nardis, and M. Fagotti, Phys. Rev. Lett. **117**, 207201 (2016).

[52] J.-M. Stéphan, Journal of Statistical Mechanics: Theory and Experiment **2017**, 103108 (2017).

[53] M. Ljubotina, M. Žnidarič, and T. Prosen, Journal of Physics A: Mathematical and Theoretical **50**, 475002 (2017).

[54] A. L. de Paula, H. Bragança, R. G. Pereira, R. C. Drumond, and M. C. O. Aguiar, Phys. Rev. B **95**, 045125 (2017).

[55] L. Vidmar, D. Iyer, and M. Rigol, Phys. Rev. X **7**, 021012 (2017).

[56] M. Ljubotina, M. Žnidarič, and T. Prosen, Nature Communications **8** (2017), 10.1038/ncomms16117.

[57] G. Misguich, K. Mallick, and P. L. Krapivsky, Phys. Rev. B **96**, 195151 (2017).

[58] M. Collura, A. De Luca, and J. Viti, Phys. Rev. B **97**, 081111 (2018).

[59] G. Misguich, N. Pavloff, and V. Pasquier, SciPost Phys. **7**, 025 (2019).

[60] V. B. Bulchandani and C. Karrasch, Phys. Rev. B **99**, 121410 (2019).

[61] J.-M. Stéphan, SciPost Phys. **6**, 057 (2019).

[62] M. Ljubotina, M. Žnidarič, and T. Prosen, Phys. Rev. Lett. **122**, 210602 (2019).

[63] M. Gruber and V. Eisler, Phys. Rev. B **99**, 174403 (2019).

[64] H. Moriya, R. Nagao, and T. Sasamoto, Journal of Statistical Mechanics: Theory and Experiment **2019**, 063105 (2019).

[65] M. Collura, A. De Luca, P. Calabrese, and J. Dubail, Phys. Rev. B **102**, 180409 (2020).

[66] V. Alba, B. Bertini, M. Fagotti, L. Piroli, and P. Ruggiero, Journal of Statistical Mechanics: Theory and Experiment **2021**, 114004 (2021).

[67] V. B. Bulchandani, S. Gopalakrishnan, and E. Ilievski, Journal of Statistical Mechanics: Theory and Experiment **2021**, 084001 (2021).

[68] J.-M. Stéphan, Journal of Physics A: Mathematical and Theoretical **55**, 204003 (2022).

[69] S. Scopa, P. Calabrese, and J. Dubail, SciPost Phys. **12**, 207 (2022).

[70] S. Scopa and D. Karevski, The European Physical Journal Special Topics (2023), 10.1140/epjs/s11734-023-00845-1.

[71] V. Eisler, F. Maislinger, and H. G. Evertz, SciPost Phys. **1**, 014 (2016).

[72] M. Kormos, SciPost Phys. **3**, 020 (2017).

[73] V. Eisler and F. Maislinger, Phys. Rev. B **98**, 161117 (2018).

[74] M. Medenjak and J. De Nardis, Phys. Rev. B **101**, 081411 (2020).

[75] V. Eisler and F. Maislinger, SciPost Phys. **8**, 037 (2020).

[76] J. Lancaster, E. Gull, and A. Mitra, Phys. Rev. B **82**, 235124 (2010).

[77] E. Langmann, J. L. Lebowitz, V. Mastropietro, and P. Moosavi, Communications in Mathematical Physics **349**, 551 (2016).

[78] D. X. Horváth, S. Sotiriadis, M. Kormos, and G. Takács, SciPost Phys. **12**, 144 (2022).

[79] O. Gamayun, Y. Miao, and E. Ilievski, Phys. Rev. B **99**, 140301 (2019).

[80] F. Balducci, A. Gambassi, A. Lerose, A. Scardicchio, and C. Vanoni, Phys. Rev. Lett. **129**, 120601 (2022).

[81] F. Balducci, A. Gambassi, A. Lerose, A. Scardicchio, and C. Vanoni, Phys. Rev. B **107**, 024306 (2023).

[82] B. Derrida and A. Gerschenfeld, Journal of Statistical Physics **136**, 1 (2009).

[83] M. Kardar, G. Parisi, and Y.-C. Zhang, Phys. Rev. Lett. **56**, 889 (1986).

[84] D. Wei, A. Rubio-Abadal, B. Ye, F. Machado, J. Kemp, K. Srakaew, S. Hollerith, J. Rui, S. Gopalakrishnan, N. Y. Yao, I. Bloch, and J. Zeiher, Science **376**, 716 (2022).

[85] A. Scheie, N. E. Sherman, M. Dupont, S. E. Nagler, M. B. Stone, G. E. Granroth, J. E. Moore, and D. A. Tennant, Nature Physics **17**, 726 (2021).

[86] H. Castella, X. Zotos, and P. Prelovšek, Phys. Rev. Lett. **74**, 972 (1995).

[87] P. Calabrese and J. Cardy, Journal of Statistical Mechanics: Theory and Experiment **2005**, P04010 (2005).

[88] T. Prosen, Phys. Rev. Lett. **106**, 217206 (2011).

[89] R. G. Pereira, V. Pasquier, J. Sirker, and I. Affleck, Journal of Statistical Mechanics: Theory and Experiment **2014**, P09037 (2014).

[90] E. Ilievski, J. De Nardis, B. Wouters, J.-S. Caux, F. H. L. Essler, and T. Prosen, Phys. Rev. Lett. **115**, 157201 (2015).

[91] O. A. Castro-Alvaredo, B. Doyon, and T. Yoshimura, Phys. Rev. X **6**, 041065 (2016).

[92] E. Ilievski, M. Medenjak, T. Prosen, and L. Zadnik, Journal of Statistical Mechanics: Theory and Experiment **2016**, 064008 (2016).

[93] V. Alba and P. Calabrese, Proceedings of the National Academy of Sciences **114**, 7947 (2017).

[94] E. Ilievski and J. De Nardis, Phys. Rev. Lett. **119**, 020602 (2017).

[95] B. Bertini, F. Heidrich-Meisner, C. Karrasch, T. Prosen, R. Steinigeweg, and M. Žnidarič, Rev. Mod. Phys. **93**, 025003 (2021).

[96] S. Gopalakrishnan and R. Vasseur, Reports on Progress in Physics **86**, 036502 (2023).

[97] S. Gopalakrishnan, D. A. Huse, V. Khemani, and R. Vasseur, Phys. Rev. B **98**, 220303 (2018).

[98] A. Nahum, S. Vijay, and J. Haah, Phys. Rev. X **8**, 021014 (2018).

[99] C. W. von Keyserlingk, T. Rakovszky, F. Pollmann, and S. L. Sondhi, Phys. Rev. X **8**, 021013 (2018).

[100] A. Saenz, C. A. Tracy, and H. Widom, "Domain walls in the heisenberg-ising spin-1/2 chain," (2022), arXiv:2202.07695 [math.PR] .

[101] M. V. Berry, New Journal of Physics **20**, 053066 (2018).

[102] L. M. Farrell, C. J. Howls, and D. H. J. O'Dell, Journal of Physics A: Mathematical and Theoretical **56**, 044001 (2023).

[103] W. Kirkby, J. Mumford, and D. H. J. O'Dell, Phys. Rev. Res. **1**, 033135 (2019).

[104] E. Wigner and P. Jordan, Z. Phys **47**, 46 (1928).

[105] H. Bethe, Z. Phys. **71**, 205 (1931).

[106] S. Gopalakrishnan and R. Vasseur, Phys. Rev. Lett. **122**, 127202 (2019).

[107] E. Ilievski, J. De Nardis, M. Medenjak, and T. c. v. Prosen, Phys. Rev. Lett. **121**, 230602 (2018).

[108] J. De Nardis, M. Medenjak, C. Karrasch, and E. Ilievski, Phys. Rev. Lett. **123**, 186601 (2019).

[109] J. De Nardis, S. Gopalakrishnan, R. Vasseur, and B. Ware, Phys. Rev. Lett. **127**, 057201 (2021).

[110] E. Ilievski, J. De Nardis, S. Gopalakrishnan, R. Vasseur, and B. Ware, Phys. Rev. X **11**, 031023 (2021).

[111] A. Das, M. Kulkarni, H. Spohn, and A. Dhar, Phys. Rev. E **100**, 042116 (2019).

[112] E. Rosenberg, T. Andersen, R. Samajdar, A. Petukhov, J. Hoke, D. Abanin, A. Bengtsson, I. Drozdov, C. Erickson, P. Klimov, *et al.*, arXiv:2306.09333 (2023).

[113] J. Quastel and H. Spohn, Journal of Statistical Physics **160**, 965–984 (2015).

[114] J. De Nardis, S. Gopalakrishnan, and R. Vasseur, arXiv:2212.03696 (2022).

[115] D. Loison, C. Qin, K. Schotte, and X. Jin, The European Physical Journal B-Condensed Matter and Complex Systems **41**, 395 (2004).

[116] J. De Nardis, S. Gopalakrishnan, E. Ilievski, and R. Vasseur, Phys. Rev. Lett. **125**, 070601 (2020).

[117] B. Bertini, F. H. L. Essler, S. Groha, and N. J. Robinson, Phys. Rev. Lett. **115**, 180601 (2015).

[118] F. Lange, Z. Lenarčič, and A. Rosch, Nature Communications **8**, 15767 (2017).

[119] Y. Tang, W. Kao, K.-Y. Li, S. Seo, K. Mallayya, M. Rigol, S. Gopalakrishnan, and B. L. Lev, Phys. Rev. X **8**, 021030 (2018).

[120] M. Žnidarič, Phys. Rev. Lett. **125**, 180605 (2020).

[121] J. Durnin, M. J. Bhaseen, and B. Doyon, Phys. Rev. Lett. **127**, 130601 (2021).

[122] A. Bastianello, A. D. Luca, and R. Vasseur, Journal of Statistical Mechanics: Theory and Experiment **2021**, 114003 (2021).

[123] V. B. Bulchandani, D. A. Huse, and S. Gopalakrishnan, Phys. Rev. B **105**, 214308 (2022).

[124] J. Ford, Physics Reports **213**, 271 (1992).

[125] G. P. Berman and F. M. Izrailev, Chaos: An Interdisciplinary Journal of Nonlinear Science **15**, 015104 (2005).

[126] F. Jin, T. Neuhaus, K. Michielsen, S. Miyashita, M. Novotny, M. I. Katsnelson, and H. De Raedt, New Journal of Physics **15**, 033009 (2013).

[127] Z. Dong, R. Moessner, and M. Haque, Journal of Statistical Mechanics: Theory and Experiment **2018**, 063106 (2018).

[128] X. Cao, V. B. Bulchandani, and J. E. Moore, Phys. Rev. Lett. **120**, 164101 (2018).

[129] C. Danieli, T. Mithun, Y. Kati, D. K. Campbell, and S. Flach, Phys. Rev. E **100**, 032217 (2019).

[130] T. Mithun, C. Danieli, Y. Kati, and S. Flach, Phys. Rev. Lett. **122**, 054102 (2019).

[131] P. W. Anderson, Phys. Rev. **109**, 1492 (1958).

[132] D. M. Basko, I. L. Aleiner, and B. L. Altshuler, Ann. Phys. (Amsterdam) **321**, 1126 (2006).

[133] I. V. Gornyi, A. D. Mirlin, and D. G. Polyakov, Phys. Rev. Lett. **95**, 206603 (2005).

[134] V. Oganesyan and D. A. Huse, Phys. Rev. b **75**, 155111 (2007).

[135] C. Monthus and T. Garel, Phys. Rev. B **81**, 134202 (2010).

[136] T. C. Berkelbach and D. R. Reichman, Phys. Rev. B **81**, 224429 (2010).

[137] A. Pal and D. A. Huse, Phys. Rev. B **82**, 174411 (2010).

[138] D. J. Luitz, N. Laflorencie, and F. Alet, Phys. Rev. B **91**, 081103 (2015).

[139] R. K. Panda, A. Scardicchio, M. Schulz, S. R. Taylor, and M. Žnidarič, Europhys. Lett. **128**, 67003 (2020).

[140] J. Šuntajs, J. Bonča, T. Prosen, and L. Vidmar, Phys. Rev. E **102**, 062144 (2020).

[141] P. Sierant, D. Delande, and J. Zakrzewski, Phys. Rev. Lett. **124**, 186601 (2020).

[142] D. Sels and A. Polkovnikov, Phys. Rev. E **104**, 054105 (2021).

[143] D. Abanin, J. Bardarson, G. De Tomasi, S. Gopalakrishnan, V. Khemani, S. Parameswaran, F. Pollmann, A. Potter, M. Serbyn, and R. Vasseur, Ann. Phys. (Amsterdam) **427**, 168415 (2021).

[144] A. Morningstar, L. Colmenarez, V. Khemani, D. J. Luitz, and D. A. Huse, Phys. Rev. B **105**, 174205 (2022).

[145] P. J. D. Crowley and A. Chandran, SciPost Phys. **12**, 201 (2022).

[146] P. Sierant and J. Zakrzewski, Phys. Rev. B **105**, 224203 (2022).

[147] W. De Roeck and F. Huveneers, Phys. Rev. B **95**, 155129 (2017).

[148] K. Agarwal, S. Gopalakrishnan, M. Knap, M. Müller, and E. Demler, Phys. Rev. Lett. **114**, 160401 (2015).

[149] A. C. Potter, R. Vasseur, and S. Parameswaran, Phys. Rev. X **5**, 031033 (2015).

[150] R. Vosk, D. A. Huse, and E. Altman, Phys. Rev. X **5**, 031032 (2015).

[151] S. Gopalakrishnan, K. Agarwal, E. A. Demler, D. A. Huse, and M. Knap, Phys. Rev. B **93**, 134206 (2016).

[152] M. Žnidarič, A. Scardicchio, and V. K. Varma, Phys. Rev. Lett. **117**, 040601 (2016).

[153] M. Schulz, S. R. Taylor, C. A. Hooley, and A. Scardicchio, Phys. Rev. B **98**, 180201 (2018).

[154] J. Richter, D. Schubert, and R. Steinigeweg, Phys. Rev. Res. **2**, 013130 (2020).

[155] S. R. Taylor and A. Scardicchio, Phys. Rev. B **103**, 184202 (2021).

[156] K. Agarwal, E. Altman, E. Demler, S. Gopalakrishnan, D. A. Huse, and M. Knap, Annalen der Physik **529**, 1600326 (2017).

[157] D. J. Luitz and Y. B. Lev, Annalen der Physik **529**, 1600350 (2017).

[158] J. Feldmeier, P. Sala, G. De Tomasi, F. Pollmann, and M. Knap, Phys. Rev. Lett. **125**, 245303 (2020).

[159] C. Chamon, Phys. Rev. Lett. **94**, 040402 (2005).

[160] S. Vijay, J. Haah, and L. Fu, Phys. Rev. B **92**, 235136 (2015).

[161] A. Gromov, Phys. Rev. X **9**, 031035 (2019).

[162] E. Guardado-Sanchez, A. Morningstar, B. M. Spar, P. T. Brown, D. A. Huse, and W. S. Bakr, Phys. Rev. X **10**, 011042 (2020).

[163] M. Pretko, X. Chen, and Y. You, International Journal of Modern Physics A **35**, 2030003 (2020).

[164] H. Yan, O. Benton, L. D. Jaubert, N. Shannon, *et al.*, Phys. Rev. Lett. **124**, 127203 (2020).

[165] T. Rakovszky, P. Sala, R. Verresen, M. Knap, and F. Pollmann, Phys. Rev. B **101**, 125126 (2020).

[166] P. Sala, T. Rakovszky, R. Verresen, M. Knap, and F. Pollmann, Phys. Rev. X **10**, 011047 (2020).

[167] H. Singh, B. A. Ware, R. Vasseur, and A. J. Friedman, Phys. Rev. Lett. **127**, 230602 (2021).

[168] N. Pancotti, G. Giudice, J. I. Cirac, J. P. Garrahan, and M. C. Bañuls, Phys. Rev. X **10**, 021051 (2020).

[169] A. J. McRoberts, F. Balducci, R. Moessner, and A. Scardicchio, Phys. Rev. B **108**, 094204 (2023).

[170] D. Leibfried, R. Blatt, C. Monroe, and D. Wineland, Rev. Mod. Phys. **75**, 281 (2003).

[171] I. Bloch, J. Dalibard, and W. Zwerger, Rev. Mod. Phys. **80**, 885 (2008).

[172] M. Ueda, Nat. Rev. Phys. **2**, 669 (2020).

[173] J. M. Deutsch, Phys. Rev. A **43**, 2046 (1991).

[174] M. Srednicki, Phys. Rev. E **50**, 888 (1994).

[175] L. D'Alessio, Y. Kafri, A. Polkovnikov, and M. Rigol, Adv. Phys. **65**, 239 (2016).

[176] D. A. Abanin, E. Altman, I. Bloch, and M. Serbyn, Rev. Mod. Phys. **91**, 021001 (2019).

[177] I. Cornfeld, A. Sossinskii, S. Fomin, and Y. Sinai, *Ergodic Theory*, Grundlehren der mathematischen Wissenschaften (Springer, 1982).

[178] A. Vulpiani, F. Cecconi, and M. Cencini, *Chaos: From Simple Models to Complex Systems*, Series on Advances in Statistical Mechanics (World Scientific, 2009).

[179] G. De Tomasi, I. M. Khaymovich, F. Pollmann, and S. Warzel, Phys. Rev. B **104**, 024202 (2021).

[180] J. J. Mendoza-Arenas, M. Žnidarič, V. K. Varma, J. Goold, S. R. Clark, and A. Scardicchio, Phys. Rev. B **99**, 094435 (2019).

[181] M. Kardar, G. Parisi, and Y.-C. Zhang, Phys. Rev. Lett. **56**, 889 (1986).

[182] M. Ljubotina, M. Žnidarič, and T. Prosen, Nature Communications **8**, 16117 (2017).

[183] M. Ljubotina, M. Žnidarič, and T. Prosen, Phys. Rev. Lett. **122**, 210602 (2019).

[184] M. Dupont and J. E. Moore, Phys. Rev. B **101**, 121106(R) (2020).

[185] J. De Nardis, M. Medenjak, C. Karrasch, and E. Ilievski, Phys. Rev. Lett. **124**, 210605 (2020).

[186] T. Bilitewski, S. Bhattacharjee, and R. Moessner, Phys. Rev. B **103**, 174302 (2021).

[187] A. J. McRoberts, H. Zhao, R. Moessner, and M. Bukov, Phys. Rev. Res. **5**, 043008 (2023).

[188] J. Liu, N. Srivastava, V. S. Viswanath, and G. Müller, J. Applied Phys. **70**, 6181 (1991).

[189] O. F. de Alcantara Bonfim and G. Reiter, Phys. Rev. Lett. **69**, 367 (1992).

[190] V. Constantoudis and N. Theodorakopoulos, Phys. Rev. E **55**, 7612 (1997).

[191] N. Li, Phys. Rev. E **100**, 062104 (2019).

[192] S.-k. Ma, C. Dasgupta, and C.-k. Hu, Phys. Rev. Lett. **43**, 1434 (1979).

[193] C. Dasgupta and S.-k. Ma, Phys. Rev. B **22**, 1305 (1980).

[194] D. S. Fisher, Phys. Rev. B **51**, 6411 (1995).

[195] G. Refael and E. Altman, Comptes Rendus Physique **14**, 725 (2013).

[196] F. Iglói and C. Monthus, Eur. Phys. J. B **91**, 290 (2018).

[197] S. Alexander, J. Bernasconi, W. R. Schneider, and R. Orbach, Rev. Mod. Phys. **53**, 175 (1981).

[198] J. Haus and K. Kehr, Phys. Rep. **150**, 263 (1987).

[199] J.-P. Bouchaud and A. Georges, Phys. Rep. **195**, 127 (1990).

[200] F. J. Dyson, Phys. Rev. **92**, 1331 (1953).

[201] J. Bernasconi, W. R. Schneider, and W. Wyss, Z. Phys. B **37**, 175 (1980).

[202] T. M. Nieuwenhuizen and M. H. Ernst, Phys. Rev. B **31**, 3518 (1985).

[203] B. Derrida and J. M. Luck, Phys. Rev. B **28**, 7183 (1983).

[204] P. J. H. Denteneer and M. H. Ernst, Phys. Rev. B **29**, 1755 (1984).

[205] J. Machta, Phys. Rev. B **24**, 5260 (1981).

[206] J. Machta, J. Stat. Phys. **30**, 305 (1983).

[207] R. A. Guyer, Phys. Rev. A **29**, 2114 (1984).

[208] J. Machta, J. Phys A **18**, L531 (1985).

[209] D. J. Thouless, J. Phys. C **5**, 77 (1972).

[210] P. W. Anderson, D. J. Thouless, E. Abrahams, and D. S. Fisher, Phys. Rev. B **22**, 3519 (1980).

[211] H. Furstenberg and H. Kesten, Ann. Math. Stat. **31**, 457 (1960).

[212] H. Furstenberg, Trans. Amer. Math. Soc. **108**, 377 (1963).

[213] R. Abou-Chacra, D. J. Thouless, and P. W. Anderson, J. Phys. C **6**, 1734 (1973).

[214] F. Pietracaprina, V. Ros, and A. Scardicchio, Phys. Rev. B **93**, 054201 (2016).

[215] J. P. Hulin, J. P. Bouchaud, and A. Georges, J. Phys. A **23**, 1085 (1990).

[216] G. Parisi, S. Pascazio, F. Pietracaprina, V. Ros, and A. Scardicchio, J. Phys. A **53**, 014003 (2019).

[217] M. Mézard and G. Parisi, Eur. Phys. J. B **20**, 217 (2001).

[218] C. Laumann, A. Scardicchio, and S. L. Sondhi, Phys. Rev. B **78**, 134424 (2008).

[219] C. Laumann, A. Scardicchio, and S. L. Sondhi, Phys. Rev. E **77**, 061139 (2008).

[220] I. V. Protopopov, R. K. Panda, T. Parolini, A. Scardicchio, E. Demler, and D. A. Abanin, Phys. Rev. X **10**, 011025 (2020).

[221] D. Saraidaris, J.-W. Li, A. Weichselbaum, J. von Delft, and D. A. Abanin, arXiv:2304.03099 (2023).

[222] X. Mi, A. Michailidis, S. Shabani, K. Miao, P. Klimov, J. Lloyd, E. Rosenberg, R. Acharya, I. Aleiner, T. Andersen, *et al.*, arXiv:2304.13878 (2023).

[223] D. A. Areshkin, D. Gunlycke, and C. T. White, Nano letters **7**, 204 (2007).

[224] M. J. Bowick, N. Fakhri, M. C. Marchetti, and S. Ramaswamy, Phys. Rev. X **12**, 010501 (2022).

[225] L. Barberis and F. Peruani, Phys. Rev. Lett. **117**, 248001 (2016).

[226] L. P. Dadhichi, J. Kethapelli, R. Chajwa, S. Ramaswamy, and A. Maitra, Phys. Rev. E **101**, 052601 (2020).

[227] E. Lisin, O. Petrov, E. Sametov, O. Vaulina, K. Statsenko, M. Vasiliev, J. Carmona-Reyes, and T. Hyde, Scientific Reports **10**, 13653 (2020).

[228] J. Yan, M. Han, J. Zhang, C. Xu, E. Luijten, and S. Granick, Nature materials **15**, 1095 (2016).

[229] J. Zhang, R. Alert, J. Yan, N. S. Wingreen, and S. Granick, Nature Physics **17**, 961 (2021).

[230] M. Fruchart, R. Hanai, P. B. Littlewood, and V. Vitelli, Nature **592**, 363 (2021).

[231] A. Ghatak, M. Brandenbourger, J. Van Wezel, and C. Coulais, Proceedings of the National Academy of Sciences **117**, 29561 (2020).

[232] M. Brandenbourger, C. Scheibner, J. Veenstra, V. Vitelli, and C. Coulais, arXiv:2108.08837 (2021).

[233] D. A. Abanin, W. De Roeck, and F. Huveneers, Phys. Rev. Lett. **115**, 256803 (2015).

[234] T. Mori, T. Kuwahara, and K. Saito, Phys. Rev. Lett. **116**, 120401 (2016).

[235] A. Lazarides, A. Das, and R. Moessner, Phys. Rev. E **90**, 012110 (2014).

[236] P. T. Dumitrescu, R. Vasseur, and A. C. Potter, Phys. Rev. Lett. **120**, 070602 (2018).

[237] F. Machado, G. D. Kahanamoku-Meyer, D. V. Else, C. Nayak, and N. Y. Yao, Phys. Rev. Res. **1**, 033202 (2019).

[238] D. V. Else, W. W. Ho, and P. T. Dumitrescu, Phys. Rev. X **10**, 021032 (2020).

[239] H. Zhao, F. Mintert, R. Moessner, and J. Knolle, Phys. Rev. Lett. **126**, 040601 (2021).

[240] C. Fleckenstein and M. Bukov, Phys. Rev. B **103**, L140302 (2021).

[241] A. Kyprianidis, F. Machado, W. Morong, P. Becker, K. S. Collins, D. V. Else, L. Feng, P. W. Hess, C. Nayak, G. Pagano, *et al.*, Science **372**, 1192 (2021).

[242] N. Goldman and J. Dalibard, Phys. Rev. X **4**, 031027 (2014).

[243] M. Bukov, L. D'Alessio, and A. Polkovnikov, Advances in Physics **64**, 139 (2015).

[244] R. Moessner and S. L. Sondhi, Nature Physics **13**, 424 (2017).

[245] A. Eckardt, Reviews of Modern Physics **89**, 011004 (2017).

[246] T. Oka and S. Kitamura, Annual Review of Condensed Matter Physics **10**, 387 (2019).

[247] J. Struck, M. Weinberg, C. Ölschläger, P. Windpassinger, J. Simonet, K. Sengstock, R. Höppner, P. Hauke, A. Eckardt, M. Lewenstein, *et al.*, Nature Physics **9**, 738 (2013).

[248] M. Aidelsburger, M. Atala, M. Lohse, J. T. Barreiro, B. Paredes, and I. Bloch, Phys. Rev. Lett. **111**, 185301 (2013).

[249] C. Schweizer, F. Grusdt, M. Berngruber, L. Barbiero, E. Demler, N. Goldman, I. Bloch, and M. Aidelsburger, Nature Physics **15**, 1168 (2019).

[250] V. Khemani, A. Lazarides, R. Moessner, and S. L. Sondhi, Phys. Rev. Lett. **116**, 250401 (2016).

[251] D. V. Else, B. Bauer, and C. Nayak, Phys. Rev. Lett. **117**, 090402 (2016).

[252] N. Y. Yao, A. C. Potter, I.-D. Potirniche, and A. Vishwanath, Phys. Rev. Lett. **118**, 030401 (2017).

[253] A. Pizzi, A. Nunnenkamp, and J. Knolle, Phys. Rev. Lett. **127**, 140602 (2021).

[254] W. Beatrez, C. Fleckenstein, A. Pillai, E. Sanchez, A. Akkiraju, J. Alcala, S. Conti, P. Reshetikhin, E. Druga, M. Bukov, *et al.*, arXiv:2201.02162 (2022).

[255] I.-D. Potirniche, A. C. Potter, M. Schleier-Smith, A. Vishwanath, and N. Y. Yao, Phys. Rev. Lett. **119**, 123601 (2017).

[256] K. Wintersperger, C. Braun, F. N. Ünal, A. Eckardt, M. D. Liberto, N. Goldman, I. Bloch, and M. Aidelsburger, Nature Physics **16**, 1058 (2020).

[257] K. S. Decker, C. Karrasch, J. Eisert, and D. M. Kennes, Phys. Rev. Lett. **124**, 190601 (2020).

[258] K. Singh, C. J. Fujiwara, Z. A. Geiger, E. Q. Simmons, M. Lipatov, A. Cao, P. Dotti, S. V. Rajagopal, R. Senaratne, T. Shimasaki, M. Heyl, A. Eckardt, and D. M. Weld, Phys. Rev. X **9**, 041021 (2019).

[259] A. Rubio-Abadal, M. Ippoliti, S. Hollerith, D. Wei, J. Rui, S. Sondhi, V. Khemani, C. Gross, and I. Bloch, Phys. Rev. X **10**, 021044 (2020).

[260] A. Haldar, D. Sen, R. Moessner, and A. Das, Phys. Rev. X **11**, 021008 (2021).

[261] P. Peng, C. Yin, X. Huang, C. Ramanathan, and P. Cappellaro, Nature Physics **17**, 444 (2021).

[262] W. Beatrez, O. Janes, A. Akkiraju, A. Pillai, A. Oddo, P. Reshetikhin, E. Druga, M. McAllister, M. Elo, B. Gilbert, D. Suter, and A. Ajoy, Phys. Rev. Lett. **127**, 170603 (2021).

[263] O. Sahin, H. A. Asadi, P. Schindler, A. Pillai, E. Sanchez, M. Elo, M. McAllister, E. Druga, C. Fleckenstein, M. Bukov, *et al.*, arXiv:2206.14945 (2022).

[264] M. Heyl, P. Hauke, and P. Zoller, Science advances **5**, eaau8342 (2019).

[265] T. T. Koutserimpas and R. Fleury, Phys. Rev. Lett. **120**, 087401 (2018).

[266] H. Li, T. Kottos, and B. Shapiro, Phys. Rev. Appl. **9**, 044031 (2018).

[267] O. Howell, P. Weinberg, D. Sels, A. Polkovnikov, and M. Bukov, Phys. Rev. Lett. **122**, 010602 (2019).

[268] T. Mori, Phys. Rev. B **98**, 104303 (2018).

[269] S. Notarnicola, F. Iemini, D. Rossini, R. Fazio, A. Silva, and A. Russomanno, Phys. Rev. E **97**, 022202 (2018).

[270] A. Rajak, I. Dana, and E. G. Dalla Torre, Phys. Rev. B **100**, 100302 (2019).

[271] H.-K. Jin, A. Pizzi, and J. Knolle, arXiv:2204.01761 (2022).

[272] A. Kundu, A. Rajak, and T. Nag, Phys. Rev. B **104**, 075161 (2021).

[273] B. Ye, F. Machado, and N. Y. Yao, Phys. Rev. Lett. **127**, 140603 (2021).

[274] Y. Sadia, E. G. Dalla Torre, and A. Rajak, Phys. Rev. B **105**, 184302 (2022).

[275] S. Higashikawa, H. Fujita, and M. Sato, arXiv:1810.01103 (2018).

[276] W. W. Ho, I. Protopopov, and D. A. Abanin, Phys. Rev. Lett. **120**, 200601 (2018).

[277] M. Bukov, M. Heyl, D. A. Huse, and A. Polkovnikov, Phys. Rev. B **93**, 155132 (2016).

[278] M. Elbracht, S. Michel, and M. Potthoff, Phys. Rev. Lett. **124**, 197202 (2020).

[279] H. Bernien, S. Schwartz, A. Keesling, H. Levine, A. Omran, H. Pichler, S. Choi, A. S. Zibrov, M. Endres, M. Greiner, *et al.*, Nature **551**, 579 (2017).

[280] C. J. Turner, A. A. Michailidis, D. A. Abanin, M. Serbyn, and Z. Papić, Nature Physics **14**, 745 (2018).

[281] M. Serbyn, D. A. Abanin, and Z. Papić, Nature Physics **17**, 675 (2021).

[282] G.-X. Su, H. Sun, A. Hudomal, J.-Y. Desaules, Z.-Y. Zhou, B. Yang, J. C. Halimeh, Z.-S. Yuan, Z. Papić, and J.-W. Pan, arXiv:2201.00821 (2022).

[283] H. Zhao, A. Smith, F. Mintert, and J. Knolle, Phys. Rev. Lett. **127**, 150601 (2021).

[284] D. Hahn, P. A. McClarty, and D. J. Luitz, SciPost Physics **11**, 074 (2021).

[285] A. Pizzi, D. Malz, A. Nunnenkamp, and J. Knolle, Phys. Rev. B **106**, 214303 (2022).

[286] A. Deger, S. Roy, and A. Lazarides, Phys. Rev. Lett. **129**, 160601 (2022).

[287] Z. Cai, Phys. Rev. Lett. **128**, 050601 (2022).

[288] S. Bhattacharjee, S. Bandyopadhyay, and A. Dutta, Phys. Rev. A **106**, 022206 (2022).

[289] D. M. Long, P. J. Crowley, and A. Chandran, Phys. Rev. B **105**, 144204 (2022).

[290] R. Steinigeweg and H.-J. Schmidt, Computer physics communications **174**, 853 (2006).

[291] J. Frank, W. Huang, and B. Leimkuhler, Journal of Computational Physics **133**, 160 (1997).

[292] H. Yoshida, Qualitative and Quantitative Behaviour of Planetary Systems , 27 (1993).

[293] G. Zhong and J. E. Marsden, Physics Letters A **133**, 134 (1988).

[294] E. Faou, E. Hairer, and T.-L. Pham, BIT Numerical Mathematics **44**, 699 (2004).

[295] S.-H. Tsai, M. Krech, and D. Landau, Brazilian Journal of Physics **34**, 384 (2004).

[296] S. H. Strogatz, *Nonlinear dynamics and chaos: with applications to physics, biology, chemistry, and engineering* (CRC press, 2018).

[297] A. Auerbach, *Interacting electrons and quantum magnetism* (Springer Science & Business Media, 1998).

[298] P. A. Kuchment, *Floquet theory for partial differential equations*, Vol. 60 (Springer Science & Business Media, 1993).

[299] L. D'Alessio, Y. Kafri, A. Polkovnikov, and M. Rigol, Advances in Physics **65**, 239 (2016).

[300] B.-Y. Sun, N. Goldman, M. Aidelsburger, and M. Bukov, PRX Quantum **4**, 020329 (2023).

[301] A. Schnell, A. Eckardt, and S. Denisov, Phys. Rev. B **101**, 100301 (2020).

Appendices

Appendix A

Numerical methods

A.1 Preparation of thermal states

In Chs. 5 & 9 we make extensive use of thermal ensembles of initial states, which we construct using a heatbath Monte Carlo method [115] (rather than the more well-known Metropolis method), where we use the fact that we can precisely invert the thermal probability distribution for a single spin in a magnetic field.

The general method is known as inverse transform sampling. Let $X \in [a, b] \subseteq \mathbb{R}$ a random variable on some real interval, with probability density function $p(X)$. The cumulative distribution function (CDF) is

$$\mathcal{F}_X(x) = \int_a^x dX\ p(X), \tag{A.1}$$

i.e., the probability that a randomly sampled X is less than or equal to x. Then the random variable $Y = \mathcal{F}_X^{-1}(u)$, where u is uniformly random over $[0, 1]$, has the same probability distribution as the original variable X since, by construction,

$$\mathcal{F}_Y(x) = \int_0^{u=\mathcal{F}_X(x)} du' = \mathcal{F}_X(x). \tag{A.2}$$

The specific problem is to invert the CDF. For spins $\boldsymbol{S} \in S^2$, this can be done analytically. Letting $\boldsymbol{h} = h\hat{\boldsymbol{z}}$, the CDF for S^z is

$$\mathcal{F}_z(S^z) = \int_{-1}^{S^z} dz\ \frac{e^{\beta h z}}{\mathcal{Z}} = \frac{\int_{-1}^{S^z} dz\ e^{\beta h z}}{\int_{-1}^{1} dz\ e^{\beta h z}} = \frac{e^{\beta h S^z} - e^{-\beta h}}{e^{\beta h} - e^{-\beta h}}. \tag{A.3}$$

Then, using $\mathcal{F}_z(\mathcal{F}_z^{-1}(u)) = u$, we find that we can sample S^z as

$$S^z = \mathcal{F}_z^{-1}(u) = 1 + \frac{\log(1 - u + ue^{-2\beta h})}{\beta h}. \tag{A.4}$$

The S^x and S^y components have random direction in the plane, and magnitude set by the condition $|\boldsymbol{S}| = 1$. For a magnetic field of arbitrary direction, one need only appropriately rotate the sampled spin.

To sample a state from the canonical ensemble, we begin with a completely random (i.e., infinite-temperature) state, simply drawing every spin $\boldsymbol{S}_i$ from the uniform distribution on S^2. To cool the state to the desired temperature, then, we perform 10^4 (or, at low temperatures, 10^5) sweeps through the system, where one sweep consists of re-sampling every spin from its effective field, in a random order. This procedure produces thermal states at the desired temperature regardless of the lattice geometry or the coupling strengths or anisotropies, and is much faster than the Metropolis method at low temperatures because, by construction, no heatbath moves are rejected.

A.2 Time evolution

As this thesis is concerned almost entirely with the dynamical evolution of spin systems, and since, in all but the most trivial of settings, their equations of motion cannot be solved exactly, we need some effective numerical methods to integrate their dynamics.

The most common and universal method for solving a system of coupled first-order ordinary differential equations (which is what all of the spins' equations of motion are) is the fourth-order Runge-Kutta method (RK4). We have, however, generally avoided using RK4 (except for a very small part of Ch. 9, when it was unavoidable), because the error tends to accumulate with time, the system does not remain confined to the phase space manifold (the components of spin evolve separately, and the norm $|\boldsymbol{S}_i|$ is not conserved by RK4), and neither the energy nor the (conserved components of the) magnetisation are conserved. Since we need to reach rather long times in our simulations ($\sim 10^6 J^{-1}$ in Ch. 7) with at least some control over the errors, RK4 will not suffice.

To solve these issues, we make use of the trivial situations in which the dynamics can be exactly solved – a single spin in a magnetic field, or two spins isotropically coupled to each other.

First, a single spin in a constant magnetic field evolves as

$$\dot{\boldsymbol{S}} = \boldsymbol{M} \times \boldsymbol{S} \quad \Rightarrow \quad \boldsymbol{S}(t) = \exp(\boldsymbol{M} \cdot \boldsymbol{R}\ t)\boldsymbol{S}(0), \tag{A.5}$$

where $\boldsymbol{R}$ denotes the (vector of) the generators of rotations. We can then make progress by decomposing into sublattices $\mathcal{A}, \mathcal{B}, \mathcal{C}$, etc., where the effective field of the spins $\boldsymbol{S}_i \in \mathcal{A}$ is determined only by the spins in the other sublattices; with the same true for the sublattices $\mathcal{B}, \mathcal{C}$, etc.

We can then decompose the evolution of the full state over some time-step δt in terms of the exact evolution of the various sublattices, with the remaining error tied to the non-commutativity of the different sublattices' time evolution.

The decomposition is particularly effective for bipartite lattices. Whilst we have analysed the properties of the two-step bipartite decomposition in Ch. 9 – for which the error is $\mathcal{O}(\delta t^2)$ – when we are approximating the continuous time dynamics in all other parts of the thesis we use an 11-step, $\mathcal{O}(\delta t^4)$, decomposition [295].

The greatest advantage of the sublattice-decomposition, however, is that the spin-norms and the total energy of the state are conserved to machine precision, regardless of δt. Moreover, whilst the magnetisation is not exactly conserved by this method, the accumulated error grows sub-linearly in the simulation time, allowing us to use a larger δt than we could afford with the RK4 method – generally, we have used $\delta t = 0.05$, which leads to a magnetisation error $\sim 10^{-13}$ (per site) over the simulation time-scales. Furthermore, since the

energy of each state is conserved, if we start in a canonical ensemble, we are guaranteed to remain within the canonical ensemble.

The second method involves the dynamics of two isotropically-coupled spins, where the properties of the cross product imply that two spins $\boldsymbol{S}_1$, $\boldsymbol{S}_2$ evolve by rotating around the constant total field $\boldsymbol{S}_1 + \boldsymbol{S}_2$:

$$\begin{aligned}\dot{\boldsymbol{S}}_1 &= J\boldsymbol{S}_2 \times \boldsymbol{S}_1 = J(\boldsymbol{S}_1 + \boldsymbol{S}_2) \times \boldsymbol{S}_1 \\ \dot{\boldsymbol{S}}_2 &= J\boldsymbol{S}_1 \times \boldsymbol{S}_2 = J(\boldsymbol{S}_1 + \boldsymbol{S}_2) \times \boldsymbol{S}_2.\end{aligned} \tag{A.6}$$

This is rather less generally applicable than the bipartite site-based evolution, but, if we can decompose into even and odd bonds (as in a chain), then we can use the same 11-step, $\mathcal{O}(\delta t^4)$ method with this bond-based decomposition. This does not precisely conserve the energy, but it does exactly conserve the total magnetisation, and, again, the accumulated error grows sub-linearly with time.

There is, in fact, one place where we need to use the bond-based decomposition. The Ishimori chain (1.22) and the interpolation (2.8) cannot be solved with the site-based method, but they can be solved with the bond-based decomposition.

Recall that the equations of motion are (2.9)

$$\dot{\boldsymbol{S}}_i = 2\boldsymbol{S}_i \times \left(\frac{\boldsymbol{S}_{i-1}}{2 - \gamma + \gamma \boldsymbol{S}_i \cdot \boldsymbol{S}_{i-1}} + \frac{\boldsymbol{S}_{i+1}}{2 - \gamma + \gamma \boldsymbol{S}_i \cdot \boldsymbol{S}_{i+1}} \right). \tag{A.7}$$

The fundamental obstruction to the site based method in this case is the dot products $\boldsymbol{S}_i \cdot \boldsymbol{S}_{i\pm1}$ in the denominators – even holding $\boldsymbol{S}_{i+1}$ and $\boldsymbol{S}_{i-1}$ fixed, these factors have a non-trivial time dependence as $\boldsymbol{S}_i$ evolves.

The bond-based decomposition, however, splits this into

$$\dot{\boldsymbol{S}}_i = 2\boldsymbol{S}_i \times \frac{\boldsymbol{S}_{i+1}}{2 - \gamma + \gamma \boldsymbol{S}_i \cdot \boldsymbol{S}_{i+1}}, \qquad \dot{\boldsymbol{S}}_{i+1} = 2\boldsymbol{S}_{i+1} \times \frac{\boldsymbol{S}_i}{2 - \gamma + \gamma \boldsymbol{S}_i \cdot \boldsymbol{S}_{i+1}}, \tag{A.8}$$

and, as the two spins evolve, the factor $\boldsymbol{S}_i \cdot \boldsymbol{S}_{i+1}$ remains constant.

Appendix B

Non-reciprocal spin dynamics – supplementary information

B.1 Analytical properties of the nonreciprocal drive

Throughout this section, we will specialise, for concreteness, to the isotropic Heisenberg chain. The analogous results for other non-reciprocal bipartite spin models following Eq. (9.1) are straightforward.

B.1.1 Proof of the lack of symplectic structure in non-reciprocal dynamics

Here we demonstrate explicitly that the EOM in Eq. (9.1) are not symplectic [290, 291]; that is, they cannot be generated by any Hamiltonian. To this end, we first introduce the relevant notions from differential geometry.

The phase space for a system of L classical spins is defined as

$$\mathcal{P} = \{(\boldsymbol{S}_1, \ldots, \boldsymbol{S}_N) : |\boldsymbol{S}_j|^2 = 1, \quad \forall j \in \{1, \ldots, L\}\}, \tag{B.1}$$

with $\boldsymbol{S}_j$ a unit vector in three-dimensional space. To incorporate the norm constraint, we can parameterise each spin using its azimuthal angle φ_j and its projection on the z-axis, z_j:

$$\boldsymbol{S}_j = \left(\sqrt{1-z_j^2}\cos\varphi_j,\ \sqrt{1-z_j^2}\sin\varphi_j,\ z_j\right)^t. \tag{B.2}$$

Using these coordinates, the symplectic form ω w.r.t. the conjugate variables (φ_j, z_j), can be locally defined as

$$\omega = \sum_{j=1}^{L} \mathrm{d}\varphi_j \wedge \mathrm{d}z_j. \tag{B.3}$$

A smooth function $f : \mathcal{P} \to \mathcal{P}$ is called *symplectic*, if and only if it preserves the symplectic form, i.e., $f^*\omega = \omega$, where the asterisk denotes the pullback. Given an energy function H,

Hamilton's equations of motion read as

$$\dot{\varphi}_j = \partial_{z_j} H, \quad \dot{z}_j = -\partial_{\varphi_j} H. \tag{B.4}$$

A vector field $\boldsymbol{X}$ generates a flow on phase space defined as the solution to:

$$\frac{\mathrm{d}}{\mathrm{d}t}\boldsymbol{S}_j(t) = \boldsymbol{X}(\boldsymbol{S}_j(t)). \tag{B.5}$$

Hamilton's equations are associated with the Hamiltonian vector field $\boldsymbol{X}_H$, defined implicitly by $\iota_{\boldsymbol{X}_H}\omega = \mathrm{d}H$, where ι is the exterior derivative. The flow generated by $\boldsymbol{X}_H$ is called the Hamiltonian flow.

A major result in symplectic geometry is that any Hamiltonian flow is symplectic; conversely, if the flow of a complete vector field $\boldsymbol{X}$ is symplectic, then $\iota_{\boldsymbol{X}}\omega = \mathrm{d}K$ is a closed form ($\mathrm{d}\mathrm{d}K = 0$), and hence the flow is locally generated by some Hamiltonian K [290].

Non-symplecticity of the exact EOM in Eq. (9.1)

Having introduced these definitions, we can now demonstrate that the flow generated by the EOM (9.1) is not symplectic. To do this, without loss of generality we set $J = 1$, and consider the vector field $\boldsymbol{X}$ that generates the first half-cycle motion:

$$\begin{cases} \dot{\boldsymbol{S}}_j = (\boldsymbol{S}_{j-1} + \boldsymbol{S}_{j+1}) \times \boldsymbol{S}_j, & j \text{ even} \\ \dot{\boldsymbol{S}}_j = 0, & j \text{ odd}. \end{cases} \tag{B.6}$$

We will demonstrate that the form $\iota_X\omega$ is not closed, i.e., $\mathrm{d}\iota_{\boldsymbol{X}}\omega \neq 0$. Thus, the flow is not locally generated by a Hamiltonian, and hence it is not symplectic.

To see this, we use the definition in Eq. (B.3) to calculate

$$\begin{aligned} \iota_{\boldsymbol{X}}\omega &= \sum_{j=1}^{L} \iota_{\boldsymbol{X}} \left(\mathrm{d}\varphi_j \wedge \mathrm{d}z_j\right) = \sum_{j=1}^{L} \dot{\varphi}_j \mathrm{d}z_j - \dot{z}_j \mathrm{d}\varphi_j = \sum_{j \text{ even}} \dot{\varphi}_j \mathrm{d}z_j - \dot{z}_j \mathrm{d}\varphi_j \\ &= \sum_{j \text{ even}} \Bigg(z_{j+1} + z_{j-1} - \frac{z_j}{\sqrt{1-z_j^2}} \Big[\sqrt{1-z_{j-1}^2}\cos(\varphi_j - \varphi_{j-1}) \\ &\qquad + \sqrt{1-z_{j+1}^2}\cos(\varphi_j - \varphi_{j+1}) \Big] \Bigg) \mathrm{d}z_j \\ &\quad - \sqrt{1-z_j^2} \left[\sqrt{1-z_{j-1}^2}\sin(\varphi_j - \varphi_{j-1}) + \sqrt{1-z_{j+1}^2}\sin(\varphi_j - \varphi_{j+1}) \right] \mathrm{d}\varphi_j, \end{aligned} \tag{B.7}$$

where in the second line we used Eq. (B.6) written in the coordinate representation from Eq. (B.2). A straightforward calculation now gives $\mathrm{d}\iota_{\boldsymbol{X}}\omega \neq 0$, and hence the flow of $\boldsymbol{X}$ is not symplectic. The same argument applies to the second half-cycle. Thus, we conclude that the EOM in Eq. (9.1) cannot be generated by a Hamiltonian function.

Conservation of phase-space volume

Before, we conclude the discussion, let us also prove that the phase space volume remains conserved under Eq. (9.1). Intuitively, for a fixed half-cycle, each spin is subject to a rotation about a fixed axis, which conserves the phase-space volume; since this is true for both half-cycles, it follows that the entire dynamics preserves the phase space volume, and hence the dynamics are conservative.

Formally, the phase space volume is defined by the volume element

$$\mathrm{d}V = \bigwedge_{j=1}^{L} \omega_j = \mathrm{d}\varphi_1 \wedge \mathrm{d}z_1 \wedge \cdots \wedge \mathrm{d}\varphi_L \wedge \mathrm{d}z_L. \tag{B.8}$$

Liouville's theorem reads as

$$0 = \mathcal{L}_{\boldsymbol{X}} \mathrm{d}V = \iota_{\boldsymbol{X}} \mathrm{d}\mathrm{d}V + \mathrm{d}\iota_{\boldsymbol{X}} \mathrm{d}V = \mathrm{d}\iota_{\boldsymbol{X}} \mathrm{d}V, \tag{B.9}$$

where we used that the volume form is closed, $\mathrm{d}\mathrm{d}V = 0$, since the symplectic form itself is closed. Here $\mathcal{L}_{\boldsymbol{X}}$ denotes the Lie derivative along the flow of $\boldsymbol{X}$.

To demonstrate the validity of Liouville's theorem for Eq. (B.6), it suffices to focus on the second spin $\boldsymbol{S}_2$:

$$\begin{aligned}
\mathrm{d}\iota_{\boldsymbol{X}} \mathrm{d}V &= \mathrm{d}\iota_{\boldsymbol{X}} \left(\mathrm{d}\varphi_1 \wedge \mathrm{d}z_1 \cdots \mathrm{d}\varphi_L \wedge \mathrm{d}z_L\right) \\
&= \mathrm{d}\Bigg(z_3 + z_1 - \frac{z_2}{\sqrt{1-z_2^2}} \Bigg[\sqrt{1-z_1^2}\cos(\varphi_2 - \varphi_1) \\
&\qquad + \sqrt{1-z_3^2}\cos(\varphi_2 - \varphi_3) \Bigg] \Bigg) \mathrm{d}\varphi_1 \wedge \mathrm{d}z_1 \cdots d\varphi_L \wedge \mathrm{d}z_L \\
&\quad + \mathrm{d}\Bigg(-\sqrt{1-z_2^2} \Bigg[\sqrt{1-z_1^2}\sin(\varphi_2 - \varphi_1) \\
&\qquad + \sqrt{1-z_3^2}\sin(\varphi_2 - \varphi_3) \Bigg] \Bigg) \mathrm{d}\varphi_1 \wedge \mathrm{d}z_1 \cdots d\varphi_L \wedge \mathrm{d}z_L \\
&\quad + \text{ all other even spins} \\
&= \frac{z_2}{\sqrt{1-z_2^2}} \Bigg[\sqrt{1-z_1^2}\sin(\varphi_2 - \varphi_1) \\
&\qquad + \sqrt{1-z_3^2}\sin(\varphi_2 - \varphi_3) \Bigg] \mathrm{d}\varphi_2 \wedge \mathrm{d}\varphi_1 \wedge \mathrm{d}z_1 \wedge \mathrm{d}z_2 \cdots \mathrm{d}\varphi_L \wedge \mathrm{d}z_L \\
&\quad + \frac{z_2}{\sqrt{1-z_2^2}} \Bigg[\sqrt{1-z_1^2}\sin(\varphi_2 - \varphi_1) \\
&\qquad + \sqrt{1-z_3^2}\sin(\varphi_2 - \varphi_3) \Bigg] \mathrm{d}z_2 \wedge \mathrm{d}\varphi_1 \wedge \mathrm{d}z_1 \wedge \mathrm{d}\varphi_2 \cdots \mathrm{d}\varphi_L \wedge \mathrm{d}z_L \\
&\quad + \text{ all other even spins} \\
&= 0,
\end{aligned} \tag{B.10}$$

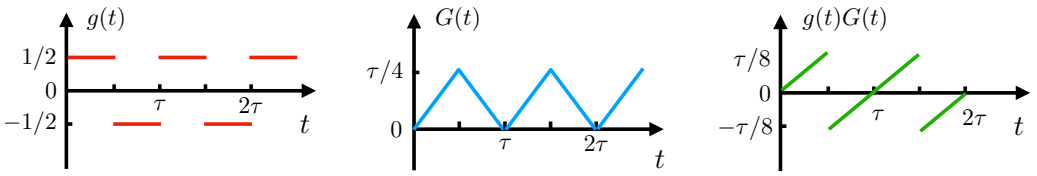

Figure B.1: Time dependence of the periodic driving function $g(t)$ (period τ) and the anti-derivative $G(t)$, as well as the product $g(t)G(t)$.

where in the last equality we have used the anti-symmetric property of the wedge product. Every symplectic map preserves the phase space volume, but as we have just shown, the converse is not true.

B.1.2 Alternative derivations of the effective dynamics

In this appendix, we provide two alternative ways to derive the effective equations of motion using (i) two-times perturbation theory, and (ii) the equation of motion for the phase space density (Liouville's equation). Both methods can be generalised to higher orders in τ in a straightforward way.

In the interests of fairness, the two-times perturbation theory approach was mainly derived by Hongzheng Zhao, and the Liouville equation approach is due to Marin Bukov.

Two-times perturbation theory

Here we illustrate an alternative method via two-times perturbation theory [296] to derive the effective EOM for the non-reciprocal drive.

We start by considering the exact EOM, given by:

$$\dot{\boldsymbol{S}}_j = -J\left[\frac{1}{2} + (-1)^j g(t)\right] \boldsymbol{S}_j \times (\boldsymbol{S}_{j-1} + \boldsymbol{S}_{j+1}), \tag{B.11}$$

where $g(t) = \frac{1}{2}\mathrm{sgn}(\sin \omega t)$. To derive an ansatz for the structure of the fast motion variable, we explicitly separate the time-average from the rest:

$$\dot{\boldsymbol{S}}_j = -\frac{J}{2}\boldsymbol{S}_j \times (\boldsymbol{S}_{j-1} + \boldsymbol{S}_{j+1}) + J(-1)^j g(t)\ \boldsymbol{S}_j \times (\boldsymbol{S}_{j-1} + \boldsymbol{S}_{j+1}). \tag{B.12}$$

For fast drivings, the local energy scale separates from the driving frequency, $\omega \gg J$. Therefore, one can decompose the resultant time evolution for spin $\boldsymbol{S}_j$ into a fast motion variable (denoted by $\boldsymbol{\eta}_j$) and slow motion (denoted by $\boldsymbol{\sigma}_j$). The slow motion reduces to the Heisenberg EOM in the fast driving limit, $\omega \to \infty$, and the fast motion captures additional corrections for any finite ω.

Thus, we consider the following decomposition

$$\boldsymbol{S}_j = \sqrt{1 - \boldsymbol{\eta}_j^2}\boldsymbol{\sigma}_j + \boldsymbol{\eta}_j, \tag{B.13}$$

which satisfies the properties $\boldsymbol{\eta}_j \ll \boldsymbol{\sigma}_j$, $, |\boldsymbol{\sigma}_j| = 1$, $\boldsymbol{\eta}_j \cdot \boldsymbol{\sigma}_j = 0$. The first relation, $\boldsymbol{\eta}_j \ll \boldsymbol{\sigma}_j$, is the statement that the fast-varying field is a small correction to the slow-varying field

$\boldsymbol{\sigma}_j$ in the high-frequency limit; the second condition imposes normalisation for the slow variable $\boldsymbol{\sigma}_j$; together with the first two, the orthogonality relation, $\boldsymbol{\eta}_j \cdot \boldsymbol{\sigma}_j = 0$, ensures the normalisation of the spin vector $\boldsymbol{S}_j$ at all times:

$$\boldsymbol{S}_j^2 = (1-\boldsymbol{\eta}_j^2)\boldsymbol{\sigma}_j^2 + \boldsymbol{\eta}_j^2 + 2\sqrt{1-\boldsymbol{\eta}_j^2}\boldsymbol{\sigma}_j \cdot \boldsymbol{\eta}_j = 1. \tag{B.14}$$

Note that a similar decomposition is commonly used in spin wave theory [297].

The time-average term exhibits slow dynamics by construction, and does not contribute to the fast motion $\boldsymbol{\eta}_j$; we thus use the remaining term to find the dependence of the fast motion $\boldsymbol{\eta}_j$ on the slow motion $\boldsymbol{\sigma}_j$. To do so, we integrate the right-hand side of Eq. B.12 with respect to the fast time, i.e., we treat the slow motion variables $\boldsymbol{\sigma}_j$ as constant; the leading order contribution to the fast motion is thus given by

$$\boldsymbol{\eta}_j(t) = -J(-1)^j \left(\int_0^t \mathrm{d}t' g(t')\right) \boldsymbol{\sigma}_j \times (\boldsymbol{\sigma}_{j-1} + \boldsymbol{\sigma}_{j+1}) := -J(-1)^j G(t) \boldsymbol{\sigma}_j \times (\boldsymbol{\sigma}_{j-1} + \boldsymbol{\sigma}_{j+1}). \tag{B.15}$$

Note that $G(t)$, shown in Fig. B.1, has the maximum value $\tau/4$, and is thus $\mathcal{O}(\omega^{-1})$. The fast motion $\boldsymbol{\eta}_j$ is therefore also $\mathcal{O}(\omega^{-1})$ and, as expected, vanishes as $\omega \to \infty$.

Our goal is to derive an EOM to order ω^{-1} for the slow motion $\boldsymbol{\sigma}_j$. Taking the full time derivative of Eq. (B.13) (w.r.t. the time t which contains both the slow and the fast time variable), one obtains

$$\dot{\boldsymbol{\sigma}}_j = \frac{\dot{\boldsymbol{S}}_j - \dot{\boldsymbol{\eta}}_j}{\sqrt{1-\boldsymbol{\eta}_j^2}} + \frac{\dot{\boldsymbol{\eta}}_j \cdot \boldsymbol{\eta}_j}{1-\boldsymbol{\eta}_j^2}\boldsymbol{\sigma}_j. \tag{B.16}$$

We now want to eliminate the $\boldsymbol{\eta}_j$ and $\boldsymbol{S}_j$ dependence from the right-hand side. We first use the fact that $\boldsymbol{\eta}_j$ is $\mathcal{O}(\omega^{-1})$ to simplify the denominators by discarding any terms of higher-order than ω^{-1} in inverse-frequency, which yields

$$\sqrt{1-\boldsymbol{\eta}_j^2} = 1 + \mathcal{O}(\omega^{-2}), \qquad 1-\boldsymbol{\eta}_j^2 = 1 + \mathcal{O}(\omega^{-2}). \tag{B.17}$$

Then we can find an expression for $\dot{\boldsymbol{S}}_j$ by inserting the ansatz from Eq. (B.13) into Eq. (B.11), which leads to

$$\dot{\boldsymbol{S}}_j = -J\left[\frac{1}{2} + (-1)^j g(t)\right](\boldsymbol{\sigma}_j + \boldsymbol{\eta}_j) \times [(\boldsymbol{\sigma}_{j-1} + \boldsymbol{\eta}_{j-1}) + (\boldsymbol{\sigma}_{j+1} + \boldsymbol{\eta}_{j+1})] + \mathcal{O}(\omega^{-2}), \tag{B.18}$$

where we also made use of Eq. (B.17). At the same time, taking the derivative of Eq. (B.15) w.r.t. the full time variable (fast and slow), we arrive at

$$\dot{\boldsymbol{\eta}}_j = -J(-1)^j g(t)\, \boldsymbol{\sigma}_j \times (\boldsymbol{\sigma}_{j-1} + \boldsymbol{\sigma}_{j+1}) - J(-1)^j G(t) \frac{\mathrm{d}}{\mathrm{d}t}\left[\boldsymbol{\sigma}_j \times (\boldsymbol{\sigma}_{j-1} + \boldsymbol{\sigma}_{j+1})\right]. \tag{B.19}$$

The two equations above for the derivatives $\dot{\boldsymbol{\eta}}_j$ and $\dot{\boldsymbol{S}}_j$ can now be inserted in Eq. (B.16):

$$\begin{aligned}\dot{\boldsymbol{\sigma}}_j &= \dot{\boldsymbol{S}}_j - \dot{\boldsymbol{\eta}}_j + \dot{\boldsymbol{\eta}}_j \cdot \boldsymbol{\eta}_j \boldsymbol{\sigma}_j + \mathcal{O}(\omega^{-2}) \\ &= -J\left[\frac{1}{2} + (-1)^j g(t)\right][\boldsymbol{\sigma}_j \times (\boldsymbol{\sigma}_{j-1} + \boldsymbol{\sigma}_{j+1}) + \boldsymbol{\eta}_j \times (\boldsymbol{\sigma}_{j-1} + \boldsymbol{\sigma}_{j+1}) + \boldsymbol{\sigma}_j \times (\boldsymbol{\eta}_{j-1} + \boldsymbol{\eta}_{j+1})] \\ &\quad + J(-1)^j g(t)\, \boldsymbol{\sigma}_j \times (\boldsymbol{\sigma}_{j-1} + \boldsymbol{\sigma}_{j+1}) + J(-1)^j G(t) \frac{\mathrm{d}}{\mathrm{d}t}[\boldsymbol{\sigma}_j \times (\boldsymbol{\sigma}_{j-1} + \boldsymbol{\sigma}_{j+1})] \\ &\quad + J^2 G(t) g(t)\, \boldsymbol{\sigma}_j [\boldsymbol{\sigma}_j \times (\boldsymbol{\sigma}_{j-1} + \boldsymbol{\sigma}_{j+1})]^2 \\ &\quad + \mathcal{O}(\omega^{-2}),\end{aligned} \tag{B.20}$$

where, again, Eq. (B.17) has been used. There are two remaining sources of fast motion on the right-hand side of this equation. We eliminate the first, the variable $\boldsymbol{\eta}_j$, using Eq. (B.15). The second source is the time-dependence of the functions $g(t)$ and $G(t)$, which oscillate rapidly in the high-frequency regime $\omega \gg J$ - we thus also need to average over the fast timescale.

To do this, for any function $h(t)$, we define $\overline{h} = \tau^{-1} \int_0^\tau h(t)\mathrm{d}t$ as the time averaged value over one period τ, and obtain [cf. Fig. B.1]

$$\overline{g(t)} = 0, \qquad \overline{G(t)} = \frac{\tau}{8}, \qquad \overline{g(t)G(t)} = 0, \tag{B.21}$$

see Fig. B.1. Next, we insert Eq. (B.15) into Eq. (B.20) and perform the time average of the resulting equation over a single period τ. In the limit $\omega \gg J$, one may assume that the slow variable $\boldsymbol{\sigma}_j$ does not change over the time τ. This yields

$$\begin{aligned}\dot{\boldsymbol{\sigma}}_j = &-\frac{J}{2}\boldsymbol{\sigma}_j \times (\boldsymbol{\sigma}_{j-1} + \boldsymbol{\sigma}_{j+1}) + \frac{(-1)^j J^2 \overline{G}}{2}\,[\boldsymbol{\sigma}_j \times (\boldsymbol{\sigma}_{j-1} + \boldsymbol{\sigma}_{j+1})] \times (\boldsymbol{\sigma}_{j-1} + \boldsymbol{\sigma}_{j+1}) \\ &- \frac{J^2(-1)^j \overline{G}}{2}\,\boldsymbol{\sigma}_j \times [\boldsymbol{\sigma}_{j-1} \times (\boldsymbol{\sigma}_{j-2} + \boldsymbol{\sigma}_j) + \boldsymbol{\sigma}_{j+1} \times (\boldsymbol{\sigma}_j + \boldsymbol{\sigma}_{j+2})] \\ &+ J(-1)^j \overline{G}\,[\dot{\boldsymbol{\sigma}}_j \times (\boldsymbol{\sigma}_{j-1} + \boldsymbol{\sigma}_{j+1}) + \boldsymbol{\sigma}_j \times (\dot{\boldsymbol{\sigma}}_{j-1} + \dot{\boldsymbol{\sigma}}_{j+1})] \\ &+ \mathcal{O}(\omega^{-2}).\end{aligned} \tag{B.22}$$

Finally, in order to derive a self-consistent EOM for $\boldsymbol{\sigma}_j$, we need to eliminate $\dot{\boldsymbol{\sigma}}_j$ from the terms on right-hand side. This can be done by noting that all such terms come with an $\mathcal{O}(\omega^{-1})$ prefactor, since $\overline{G}$ is $\mathcal{O}(\omega^{-1})$. Hence, the derivatives $\dot{\boldsymbol{\sigma}}_j$ on the right-hand-side can be eliminated by using the EOM, Eq. (B.22) itself, but in this instance retaining only terms of $\mathcal{O}(1)$,

$$\dot{\boldsymbol{\sigma}}_j = -\frac{J}{2}\boldsymbol{\sigma}_j \times (\boldsymbol{\sigma}_{j-1} + \boldsymbol{\sigma}_{j+1}) + \mathcal{O}(\omega^{-1}). \tag{B.23}$$

Inserting this back in Eq. (B.22), we arrive at the effective EOM for the slow variable $\boldsymbol{\sigma}_j$,

$$\begin{aligned}\dot{\boldsymbol{\sigma}}_j = \frac{J}{2}(\boldsymbol{\sigma}_{j-1} + \boldsymbol{\sigma}_{j+1}) \times \boldsymbol{\sigma}_j - (-1)^j \frac{J^2 \tau}{8}[(\boldsymbol{\sigma}_{j-2} + \boldsymbol{\sigma}_j) \times \boldsymbol{\sigma}_{j-1} + (\boldsymbol{\sigma}_j + \boldsymbol{\sigma}_{j+2}) \times \boldsymbol{\sigma}_{j+1}] \times \boldsymbol{\sigma}_j \\ + \mathcal{O}(\omega^{-2}).\end{aligned} \tag{B.24}$$

Effective Liouville equation approach

The modern theoretical analysis of prethermalisation is based on Floquet's theorem, which requires the linearity of the equations of motion (EOM) [298]. Since thermalisation can microscopically be traced back to chaotic trajectories, and chaos in classical systems can only occur in non-linear EOM [299], this might at first appear paradoxical. A similar "problem" with Floquet's theorem occurs for quantum dynamics in the Heisenberg picture, where the EOM are also non-linear. The application of Floquet's theorem in these cases is justified by the linearity of the alternative Schrödinger picture based on the Liouville-von Neumann equation for the density operator (phase-space density) [275], which is defined by means of a commutator (Poisson bracket) structure in Hamiltonian mechanics [268]. For classical systems, it is equivalent to the existence of conjugate variables, and induces a symplectic structure on phase space.

Yet a third way to obtain the effective EOM in a systematic expansion controlled by ω^{-1} is as follows: note that the Liouville equation, Eq. (B.9), is a linear, time-periodic ODE for the phase space density. Although, for our system, it cannot be written in its familiar form using the Poisson bracket due to the lack of a symplectic structure, the latter is not required to apply Floquet's theorem.

Indeed, by exploiting this fact, it was shown in Ref. [275] that the Floquet-Magnus expansion can be applied to differential equations of the form

$$\dot{\vec{\boldsymbol{S}}} = \vec{\boldsymbol{X}}(\vec{\boldsymbol{S}}, t), \qquad \vec{\boldsymbol{X}}(\vec{\boldsymbol{S}}, t+\tau) = \vec{\boldsymbol{X}}(\vec{\boldsymbol{S}}, t), \tag{B.25}$$

where $\vec{\boldsymbol{S}}$ denotes all spin variables of the system, and $\vec{\boldsymbol{X}}$ is a (possibly non-linear) but time-periodic vector field flow.

The slow dynamics of the system is then captured by the effective EOM

$$\dot{\vec{\boldsymbol{S}}} = \vec{\boldsymbol{X}}_{\text{eff}}(\vec{\boldsymbol{S}}); \tag{B.26}$$

To leading order in the inverse-frequency, the Floquet-Magnus expansion, we have

$$\begin{aligned}
\vec{\boldsymbol{X}}_{\text{eff}} &= \sum_{n=0}^{\infty} \vec{\boldsymbol{X}}_{\text{eff}}^{(n)}, & \vec{\boldsymbol{X}}_{\text{eff}}^{(n)} &\propto \omega^{-n}, \\
\vec{\boldsymbol{X}}_{\text{eff}}^{(0)} &= \frac{1}{\tau}\int_0^t \mathrm{d}t \vec{\boldsymbol{X}}(\vec{\boldsymbol{S}}, t), \\
\vec{\boldsymbol{X}}_{\text{eff}}^{(1)} &= \frac{1}{4\pi\omega}\int_0^t \mathrm{d}t_1 \int_0^{t_1} \mathrm{d}t_2 \left[\vec{\boldsymbol{X}}(\vec{\boldsymbol{S}}, t_1), \vec{\boldsymbol{X}}(\vec{\boldsymbol{S}}, t_2)\right]_{\mathcal{L}},
\end{aligned} \tag{B.27}$$

where the Lie bracket $[\cdot,\cdot]_{\mathcal{L}}$ of two vector fields $\vec{\boldsymbol{X}}(\vec{\boldsymbol{S}})$ and $\vec{\boldsymbol{Y}}(\vec{\boldsymbol{S}})$ is defined as

$$\mathcal{L}_{\vec{\boldsymbol{X}}}\vec{\boldsymbol{Y}} = \left[\vec{\boldsymbol{X}}(\vec{\boldsymbol{S}}), \vec{\boldsymbol{Y}}(\vec{\boldsymbol{S}})\right]_{\mathcal{L}} = \vec{\boldsymbol{X}}(\vec{\boldsymbol{S}}) \cdot \vec{\nabla}_{\vec{\boldsymbol{S}}}\vec{\boldsymbol{Y}}(\vec{\boldsymbol{S}}) - \vec{\boldsymbol{Y}}(\vec{\boldsymbol{S}}) \cdot \vec{\nabla}_{\vec{\boldsymbol{S}}}\vec{\boldsymbol{X}}(\vec{\boldsymbol{S}}). \tag{B.28}$$

Performing the derivatives and calculating the time-ordered integral, we arrive at the effective EOM in Eq. (9.18).

B.2 Comparison between Hamiltonian (reciprocal) and non-reciprocal drives

In Ch. 9 we analysed a non-reciprocal drive for the classical Heisenberg chain, given by the successive evolution of even and odd-numbered sites. A natural complement of this is to consider a drive given by the successive evolution of even and odd-numbered *bonds* (cf. App. A).

In contrast to the non-reciprocal site-based drive considered in the main text, the bond-based drive *is* reciprocal, and is generated by the time-dependent Hamiltonian

$$H_{\mathrm{rec}}(t) = J \sum_j \left(\frac{1}{2} + (-1)^j g(t) \right) \boldsymbol{S}_j \cdot \boldsymbol{S}_{j+1}, \tag{B.29}$$

which has the same infinite-frequency limit H_∞ as the non-reciprocal drive; the two drives differ in the way they approach the infinite-frequency limit.

As in the non-reciprocal case, each step of the reciprocal drive is exactly solvable. In contrast to the non-reciprocal drive, the reciprocal drive exactly conserves the magnetisation; it does not, however, conserve the energy H_∞ (at finite frequency). This is the canonical situation to which rigorous estimates for the rate of energy absorption [268] apply, and we numerically verify these predictions.

We take the same initial ensemble at $\beta = 1$ as we used for the non-reciprocal evolution in Ch. 9. In Fig. B.2, we find that the system heats up to the maximum entropy state consistent with the conserved magnetisation (i.e., $\langle E \rangle \to J \langle M \rangle^2$), and that, as expected from Ref. [268], the heating time t_E is exponentially suppressed with the driving frequency, $t_E \sim \exp(-c\,\omega)$, for some model-dependent constant c. This stands in stark contrast to the algebraic suppression observed for the non-reciprocal drive in Ch. 9.

B.3 Time-reversal symmetry breaking drives – the triangular lattice

The bipartite non-reciprocal drive from Eq. (9.1) preserves time-reversal symmetry, in the sense that there exists a Floquet gauge t_0 [243] in which the drive is symmetric under time-reversal. This implies that the first-order correction in the van Vleck IFE must vanish [243], and hence $\mathcal{H}_{\mathrm{eff}} \sim \mathcal{H}^{(0)}_{\mathrm{eff}} + \mathcal{H}^{(2)}_{\mathrm{eff}}$. As discussed in 9.4.3, this may lead one to the incorrect conclusion that the ω^4-scaling arises perturbatively in the IFE using Fermi's Golden rule.

As we explain in detail below, however, this is not the case. To see why, notice first that, according to Floquet theory, drives that break time-reversal symmetry necessarily have a non-vanishing first-order correction $\mathcal{H}^{(1)}_{\mathrm{eff}}$ [243]. Fermi's Golden rule would then naively imply an ω^2 scaling. However, the triangular lattice Heisenberg model, under a time-reversal-symmetry breaking drive, which we discus in detail below, exhibits an ω^4 prethermal behaviour (Fig. 9.2, triangles). This shows that the ω^4 law is not captured by the perturbative IFE.

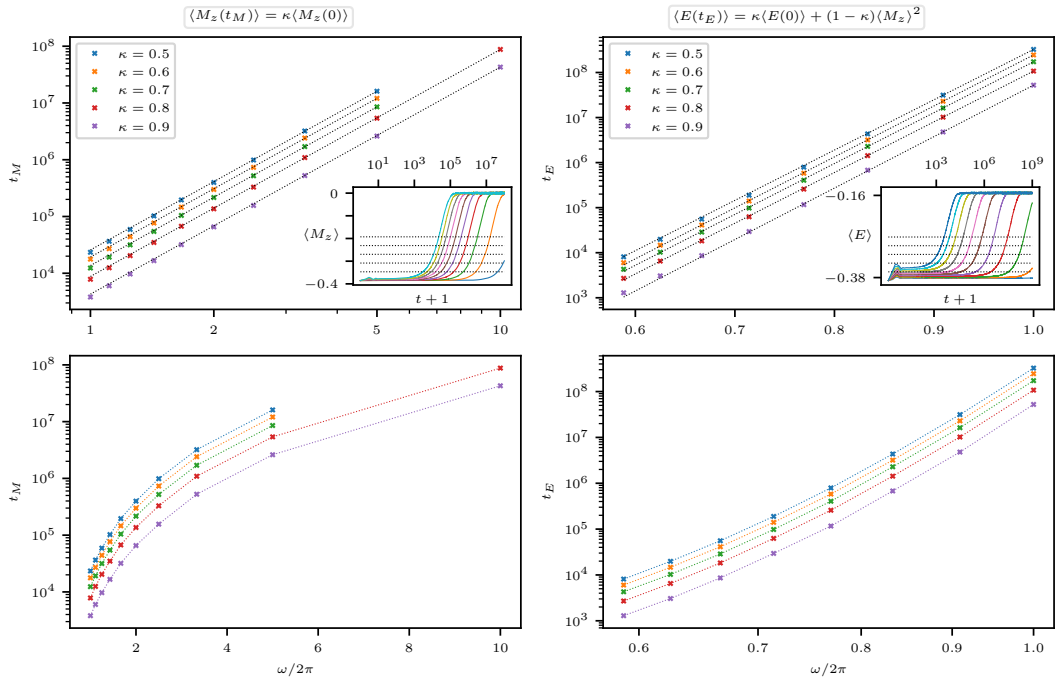

Figure B.2: Comparison between the magnetisation loss in the *non-reciprocal* drive (left) and Floquet heating in the *reciprocal* (Hamiltonian) drive (right), for the same initial ensemble (2000 states, $\beta = 1$, $L = 128$). (Upper panels) Both drives exhibit a prethermal plateau (see insets), but heating in the reciprocal drive is suppressed exponentially, compared to the power-law suppression in the non-reciprocal drive. Inset for the non-reciprocal drive shows the curves from $\tau = 0.1$ (rightmost) to $\tau = 1.0$ (leftmost); inset for the reciprocal drive shows the curves from $\tau = 0.8$ (rightmost) to $\tau = 1.8$ (leftmost). The functional form of the suppression is independent of the threshold value (controlled by κ) used to define t_M and t_E – the dotted lines in the insets correspond to $\kappa = 0.5$ (top) to $\kappa = 0.9$ (bottom). (Lower panels) show convincingly that the non-reciprocal drive is not described by an exponential suppression, and, conversely, that the reciprocal drive is not described by a power-law suppression.

The general tripartite non-reciprocal periodic drive has the equations of motion:

$$\begin{cases} \dot{\boldsymbol{S}}_j^\mu = \epsilon^{\mu\nu\lambda}\left(\sum_i J_{ij}^\nu \boldsymbol{S}_i^\nu\right)\boldsymbol{S}_j^\lambda, & j\in\mathcal{A} \\ \dot{\boldsymbol{S}}_j = 0, & j\in\mathcal{B} \\ \dot{\boldsymbol{S}}_j = 0, & j\in\mathcal{C} \end{cases} ; \quad \text{for } t\in\left[0,\tfrac{\tau}{3}\right),$$

$$\begin{cases} \dot{\boldsymbol{S}}_j = 0, & j\in\mathcal{A} \\ \dot{\boldsymbol{S}}_j^\mu = \epsilon^{\mu\nu\lambda}\left(\sum_i J_{ij}^\nu \boldsymbol{S}_i^\nu\right)\boldsymbol{S}_j^\lambda, & j\in\mathcal{B} \\ \dot{\boldsymbol{S}}_j = 0, & j\in\mathcal{C} \end{cases} ; \quad \text{for } t\in\left[\tfrac{\tau}{3},\tfrac{2\tau}{3}\right), \tag{B.30}$$

$$\begin{cases} \dot{\boldsymbol{S}}_j = 0, & j\in\mathcal{A} \\ \dot{\boldsymbol{S}}_j = 0, & j\in\mathcal{B} \\ \dot{\boldsymbol{S}}_j^\mu = \epsilon^{\mu\nu\lambda}\left(\sum_i J_{ij}^\nu \boldsymbol{S}_i^\nu\right)\boldsymbol{S}_j^\lambda, & j\in\mathcal{C} \end{cases} ; \quad \text{for } t\in\left[\tfrac{2\tau}{3},\tau\right),$$

where $\mathcal{A}$, $\mathcal{B}$, $\mathcal{C}$ denote the three sublattices, cf. Fig. B.3. The $\mathcal{ABCABC}$ pattern of this drive (where each step is labelled by the sublattice which is evolving) violates time-reversal because there is no time t_0 about which this drive is even – time-reversal will always flip this to a $\mathcal{CBACBA}$ pattern. By contrast, the bipartite drive, as written in Eq. (9.1), *is* time-reversal symmetric about $t_0 = \tau/4$.

Like Eq. (9.1), this non-reciprocal drive is not generated from any Hamiltonian for the $\boldsymbol{S}$-degrees of freedom alone. Again, however, we may use the auxiliary degrees of freedom to construct a Hamiltonian amenable to analysis by IFE. This is more involved than in the bipartite case, since we now require couplings between different auxiliaries. We write the Hamiltonian of the extended system as

$$\mathcal{H}(t) = \sum_{i,j} J_{ij}\boldsymbol{S}_i\cdot\boldsymbol{S}_j + \sum_{i,j}\boldsymbol{a}_i\cdot\left(f_{ij}(t)\boldsymbol{S}_j + g_{ij}(t)\boldsymbol{a}_j\right). \tag{B.31}$$

Note that $f_{ij}(t)\neq f_{ji}(t)$. We show the values of these couplings in Fig. B.3.

Now, following Ref. [300], the first-order term in the van Vleck IFE is

$$\mathcal{H}_{\text{eff}}^{(1)} = \frac{1}{2!\tau}\int_0^\tau dt_1\int_0^{t_1} dt_2\ \frac{2}{\tau}\left[\left(\frac{\tau}{2}-(t_1-t_2)\right)\mathrm{mod}\tau\right]\{\mathcal{H}(t_1),\mathcal{H}(t_2)\}. \tag{B.32}$$

A straightforward calculation shows that the relevant Poisson bracket is

$$\begin{aligned}\{\mathcal{H}(t_1),\mathcal{H}(t_2)\} = \sum_{ijl}\epsilon^{\mu\nu\lambda}\Big(& J_{ij}\left[f_{lj}(t_2)-f_{li}(t_2)-f_{lj}(t_1)+f_{li}(t_1)\right]a_l^\nu S_i^\mu S_j^\lambda \\ &+ f_{lj}(t_1)f_{il}(t_2)a_i^\mu S_j^\nu S_l^\lambda \\ &+ \left[f_{il}(t_1)f_{jl}(t_2)-2f_{il}(t_1)g_{ij}(t_2)-2g_{ij}(t_1)f_{il}(t_2)\right]a_i^\mu a_j^\nu S_l^\lambda \\ &+ \left[2g_{ij}(t_1)g_{il}(t_2)-2g_{ij}(t_1)g_{jl}(t_2)\right]a_i^\mu a_j^\nu a_l^\lambda\Big).\end{aligned} \tag{B.33}$$

To show that $\mathcal{H}_{\text{eff}}^{(1)}\neq 0$, it suffices to show that any one of the unlike terms is non-zero, so we focus on the *a*-*a*-*a* term,

$$\sum_{ijl}\epsilon^{\mu\nu\lambda}\left[2g_{ij}(t_1)g_{il}(t_2)-2g_{ij}(t_1)g_{jl}(t_2)\right]a_i^\mu a_j^\nu a_l^\lambda. \tag{B.34}$$

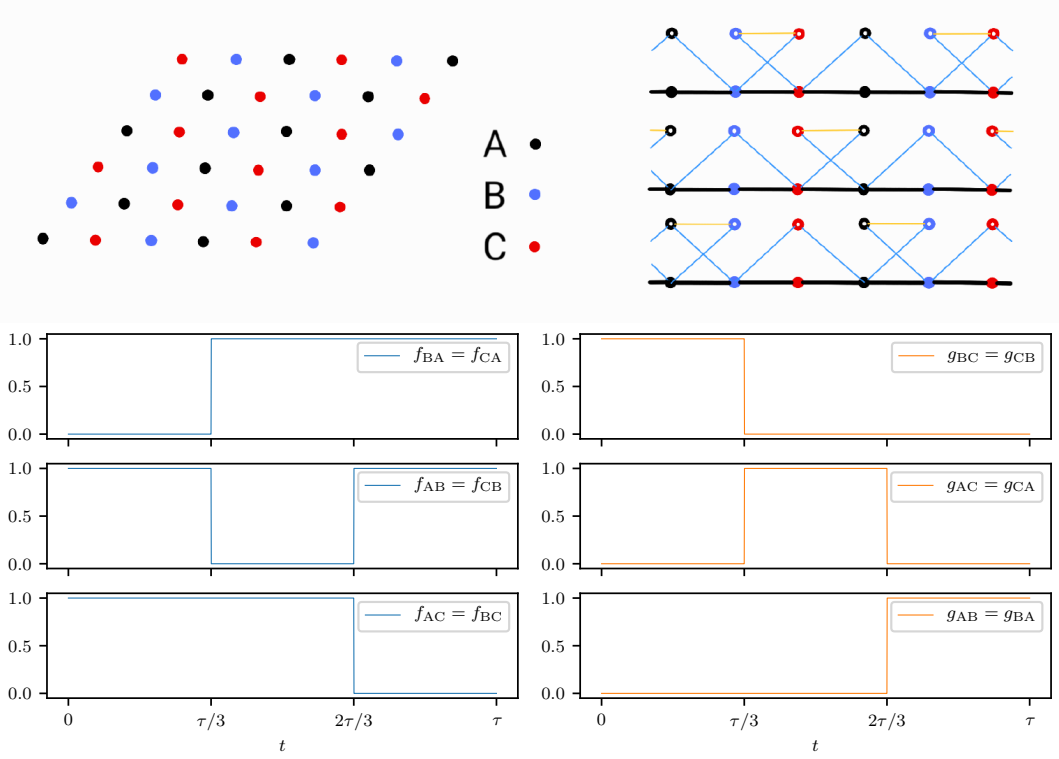

Figure B.3: The tripartite drive for the triangular lattice. (Top left): an example tripartite decomposition of the triangular lattice. (Top right): configuration of couplings f and g (blue and orange lines, respectively), for each step of the drive ($\mathcal{ABC}$, from the top down); the black lines show the $\boldsymbol{S} - \boldsymbol{S}$ couplings, which are always on. $\boldsymbol{S}$-degrees of freedom are represented by filled circles; the auxiliaries by empty circles. (Lower panels): the values of the couplings f and g across one drive-period for the tripartite drive.

Now, under the sum, we must have that i, j, l are distinct sites, or the anti-symmetric tensor will kill the term. Without loss of generality, let $i \in \mathcal{A}$. Since $\mathcal{A}$ sites are not nearest-neighbours of $\mathcal{A}$ sites, we must then have $j \in \mathcal{B}, \mathcal{C}$ (or $g_{ij} = 0$ will kill the term); again, without loss of generality, let $j \in \mathcal{B}$.

Now, *a priori*, l may belong to any sublattice, so long as $l \neq i, j$. The various cases yield:

$$\begin{cases} l \in \mathcal{A}: & 2g_{AB}(t_1)g_{AA}(t_2) - 2g_{AB}(t_1)g_{BA}(t_2) = -2g_{AB}(t_1)g_{BA}(t_2) \\ l \in \mathcal{B}: & 2g_{AB}(t_1)g_{AB}(t_2) - 2g_{AB}(t_1)g_{BB}(t_2) = 2g_{AB}(t_1)g_{BA}(t_2) \\ l \in \mathcal{C}: & 2g_{AB}(t_1)g_{AC}(t_2) - 2g_{AB}(t_1)g_{BC}(t_2) = 0. \end{cases} \tag{B.35}$$

The relevant time-ordered integral in the IFE, therefore, is

$$\frac{1}{2!\tau}\int_0^\tau dt_1 \int_0^{t_1} dt_2 \; \frac{2}{\tau}\left[\left(\frac{\tau}{2} - (t_1 - t_2)\right) \mathrm{mod}\tau\right] g_{AB}(t_1)g_{AB}(t_2) = \frac{7\tau}{648} \neq 0. \tag{B.36}$$

This implies, at least, that the a-a-a terms do not vanish.

It follows that $\mathcal{H}^{(1)}_{\text{eff}} \neq 0$, as expected in the absence of time-reversal symmetry, and that the ω^4-scaling of the prethermal lifetime in the non-reciprocal periodically-driven spin dynamics cannot be explained perturbatively using the IFE.

B.4 Details of the numerical simulations

In this appendix we provide further details of our numerical procedures. We first discuss the construction of the initial states in the thermal ensembles, and then give an overview of the integration of the equations of motion.

B.4.1 Initial ensemble

The initial states are constructed using heatbath Monte Carlo (MC) simulations [115], which uses the fact that the thermal distribution of a single spin $\boldsymbol{S}_i$ in its local field $\boldsymbol{S}_{i-1}+\boldsymbol{S}_{i+1}+h\hat{\boldsymbol{z}}$ is exactly invertible (cf. App. A). We use ensembles of 2000 states, and each state begins as a completely independent random configuration. We then perform 10^5 heatbath sweeps to cool the state to the desired temperature. We use the same set of 2000 initial states for all dynamical evolution protocols (for a fixed L and β), to ensure a fair comparison between the reciprocal and non-reciprocal drives, and between the exact non-reciprocal dynamics and the dynamics given by the effective Floquet-Magnus Hamiltonian; we have checked that using different initial ensembles does not change the reported results.

B.4.2 Dynamical evolution

We now turn to the details of the dynamical evolution. The non-reciprocal drive, Eq. (9.1), and the reciprocal drive in Eq. (B.29), can be integrated to machine precision, since the exact solution can be written in closed form for each step of the drive: a single spin in a constant magnetic field evolves as

$$\dot{\boldsymbol{S}} = \boldsymbol{M} \times \boldsymbol{S} \quad \Rightarrow \quad \boldsymbol{S}(t) = \exp(\boldsymbol{M} \cdot \boldsymbol{R}\ t)\boldsymbol{S}(0), \tag{B.37}$$

where $\boldsymbol{R}$ denotes the (vector of) the generators of rotations. For the non-reciprocal drive, half of the spins $\boldsymbol{S}_i$ evolve in the constant (over the half-period) field $\boldsymbol{S}_{i-1} + \boldsymbol{S}_{i+1}$; for the reciprocal drive, the spins on a bond $\{i, i+1\}$ evolve in the constant field $\boldsymbol{S}_i + \boldsymbol{S}_{i+1}$ (see also App. A).

The fact that each step of the drive is exactly solvable means that the numerical evolution is very efficient and accumulates only machine precision errors, allowing us to evolve to long times $t_f = 10^8$, or even $t_f = 10^9$. The values of the energy H_∞ and the magnetisation $\boldsymbol{M}_z$ are stored at 10^4 stroboscopic times on a log-spaced (to the nearest stroboscopic time $t \in \tau\mathbb{Z}$) grid.

In contrast, the dynamics generated by the effective Hamiltonians $\mathcal{H}^{(1)}_F$ and $\mathcal{H}^{(2)}_F$ are not exactly integrable, and we use the standard fourth-order Runge-Kutta (RK4) method with a time-step of $\delta t = 0.001$ (in units of $|J| = 1$). We store the values of the observables at the stroboscopic times on the log-spaced grid used for the exact dynamics, up to the final time of the RK4 simulations, $t_f = 10^6$. With these values of δt and t_f, the typical error in the

energy density over the simulations (which should be conserved by the non-reciprocal drive and its effective Hamiltonians) is $\sim 10^{-12}$.

B.5 Contradictions in the canonical quantisation of the non-reciprocal periodic drive

In this section, we argue that a physical quantum version of the non-reciprocal periodic drive in Eq. (9.1) does *not* exist. In particular, we show that there exists no completely positive trace-preserving (CPTP) time-periodic map, such that: (i) in the infinite-frequency limit, the dynamics reduces to that of the quantum Heisenberg model, and (ii) in the classical limit, the dynamics reduces to Eq. (9.1).

It suffices to restrict to a two-spin system and set $J = 1$. Now, the classical Liouville equation for the phase space density $\rho(\boldsymbol{S}_1, \boldsymbol{S}_2; t)$, which evolves following the flow field corresponding to Eq. (9.1), is

$$\begin{cases} \partial_t \rho(\boldsymbol{S}_1, \boldsymbol{S}_2; t) = S_2^\alpha \{S_1^\alpha, \rho(\boldsymbol{S}_1, \boldsymbol{S}_2; t)\}, & t \in \left[0, \frac{\tau}{2}\right), \\ \partial_t \rho(\boldsymbol{S}_1, \boldsymbol{S}_2; t) = S_1^\alpha \{S_2^\alpha, \rho(\boldsymbol{S}_1, \boldsymbol{S}_2; t)\}, & t \in \left[\frac{\tau}{2}, \tau\right), \end{cases} \tag{B.38}$$

where, $\{\cdot, \cdot\}$ denotes the Poisson bracket. These equations satisfy condition (i) above, which can be seen by taking the time-average.

Naively, quantising Eqs. (B.38) is straightforward: one replaces the spin variables by the corresponding operators, $\{\cdot, \cdot\} \mapsto -i[\cdot, \cdot]$, and the product of two functions by half their anti-commutator, $f(\boldsymbol{S}_1, \boldsymbol{S}_2) g(\boldsymbol{S}_1, \boldsymbol{S}_2) \mapsto \frac{1}{2}[f(\boldsymbol{S}_1, \boldsymbol{S}_2), g(\boldsymbol{S}_1, \boldsymbol{S}_2)]_+$. This leads to a von Neumann-like equation for the quantum density matrix:

$$\begin{cases} \partial_t \hat{\rho}(t) = -\frac{i}{2}[S_2^\alpha, [S_1^\alpha, \hat{\rho}(t)]]_+ , & \text{for } t \in \left[0, \frac{\tau}{2}\right), \\ \partial_t \hat{\rho}(t) = -\frac{i}{2}[S_1^\alpha, [S_2^\alpha, \hat{\rho}(t)]]_+ , & \text{for } t \in \left[\frac{\tau}{2}, \tau\right). \end{cases} \tag{B.39}$$

Note that the second equation is equivalent to the first under the exchange of the spin variables, $\boldsymbol{S}_1 \leftrightarrow \boldsymbol{S}_2$, as expected.

Next, we rewrite these equations to isolate the period-averaged contribution:

$$\begin{cases} \partial_t \hat{\rho}(t) = -\frac{i}{2}[S_1^\alpha S_2^\alpha, \hat{\rho}(t)] - \frac{i}{2}\left(S_2^\alpha \hat{\rho} S_1^\alpha - S_1^\alpha \hat{\rho} S_2^\alpha\right) , & \text{for } t \in \left[0, \frac{\tau}{2}\right), \\ \partial_t \hat{\rho}(t) = -\frac{i}{2}[S_1^\alpha S_2^\alpha, \hat{\rho}(t)] - \frac{i}{2}\left(S_1^\alpha \hat{\rho} S_2^\alpha - S_2^\alpha \hat{\rho} S_1^\alpha\right) , & \text{for } t \in \left[\frac{\tau}{2}, \tau\right). \end{cases} \tag{B.40}$$

Clearly, Eqs. (B.40) obey conditions (i) and (ii). Moreover, it is straightforward to check that Eqs. (B.40) preserve the trace of the density matrix $\hat{\rho}$. However, Eqs. (B.40) do not define completely positive maps – that is, some eigenvalues of $\hat{\rho}(t)$ may become negative; a contradiction if the density matrix is to be interpreted as a probability distribution. To see this, it suffices to focus on the first half-cycle, and re-write the second term as

$$\begin{aligned} -\frac{i}{2}\left(S_2^\alpha \hat{\rho} S_1^\alpha - S_1^\alpha \hat{\rho} S_2^\alpha\right) &= -\frac{i}{2}\left(S_2^\alpha \hat{\rho} S_1^\alpha - S_1^\alpha \hat{\rho} S_2^\alpha - \frac{1}{2}[S_1^\alpha S_2^\alpha, \hat{\rho}]_+ + \frac{1}{2}[S_1^\alpha S_2^\alpha, \hat{\rho}]_+\right) \\ &=: \sum_{m,n} h_{mn}\left(L_m \hat{\rho} L_n^\dagger - \frac{1}{2}[L_n^\dagger L_m, \hat{\rho}]_+\right), \end{aligned} \tag{B.41}$$

with $L_m = (S_1^x, S_1^y, S_1^z, S_2^x, S_2^y, S_2^z)_m$ and $L_n^\dagger = (S_2^x, S_2^y, S_2^z, S_1^x, S_1^y, S_1^z)_n$. One can convince oneself that, with the above definition, $h_{mn} = h_{nm}^* \in i\mathbb{R}$ is both Hermitian and purely imaginary. Hence, the eigenvalues of h come in pairs, $(-\lambda_i, \lambda_i)$, of positive and negative numbers. This implies that h is not positive semi-definite, and thus the above equation does not define a completely positive map, despite its formal similarity with the Lindblad master equation. It follows that the quantised equations of motion, Eq. (B.40), are not CPTP maps, and thus do not govern the dynamics of a physical quantum system.

This implies the non-reciprocal drive provides an example of a system with a well-defined classical phase space dynamics (via Eq. (B.38)) for which no quantum equivalent exists. Recently, it was demonstrated that periodically-driven open quantum systems do not always possess a Floquet Lindbladian [301], which might be related to symplecticity breaking.

List of Publications

- A. J. McRoberts, T. Bilitewski, M. Haque, and R. Moessner
  Anomalous dynamics and equilibration in the classical Heisenberg chain
  Phys. Rev. B **105**, L100403 (2022)

- A. J. McRoberts, T. Bilitewski, M. Haque, and R. Moessner
  Long-lived solitons and their signatures in the classical Heisenberg chain
  Phys. Rev. E **106**, L062202 (2022)

- A. J. McRoberts, J. F. Mendez-Valderrama, R. Moessner, and D. Chowdhury
  Intermediate-scale theory for electrons coupled to frustrated local-moments
  Phys. Rev. B **107**, L020402 (2023)

- A. J. McRoberts, F. Balducci, R. Moessner, and A. Scardicchio
  Subdiffusive spin transport in disordered classical Heisenberg chains
  Phys. Rev. B **108**, 094204 (2023)

- A. J. McRoberts, H. Zhao, R. Moessner, and M. Bukov
  Prethermalization in periodically-driven nonreciprocal many-body spin systems
  Phys. Rev. Research **5**, 043008 (2023)

- A. J. McRoberts, T. Bilitewski, M. Haque, and R. Moessner
  Domain wall dynamics in classical spin chains:
  free propagation, subdiffusive spreading, and topological soliton emission
  arXiv 2306.15351

Versicherung

Hiermit versichere ich, dass ich die vorliegende Arbeit ohne unzulässige Hilfe Dritter und ohne Benutzung anderer als der angegebenen Hilfsmittel angefertigt habe; die aus fremden Quellen direkt oder indirekt übernommenen Gedanken sind als solche kenntlich gemacht. Die Arbeit wurde bisher weder im Inland noch im Ausland in gleicher oder ähnlicher Form einer anderen Prüfungsbehörde vorgelegt.

Adam McRoberts

Dresden